Crystallization of membrane proteins with an automated microfluidic pipeline

Sofia Jaho

THÈSE

Pour obtenir le grade de

DOCTEUR DE L'UNIVERSITÉ GRENOBLE ALPES

Spécialité : Physique pour les Sciences du Vivant

Arrêté ministériel : 25 mai 2016

Présentée par

Sofia JAHO

Thèse dirigée par **Monika SPANO**,Maître de Conférence, Université Grenoble Alpes

préparée au sein du **Laboratoire Institut de Biologie Structurale** dans **l'École Doctorale Physique**

Cristallisation des protéines membranaires avec une plateforme microfluidique automatisée

Crystallization of membrane proteins with an automated microfluidic pipeline

Thèse soutenue publiquement le **8 juin 2021**, devant le jury composé de :

Monsieur AHMED HAOUZ
INGENIEUR HDR, INSTITUT PASTEUR, Rapporteur
Monsieur SEBASTIEN TEYCHENE
MAITRE DE CONFERENCE HDR, TOULOUSE INP, Rapporteur
Monsieur WIM BURMEISTER
PROFESSEUR DES UNIVERSITES, UNIVERSITE GRENOBLE ALPES, Président
Madame MIRJAM CZJZEK
DIRECTEUR DE RECHERCHE, CNRS BRETAGNE ET PAYS DE LA LOIRE, Examinatrice
Monsieur JEAN-BAPTISTE SALMON
DIRECTEUR DE RECHERCHE, CNRS DELEGATION AQUITAINE, Examinateur
Monsieur WILLIAM SHEPARD
CHARGE DE RECHERCHE, CNRS DELEGATION ILE-DE-FRANCE SUD, Examinateur

Acknowledgements

I started my PhD in October 2017 and now, it's summer of 2021. I genuinely like writing and writing my thesis was a pleasant procedure, despite the associated stress and eagerness to present the hard work of nearly 4 years. However, I find it more difficult to write down my acknowledgements. How can I thank enough and acknowledge all the people who accompanied me in this journey? And it has been a long journey that started way before October 2017, when I was still a kid and somehow, I knew that no matter what life brings on, I wanted to be a scientist. I hope that over the years, I showed my gratitude to everyone who helped me, stood by me, encouraged me and believed in me. And I hope that in the following lines, I will remind them how grateful I feel for their support.

First of all, I would like to acknowledge the contribution of my thesis supervisor Monika Spano. Monika, 4 years ago you gave me the opportunity to leave Greece and join you in Grenoble in the framework of our European project. I think I have told you the story of how I found this position. It was actually a friend of mine who found the advertisement of the position, and knowing my passion for crystallization, he suggested me to apply. You know the rest of the story since we shared it together over the past years. I am grateful for this opportunity. I am grateful that you were supporting, guiding and trusting me during the course of the project. Many times, I had the feeling that you treated me as a partner and not just a student, contributing to the development of my professional qualifications. I hope my work and my presence in the lab made you content for your choice. Maybe, this part of my journey has come to an end, but I would like you to know that I will always feel a member of this project and I know that our communication will continue in the future.

I would like to express my immense gratitude to the members of my thesis committee. I want to thank Ahmed Haouz and Sébastien Teychené who accepted to be my reporters. I hope you enjoyed reading the manuscript. I want to thank Wim Burmeister for accepting to be the president of the jury and coordinate the discussion and the procedure during my defense. Mirjam Czjzek, Jean-Baptiste Salmon and William Shepard thank you for being members of my jury and contributing in the rich, prolific discussion during my defense. Thank you all for this honor and for making my defense day a memorable day for me. I hope our paths will cross again in the future.

As I briefly mentioned above, my thesis was part of the Innovative Training Network (ITN) RAMP (RAtionalizing Membrane Protein crystallization), funded from the European Union's Horizon 2020 Research and Innovation program under the Marie Skłodowska Curie grant agreement no 722687. Working with other RAMP partners and spending time in their labs during my secondments, was a major part of my PhD journey. I spent time in LOF (Laboratory of the Future, Bordeaux, France) working with Jean-Baptiste Salmon and his collaborators Camille Keita and Hoang-Thanh Nguyen, whom I thank for their help. Jean-Baptiste, thank you for introducing me to the wonderful world of microfluidics, for teaching me and mentoring me whenever I needed your guidance. It was a great pleasure to meet you and work with you. I also want to thank Danièle Centanni and LIPhy (UGA), where I fabricated my microchips when I was in Grenoble. I spent time in Trinity College Dublin (TCD) in the lab of Martin Caffrey (Membrane Structural and Functional Biology/MSFB lab) where I learned the LCP crystallization method. I would like to thank Martin and all the people

in the MSFB lab for welcoming me and introducing me to the eminent work that they are doing. Another one of my secondments was accommodated in the Center for Free Electron Lasers (CFEL) in the laboratory of Arwen Pearson where I worked with another RAMP student, Diogo Melo. Arwen thank you for having me in your lab. It was a time well-spent that I will always value. Diogo, thank you for helping me, for teaching me, for all the discussions we have had over the years, for your friendship and the time we spent in Hamburg and in Grenoble. My final secondment was in Gothenburg where I worked in AstraZeneca in collaboration with Margareta Ek. I am grateful to Margareta and all the people that I met there, who were interested in trying my microchips for crystallization and for giving me the opportunity to experience and work in an environment other than the academic.

Being a RAMP member was one of my greatest joys over the past years. The feeling of belonging to our "RAMP family", the anticipation of meeting the other students and partners during the secondments and workshops, the trips, the laughters, the support, the drinks, the funny moments, the science, the questions, the common goals,... I wouldn't change any part of our common experience and PhD journey. My dear RAMP friends, Elham, Claudia, Jannik, Sofia, Marty, Cristina, Diogo, My, Virginia, Swati, Sam and Jessica, my sincere gratitude for your friendship and for teaching me so many things in a scientific and personal level. I feel lucky for meeting you all and truly wish that one day we shall meet again for a RAMP reunion. At this point, I also want to thank Jannik and Sam for providing me their precious protein samples to be tested for crystallization with my microchips.

In Grenoble, I was a member of the GSY group at IBS while I spent also most of my time at ESRF. I want to express my gratitude to all the members of the GSY group for their help, their acceptance and their genuine interest in me and my work. Dear Jean-Luc Ferrer, you were our group leader and you tried your best despite your busy schedule to make sure that I was conducting my thesis without any troubles. Your loss was difficult for us all, but I will always remember your warmth and your support. Antoine Royant, thank you very much for all your help and for making sure that I could finish my PhD under the best possible conditions, even during the coronavirus pandemics. Franck Borel and David Cobessi, thank you both for teaching me crystallography and for being patient with me. I will always cherish our trips to Barcelona and Hamburg, the coffee breaks in the office, the discussions and your unique sense of humour. I would also like to thank all the people of the Metallo group at IBS who practically helped me several times in the lab. Yoann Sallaz-Damaz, thank you for being my friend, my mentor. I recall our discussions, our jokes, our work together and I am so grateful for all the moments. It is a pity that now you should find someone else to carry around detectors and cables! Christophe Berzin, it was such a pleasure to share the office with you over the past 1 year. Thank you for your help, for your understanding and for inspiring me to keep developing my photography skills. Philippe Jacquet, you were the first person with whom I shared my office. Thank you for all your help in technical parts but also in discovering and enjoying Grenoble. Eric Rivé-Mathieu, you came to our group during the construction of the new beamline and your integration in the group was a great pleasure. Thank you so much for your help, your kindness, your vast knowledge and your sincere interest. I am also grateful for meeting the people of the French CRG group at ESRF and sharing nearly 4 wonderful years with them. Since my arrival at ESRF, they made me feel like home. I

already miss our lunch time together, our discussions, our laughters, our pots de Nöel,… Thank you for your kindness and your interest. Thank you for encouraging me to learn how to bike and for tolerating my poor level of speaking French. I hope I will meet you again in the future when I return to ESRF as a user. And last but not least, I want to thank a former member of the GSY group, Niels Junius, who's work, before my arrival, was fundamental to my PhD. Niels, you started the work with the dialysis microchips and I want to sincerely thank you for your help during these 4 years. I hope you saw the project evolve the way you imagined it when you finished your thesis.

My life in Grenoble has also been made memorable by the presence of unique, wonderful people that I've met over the years. Dear Elham, we started and we successfully finished this journey together. Thank you for all your help in the lab, for sharing your protocols with me, for supporting me. I will always remember our coffee breaks at the bench at ESRF, my short visits to your office, the annoying knocking on the door, the adventures we had together in Grenoble and all around Europe, Budapest and Muse,… So many memories in such a short time. I already miss our everyday life together. My dear Kypriane, you were the first person that I met in Grenoble. Over the past two years you have been my safe place. I am grateful for your presence in my life, your friendship, the long discussions, the movie nights, the coffee breaks during laundry, the late-night calls, and for so many moments that I deeply cherish. I keep you in my thoughts and my heart. My glykaki Dorina, you came to my life only recently but I am grateful for our meeting, for your presence in my life, for your compassion, your friendship. Rémi, thank you for all your help in the lab, for being a good friend, for all the randonées and of course for the unforgettable experience of canyoning. Mary, Aggeliki, Taki, Vicky, Yrw, Gianni, Jola, Alex, Aki, Spyro, Maria, Kavya, Nikola, Yiorgo, Sofia, Laetitia thank you so much for your love, your friendship and support over the years. You are always by my side, no matter the distance.

Finally, I would like to thank my family. This PhD and my course so far is dedicated to them, to my parents and my brother. They have always been an endless inspiration of love, dedication, hard work and kindness. They stand by my side no matter what, they believe in me, they just want to see me grow and be a nice person. And I just want to make them proud. Albano, Xhemil and Nadja, you made this dream come true.

"Only those who will risk going too far can possibly find out how far one can go." (T. S. Eliot)

Abstract

Crystallization and crystallographic studies with various diffraction techniques are the key steps in deciphering protein structures and understanding the mechanisms of their action in relation to their biological functions. The most predominant and advanced technique applied for structural studies of biological macromolecules is synchrotron X-ray diffraction. Acquiring protein crystals with an adequate diffraction quality that can reveal structural details near to atomic resolution can be challenging. Conventional crystallization methods like vapor diffusion or batch have been employed for protein crystallization and instrumental developments, concentrating over the years on reducing the sample consumption in parallel experiments for screening crystallization conditions. However, finding optimal conditions for yielding well-diffracting crystals can be compromised if sensitive variables that affect crystallization cannot be precisely controlled.

Instrumental and methodological developments were implemented to address some of the challenges encountered in protein crystallography. We have developed a microfluidic chip and a platform (MicroCrys) for optimizing and rationalizing protein crystallization. Model soluble and membrane proteins were crystallized on chip with the microdialysis method and the crystals were used for *in situ* synchrotron serial X-ray crystallography (SSX). Microdialysis, combined with temperature control, offers a reversible and precise control over crystallization and can be used to decouple nucleation from crystal growth for investigating protein phase diagrams. Automating the on chip crystallization process with MicroCrys allows crystallization solutions to be dynamically exchanged within the microfluidic channel in a continuous circulation mode, without wasting the protein sample. Thus, crystallization conditions can be screened and phase diagrams can be explored using the dialysis chip. Custom-built computer software provides a user-friendly graphical interface to manipulate the visualization, the fluidic and the thermal components of MicroCrys. Moreover, the lipidic cubic phase (LCP) method for protein crystallization was used on chip in combination with microdialysis. Numerous, isomorphous and well-diffracting micro-crystals of soluble proteins grew on chip applying the LCP approach.

Further studies were conducted to strengthen the direction of our developments and to validate them. The background noise generated by the materials comprising our microfluidic device was minimized rendering the chips compatible with *in situ* diffraction data collection. The current microchip uses a RC membrane, integrated within two layers of the device, for on chip microdialysis crystallization. However, the novel approach of fabricating hydrogel membranes directly on microchips via *in situ* photo-polymerization was considered and such a chip was designed for preliminary tests. Finally, the effect of radiation damage on the protein crystals during *in situ* X-ray diffraction experiments at room temperature was investigated in order to evaluate and propose data collection strategies for future SSX experiments.

Résumé

La cristallisation et les études cristallographiques à l'aide de diverses techniques de diffraction sont les étapes clés pour élucider les structures des protéines et comprendre les mécanismes de leur action en lien avec leurs fonctions biologiques. La technique la plus prédominante et la plus avancée appliquée aux études structurales des macromolécules biologiques est la diffraction des rayons X au synchrotron. L'acquisition de cristaux de protéines présentant une qualité de diffraction adéquate et pouvant révéler des détails structurals proches de la résolution atomique peut s'avérer difficile. Les méthodes conventionnelles de cristallisation, comme la diffusion en phase vapeur ou le batch, ont été utilisées pour la cristallisation des protéines et les développements instrumentaux se sont concentrés au fil des années sur la réduction de la consommation d'échantillons dans des expériences à haut debit parallèles pour cribler les conditions de cristallisation. Cependant, la recherche de conditions optimales pour obtenir des cristaux bien diffractants peut être compromise si les variables sensibles qui affectent la cristallisation ne peuvent pas être contrôlées avec précision.

Des développements instrumentaux et méthodologiques ont été mis en œuvre pour relever certains des défis rencontrés en cristallographie des protéines. Nous avons développé une puce microfluidique et une plateforme (MicroCrys) pour optimiser et rationaliser la cristallisation des protéines. Des protéines solubles et membranaires modèles ont été cristallisées sur la puce avec la méthode de microdialyse et les cristaux ont été utilisés pour la cristallographie sérielle aux rayons X *in situ* au synchrotron (SSX). La microdialyse, combinée au contrôle de la température, offre un contrôle réversible et précis de la cristallisation et peut être utilisée pour découpler la nucléation de la croissance des cristaux afin d'étudier les diagrammes de phase des protéines. L'automatisation du processus de cristallisation sur puce avec MicroCrys permet à la solution de cristallisation d'être dynamiquement échangée dans le canal microfluidique dans un mode de circulation continue, sans gaspiller l'échantillon de protéine. Ainsi, les conditions de cristallisation peuvent être criblées et les diagrammes de phase peuvent être explorés en utilisant la puce de dialyse. Un logiciel personnalisé fournit une interface graphique conviviale pour manipuler la visualisation, les composants fluidiques et thermiques de MicroCrys. De plus, la méthode de cristallisation des protéines en phase cubique lipidique (LCP) a été utilisée sur la puce en combinaison avec la microdialyse. De nombreux microcristaux de protéines solubles, isomorphes et bien diffractés, ont poussé sur la puce en appliquant l'approche LCP.

Des études supplémentaires ont été menées pour renforcer l'orientation de nos développements et les valider. Le bruit de fond généré par les matériaux composant notre dispositif microfluidique a été minimisé, rendant la puce compatible avec la collecte de données de diffraction *in situ*. La micropuce actuelle utilise une membrane RC, intégrée dans deux couches du dispositif, pour la cristallisation par microdialyse sur puce. Cependant, la nouvelle approche consistant à fabriquer des membranes d'hydrogel directement sur les micropuces par photopolymérisation *in situ* a été envisagée et une telle puce a été conçue pour des tests préliminaires. Enfin, l'effet des dommages causés par le rayonnement sur les cristaux de protéines pendant les

expériences de diffraction des rayons X *in situ* à temperature ambiante a été étudié afin d'évaluer et de proposer des stratégies de collecte de données pour les futures expériences SSX.

Preface

Unravelling the three-dimensional structure of biological macromolecules, such as proteins, is the core of structural biology where X-ray crystallography remains the predominant investigation technique. Elucidating the structural details of proteins is a key parameter for understanding the mechanisms of their action in various organisms and their connection to essential biological functions. Synchrotron radiation and X-ray free electron lasers (XFELs) are continuously upgrading in order to provide powerful and state-of-the-art tools necessary for the determination of proteins' structure near to atomic resolution. However, the use of X-ray crystallography comes along with intrinsic limitations to X-ray radiation and the crystallization process. Despite the wide range of crystallization methods, growing well-diffracting protein crystals is a difficult task requiring an extensive screening and optimization of crystallization conditions. Moreover, when protein crystals are grown to an adequate size, they must be prepared for X-ray diffraction experiments. This step is performed manually by harvesting the fragile protein crystals from the mother liquor in which they grow and using cryogenic cooling to protect them from radiation damage provoked by the high X-ray flux and the long exposure time to X-ray radiation. Finding the optimal crystallization conditions with conventional methods may require large amounts of proteins, the production and purification procedure for which, in some cases, may become time-consuming and expensive, providing only small samples. This only adds extra layers to the considerations of applying conventional protein crystallography techniques.

Microfluidic technology has been proven valuable to protein X-ray crystallography exhibiting many advantages, such as minute sample consumption per crystallization experiment (typically few nL - μL). Multiple crystallization experiments can be set up in parallel facilitating high-throughput screening and optimization. The inherent large surface area-to-volume ratio at the microfluidic scale and the diffusion-limited transport phenomena enable accurate control over temperature or concentration gradients. Crystal size and population uniformity can be controlled. Moreover, crystallographic studies can be performed directly on microchips via *in situ* X-ray diffraction, eliminating any manipulation and potential relative deterioration of the crystal quality. A wide range of materials with high transparency to X-rays and low background noise is available for fabricating microchips compatible with *in situ* X-ray diffraction studies. Finally, the serial data collection strategy is easier to implement, as numerous, small, isomorphous and randomly oriented protein crystals grown on microchips can be used to merge multiple partial diffraction data sets collected *in situ*.

This manuscript presents the research project, being part of the Innovative Training Network (ITN) RAMP (**RA**tionalizing **M**embrane **P**rotein crystallization), carried out during my PhD studies and funded from the European Union's Horizon 2020 Research and Innovation program under the Marie Skłodowska Curie grant agreement no 722687. It is divided in four main chapters and a final chapter (Chapter 5) including the main concluding remarks and perspectives for future implementations.

General concepts on crystallization principles and microfluidics are presented in the introductory chapter (Chapter 1). Specifically, methods for crystallizing proteins are emphasized and compared to dialysis that was thoroughly used in this work. Membrane protein crystallization methods, like the lipidic cubic phase method and the importance of investigating protein phase diagrams are also discussed. Moreover, all six soluble and membrane protein systems used for on chip crystallization and *in situ* X-ray diffraction studies are briefly presented. Finally, protein crystallization in microfluidic devices is reviewed and examples from the literature are provided.

A microfluidic chip has been developed coupling the advantages of the microfluidic technology and the microdialysis protein crystallization method allowing for accurate, fine-tuned and reversible control over the experimental parameters of the on chip crystallization. The work related to the design and functionality of the microchips is presented in Chapter 2. Microchips with 0.1 μL and 0.3 μL maximum volume of the protein reservoir have been developed for the on chip crystallization of proteins via microdialysis. A small piece of regenerated cellulose dialysis membrane is embedded within two layers of the chip. The molecular weight cut-off of the membrane can be chosen according to the molecular weight of the protein sample and the precipitant solution. The membrane separates the protein and the precipitant solution and supersaturation is achieved by the diffusion of the precipitant through the membrane towards the compartment containing the protein sample. Dialysis offers a kinetic trajectory that allows an extensive exploration of the phase diagram and it can be used in combination with temperature control to decouple nucleation from crystal growth, while a multitude of crystallization conditions can be screened with the same protein sample. In the case of the dialysis microchip, the crystallization solution can be injected within the fluidic channel with a continuous circulation mode allowing conditions to be changed dynamically without wasting the protein sample or the chip.

Chapter 3 includes the instrumental developments concerning a platform (MicroCrys) that has been designed to automate the on chip crystallization via microdialysis for investigating crystallization phase diagrams through chemical composition and temperature control. The platform contributes to the overall goal of optimizing and rationalizing protein crystallization. All the separate components of the platform are controlled by a custom-built LabVIEW software displaying a user-friendly graphical interface designed to manipulate the spatial movement of the support for the chips, the focus of the camera, the illumination level through LED lights and to record images with a frequency allocated by the user. Moreover, a commercial fluidic system (Elveflow) for mixing and circulating the crystallization solution under constant flow or under constant differential pressure between the inlet and the outlet port of the fluidic channel has been incorporated in the MicroCrys platform. This fluidic system contributes to the automation of the on chip crystallization via microdialysis allowing the exchange of crystallization solutions in the fluidic channel of the chip. Finally, a prototype for thermal regulation using the Peltier effect has been developed in order to couple the on chip microdialysis with temperature control to quench the study of protein phase diagrams. A LabVIEW program has been written for real-time acquisition, displaying and recording of the temperature value at the protein reservoir of the chip. Once, the thermal regulation system and the pressure-driven fluidic

system will be integrated into the main software of the platform, MicroCrys will be a fully-automated, user-friendly platform for on chip crystallization experiments.

Chapter 4 includes the results of the on chip crystallization experiments and *in situ* serial X-ray diffraction studies. Two model soluble proteins (Hen Egg White Lysozyme (HEWL) and Thaumatin from *Thaumatococcus danielli*) and four membrane proteins (AcrB from *Escherichia coli*, ShuA from *Shigella dysenteriae*, SERCA from *Oryctolagus cuniculus* and TmPPase from *Thermotoga maritima*) were crystallized on chip with the microdialysis method and used for room temperature *in situ* X-ray diffraction experiments at various synchrotron beamlines. The background noise generated by the interaction of X-rays with the materials comprising the dialysis chip was evaluated, rendering the chips compatible with *in situ* X-ray data collection (Chapter 2). Detailed electron density maps were produced for HEWL crystals at a resolution higher than 2 Å. Moreover, partial diffraction data sets were collected from numerous, small Thaumatin crystals and HEWL crystals grown on chip with the lipidic cubic phase (LCP) crystallization method, validating the compatibility of the chip for *in situ* synchrotron serial X-ray crystallography (SSX). As expected, in the case of membrane protein targets, on chip crystallization was more challenging. However, the crystals of three membrane proteins tested were produced on the dialysis chips. SERCA crystals diffracted close to 7 Å, which gives the best resolution so far acquired with membrane protein crystals on our chip.

Table of Contents

Table of Figures

List of Tables

Abbreviations

Acriflavine resistance protein B (AcrB)
Adenosine Diphosphate (ADP)
Adenosine Triphosphate (ATP)
Classical Nucleation Theory (CNT)
Critical Micelle Concentration (CMC)
Cyclic Olefin Copolymer (COC)
Direct Current (DC)
n-Dodecyl β-D-Maltoside (DDM)
European Synchrotron Radiation Facility (ESRF)
Free Interface Diffusion (FID)
Hen Egg White Lysozyme (HEWL)
Hexamethyldisilazane (HMDS)
International System of Units (SI)
Light Emitting Diode (LED)
Lipidic Cubic Phase (LCP)
Macromolecular X-ray crystallography (MX)
Membrane-bound PyroPhosphatase from *Thermotoga maritima* (TmPPase)
Metastable Zone Width (MSZW)
Molecular Weight Cut-Off (MWCO)
MonoAcylGlycerol (MAG)
National Institute of Standards and Technology (NIST)
Negative Temperature Coefficient (NTC)
Norland Optical Adhesive (NOA)
n-Octyl-β-D-Glucopyranoside (β-OG)
octyl-PolyOxyEthylene (octyl-POE)
Operational System (OS)
PolyDiMethylSiloxane (PDMS)
PolyEther Ether Ketone (PEEK)
PolyEthylene Glycol (PEG)
PolyEthylene Glycol Diacrylate (PEGDA)
Poly(Methyl MethAcrylate) (PMMA)
PolyTetraFluoroEthylene (PTFE)
Post-Exposure Bake (PEB)
Propylene Glycol Methyl Ether Acetate (PGMEA)
Proportional Integral Derivative (PID)
Protein Data Bank (PDB)
Pulse-Width Modulation (PWM)
Regenerated Cellulose (RC)
Sarco-Endoplasmic Reticulum Ca^{2+}-ATPases (SERCA)
Serial Femtosecond X-ray crystallography (SFX)
Serial Synchrotron X-ray crystallography (SSX)
Small-Angle X-ray Scattering (SAXS)
UltraViolet (UV)
Virtual Instrument (VI)
X-ray Free-Electron Laser (XFEL)

Chapter 1

Introduction

Chapter 1

Introduction

1.1 Principles of Crystallization

The main objective of this work is the development of microfluidic chips for on chip protein crystallization via the microdialysis method and *in situ* X-ray diffraction studies. Moreover, a platform for the automation of the on chip crystallization through temperature and chemical composition control has been developed. Understanding the principles ruling crystallization contributes towards the rationalization of protein crystallization and structure determination. Many books, papers and reviews have been written on the principles governing crystallization. The following section derives from the work of Mullin[1], de Yoreo and Vekilov[2] and others[3–5].

1.1.1 Nucleation theory

Crystallization is a process where matter undergoes a phase transition from a high free energy state to a lower energy state resulting in the crystal lattice. Crystallization occurs in nature and biological systems (biomineralization) and is vital for the chemical, pharmaceutical and food industry, as a particle formation and purification process. Producing particles with desirable characteristics such as size, shape, form and chemical purity is the main goal of crystallization from solutions. Solution crystallization is a multiple-step procedure including nucleation and crystal growth, and decoupling these two steps for better understanding and control has been a long-term pursuit for crystallographers. The first step in crystallization is forming a supersaturated solution in a non-equilibrium state where the new phase can emerge spontaneously. When supersaturation is achieved, molecules within the solution start to aggregate forming nuclei which are the minimum amount of the new phase that can exist independently in a metastable phase and are the active centers for crystal growth. Nucleation is a first-order phase transition, followed by crystal growth where particles within the solution diffuse to the surface of the nuclei and the crystal lattice forms.

Primary nucleation is widely described by the classical nucleation theory (CNT), developed originally by Gibbs in the 19th century studying the thermodynamic aspect of this process and formalized in the 20th century for the case of drop condensation from its vapor phase[6,7]. The change in free energy (ΔG) required for nuclei formation has two components (Eq. (1.1)). The first component is the change of free energy for the phase transformation (ΔG_V) and describes the spontaneous formation of solid state (crystal nuclei) in a supersaturated solution. The second component is the change in free energy for surface formation (ΔG_S). Therefore, the formation of the nuclei in the supersaturated solution is an energetically driven competition between the decrease in the negative volume component favoring growth and the increase in the positive surface component favoring dissolution. Figure 1.1.1 (a) is a qualitative schematic representation of the free energy change (ΔG) as a function of the nuclei radius (r). For small values of r, ΔG_S dominates causing an increase in

the total free energy which reaches a maximum (ΔG_C) at a critical r value and then decreases favoring the formation and growth of the nuclei. The critical radius (r_C) is the size of the critical nuclei which have the same probability of either growth or dissolution, and the energetic barrier of ΔG_C has to be crossed for the formation of the stable nuclei and their substantial growth.

$$\Delta G = \Delta G_V + \Delta G_S \quad (1.1)$$

The volume term in Eq. (1.1) is given by the difference in chemical potentials of n molecules in solution, μ_α, and the solid phase, μ_β:

$$\Delta G_V = -n(\mu_\alpha - \mu_\beta) \quad (1.2)$$

However, the chemical potential can be expressed through the activity (α_i) of the molecules in the solution or in the solid phase:

$$\mu_i = \mu_i^0 + kT\ln\alpha_i \quad (1.3)$$

Where μ_i^0 is the reference chemical potential of the i species. The surface term in the total free energy is the product of the nuclei's surface area and the specific energy of the surface (γ). For spherical nuclei:

$$\Delta G_S = 4\pi r^2\gamma \quad (1.4)$$

Combining Eq. (1.1) – (1.4), the overall free energy change for nucleation can be expressed through the Gibbs-Thomson relationship:

$$\Delta G = \frac{\frac{4}{3}\pi r^3}{V} kT\ln S + 4\pi r^2\gamma \quad (1.5)$$

Where k is the Boltzmann constant, T is the temperature in K and V the molar volume. S, the supersaturation, is defined as the ratio of the solution activity divided by the activity at equilibrium.

It has been made clear so far that the driving force for nucleation can be expressed through energy terms as the change in the total free energy (ΔG) or through the change in chemical potential ($\Delta\mu$)[1]. Rather than using $\Delta\mu$, crystallographers use supersaturation, S, or absolute supersaturation, σ. Differentiating Eq. (1.5) with respect to r and setting it to zero (i.e. finding the mathematical maximum), the critical radius r_C can be calculated. Then, the activation barrier ΔG_C for nucleation can be found by substituting r_C in Eq. (1.5):

$$\Delta G_C = \frac{16\pi V^2\gamma^3}{3(kT\ln S)^2} \quad (1.6)$$

Figure 1.1.1 (b) illustrates the Gibbs-Thomson equation (ΔG) as a function of the nuclei size (r) for three supersaturation values (S). The critical values for the crystal nuclei size and the free energy activation barrier are inversely proportional to supersaturation.

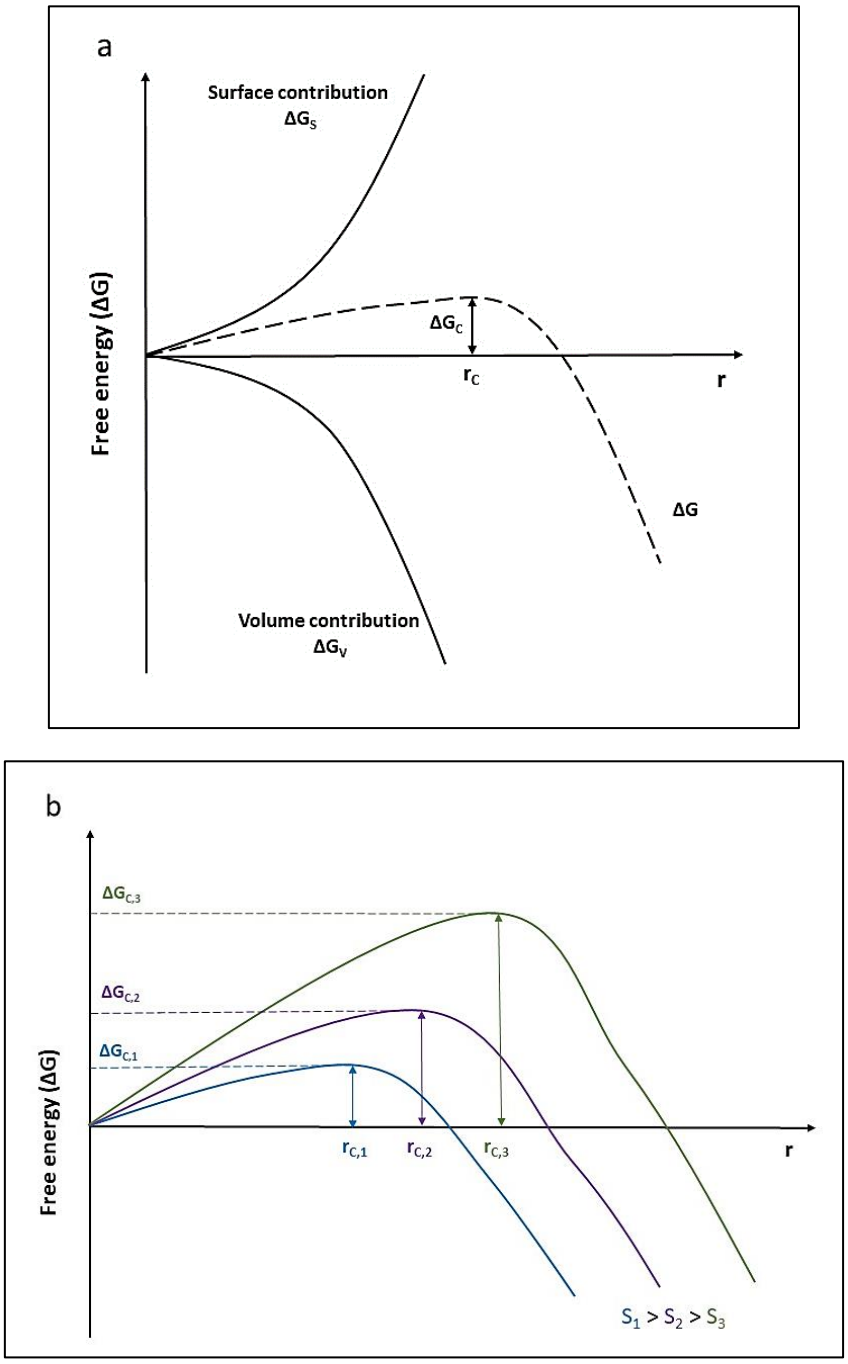

Figure 1.1.1: Schematic representation of (a) the free energy change (ΔG) during nucleation as a function of the cluster radius (r) and (b) the critical value of ΔG as a function of the supersaturation (S). Redrawn from [3].

Nucleation, as described so far, is a probabilistic process. The nucleation of a new phase results from density fluctuations occurring in the bulk solution in order to bring together

molecules forming clusters of a critical size. The spatial and temporal distribution of these fluctuations is random, but the nucleation probability is strongly related to the critical nuclei size. The critical size, however, is proportional to the interfacial energy. Therefore, the probability of nucleation can be controlled through the solution composition or the supersaturation. Based on Boltzmann's distribution law, the nucleation kinetics can be predicted. The number of the critical nuclei formed per unit volume of the system (V_t) and time, named nucleation rate (J) can be calculated as:

$$J = k_0 V_t \exp\left(\frac{-\Delta G_C}{kT}\right) \quad (1.7)$$

The exponential term in Eq. (1.7) is related to the critical nuclei and the activation barrier, while the pre-exponential term k_0 is a kinetic factor depending on several parameters like the molecular mobility, temperature, solution viscosity, solution density and the molecular charge and volume[3,4]. The theoretical value is given as 10^{30} $cm^{-3}s^{-1}$.[4] Comparing Eq. (1.6) and (1.7), it can be concluded that the nucleation rate depends on the 2nd power of supersaturation and the 3rd power of interfacial energy within an exponential factor. J is low for low supersaturation values and increases dramatically after a critical supersaturation value. This dependence of the nucleation rate on the supersaturation value explains the width of the metastable zone (MSZW) in the phase diagram (Figure 1.1.2). Finally, Eq. (1.7) suggests that the nucleation rate is proportional to the volume of the system, V_t, requiring caution when scaling-up or scaling-down crystallization conditions[3,6,8].

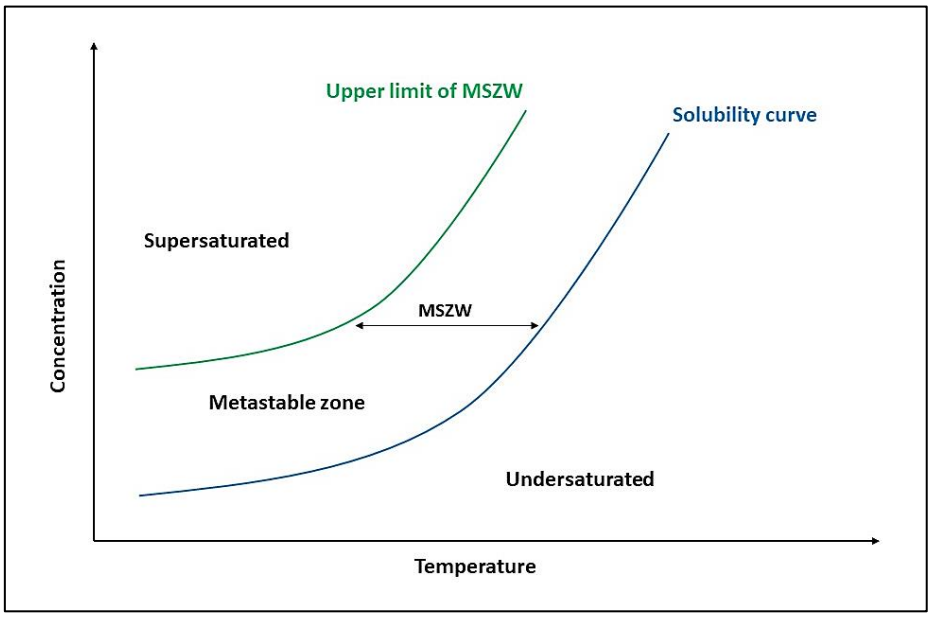

Figure 1.1.2: Schematic representation of a phase diagram as a function of temperature for proteins with direct solubility. The metastable zone width is shown as MSZW.

The metastable zone is confined within two curves. The solubility curve is the lower limit and it is fixed. It represents the solution at equilibrium state for various concentration values of the system (for example protein) and the crystallization parameter (for example precipitant concentration) and it is thermodynamically defined. The nucleation probability is zero, while the solution is practically stable for infinite time. The upper limit of the metastable zone is represented by another curve, the nucleation probability of which is one and the nucleation induction time (τ) is considered to be zero. This means that nucleation is spontaneous. The induction time depends strongly on the supersaturation: higher supersaturation value leads to shorter induction time for nucleation. Consequently, the location of this second curve is defined by the nucleation kinetics. It is not stable but depends on the rate of achieving supersaturation. Therefore, the MSZW depends on both supersaturation (S) and the rate that supersaturation occurs (dS/dt), explaining why in some cases nucleation doesn't start even if the solution is supersaturated. If the metastability zone is crossed very fast, the solution will be supersaturated before inducing nucleation[3].

Theoretically, the induction time is the time interval between achieving supersaturation within a solution and the formation of the critical nuclei:

$$\tau = \frac{k^{\tau e}}{J} \quad (1.8)$$

Where J is the nucleation rate as defined by Eq. (1.7). Practically, τ is one of the very few nucleation parameters that can be measured experimentally, decoupling nucleation from crystal growth.

The CNT model presented so far assumes primary homogeneous nucleation in pure solutions where the fluctuation probability is identical over the whole system volume. Yet, under realistic experimental conditions or in the case of on chip crystallization where a foreign surface already exists, nucleation is heterogeneous. In this case, the nucleation probability is locally increased since the presence of a foreign surface decreases the energy activation barrier for the formation of critical nuclei. The activation energy between heterogeneous and homogeneous nucleation is given by:

$$\Delta G_{\text{heterogeneous}} = \Delta G_{\text{homogeneous}} \cdot f(\theta) \quad (1.9)$$

Where $f(\theta)$ is a function of the contact angle θ between the crystal nucleus and the substrate:

$$f(\theta) = \frac{2 - 3\cos\theta + \cos^3\theta}{4} \quad (1.10)$$

Investigating Eq. (1.9) and (1.10), one concludes that the smaller the contact angle value, the smaller the nucleation activation barrier is, while the nucleation is practically homogeneous when the nucleus wets completely the substrate, i.e. when θ = 180°. According to Turnbull[6], heterogeneous nucleation probability should be minimized in small volume systems, as for example within the micro- or nano-liter scale of protein crystallization experiments. However, this assumption has not yet been proven experimentally[3].

CNT assumes that the nuclei are spherical with uniform densities and uses the capillary approximation theory[9]. In a few words, this approximation suggests that the molecular arrangement in a nucleus is identical to that of the crystal, implying that the surface tension of these two entities is equal. Moreover, CNT assumes that the nuclei grow by the addition of one monomer at a time, ignoring any interaction between particles or pre-existing nuclei. The theory kinetics is modelled in steady state conditions ignoring the time dependence of nucleation. In order to circumvent the simplification assumptions of CNT, the two-step nucleation theory has been proposed for systems displaying a liquid-liquid immiscibility region such as protein-precipitant solutions[10,11]. Density fluctuations in a protein-precipitant solution near the liquid-liquid boundary lead to the formation of high-density protein drops. In this non-classical approach, the first step to nucleation is the formation of the high-density protein drops and the second step is the formation of small crystals within the drops, surrounded by a highly concentrated liquid film. This is an on-going research field with promising results.

1.1.2 Crystal growth kinetics

Growth kinetics is governed by mass transfer phenomena, specifically by the diffusion of molecules from the supersaturated solution to the crystal surface. It has been proposed that the growing crystal surface consists of flat areas (terraces) and partially raised regions (steps)[1,2,12,13]. The steps contain sites called kinks where diffusing molecules attach by bonding to neighboring molecules. Due to existing bonding sites in the kinks, the probability of molecular attachment is higher than in other positions on the crystal's surface, as in terraces or edges. Crystal growth occurs because the rate of the attachment of molecules on the crystal's surface is higher than the rate of detachment. The energy barrier for the detachment of a molecule by breaking the bonds from adjacent molecules is higher than the barrier required for the attachment to a step. This molecular flux depends on the solute concentration and changing the solubility can alter the kinetics of the crystal growth. An important aspect on the growth kinetics is the introduction of impurities (ions, additives, molecules, poisons, surfactants) on the surface that can alter the attachment/detachment rates and modify the shape of the growing crystal. In protein crystallography, this external intervention on crystal growth is crucial when well-formed, high-quality crystals are required for structure determination through X-ray diffraction.

1.1.3 Protein crystallization

The crystallization of macromolecules like proteins, nucleic acids and viruses is driven by supersaturation under conditions that do not intervene or alter their natural state related to their biological significance. Compared to crystals of small molecules, macromolecular crystals are usually smaller in size, less robust, dehydrate faster due to a very high content of the solvent (27 to 65 %)[14] and have weaker optical or X-ray diffraction properties. Moreover, macromolecular crystals are very sensitive to temperature variations and undergo extensive radiation damage when not treated properly. Understanding the principles of protein crystallization and the factors affecting it, can contribute significantly to X-ray crystallography, developed to elucidate the three-dimensional (3D) structure of these macromolecules and

their role in biological functions. The following section is based on the work of Krauss *et al.*[15], McPherson and coworkers[16,17] and Asherie[18].

Even though protein nucleation is not yet fully understood, the growth step can be described by classical mechanisms[17,19]. The crystal growth can be represented graphically in a two-dimensional phase diagram (Figure 1.1.2). The protein solution is supersaturated when the protein concentration increases over the solubility limit. The supersaturation area of the phase diagram consists of the metastable region supporting only crystal growth, the labile region where both nucleation and growth are promoted and the precipitation zone where the supersaturation value is high and amorphous aggregates are formed. While the solubility curve is defined thermodynamically, the other regions in the phase diagram are defined by kinetics and their boundaries are not fixed. The correlation of the MSZW to nucleation kinetics was explained in Section 1.1.1. Supersaturation is not an equilibrium condition. In order to establish equilibrium while moving from a supersaturated condition, a solid state (the crystal) is formed until equilibrium is reached at the solubility limit. The phase diagram illustrated in Figure 1.1.2 is for proteins with direct solubility, where the solubility of the protein increases with temperature.

Protein crystallization is affected by numerous chemical, physical or biochemical factors. These factors can be used to induce or control supersaturation and indirectly the nucleation or growth rates which are strongly related to the supersaturation value. Lists and detailed descriptions of the factors affecting protein crystallization are provided in the literature[15,17]. In this study using the dialysis crystallization method, temperature, pH, the sample purity, the precipitant and the effect of additives are mainly considered.

- Temperature is related to protein solubility. When the protein solubility increases with increasing temperature, the solubility is called direct. Otherwise, the protein displays indirect solubility. In the case of direct solubility, crystallization is driven mainly by enthalpy effects on the free energy of the system, whereas the crystallization of proteins with indirect solubility is entropy-driven and the sample is less soluble at higher temperatures[20]. This temperature dependence is attributed to variations of the acid/base reaction constant of the protein's side chain. Protein crystals are usually grown at 4 or 20 °C. The on chip crystallization of soluble and membrane proteins and the *in situ* X-ray diffraction experiments in this work were performed at room temperature. However, due to the significance of the temperature effect on protein crystallization, a prototype system for on chip thermal regulation was developed (Chapter 3).
- Moreover, protein solubility is considerably affected by pH variations. Proteins contain many ionizable groups and own a characteristic pH value known as the isoelectric point (pI), where the positively charged groups of the protein molecules balance the negative charges. Variations on pH can change this balance of electrostatic interactions and the protein-protein interactions that are important for crystal packing, binding specificity of the protein, the formation of hydrogen bonds and salt bridges and the folded protein structure[21].
- The precipitants are compounds used for protein crystallization to decrease the solubility of the macromolecule. Salts, for example, can change the activity coefficient of water, organic compounds can alter the dielectric constant, while PEGs (polyethylene glycol polymers) can increase the molecular crowding and reinforce the

interactions among protein molecules. Precipitants are usually combined in solutions to increase the probability of crystallization.

- The impact of additives on the kinetics of crystal growth has already been highlighted. In protein crystallization, an additive is any compound added to the crystallization solution apart from the precipitant, the buffer and the protein itself. An additive can modify the natural protein conformation, the interactions between protein molecules or between protein and solvent molecules, the crystallization phase and the crystal's surface energy[15,22]. In the case of some proteins, ligand molecules are used to bind on specific sites to maintain the protein conformational state. Ligands are bounded on the macromolecule in advance or can be added by soaking or co-crystallization[22]. In the case of membrane proteins, the most prominent additives are the solubilizing agents and the detergents.

1.1.3.1 Conventional crystallization methods

There are several methods for protein crystallization and each one offers a different kinetic pathway for reaching supersaturation and exploring the phase diagram[15,17,23]. Figure 1.1.3 illustrates a phase diagram where protein concentration is plotted against the concentration of the precipitating agent and the kinetic trajectories of the various crystallization methods are indicated with colored arrows. The most commonly used protein crystallization method is vapor diffusion which is based on the evaporation and diffusion of water molecules in a sealed container[24,25]. A droplet of μL volume containing the protein sample and the crystallization solution (buffer and precipitant) is deposited on a siliconized glass cover slide and is equilibrated over time against a well solution containing only the buffer and the precipitant. The concentration of the precipitant in the well is higher than the respective concentration in the drop. Through vapor diffusion, the protein and precipitant concentration increases with time until supersaturation is achieved. This concentration difference (Δc) of the precipitant in the drop and the well is the driving force for inducing nucleation. The vapor diffusion method includes the hanging drop, sitting drop or sandwich drop approach. The small volumes of protein samples and the advent in robotics and automation have made vapor diffusion a vastly used method for screening crystallization conditions.

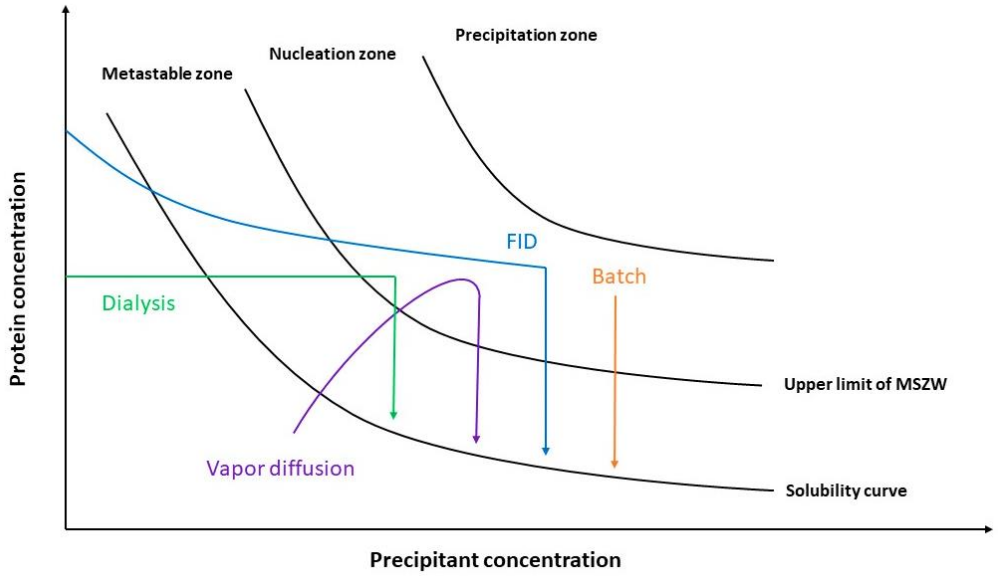

Figure 1.1.3: Schematic representation of a two-dimensional phase diagram as a function of the precipitant's concentration. The kinetic pathways for four crystallization methods are shown with colored arrows: green for dialysis, purple for vapor diffusion, blue for FID and orange for batch crystallization. Redrawn from [15].

For applying the batch crystallization method, the protein sample and the precipitant, or any other additive, are mixed directly in a container which is sealed and left aside until crystals are observed. The supersaturation is achieved by the direct mixing of the solutions; therefore, the kinetic trajectory of this technique has its starting point above the upper limit of the metastable zone (Figure 1.1.3). The phase diagram cannot be explored with this method. However, the microbatch method was developed[26] where the protein and precipitant solution are mixed in droplets of a few µL volume. The droplet is usually covered with inert oil to prevent evaporation. The microbatch method can be used for screening crystallization conditions by preparing several small droplets.

For the Free Interface Diffusion (FID) method, supersaturation is achieved by diffusive mixing of the protein sample and the precipitant in a capillary. The two solutions inter-diffuse over time until equilibrium is reached. FID offers a better control over the supersaturation value, producing high quality crystals for X-ray diffraction. Nevertheless, large protein volumes are required and setting up an experiment in a capillary can be practically difficult or disrupted by convective phenomena due to high-density differences. Screening conditions with the FID method can be implemented in microfluidic devices[27,28] where only nL volumes of the protein sample are required.

A relatively new method for protein crystallization has been introduced by García-Ruiz and coworkers[29,30]. The counter-diffusion method is based on creating an interface between the protein sample and the precipitant solution and uses gelled media where a gel layer can separate the protein and precipitant solution or one of the solutions can be gelled before being introduced in a capillary. The most common approach is to introduce the protein solution in a capillary, fix one end of the capillary in a gel and pour the precipitant solution over the gel. The precipitant solution diffuses over time through the gelled medium towards

the capillary, increasing the protein supersaturation. A precipitant concentration gradient is achieved across the capillary axis, where small crystals or aggregates are formed at high supersaturation near the end of the capillary that is in direct contact with the gel, while fewer, bigger, high diffraction quality crystals are formed as the supersaturation decreases across the capillary. In a sense, screening of crystallization conditions is achieved within the capillary.

1.1.3.2 The dialysis method

Dialysis is based on the diffusion and equilibration of the precipitant molecules through a semi-permeable membrane. The membrane separates the protein and the precipitant solution and supersaturation is achieved by the diffusion of the precipitant through the membrane towards the compartment containing the protein sample. The most common way of using dialysis in protein crystallography is using the microdialysis buttons where the protein sample is placed within a few μL volume chamber and covered with a semi-permeable membrane. Then, the button is placed within a reservoir containing the buffer and the precipitant solution. The semi-permeable membrane usually applied is a regenerated cellulose (RC) dialysis membrane that is commercially available and comes in various pore sizes or molecular weight cut-offs (MWCO). The MWCO of the dialysis membrane is chosen accordingly and serves a double purpose: it must retain the protein sample within the chamber and the MWCO of the RC membrane should be smaller than the molecular weight of the protein, while at the same time it should allow the diffusion of the precipitant molecules across the membrane.

Dialysis offers a kinetic trajectory that allows an extensive exploration of the phase diagram (Figure 1.1.3). The dialysis kinetics depends on several factors such as the MWCO of the dialysis membrane, the volume of the system (dialysis button) and the precipitant concentration. Merely changing the precipitant concentration difference across the membrane can modulate the rate at which equilibrium is reached. Moreover, several crystallization conditions can be screened while using the same protein sample. This feature is very important in the case of membrane proteins that are hard to produce or come in minute quantities. When using microdialysis buttons, this can be achieved by transferring the button in another reservoir where the precipitant concentration is different or by exchanging the precipitant solution in the same reservoir. This procedure can be applied several times as long as the protein sample is not damaged, dehydrated or denatured. The main disadvantage of the dialysis method comes from concentrated PEG solutions, as they tend to dehydrate the protein solution within the button. An interesting work on the diffusion of salt and PEG mixtures across semi-permeable membranes was published recently[31].

The reversibility of the dialysis method and the precise control over the crystallization conditions are applied on the microfluidic chips that we have developed for on chip protein crystallization via microdialysis[32,33]. A small piece of RC dialysis membrane of appropriate MWCO is incorporated within the microchip allowing precipitant molecules to diffuse across the membrane towards the protein chamber of the chip.

1.1.4 Crystallization of membrane proteins

Membrane proteins consist approximately 30 % of the proteins produced by some organisms like *Homo sapiens* or *Escherichia coli* according to genomic sequence data[34,35], while at the same time they are considered possible drug targets to a percentage up to 60 %[36]. The number of known membrane protein structures was quite limited at the beginning of the 21st century, when less than 100 unique membrane protein structures were posted in the Protein Data Bank (PDB)[37]. The first membrane protein structure was published in 1985[38]. By 2019, this number raised up to approximately 3500 structures of 1000 unique membrane proteins[39]. This impressive increase in the quantity of unique membrane protein structures can be attributed significantly on the advent of crystallization methods compatible with the nature and the challenges coming from these biological macromolecules.

The main difficulty confronted when working with membrane proteins is the fact that these macromolecules in the living cells of the organism are embedded in a lipid bilayer, the cellular membrane, exhibiting an amphipathic surface[40,41]. The hydrophobic surface of membrane proteins emerges within the lipid bilayer forming contacts with the alkyl chains of the lipids, while the hydrophilic surface comes in contact with the polar groups of the lipids or the aqueous phase surrounding the membrane. In order to work with membrane proteins, one has to extract them from their native environment and form an artificial environment where the amphipathic macromolecules can be hosted *in vitro*. Usually, membrane proteins are purified and crystallized in the presence of solubilizing agents such as detergents. However, extracting membrane proteins from their natural environment and overexpressing them in heterologous systems, as for example in bacterial cells, is a time-consuming, laborious task, while the use of detergents multiplies the overall production cost. Moreover, the amount of a membrane protein when successfully purified is rather limited rendering every μg of the protein precious for crystallization screening.

There are two main methods for membrane protein crystallization: the *in surfo* method where detergents are used to solubilize the membrane proteins and the *in meso* methods where the lipidic mesophases are used to reconstitute the protein in a lipid bilayer simulating their natural occurring environment. There are numerous publications and reviews on membrane protein crystallization and the following section is based on some of them[37,40–45].

1.1.4.1 *In surfo* crystallization

Detergents are amphiphilic molecules containing a polar head group and a hydrophobic chain. In aqueous environment, they spontaneously form micellar structures. Membrane proteins can be solubilized in the detergent micelles which mimic the natural lipid bilayer where membrane proteins are encountered. Detergents are classified as ionic, nonionic, bile salts and zwitterionic[41]. Some of the most commonly used detergents with membrane proteins and their physicochemical properties are provided by le Maire *et al.*[46]. The most prominent property for detergents is the critical micelle concentration (CMC) which is the minimum concentration required to form micelle clusters from individual detergent molecules, at a given temperature. The formation of the micelle depends strongly on the detergent's molecular shape and it is described by the packing parameter, P. The critical

packing parameter (CPP) is a function of the chain's volume, the cross-sectional area of the headgroup and the length of the chain. For small CPP values (P < 1/3) spherical micelles are formed, while for higher values (P > 1/2) lamellar detergent aggregates form[47], as shown in Figure 1.1.4 (a)[48]. Figure 1.1.4 (b) illustrates how membrane proteins bind detergent micelles[46]. The repulsive forces of the head group and the hydrophobic interactions of the tail determine CMC. CMC depends on many parameters such as the temperature, pH, ionic strength or the presence of protein and lipids.

a

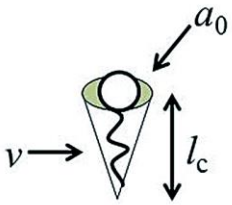

$$\mathrm{CPP} = v/a_0 l_c$$

Critical Packing Parameter ($v/a_0 l_c$)	Critical Packing Shape	Structures Formed
< 1/3	Cone	Spherical micelles
1/3 – 1/2	Truncated cone	Cylindrical micelles
1/2 -1	Truncated cone	Flexible bilayers, vesicles
~1	Cylinder	Planar bilayers
>1	Inverted truncated cone or wedge	Inverted micelles

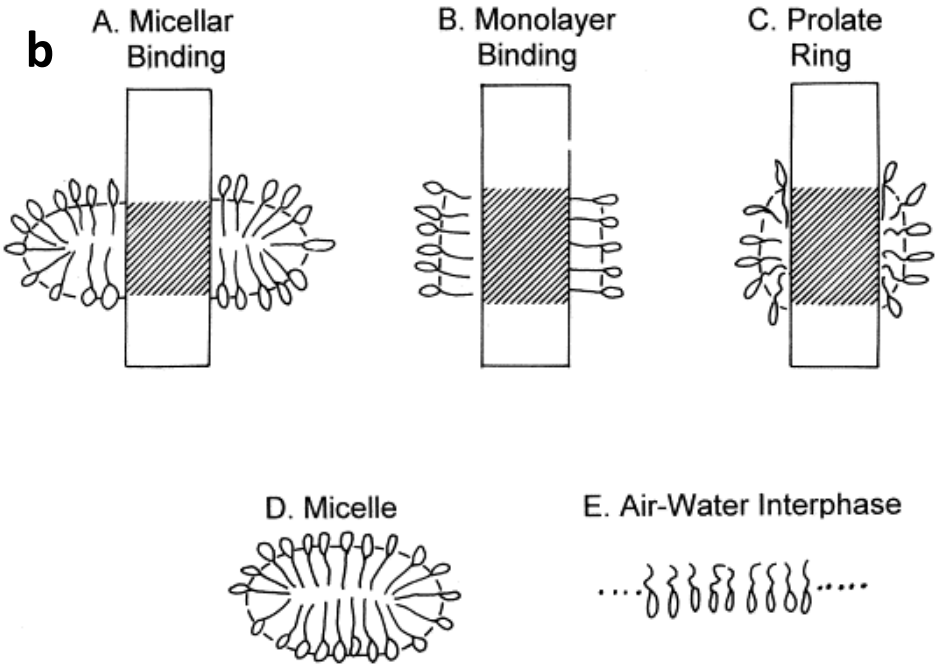

Figure 1.1.4: (a) Molecular shape and CPP for detergents. Used with permission from [48]. (b) Different binding arrangements (A: micellar, B: monolayer and C: prolate ring) of detergents by membrane proteins. The structure of a detergent's micelle is shown in D, while the arrangement of detergent molecules in the air-water interphase is shown in E. Used with permission from [46].

The phase diagram of detergents as a function of temperature is provided in Figure 1.1.5[49]. For concentrations below CMC, only detergent's monomers exist in the solution, while above the critical concentration there exists equilibrium between monomers and micelles. At very high detergent concentration, the liquid-crystalline phase exists which is immiscible in water and its structure can be lamellar, hexagonal or reverse hexagonal. When detergents are used for membrane protein extraction, in the equilibrium state (above CMC) exist three states instead of two: the detergent monomers, the detergent micelles and the micelles embedding the protein molecule. Therefore, crystallizing membrane proteins in the presence of detergents and studying the phase diagram is not as straight forward as in the case of soluble proteins, described by the CNT model. When determining the solubility curve or the supersaturation and the metastability region, one must bear in mind that membrane protein molecules are bound to detergent micelles and what actually crystallizes is the macromolecule-detergent complex. Once the detergent solubilizes the membrane protein molecules, the crystallization methods that can be applied are the same conventional methods used for soluble proteins, such as vapor diffusion, batch, dialysis and FID or counter diffusion.

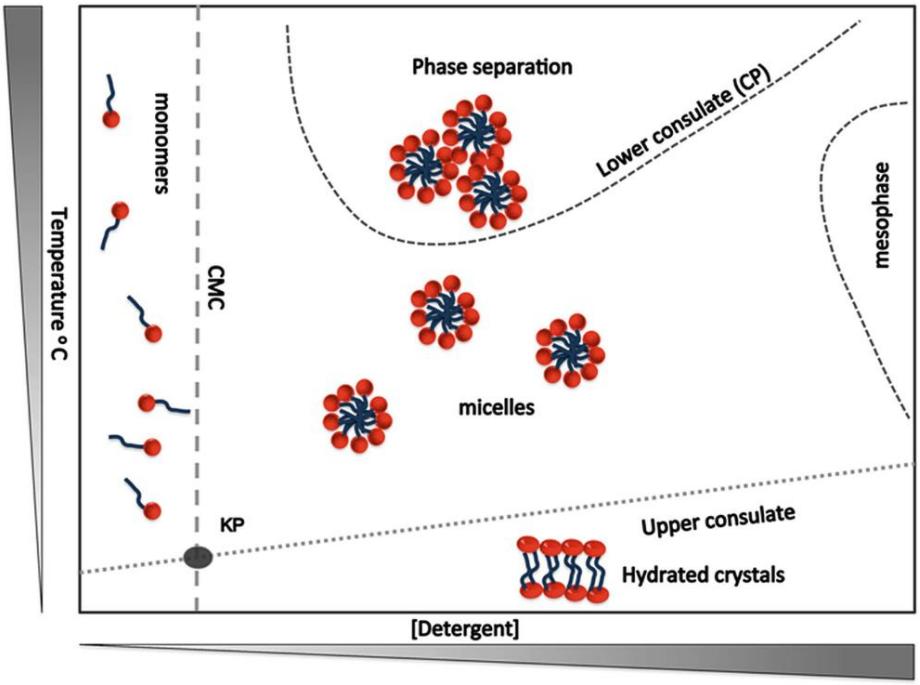

Figure 1.1.5: Phase diagram for detergents as a function of temperature. The detergent molecules can exist in various phases (monomers, micelles, hydrated crystals) depending on the concentration and temperature value. CMC is the critical micelle concentration and KP is the Krafft point (the temperature at which the detergent's solubility is equal to CMC at the same temperature). Used with permission from [49].

The choice of detergent is crucial for membrane protein crystallization because the detergent micelle must optimally fit the crystal lattice. Attractive interactions between the polar groups of the detergent micelles appear to stabilize the crystal lattice[40]. The protein stability in the presence of the chosen detergent and the concentration of the detergent in protein-detergent complex should be optimized prior to crystallization assays. At the final step of the purification, the membrane protein sample is usually being concentrated by centrifugation to increase the final concentration. However, during this procedure, the detergent's concentration may increase as well. If this concentration is too high, protein denaturation or phase separation during crystallization can occur. Dialysis can be used to decrease detergent's concentration[44].

1.1.4.2 *In meso* crystallization

The second approach for membrane protein crystallization relies on the spontaneous self-assembly of lipids and detergents in vesicles, discoidal micelles or bicelles and liquid crystals or mesophases. These methods are collectively called as bilayer methods[37], where a bilayer of lipids, detergents and protein is formed. Using lipids to crystallize membrane proteins can be an alternative for membrane proteins that are not stable only in the presence of detergents. The bicelle method is based on the reconstitution of the protein sample in discoidal micelles of lipids and detergents, while the vesicle method was introduced by Takeda

et al.[50] producing high-quality crystals of bacteriorhodopsin (bR). The lipidic cubic phase (LCP) method uses the mesophases of lipids and was first introduced by Landau and Rosenbusch, who crystallized bR in the cubic phase of monoolein that diffracted to 1.55 Å resolution[51]. Understanding the lipid mesophases and their phase behavior is crucial for applying the LCP method for membrane protein crystallization.

1.1.4.3 Lipidic mesophases

Lipids can self-assembly in different mesophases depending on the lipid's nature and concentration, the concentration of the aqueous medium, the temperature and the pressure. The self-assembly process is spontaneous since no external energy source is required and is a result of the hydrophobic effect when lipids are immersed in water. Lipids have an amphiphilic nature containing polar and hydrophobic parts. The lipidic mesophases are optically transparent, non-birefringent, gel-like materials and are categorized in the lamellar phase, with the planar lipid bilayer being the sole representative, and in non-lamellar phases such as the cubic and the inverted hexagonal phase[37] (Figure 1.1.6). The mesophases represent a liquid-crystalline state.

The representation of the lipidic cubic phases is based on a mathematical description of three-dimensional, infinitely periodic minimal surfaces. These minimal surfaces lie within the lipid bilayer. The bicontinuous, cubic Pn3m phase, which is used for the LCP crystallization method, is a surface containing a bilayer that separates two interpenetrating water channels forming a diamond-like lattice[52]. The size of the water channels is crucial for the reconstitution of a membrane protein molecule within the cubic phase. It has been measured that the size of water channels at room temperature is approximately 50 Å and the unit cell size of monoolein for the cubic phase is 69 – 113 Å at 92 – 0 °C [53].

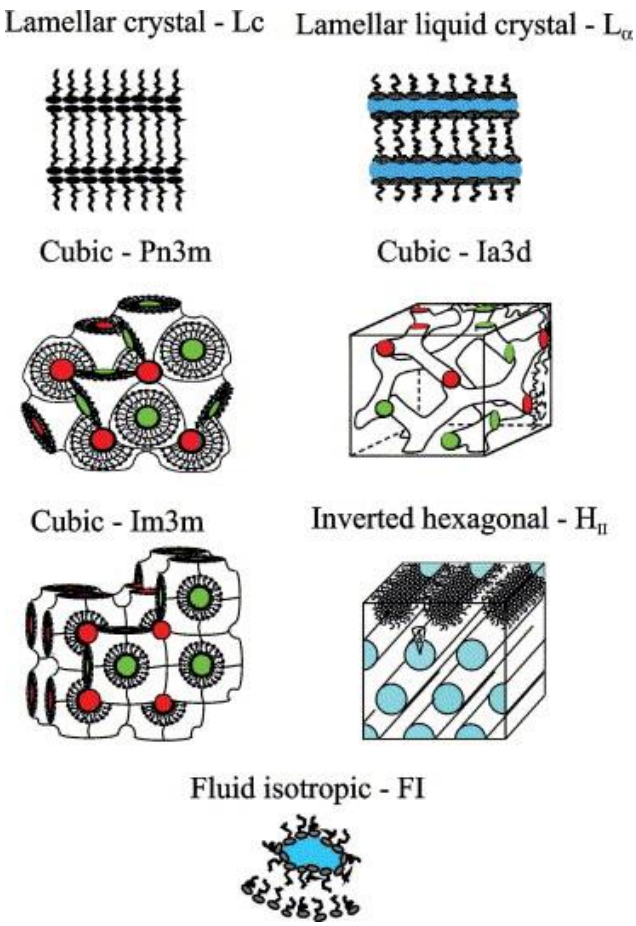

Figure 1.1.6: Schematic representation of lipidic mesophases including the lamellar phase (L_c and L_a), the non-lamellar phases (cubic Pn3m, Ia3d or Im3m and inverted hexagonal H_{II}) and the fluid isotropic phase (FI). Used with permission from [37].

1.1.4.4 The phase diagram

The phase behavior of lipids in water is represented by temperature versus composition phase diagrams in equilibrium. These diagrams represent regions of the mesophases of a specific lipid as a function of water concentration and temperature and follow the Gibbs phase rule. In regions where two mesophases coexist, their composition remains constant while the overall composition of the sample and the relative amounts of the two phases change isothermally[37].

The most commonly used lipids with the cubic phase crystallization method are the *cis* monounsaturated monoacylglycerols (MAGs). These lipids have a simple molecular structure and are well suited for the investigation of phase behavior which is intrinsically related to lipid form and function. The phase diagram of monoolein or 9.9 MAG is the most studied in the literature[53,54] and is widely used for protein crystallization with the cubic phase method at 20 °C. The equilibrium phase diagram of the monoolein-water system is shown in Figure 1.1.7[54]. The Pn3m cubic phase is formed at a composition of 40 % water and 60 % monoolein at 20 °C. A comprehensive review on monoolein mesophases structure characterization and phase behavior is provided by Kulkarni *et al*.[55]. Small-Angle X-ray Scattering (SAXS) is used to identify

the phases of the lipid and the respective lattice size when the lipid is mixed only with water[54] or when mixed with aqueous solutions containing crystallizing agents as salts and PEGs[56,57] and detergents[58].

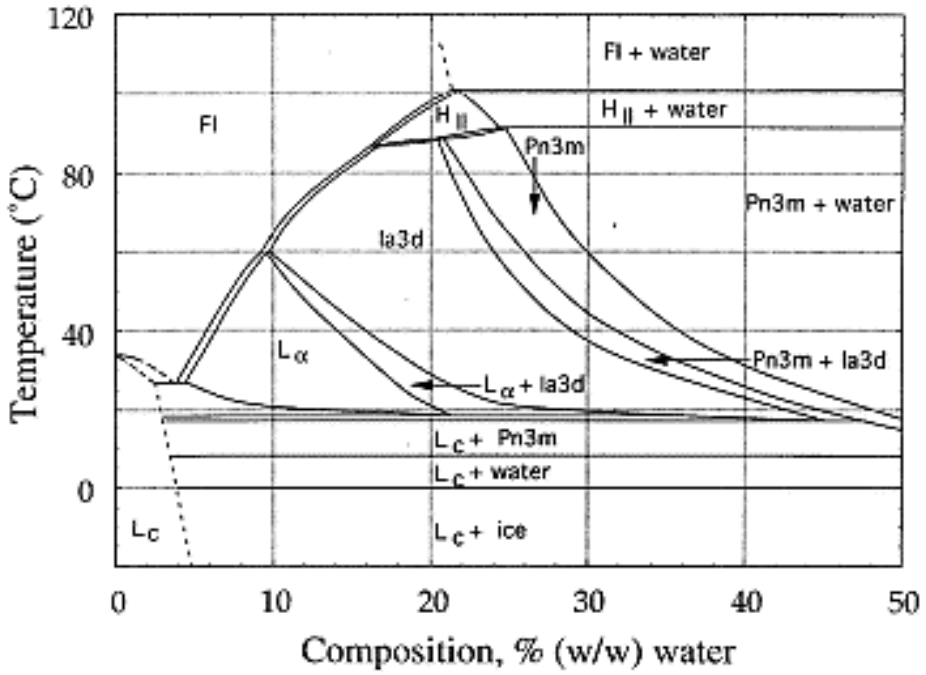

Figure 1.1.7: The equilibrium temperature-composition phase diagram of the monoolein-water system as determined by Qui and Caffrey[54]. The Pn3m cubic phase is formed at a composition of 40 % water and 60 % monoolein at 20 °C.

1.1.4.5 The crystallization protocol

The LCP method relies on the bicontinuous cubic phase of MAGs (e.g., monoolein) and water. The cubic phase forms spontaneously by mixing monoolein and protein sample at a 3:2 ratio at 20 °C. In the case of membrane proteins, the protein sample is actually a protein-detergent complex because detergents are used to solubilize membrane proteins during their purification process. To induce crystallization, mixtures of salts, buffers, PEGs, or any other agent provoking supersaturation, are added above the cubic phase and the sample is incubated at appropriate temperature and humidity conditions for nucleation and crystal growth. This is the basis of the method which works with membrane proteins and soluble proteins as well[59]. Performing all the steps of the method at room temperature and yielding high diffraction quality crystals are some of the advantages of the method. The detailed protocol of membrane protein crystallization in lipidic mesophases is given by Caffrey and Cherezov[60]. This protocol used for the on chip crystallization of Hen Egg White Lysozyme (HEWL) in the lipidic cubic phase of monoolein using microdialysis at room temperature is

presented in Chapter 4. Finally, it is worth mentioning that LCP crystallization follows the trends and the progress of protein crystallization. Automated, robotic systems have been developed for screening crystallization in lipid mesophases[61], while plates have been developed for *in meso* and *in situ* X-ray diffraction experiments[62]. A microfluidic device made of PDMS (polydimethylsiloxane) and COC (cyclic olefin copolymer) has been designed for the on chip mixing and preparation of monoolein lipidic mesophases and *in situ* SAXS phase determination[63].

1.2 Protein systems

1.2.1 Soluble proteins

1.2.1.1 Hen Egg White Lysozyme

Lysozyme, a protein also known as muramidase or N-acetylmuramide glycanhydrolase, is an enzyme functioning as an antibacterial agent. Specifically, lysozyme catalyzes the hydrolysis of 1,4-beta-linklages between N-acetylmuramic acid and N-acetyl-D-glucosamine residues in peptidoglycan and between N-acetyl-D-glucosamine residues in chitodextrin. Peptidoglycan is the main component of the gram-positive bacterial cell wall and the hydrolysis, triggered by lysozyme, causes lysis of the bacterial cell wall. Lysozyme is found in various biological secretions, such as saliva, tears, mucus or human milk and it is abundant in egg white. Lysozyme was discovered by Fleming in 1922 and was the first enzyme sequenced, the first protein used for X-ray crystallography[64] and the first enzyme with an action mechanism[65]. Ever since, lysozyme has been a model system for multitudes of studies as it is commercially available at affordable price.

HEWL was used in this study to validate on chip protein crystallization via microdialysis. HEWL crystals grown on chip were used for *in situ* X-ray diffraction experiments and full data sets were collected at BM30A-FIP at the European Synchrotron Radiation Facility (ESRF). HEWL is a positively charged polypeptide consisting of 129 amino acids with a molecular weight of 14.4 kDa. The protein is stable in acid solutions within a wide range of temperatures, while in alkaline solutions its activity decreases with increasing temperature[66]. The isoelectric point of lysozyme is pI = 11. Numerous crystallization conditions have been screened for lysozyme either through conventional crystallization methods or with microfluidic devices, yielding robust, well-shaped and well-oriented crystals for X-ray diffraction studies. The structure of tetragonal HEWL crystals determined at 0.94 Å resolution by X-ray diffraction and crystallized in the $P4_32_12$ space group (PDB entry 1IEE) is shown in Figure 1.2.1 (b). The crystals were grown by the counter-diffusion method[67] at 293 K. Figure 1.2.1 (a) shows HEWL crystals grown in a 30 µL dialysis button under 0.7 M sodium chloride (NaCl) and 400 mM sodium acetate (CH_3COONa) pH 4.0 at 293 K. The protein concentration was ~30 mg mL^{-1} in water and the volume of the reservoir solution was 500 µL. The MWCO of the RC dialysis membrane was 6 – 8 kDa.

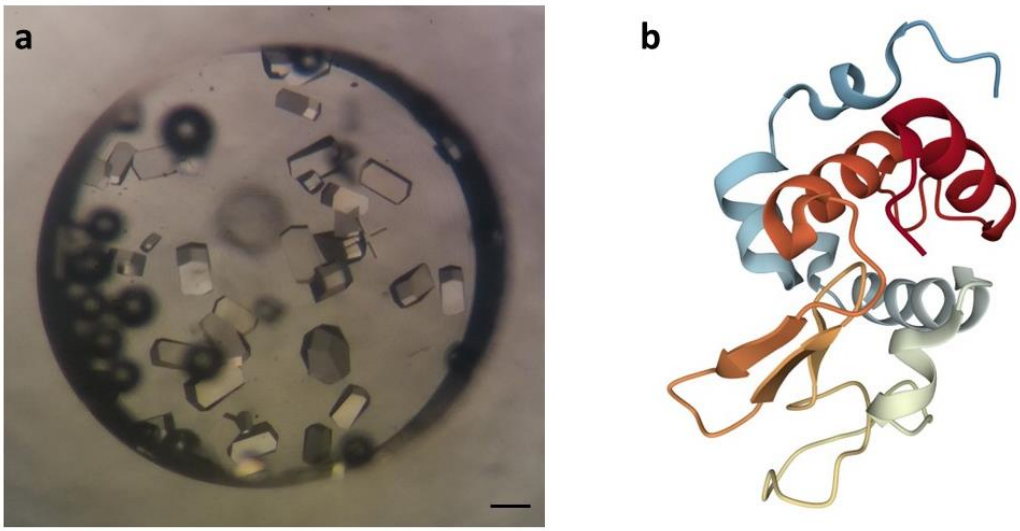

Figure 1.2.1: (a) HEWL (~30 mg mL^{-1}) crystals grown in a 30 µL dialysis button under 0.7 M NaCl and 400 mM CH_3COONa pH 4.0 at 293 K. The scale bar represents 100 µm. (b) The structure of tetragonal HEWL crystals determined at 0.94 Å resolution by X-ray diffraction (PDB entry code 1IEE).

1.2.1.2 Thaumatin from *Thaumatococcus danielli*

Thaumatin was first isolated in 1972 from *Thaumatococcus danielli* (katemfe), a fruit found in West Africa. The fruit contains both Thaumatin I and Thaumatin II which have almost the same molecular weight (22 kDa) and the same amino acid sequence (207 amino acids in total), apart from five residues[68]. Thaumatin proteins are produced in plants when attacked by a pathogenic agent. Katemfe produces Thaumatin as a response mechanism to viral pathogens. It is a taste-modifying protein functioning as natural sweetener or flavor enhancer. Thaumatin is one of the sweetest known compounds and it is estimated to be 100000 times sweeter than sucrose on a molar basis[69]. It has been found that the cysteine-rich domain of the human taste receptors T1R3 are involved in the sweet tasting of Thaumatin[70].

Thaumatins constitute a family of single-domain, globular proteins containing eight disulfide bonds. The isoelectric point of Thaumatin is pI = 12. Bipyramidal, Thaumatin crystals were first grown in the presence of L-tartrate ions in the C2, $P4_12_12$ and $P2_12_12_1$ space groups[71]. Ever since, Thaumatin has been used as a model system for protein crystallography and has been crystallized with many conventional crystallization methods and novel methods, such as in microgravity[72] and within microfluidic chips by counter diffusion[73]. Thaumatin is highly soluble in water, but concerning the temperature dependence, the protein solubility varies with the chirality of the tartrate ion. Specifically, in the presence of L-tartrate, the solubility increases with temperature, while the protein has a reverse solubility in D-tartrate[74].

The structure of tetragonal Thaumatin I crystals determined at 1.05 Å resolution by X-ray diffraction and crystallized in the $P4_12_12$ space group (PDB entry 1RQW) is shown in Figure 1.2.2 (b). The crystals were grown by the vapor diffusion method (hanging drop) at 298 K. Figure 1.2.2 (a) shows Thaumatin crystals grown by hanging drop under 1 M potassium sodium

tartrate ($KNaC_4H_4O_6$) and 50 mM ADA ($C_6H_{10}N_2O_5$) pH 6.5 at 293 K. The protein concentration was ~41 mg mL^{-1} in water and the volume of the reservoir solution was 500 µL. The drop consisted of 2 µL protein and 2 µL of the precipitant solution. The Thaumatin lyophilized powder (Sigma-Aldrich) was a mixture of Thaumatin I and Thaumatin II.

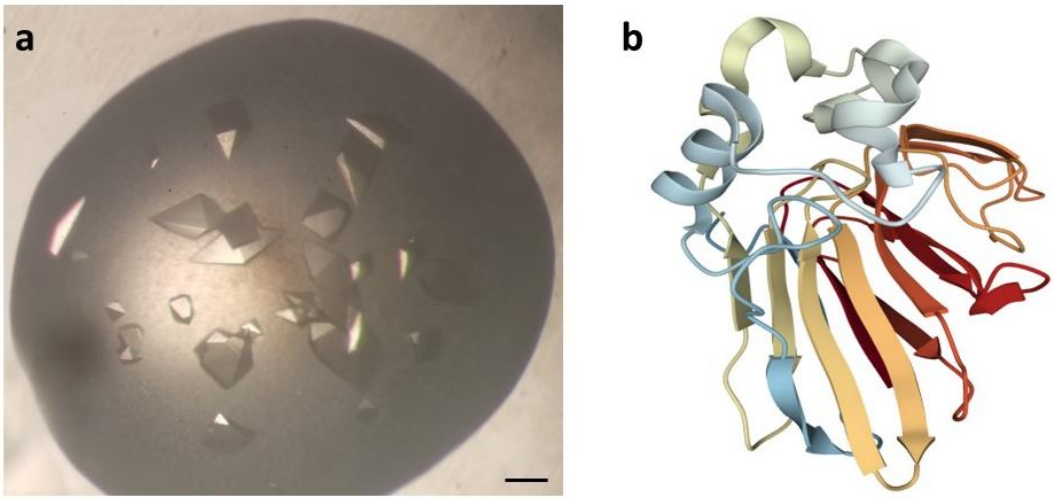

Figure 1.2.2: (a) Thaumatin (~41 mg mL^{-1}) crystals grown by hanging drop under 1 M potassium sodium tartrate and 50 mM ADA pH 6.5 at 293 K. The scale bar represents 100 µm. (b) The structure of tetragonal Thaumatin I crystals determined at 1.05 Å resolution by X-ray diffraction (PDB entry code 1RQW).

1.2.2 Membrane proteins

1.2.2.1 ShuA from *Shigella dysenteriae*

Iron is an essential nutrient for most living organisms and plays an important role for the characterization of virulence of pathogenic bacteria. Under aerobic conditions, iron oxidizes rapidly and due to this capability of gaining or losing an electron, it participates in critical metabolic processes such as oxygen metabolism, electron transfer and deoxyribonucleotide synthesis. As a result of the insolubility of iron under aerobic conditions, its biological concentration is very low[75] (10^{-18} M). The concentration required for bacterial growth has been estimated at 10^{-8} - 10^{-7} M[76]. In humans, iron is majorly bound to heme in hemoglobin.

In order to circumvent iron-depleted conditions and meet their nutrient requirements, pathogenic Gram-negative bacteria have developed mechanisms for iron uptake through iron-chelating compounds, known as siderophores. Siderophores have a low molecular weight (500 – 1500 kDa) and are categorized to catechols, hydroxycarboxylates and hydroxamates[77]. Ferric iron (Fe^{3+}) is bound in siderophores which can be transported across the outer membrane of

Gram-negative bacteria by TonB-dependent transporters (TBDT). Specifically, iron acquisition in Gram-negative bacteria is undertaken by a complex consisting of an outer membrane receptor, a periplasmic binding protein (PBP) and a cytoplasmic (inner) membrane ABC (ATP-Binding Cassette) transporter[78]. Outer membrane receptors transport siderophores into the periplasm against a concentration gradient using the energy-dependent mechanism of proton motive force and ATP (adenosine triphosphate) hydrolysis. The cytoplasmic proteins associated to the siderophores uptake are TonB, ExbB and ExbD and the outer membrane proteins are called TonB-dependent receptors[77,79]. Figure 1.2.3 illustrates the transport process of ferric iron in Gram-negative bacteria[80].

TonB-dependent uptake systems are targets for antibiotics because they allow specific permeability of the cell envelope in Gram-negative bacteria[79]. Bacteria may express more than one system for iron uptake but each one is specific for a single siderophore. For example *E. coli* synthesizes 7 TonB-dependent transporters[80]. Other compounds transported through TBDTs are vitamin B_{12}, nickel and carbohydrates[81]. The first crystal structures of two TBDTs (FhuA and FepA) from *E. coli* were publish in 1998 and several structures have been solved with X-ray diffraction ever since[80].

Shigella dysenteriae is a Gram-negative human pathogenic bacterium of the *Entobacteriaceae* family responsible for dysentery. *Shigella dysenteriae* uses free heme or heme from hemoglobin as an iron source which binds to the TonB-dependent outer membrane transporter ShuA[82]. Heme is transported through the outer membrane into the periplasm and then, it is transferred to the cytoplasm with an ABC transporter. The structure of ShuA was solved by Cobessi *et al.*[83] at 2.6 Å resolution in the presence of heavy atoms (Pb^{2+}) through X-ray diffraction (PDB entry code 3FHH). The expression and purification protocol was developed by the same group[84]. ShuA was overexpressed in *E. coli* and the outer membranes were solubilized with octyl-polyoxyethylene (octyl-POE) detergent. Octyl-POE was exchanged to n-octyl-β-D-glucopyranoside (β-OG) for crystallization. The protein crystallized in the orthorhombic $P2_12_12_1$ space group via the vapor diffusion method (sitting drop) at 290 K. The structure of ShuA (PDB entry code 3FHH) is shown in Figure 1.2.4 (a), while Figure 1.2.4 (b) shows a 3D printed model of the protein. The polypeptide consists of 621 amino acid residues and the molecular weight is approximately 71.7 kDa. The structure consists of a transmembrane β-barrel with 22 strands, filled by the N-terminal plug domain. The strands of the β-barrel are connected by flexible extracellular loops involved in the ligand recognition. It is suggested that the heme group binds to two histidines, His86 and His420 which are 9.86 Å apart. His86 is located at the apex of the plug and His420 in the extracellular loop L7. A conformational change of the apex and the L7 loop is suggested for the heme binding in ShuA[83].

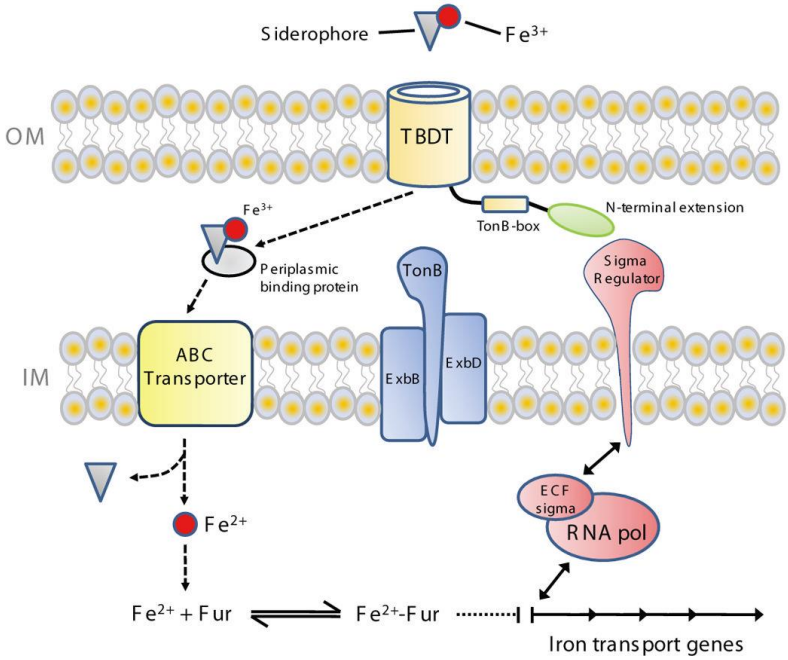

Figure 1.2.3: Schematic representation of the transport mechanism and regulation of ferric siderophores in Gram-negative bacteria. The TBDT transporter is located in the outer membrane (OM) of the cell wall. Used with permission from [80].

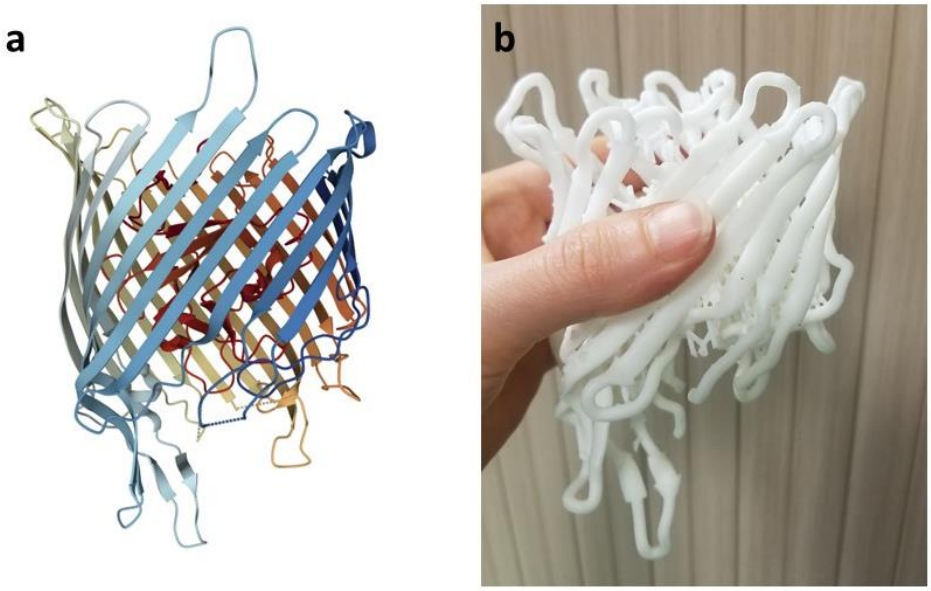

Figure 1.2.4: (a) The structure of ShuA solved at 2.6 Å resolution through X-ray diffraction (PDB entry code 3FHH) and (b) a 3D printed model of ShuA.

1.2.2.2 AcrB from *Escherichia coli*

Multidrug transporters are involved in serious implications in cancer chemotherapy and the antibiotic resistance of pathogenic bacteria. In bacterial cells, multidrug resistance is associated to the overexpression of multidrug efflux systems[85]. Multidrug transporters recognize and extrude toxic compounds from the cells. In mammalian cells, ABC are the majority of multidrug efflux transporters. In human cells, P-glycoprotein is a multidrug efflux pump preventing toxic compounds entering the mucosal surface of the intestinal tract and when overexpressed, it increases the drug resistance of cancer cells[86].

The Acriflavine resistance protein B, AcrB, is a multidrug transporter in *E. coli*, responsible for the resistance of *E. coli* against antibiotics, dyes, disinfectants and detergents. AcrB is an inner membrane protein forming a complex with the periplasmic fusion protein AcrA and the outer membrane channel TolC. AcrA links AcrB and TolC proteins. The AcrA-AcrB-TolC complex ejects compounds from the inner cell directly into the surrounding environment without using the periplasm. AcrB belongs to the resistance nodulation division (RND) transporters[87], one of the five families of bacterial multidrug transporters[88]. The transport mechanism of AcrB is fueled by proton motive force. AcrB in *E. coli* is responsible for transporting drugs, while the only RND member in *E. coli* responsible for exporting heavy metals (copper, silver) is CusA[89].

The first structure of native AcrB crystals was published in 2002[90] (PDB entry code 1IWG) and is shown in Figure 1.2.5 (a). The protein was overexpressed in *E. coli* cells and the membranes were solubilized with n-dodecyl β-D-maltoside (DDM) detergent. The structure was determined at 3.5 Å resolution by X-ray diffraction and the protein crystallized in the H32 space group with the sitting drop method at 298 K. AcrB is a homotrimer and each monomer consists of a transmembrane region with 12 helices and a protruding head which opens like a funnel for the TolC docking. A central cavity (Figure 1.2.5 (b)) is formed at the bottom of the head suggesting that compounds are transported through the pore into the TolC channel. The molecular weight of the monomer is approximately 114 kDa and it consists of 1049 amino acids. Ever since, AcrB has been co-crystallized in the presence of many ligands, shedding more light to the binding mechanism of this multidrug efflux transporter.

Trimeric, wild-type AcrB was crystallized in the presence of rhodamine 6G, ethidium, dequalinium and ciprofloxacin and the structure suggested that three molecules of each ligand bind simultaneously to the central cavity by hydrophobic, aromatic or van der Waals interactions, but each ligand uses different residues for binding[86]. Several drugs were also used to determine the structure of a mutant AcrB, indicating that ligands bind not only to the wall of the central cavity but also to a periplasmic site formed by the C-terminal loop[91]. AcrB was also crystallized in the symmetric R32 and the asymmetric C2 space groups and the structures suggested that the protein captures ligands mainly from the periplasm. However, ligands can enter the cavity of the transporter from the cytoplasm possibly through interactions with phenylalanine residues of the N-terminus[92]. AcrB monomers cycle among three conformational states: a loose, L (or access) state, a tight, T (or binding) state and an open, O (or extrusion) state. Drugs of low molecular weight bind directly to the distal pocket of the T monomer. However, high molecular weight drugs, such as rifampicin and erythromycin, bind first to the proximal pocket of the L monomer and then to the distal pocket by a peristaltic mechanism[93]. The access pocket of the L monomer is separated by the binding pocket of the T monomer by a switch-loop[94,95].

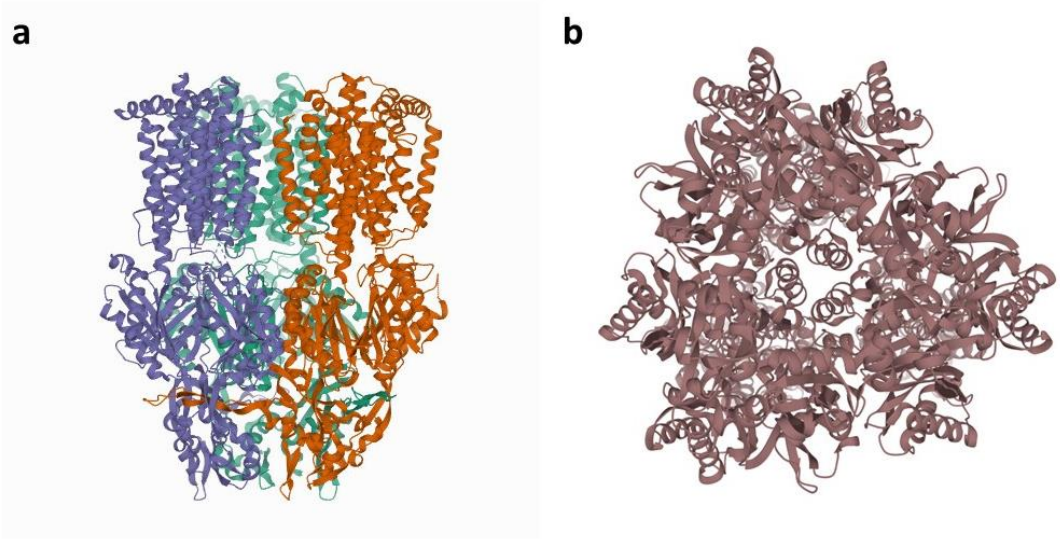

Figure 1.2.5: (a) The structure of AcrB determined at 3.5 Å resolution by X-ray diffraction and (b) the central cavity (pore) of the AcrB homotrimer serving at transporting compounds (PDB entry code 1IWG).

1.2.2.3 SERCA from *Oryctolagus cuniculus*

P-type ATPases are a family of enzymes found in eukaryotic and prokaryotic organisms involved in pumping cations across the cell membrane. These P-type cation pumps, also known as ion motive ATPases, catalyze the hydrolysis of ATP into ADP (adenosine diphosphate) and inorganic phosphate (P_i). This dephosphorylation reaction releases chemical energy within the cells used in other processes. The enzymes also catalyze the reverse process of phosphorylation. P-type ATPases are integral membrane proteins which apart from being involved in the ATP cycle, pump ions across the membrane against an electrochemical gradient. The phosphorylation and the binding site of the ion are separated in the tertiary structure of the protein. P-type ATPases are categorized in Type I, usually involved in the transport of heavy atoms (Cu^{2+}, Cd^{2+}, Hg^{2+}) and Type II that transfer cations with lower atomic mass (Na^+, K^+, Ca^{2+}, H^+)[96].

In eukaryotic cells, the Ca^{2+}-ATPases are involved in the regulation of calcium concentration and are located in the plasma membranes (PMCA), the sarco-endoplasmic reticulum (SERCA) or the secretory pathway (SPCA)[97]. The calcium-transporting ATPases play an important role for muscle functioning and calcium signaling or transport. There are various types of SERCA proteins, as for example SERCA1a expressed in the adult human fast-twitch muscle or SERCA2A in cardiac and slow-twitch muscles. Malfunctions on P-type ATPases are associated with severe diseases in humans. For example, SERCA1 is related to Brody myopathy and SERCA2 to heart failure and Darier disease[97]. SERCA transports calcium and proton ions through the endoplasmic reticulum membrane in opposite directions. The energy of this

process in produced by the hydrolysis of ATP molecules. A scheme for the four-step reaction mechanism of SERCA is provided in Figure 1.2.6 (a)[98]. In general, SERCA alternates between the high energy E1 state, related to phosphorylation, and the lower energy E2 state, related to dephosphorylation. First, the phosphorylated intermediate with bound cytoplasmic ions (Ca_2E1) is formed. Then, the bound calcium ions are released across the membrane through conformational changes driven by the ATP hydrolysis. During this step, there is a conversion to the low-energy state (H_nE2P) where the affinity for Ca^{2+} is low and protons are attached to the intermediate. Then, phosphate is removed (H_nE2) and the enzyme goes through this cycle again by binding calcium ions (Ca_2E1). In the final step, there is a Ca^{2+}/H^+ exchange in opposite direction[96,97,99]. Neutron macromolecular crystallography has been proposed to study the protonation process in SERCA[98]. In this study, we used the rabbit SERCA Ca_2E1-AMPPCP form for on chip crystallization via microdialysis and *in situ* X-ray diffraction. The protein was provided by Dr. Samuel J. Hjorth-Jensen and Prof. Poul Nissen from the Department of Molecular Biology and Genetics – DANDRITE (Aarhus University, Denmark)[100]. The structure of SERCA1 in complex with the non-hydrolyzable ATP analogue AMPPCP (β,γ-methylene ATP) was determined at 2.6 Å resolution[101] and the dephosphorylation process were studied[102].

The first structure of SERCA near to atomic resolution (2.6 Å) was solved in 2000[103] (PDB entry code 1SU4) in the Ca_2E1 open conformation without any ATP molecule bound. The two calcium ions (shown in Figure 1.2.6 (b) in green color) are bound in the transmembrane domain comprised of 10 α-helices. The cytoplasmic part of the membrane consists of three domains: the central catalytic or phosphorylation domain (P-domain where the Na^+ ion is shown in Figure 1.2.6 (b) in purple color), the nucleotide-binding domain (N-domain) and the N-terminal or A-domain. The molecular weight of the monomer is approximately 110 kDa and it consists of 994 amino acids. The protein crystallized in the C121 space group through the microdialysis method and the X-ray data collection was performed at cryogenic conditions (100 K).

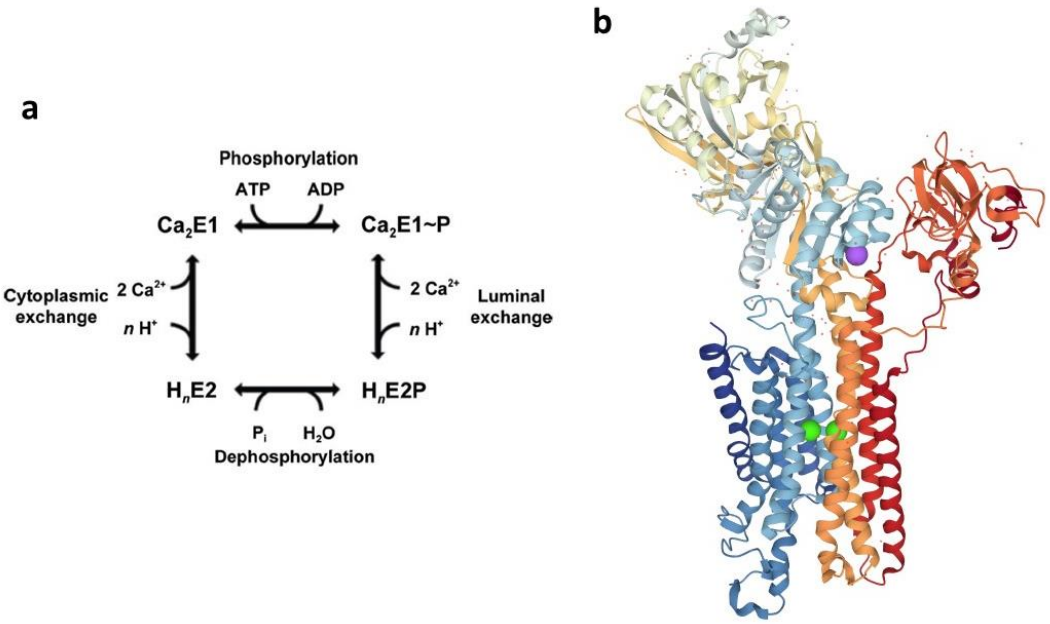

Figure 1.2.6: (a) Schematic representation of the four-step reaction mechanism of SERCA. SERCA transports Ca^{2+} and H^+ ions in opposite directions across the endoplasmic reticulum membrane using energy from the ATP hydrolysis. Used with permission from [98]. (b) The structure of SERCA in the Ca_2E1 open conformation determined at 2.6 Å resolution by X-ray diffraction (PDB entry code 1SU4). The two Ca^{2+} ions the Na^+ ion are shown in green and purple, respectively.

1.2.2.4 TmPPase from *Thermotoga maritima*

Membrane-bound pyrophosphatases (M-PPase) are enzymes coupling the synthesis and hydrolysis of pyrophosphate (PP_i) to the generation of potentials across biological membranes. M-PPases are homodimers consisting of 15 – 17 transmembrane helices. Their catalytic substrate is Mg_2PP_i and they all bind Mg^{2+} ions. M-PPases are found in prokaryotes and eukaryotes and their role is crucial for cells to survive under abiotic conditions, such as cold or drought. They are categorized in four classes based on the monovalent cation binding and pumping specificity: the K^+-independent H^+-PPases, the K^+-dependent H^+-PPases, the Na^+-PPases and the Na^+/H^+-PPases[104]. The sodium-pumping PPases are found only in prokaryotic cells. Na^+-PPases and the Na^+/H^+-PPases bind sodium ions required for their activity. In low concentration of Na^+, Na^+-PPases can pump both protons and sodium ions[105], but very high concentrations have an inhibitory effect[106].

The first structure of M-PPases was published in 2012 at 2.6 Å resolution[107]. It is the structure of the Na^+-pumping M-PPase from *Thermotoga maritima* (TmPPase) in the resting state with bound Mg^{2+} and Ca^{2+} ions, as shown in Figure 1.2.7 (b) (PDB entry code 4AV3). The protein crystallized in the $P12_11$ space group by sitting drop at 295 K. The molecular weight of the homodimer is approximately 157 kDa. Each monomer consists of 16 transmembrane helices. The active site has four regions: the hydrolytic center above the surface of the

membrane, the coupling funnel, the gate below the membrane surface and a channel for exiting Na^+ ions. In the native state, the gate is closed. The authors proposed a binding mechanism, shown in Figure 1.2.7 (a). They suggest that the substrate (PP_i) binding leads to the closure of the active site by a conformational movement of helices 5 and 6. At the same time, movement of helices 11 and 12 opens the gate and the cation (Na^+) can exit to the extra-cellular environment. The active site can open only right after the hydrolysis of the pyrophosphate group, when the two phosphates are released. Further studies of the group on TmPPase structures in various catalytic states, support and provide further insights into the proposed binding mechanism[108]. In this study, we used TmPPase for on chip crystallization via microdialysis and *in situ* X-ray diffraction. The protein was provided by Jannik Strauss and Prof. Adrian Goldman from the Astbury Centre for Structural Molecular Biology (University of Leeds, UK).

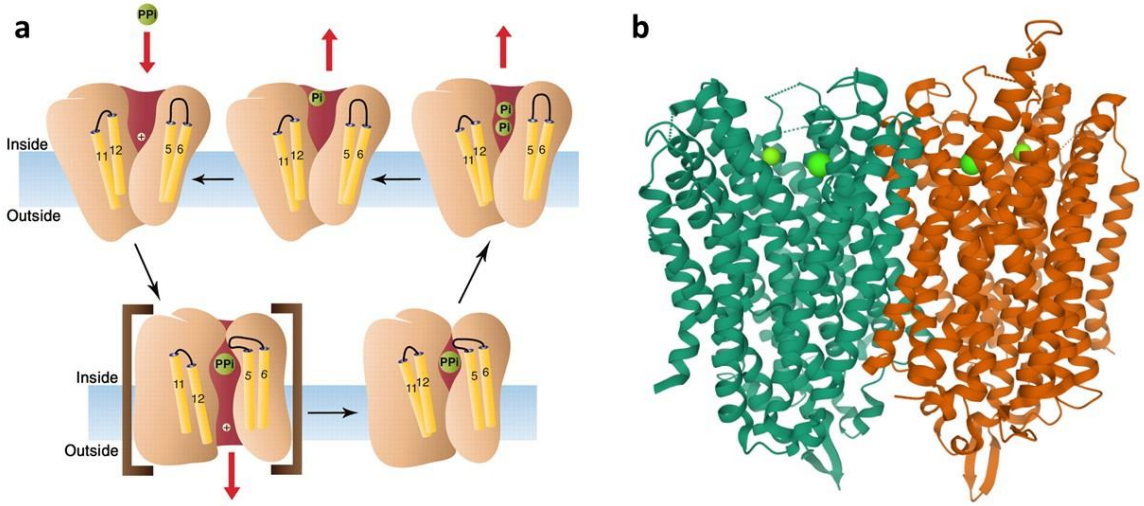

Figure 1.2.7: (a) Binding mechanism of M-PPases proposed by Kellosalo *et al*.[107]. Substrate (PP_i) binding leads to the closure of the active site by movement of helices 5 and 6, while movement of helices 11 and 12 opens the gate and Na^+ can exit to the extra-cellular environment. (b) Structure of TmPPase in the resting state with bound Mg^{2+} and Ca^{2+} ions determined at 2.6 Å resolution by X-ray diffraction (PDB entry code 4AV3).

1.3 Microfluidics

1.3.1 General concepts

In this section, some general concepts on the flow at the microfluidic scale are presented based on the book of P. Tabeling "Introduction to Microfluidics"[109] and critical review papers[110,111]. The microfluidic world and its inherent properties are vast and, in several cases, well studied and characterized. In this section, simple notions relevant to our microfluidic application are discussed to provide a comprehensive insight of the microdialysis crystallization on microchips.

Fundamental physics acts differently at the microfluidic scale. For example, inertia effects, responsible for instabilities in fluid mechanics and the generation of chaotic turbulence, are negligible at the microfluidic scale. Some dimensionless numbers expressing the importance of phenomena such as convection or diffusion can describe fluid physics. Assuming continuum, incompressible (constant density), monophasic, Newtonian fluids, the conservation of mass (Eq. (1.11)) and momentum (Eq. (1.12)) can be expressed through the Navier-Stokes equations (Eq. (1.13)). A fluid is Newtonian when the stress tensor is linearly correlated to the deformation tensor at every point.

$$\frac{\partial \rho}{\partial t} + \nabla(\rho \cdot \mathbf{u}) = 0 \quad (1.11)$$

$$\rho \frac{D\mathbf{u}}{Dt} = \nabla \cdot \boldsymbol{\sigma} + \mathbf{F} \quad (1.12)$$

$$\rho \frac{D\mathbf{u}}{Dt} = -\nabla P + \nu \nabla^2 \mathbf{u} + \rho \mathbf{g} \quad (1.13)$$

Where ρ is the density (kg m^{-3}), t is the time (s), **u** is the flow velocity field (m s^{-1}), **∇** is the divergence (a vector operating on a vectorial field like the velocity), **σ** is the Cauchy stress tensor (including both pressure and shear stress), **F** is the external force sum (N) acting throughout the body volume, P is the pressure (N m^{-2}), μ is the shear viscosity (N s m^{-2}) and g is the gravitational acceleration (~9.81 m s^{-2}).

The material derivative has a temporal and spatial term and can be written as:

$$\frac{D}{Dt} = \frac{\partial}{\partial t} + \mathbf{u} \nabla \quad (1.14)$$

Combining Eq. (1.13) and (1.14), the Navier-Stokes equation for Newtonian fluids is:

$$\rho \left(\frac{\partial \mathbf{u}}{\partial t} + \mathbf{u} \nabla \mathbf{u} \right) = -\nabla P + \mu \nabla^2 \mathbf{u} + \rho \mathbf{g} \quad (1.15)$$

The inertial forces appear on the left of Eq. (1.15) and the external forces on the right. In this case, we assume that the external forces acting on the fluid are pressure, viscous stress and gravity. The kinematic viscosity (ν = μ/ρ) is a measure of the diffusivity for fluid flow.

Moreover, it should be mentioned that the incompressibility assumption is valid when the fluid velocity is much lower than the speed of sound.

Assume a planar Poiseuille flow of incompressible, Newtonian fluid in a rectangular channel of width w (y coordinate), height h (z coordinate) and length l (x coordinate), where l >> w, h. The velocity has only the x component, there is no acceleration and the flow is laminar (low Reynolds number). Then, Eq. (1.16) describes the pressure drop induced only by the viscosity:

$$\frac{\mathrm{dP}}{\mathrm{dx}} = \mu\left(\frac{\partial^2 u}{\partial y^2} + \frac{\partial^2 u}{\partial z^2}\right) \quad (1.16)$$

For a channel length L, the pressure drop is related to the volumetric flow rate, Q ($m^3\ s^{-1}$):

$$\mathrm{Q} = \frac{\Delta \mathrm{P}\ \mathrm{w}\ h^3}{12\ \mu\ L} \quad (1.17)$$

Eq. (1.17) is important for calculating the hydrodynamic resistance within a rectangular microfluidic channel with a length L. In analogy to the electronic circuits, it can be deduced from Eq. (1.17):

$$\Delta \mathrm{P} = \mathrm{R} \cdot \mathrm{Q} \quad (1.18)$$

Combining Eq. (1.17) and (1.18), the hydrodynamic resistance of the fluidic channel is:

$$\mathrm{R} = \frac{12\ \mu\ \mathrm{L}}{\mathrm{w\ h^3}} \quad (1.19)$$

1.3.2 Inertia at the microscale

The Reynolds number (Re) is associated to inertial forces and is frequently mentioned in microfluidic applications where inertial effects are negligible. Re is a dimensionless number comparing inertial against viscous forces. It derives from the Navier-Stokes equations (Eq. (1.15)) assuming steady flow in one spatial direction of an incompressible, Newtonian fluid. The Reynolds number is given by the following equation, where ρ is the density ($kg\ m^{-3}$), u is the fluid velocity ($m\ s^{-1}$), L_0 is the characteristic dimension of the microfluidic channel (m) and μ is the shear viscosity ($N\ s\ m^{-2}$):

$$\mathrm{Re} = \frac{\rho\ \mathrm{u}\ L_0}{\mu} = \frac{\text{inertial forces}}{\text{viscous forces}} \quad (1.20)$$

In the microscale, the Reynolds number ranges between 10^{-6} – 10 for typical velocity values of a few μm s^{-1} to a few cm s^{-1}, length values between 1 – 100 μm and assuming the viscosity and density of water[110]. The low Re values in microfluidic applications confirm that inertial forces are negligible and the flow is laminar. A flow is laminar when Re < 2300 and turbulent when Re > 3000. For Re in between these values, the flow is called intermittent. At moderate Re numbers at the microscale produced for example by inkjet printer, where the

velocity reaches a few meters per second, irreversibility can be observed leading to boundary layer separation[109].

1.3.3 Convection, diffusion and mixing at the microscale

For high Re values, turbulent mixing occurs, but for the low Re regime of microfluidics only diffusive mixing takes place. The dimensionless number comparing convection against diffusion is the Péclet number (Pe):

$$\mathrm{Pe} = \frac{\mathrm{u}\,\mathrm{L_0}}{\mathrm{D}} = \frac{\text{convection}}{\text{diffusion}} \quad (1.21)$$

Where D is the mass diffusion coefficient ($m^2\ s^{-1}$) derived from Fick's law of diffusion. For simple liquids, typical values of D are in the order of $10^{-5}\ m^2\ s^{-1}$. The higher the Pe number, the more flow dominates over molecular diffusion. In mass related transport phenomena, Pe is the product of Re and Schmidt's number (Sc) correlating momentum diffusivity and mass diffusivity in fluids. Assuming a linear channel with width w, where two fluids flow in parallel, it would take a time of approximately w^2/D for the fluids' particles to diffuse freely across the whole length of the channel. Therefore, Pe varies approximately to the square of the characteristic dimension of the microchannel (~ L_0^2), suggesting that the microscale is mainly governed by diffusion which can be too slow. However, there is no characteristic value regime for the Pe number at the microscale, as opposed to the Re number.

There are several mixing microfluidic systems, such as the T junction[112], micromixers based on size sorting[113], the H filter[114], circular micromixers[115] or the herringbone micromixer[116]. While for the first examples, mixing occurs slowly through diffusion among laminar fluidic streams, in the case of the circular and herringbone mixers, stirring motion is used in order to reduce the mixing length. The main idea behind these systems is that the fluids are mixed rapidly enough so the system is reaction-, and not diffusion-limited.

In the case of our microfluidic devices, if microdialysis occurs under static conditions (no flow of the crystallization solution within the microfluidic channel), diffusion dominates over convection. However, in the case where the crystallization solution circulates within the microchannel under constant flow with the aid of an external pressure-driven system, the flow is still driven by diffusion if the velocity flux remains low.

1.3.4 Interface phenomena

The surface-to-volume ratio at the microscale is much larger than the respective one in other fluidic systems, indicating the importance of interface phenomena for microfluidic applications. The surface energy is called interfacial tension, γ ($J\ m^{-2}$). In a microfluidic channel, the wetting of the channel by the fluid (crystallization solution) can be described by three interfaces: the interface between the solid substrate of the channel (S) and the fluid (L) with a surface energy γ_{SL}, the interface between the solid substrate and the air/gas within the

channel (G) with γ_{SG} surface energy and between the fluid and the air with interfacial energy γ_{LG} (Figure 1.3.1). Young's law describes this system in equilibrium:

$$\gamma_{SG} + \gamma_{SL} + \gamma_{LG} \cdot \cos\theta = 0 \quad (1.22)$$

Where θ is the wetting angle between the fluid and the solid substrate. For low θ values, the spreading of the fluid on the solid surface is high and the surface can be characterized as hydrophilic. In the case of high θ values the surface is hydrophobic. Knowing the wettability of a solution on a surface is quite important. Several chemicals, such as silanes or surfactants, can change the hydrophobicity of the surface. In the case of protein crystallization, detergents are used to solubilize membrane proteins, PEGs are used in the crystallization solution as precipitants or lipids are used for the reconstitution of proteins in lipidic mesophases. All these factors can affect the wetting of the microchannel's surface.

Interfacial phenomena are also important for droplet-based microfluidics[117], where droplets are formed between two immiscible fluids. In this system, there are two competing forces: the surface tension acting on reducing the interfacial area and the viscous forces acting on extending the interface, leading eventually to the droplet formation. The dimensionless capillary number (Ca) describes the competition between interfacial and viscous forces:

$$\mathrm{Ca} = \frac{\mu\, u}{\gamma} = \frac{\text{interfacial stress}}{\text{viscous stress}} \quad (1.23)$$

Where γ is the interfacial energy between the two immiscible fluids (J m^{-2}), u is the fluid velocity (m s^{-1}) and μ is the shear viscosity (N s m^{-2}).

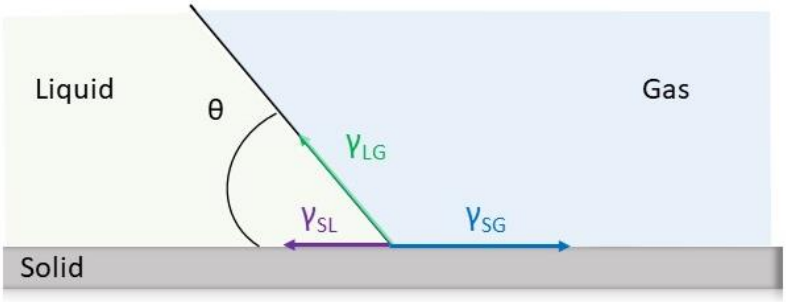

Figure 1.3.1: Schematic representation of Young's law illustrating the interfaces among a solid substrate, liquid and gas and the respective surface energy vectors (γ).

1.3.5 Microfluidic crystallization

Microfluidics exhibit many advantages for the crystallization of biological macromolecules[111,118–121]. First of all, crystallization on microfluidic devices requires minute amounts of protein sample (typically on the nL scale) reducing significantly the production and purification cost of these high-valued biological macromolecules. Moreover, microfluidic devices yield a large surface-to-volume area, compared to traditional methods for protein crystallization, enabling a fine control over interfacial phenomena critical for droplet formation or heterogeneous nucleation. At the same time, the flow of solutions in microfluidic channels is laminar, characterized by low Re numbers, allowing diffusive mixing and short mixing times. Inertial and convective phenomena are limited at the microfluidic scale and turbulent mixing or gravitational effects are negligible. This control over transport phenomena in microfluidic environments facilitates a fine tuning of concentration or temperature gradients, or the generation of supersaturation, necessary for controlling the nucleation and subsequent growth of crystals with desired size distribution and diffraction quality. These advantages render microchips proper devices for investigating phase diagrams[122–125] and performing high-throughput screening and optimization of crystallization conditions, using merely a few nL - µL of the valuable protein sample. Furthermore, on chip crystallization addresses another hurdle in protein crystallography, which is the manipulation of the fragile protein crystals. Manual handling, harvesting or cryo-preservation leading to concealed conformational changes of the 3D protein structure[126] can be avoided.

But how exactly does the microscale affect crystallization? As already mentioned in Section 1.1, crystallization is a process governed by both kinetic and thermodynamic parameters. Thermodynamics controls the solubility through temperature, pH, solvent concentration and other factors, while the kinetic trajectories on the phase diagram affect the size, number and morphology of the crystals. Studying crystallization kinetics is essential for decoupling nucleation from crystal growth. According to CNT, the induction time for nucleation is strongly dependent on the supersaturation (Eq. (1.8), Section 1.1.1) and practically, it can define the MSZW in the phase diagram. There are two models for the theoretical determination of the induction time: the mononuclear mechanism suggesting that the formation of the first, single nucleus drives the system out of metastability and the polynuclear mechanism suggesting that this occurs only when a number of nuclei are formed up to an adequate size. In both cases, the induction time is defined as[136]:

$$t_i = \frac{1}{J V_t} + \left(\frac{\alpha}{\alpha_n J G^{n-1}}\right)^{1/n} \quad (1.24)$$

Where J is the nucleation frequency ($m^{-3}\ s^{-1}$), V_t is the system volume (m^3), $\alpha = V_m/V_t$, V_m is the volume of a nucleus, α_n is a shape factor determined by the growth mechanism and G is the growth rate. Eq. (1.24) is a generalized formula for all growth mechanisms of the nuclei and it is independent on whether the mechanism is mononuclear or polynuclear. The first term of the sum ($1/JV_t$) is the mean induction time of the mononuclear mechanism and the second term of the sum, being independent of the system's volume, corresponds to polynuclear mechanism.

Eq. (1.24) shows a clear correlation between the nucleation time and the system's volume. In the case of small volumes, the mononuclear mechanism prevails. The microfluidic scale, where V_t is small (order of μL), affects nucleation kinetics by prolonging the induction time for nucleation. This way, nucleation kinetics indicated by the mononuclear mechanism can be decoupled by growth kinetics and measurements of the induction time can be practically feasible. However, since induction time in microfluidics can be prolonged, supersaturation can be adjusted in order to induce nucleation within shorter time intervals. On the other hand, one must keep in mind that due to these prolonged induction times, not observing crystals inside microfluidic devices doesn't necessary translates to no nucleation at all.

As explained in Section 1.1.1, nucleation kinetics was originally described for the case of droplet condensation from its vapor phase in order to overcome the problems associated to nucleation in bulk solutions. Large volumes, impurities or heterogeneous nucleation in several sites within the bulk, complicate the measurements of nucleation rates (J) and induction time (t_i) in solutions. Nucleation in droplets is a useful approximation to study nucleation kinetics in small volumes and overcome the complications imposed by larger volumes[6,127]. However, even this approximation can be compromised by the polydispersity of the formed droplets. Droplet-based microfluidic devices offer the advantage of generating small volumes of monodisperse droplets necessary to study nucleation kinetics and phase diagrams[117,128].

1.3.6 Microfluidic devices for protein crystallization

It is beyond the scope of this work to review all the advances accomplished in the field of microfluidic crystallization or cite an extensive list of publications. There are indeed several review articles[111,117,119–121,129,130] overviewing the progress on microfluidic devices developed for protein crystallization and structure determination with the *in situ* X-ray diffraction method. However, it is important to point out that despite the versatile advances in this field, the integration of microdialysis in microfluidic devices has not been thoroughly studied.

The majority of the conventional methods for protein crystallization (Section 1.1.3) have been implemented in microfluidic devices. Simple, hybrid or multi-layered microchips have been developed for on chip protein crystallization via vapor diffusion[131], microbatch[132], FID[27], counter diffusion[73], solvent evaporation[133] or micro-seeding[134]. The on chip crystallization of more challenging protein samples, such as membrane proteins, has also been studied. For example, the group of R. F. Ismagilov[135] developed a droplet-based microfluidic approach for screening and optimizing the crystallization conditions of the reaction center from *Rhodopseudomonas viridis* and the porin from *Rdodobacter capsulatus* in nL-sized plugs. Crystallization of the reaction center from *Blastochloris viridis* was performed on the SlipChip, a well-based microfluidic device made of soda-lime glass[136]. Moreover, the group of J. A. Kenis has implemented the use of lipidic mesophases for protein crystallization at the microscale. They have developed a microfluidic platform made of thin COC (50 μm) and PDMS (35 – 70 μm) layers for on chip preparation of lipidic mesophases and phase characterization with *in situ* SAXS[63] and on chip crystallization of the photosynthetic reaction center from *Rhodobacter sphaeroides* and structure analysis with *in situ* X-ray diffraction[137].

Another emerging issue in protein crystallization at the microscale is that of high-throughput screening and optimization of crystallization conditions. A critical review on the milestones and major developments in the field of high-throughput screening with microfluidic devices has been published by Li and Ismagilov[130]. Several crystallization methods have been successfully applied in valve-, droplet- or well-based microfluidic devices for screening and optimization in protein crystallography. Droplet-based microfluidics has been the preferred technique for crystallization screening in small volumes combined with microbatch, pseudo-vapor diffusion or FID[117,138,139]. Moreover, the formation of nL - µL sized droplets facilitates the study of nucleation or reaction kinetics and phase diagrams.

Microfluidic devices provide several benefits for controlling the size uniformity and the morphology of protein crystals grown on chip. One of the most significant advantages is that microfluidic tools circumvent the need for manually handling and harvesting the fragile protein crystals prior to their use for structural analysis with the X-ray diffraction method. Many research groups working on the field of structural biology have proposed the approach of *in situ* X-ray diffraction on crystals grown directly on microchips. Microfluidic devices are being designed and developed with a double goal of serving as microscale alternatives to conventional crystallization techniques and simultaneously, as substitutes of classical methodologies for delivering protein crystals in front of the X-ray beam through cryo-loops or capillaries. Fabricating microfluidic devices compatible with *in situ* X-ray diffraction experiments encounters some restrictions related to the interactions of X-rays with matter. The composition of the fabrication materials and their thickness are parameters that should be highly considered, since attenuation induced by the absorption of X-rays from the materials, reduces the intensity of the diffracted beam. Moreover, the background noise generated by scattering of the materials should be maintained as low as possible in order to avoid restrictions or complications on the interpretation of the diffraction signal from the crystal. The interactions of X-ray radiation with matter, the constrains rising when choosing fabrication materials and some examples of microchips compatible with *in situ* X-ray diffraction experiments are provided in more detail in Chapter 2. The characterization of the materials composing our dialysis microchip is also provided in Chapter 2.

While microfluidic technology addresses the sample delivery issues in X-ray radiation facilities with the *in situ* data collection approach, another restrictive parameter in protein crystallography is the radiation damage observed in protein crystals. Cryogenic cooling of the crystals prior to their exposure to X-ray radiation has been proposed to overcome this problem. However, finding the optimal cryo-cooling conditions for each protein sample requires screening and it can be laborious and time-consuming. In addition, cryo-cooling can conceal conformational changes of the 3D protein structure. Data collection on microfluidic devices is performed mainly at room temperature, even though there are chips designed to perform crystallization and the addition of cryo-protectants in a single device[140]. Recent studies have shown that lower specific radiation damage was observed for diffraction experiments performed at room temperature[141]. The impact of radiation damage on protein crystallography and some simulations on the case of radiation damage of HEWL crystals grown on our microchips with the microdialysis method are detailed in Chapter 4.

Current studies in protein crystallography focus on more challenging protein targets due to the continuous development of increasingly bright and micro-focused X-ray beams at synchrotron facilities and the advent of X-ray free-electron lasers (XFELs). The novel approach of serial crystallography[142,143] has been introduced both at synchrotron (serial synchrotron X-

ray crystallography, SSX) and XFELs (serial femtosecond X-ray crystallography, SFX) and is based on collecting and merging partial diffraction data sets from multiple, small (200 nm to 2 μm)[142], randomly oriented crystals before their destruction due to radiation damage. A high-density multi-crystal grid fabricated by a 100 or 200 μm thick polycarbonate plastic can be used for loading crystals directly onto the ports of the device or crystals can be grown on the device by vapor diffusion or the LCP method. Moreover, the grid can be adjusted in a standard magnetic base and used for *in situ* X-ray data collection at cryogenic or room temperature conditions[144]. The structures of various protein samples have been determined at high resolution with this fixed-target approach using XFELs[145]. Single-crystalline silicon chips have been used for fixed-target SSX. The structure of myoglobin from *Physeter catodon* was determined at 1.8 Å resolution[146]. The structure of glucose isomerase was solved at 2.1 Å resolution by collecting partial data sets from numerous crystals at room temperature on chips made of a 80 μm-thick PDMS layer sealed on both sides by 25 or 50 μm-thick COC foil or 8 μm-thick Kapton foil[147]. Microfluidic chips have been also used for *in situ* time-resolved studies of the photoactive yellow protein (PYP) from *Halorhodospira halophila* at room temperature where the photoinitiation was performed with pulsed laser illumination[148].

All the devices mentioned above are only a small fraction of the developments achieved in microfluidics for protein crystallization and structure determination. Examples were given to emphasize how microfluidic technology has been evolved to keep up with the ongoing progress and requirements of protein crystallography. The main contribution of this work in this rapidly advancing field is the implementation of the microdialysis method in microchips developed for on chip and *in situ* X-ray diffraction studies of soluble and membrane proteins at room temperature.

1.3.7 Microfluidic dialysis

Dialysis as a crystallization method is based on the use of a semi-permeable membrane separating the compartments containing the precipitant and protein solutions. Supersaturation is achieved by the diffusion of the precipitant molecules through the semi-permeable membrane towards the protein solution. The kinetic pathway of the dialysis in the phase diagram (Figure 1.1.3), enables precise and reversible control over the crystallization conditions. Combined with temperature control, dialysis can be used to decouple and optimize nucleation and crystal growth kinetics independently[149] allowing the thorough investigation of phase diagrams merely by altering the precipitant concentration while using the same protein sample.

Membranes are defined as selective barriers permitting some species such as molecules or ions to pass through. The transport across a membrane is driven by a gradient in concentration, temperature, pressure or electrical potential between the two sides of the membrane. When concentration gradient is the driving force, the operation can be dialysis, pervaporation or forward osmosis. Micro-, ultra- and nano-filtration or reverse osmosis and gas separation are pressure-driven separations[150]. The transport mechanism depends on the structure of the membrane which can be dense or porous[151]. The transport across dense membranes, such as PDMS or cellulose ester, is diffusion-based and this model applies in

dialysis, reverse osmosis or pervaporation. Dense membranes are characterized by their permeability (P) and selectivity (α), both being intrinsic properties indicating the capacity and the separation efficiency of the membrane. For porous membranes, such as polysulfonate or polyether membranes, transport occurs through the pores, convectively, according to the hydrodynamic model and not through the material of the membrane. In this case, the morphology of the membrane such as the porosity (ε), the pore size and the tortuosity (τ) indicate the separation efficiency. Membranes are characterized by the MWCO in Daltons (Da). The MWCO is defined as the molecular weight retaining 90 % of the transported species. In crystallization via dialysis, the MWCO of the membrane is smaller than the molecular weight of the protein, but large enough to allow smaller molecules such as salts, PEGs or solvents, to diffuse through the membrane.

Membranes can also be further classified in homogeneous when they are entirely fabricated by a single material either polymeric or inorganic and heterogeneous when they are composed by a dense and a porous layer. In fact, there are several classifications depending on the membrane morphology or functionality[152]. For example, ion-exchange membranes allow the transportation of charged ions across the membrane, while retaining oppositely charged ions or neutral particles. The driving force for the separation is a gradient in the electrical potential. Porous, dense or electrically charged membranes are all characterized as isotropic. Anisotropic membranes consist of several layers with different structure or permeability. For example, interfacial membranes consist of a thin, dense film on the surface and a thicker, porous support. There are indeed several possible combinations of membrane characteristics and morphologies. In dialysis crystallization, RC membranes are the most commonly used. The RC dialysis membrane is hydrophilic but not soluble in water, allowing the diffusion of ions or molecules with low molecular weight, while retaining macromolecules such as proteins, due to the intermolecular hydrogen bonding among the hydroxyl groups of the membrane[153,154]. Dialysis membranes are microporous and homogeneous with high chemical and biological compatibility. In this work, RC dialysis membranes from SpectrumLabs were used with a MWCO of 6 – 8 or 12 – 14 kDa depending on the protein sample and the molecular weight of PEGs in the crystallization solution.

Several approaches have been reported for the integration of membrane technology in microfluidics. A review by de Jong *et al.*[151] summarizes the integration of membrane functionality in four main categories, while the review by Chen and Shen[150] adds the recent developments in the field. Commercially available membranes can be directly incorporated into microfluidic devices by clamping or gluing. This method is relatively simple in application and allows the choice among a variety of membrane materials and morphologies, but the sealing of the device can be a difficult task. A second method to integrate membranes in microfluidics is to prepare the membrane during the fabrication of the device where porous layers can be fabricated directly by materials used in the process. An alternative is to use the membrane properties of the materials composing the chip. PDMS has been widely studied and exploited for its high permeability to gas[155], while other polymeric materials such as polyimides can serve the same purpose. The fourth method of membrane integration is the *in situ* preparation. Since the pioneering work of Beebe *et al.*[156] for fabricating active hydrogels inside microchannels by direct photo-polymerization of the liquid phase, much progress has been reported in the use of hydrogels as membrane materials. Song *et al.*[157] fabricated nano-porous microdialysis membranes of acrylate monomers in chips by using phase separation polymerization with a UV laser beam. They fabricated two membranes with different MWCOs

showing that controlling the phase separation and the ratio between the monomer and the cross-linker can modify the MWCO of the membrane, the position and the thickness. Recently, the group of J.-B. Salmon used a maskless UV projection setup for the *in situ* photo-patterning of nano-porous hydrogel membranes in microfluidic devices made of polyethylene glycol diacrylate (PEGDA) 250 [158] or PDMS[159]. In the latter case, they fabricated membranes with a MWCO within the range compatible with protein microdialysis.

The case studies in biology integrating dialysis in microfluidic devices can be mainly listed in sample preparation, concentration or filtration and cell studies[160]. But what about protein crystallization on chips with the dialysis method? Shim *et al.*[149] developed the Phase Chip, a device made of PDMS that takes advantage of the membrane properties of the elastomer in order to implement dialysis for protein crystallization. 1 nL droplets of the protein sample (xylanase) were formulated in a continuous oil stream and stored in the wells of the chip. First, numerous, small nuclei of crystals were formed which were subsequently, dissolved by using dialysis to reduce the protein and precipitant concentration. This approach of decoupling nucleation from growth enables only a few, large, high-quality crystals to grow. Kornreich *et al.*[161] fabricated a dialysis chip made of two PDMS layers separated by a cellulose ester membrane. Dialysis was used to exchange buffer conditions in order to monitor the phase transition of the filamentous bacteriophage *fd* virus from isotropic to liquid crystal with cross polarizers. A step further on the use of dialysis for *in situ* structural studies of proteins was done by Skou *et al.*[162]. The authors developed a microfluidic setup with two separate modules. The first module is a dialysis chip where a RC dialysis membrane is ''sandwiched'' in between two PDMS sheets, clamped together with two pieces of 5 mm thick PMMA plates. The dialysis chip was used to concentrate a protein solution (lysozyme) with an imposed osmotic pressure difference across the membrane. The dialysis chip was connected to the exposure chip where a 25 µm thick polystyrene (PS) window was used for *in situ* SAXS measurements. Recently, as mentioned above, Nguyen *et al.*[159] fabricated PEGDA-based hydrogel membranes within PDMS channels using maskless UV projection photo-polymerization. The chips were used to measure the membrane permeability and estimate the MWCO (10 – 20 kDa) and to crystallize chicken egg-white lysozyme via microdialysis.

Despite the tremendous progress in the field, there hasn't been so far to our knowledge, a microfluidic device designed for on chip crystallization of proteins with the microdialysis method and compatible for *in situ* X-ray diffraction experiments. We have developed such a chip made of the photo curable NOA 81 (Norland Optical Adhesive) resin, incorporating a RC dialysis membrane. The MWCO of the RC membrane can vary and is chosen accordingly to the experimental conditions, i.e. the molecular weight of the protein sample and the precipitating agent. The chips have been used for the on chip crystallization of soluble (HEWL, Thaumatin) and membrane (ShuA from *Shigella dysenteriae*, AcrB from *Escherichia coli*, SERCA from *Oryctolagus cuniculus*, TmPPase from *Thermotoga maritima*) proteins and have been fully characterized for their compatibility with *in situ* X-ray diffraction experiments. Chapter 2 details the development of the chip's fabrication protocol, while the crystallization trials and the diffraction experiments are included in Chapter 4.

1.4 References

(1) J.W. Mullin. Crystallization. 4th ed.; Elsevier, **2001**.
(2) Yoreo, J. J. D.; Vekilov, P. G. Principles of Crystal Nucleation and Growth. *Rev. Mineral. Geochem.* **2003**, *54* (1), 57–93.
(3) Manuel García-Ruiz, J. Nucleation of Protein Crystals. *J. Struct. Biol.* **2003**, *142* (1), 22–31.
(4) Erdemir, D.; Lee, A. Y.; Myerson, A. S. Nucleation of Crystals from Solution: Classical and Two-Step Models. *Acc. Chem. Res.* **2009**, *42* (5), 621–629.
(5) Boistelle, R.; Astier, J. P. Crystallization Mechanisms in Solution. *J. Cryst. Growth* **1988**, *90* (1), 14–30.
(6) Turnbull, D. Formation of Crystal Nuclei in Liquid Metals. *J. Appl. Phys.* **1950**, *21* (10), 1022–1028.
(7) Turnbull, D.; Fisher, J. C. Rate of Nucleation in Condensed Systems. *J. Chem. Phys.* **1949**, *17* (1), 71–73.
(8) Bodenstaff, E. R.; Hoedemaeker, F. J.; Kuil, M. E.; Vrind de, H. P. M.; Abrahams, J. P. The Prospects of Protein Nanocrystallography. *Acta Crystallogr., Sect. D: Biol. Crystallogr.* **2002**, *58* (11), 1901–1906.
(9) Laaksonen, A.; Napari, I. Breakdown of the Capillarity Approximation in Binary Nucleation: A Density Functional Study. *J. Phys. Chem. B* **2001**, *105* (47), 11678–11682.
(10) Wolde, P. R. ten; Frenkel, D. Enhancement of Protein Crystal Nucleation by Critical Density Fluctuations. *Science* **1997**, *277* (5334), 1975–1978.
(11) Vekilov, P. G. Dense Liquid Precursor for the Nucleation of Ordered Solid Phases from Solution. *Cryst. Growth Des.* **2004**, *4* (4), 671–685.
(12) Chernov, A. A. The Spiral Growth of Crystals. *Sov. Phys. Usp.* **1961**, *4* (1), 116.
(13) Chernov, A. A. Formation of Crystals in Solutions. *Contemp. Phys.* **1989**, *30* (4), 251–276.
(14) Matthews, B. W. Solvent Content of Protein Crystals. *J. Mol. Biol.* **1968**, *33* (2), 491–497.
(15) Russo Krauss, I.; Merlino, A.; Vergara, A.; Sica, F. An Overview of Biological Macromolecule Crystallization. *Int. J. Mol. Sci.* **2013**, *14* (6), 11643–11691.
(16) McPherson, A.; Malkin, A.; Kuznetsov, Y. The Science of Macromolecular Crystallization. *Structure* **1995**, *3* (8), 759–768.
(17) McPherson, A. Introduction to Protein Crystallization. *Methods* **2004**, *34* (3), 254–265.
(18) Asherie, N. Protein Crystallization and Phase Diagrams. *Methods* **2004**, *34* (3), 266–272.
(19) Malkin, A. J.; Kuznetsov, Y. G.; Land, T. A.; DeYoreo, J. J.; McPherson, A. Mechanisms of Growth for Protein and Virus Crystals. *Nature Struct. Biol.* **1995**, *2* (11), 956–959.
(20) Rosenberger, F.; Howard, S. B.; Sowers, J. W.; Nyce, T. A. Temperature Dependence of Protein Solubility — Determination and Application to Crystallization in X-Ray Capillaries. *J. Cryst. Growth* **1993**, *129* (1), 1–12.
(21) Dumetz, A. C.; Chockla, A. M.; Kaler, E. W.; Lenhoff, A. M. Effects of PH on Protein–Protein Interactions and Implications for Protein Phase Behavior. *Biochim. Biophys. Acta Proteins Proteom.* **2008**, *1784* (4), 600–610.
(22) McPherson, A.; Nguyen, C.; Cudney, R.; Larson, S. B. The Role of Small Molecule Additives and Chemical Modification in Protein Crystallization. *Cryst. Growth Des.* **2011**, *11* (5), 1469–1474.
(23) McPherson, A. Introduction to Protein Crystallization. *Methods* **2004**, *34* (3), 254–265.
(24) Chayen, N. E. Comparative Studies of Protein Crystallization by Vapour-Diffusion and Microbatch Techniques. *Acta Crystallogr., Sect. D: Biol. Crystallogr.* **1998**, *54* (1), 8–15.

(25) Benvenuti, M.; Mangani, S. Crystallization of Soluble Proteins in Vapor Diffusion for X-Ray Crystallography. *Nature Protoc.* **2007**, *2* (7), 1633–1651.
(26) Chayen, N. E.; Shaw Stewart, P. D.; Maeder, D. L.; Blow, D. M. An Automated System for Micro-Batch Protein Crystallization and Screening. *J. Appl. Crystallogr.* **1990**, *23* (4), 297–302.
(27) Hansen, C. L.; Skordalakes, E.; Berger, J. M.; Quake, S. R. A Robust and Scalable Microfluidic Metering Method That Allows Protein Crystal Growth by Free Interface Diffusion. *PNAS* **2002**, *99* (26), 16531–16536.
(28) Li, L.; Du, W.; Ismagilov, R. F. Multiparameter Screening on SlipChip Used for Nanoliter Protein Crystallization Combining Free Interface Diffusion and Microbatch Methods. *J. Am. Chem. Soc.* **2010**, *132* (1), 112–119.
(29) García-Ruiz, J. M. Counterdiffusion Methods for Macromolecular Crystallization. *Meth. Enzymol.* **2003**, 368, 130–154.
(30) Ng, J. D.; Gavira, J. A.; García-Ruíz, J. M. Protein Crystallization by Capillary Counterdiffusion for Applied Crystallographic Structure Determination. *J. Struct. Biol.* **2003**, *142* (1), 218–231.
(31) Apostolopoulou, V.; Junius, N.; Sear, R. P.; Budayova-Spano, M. Mixing Salts and Poly(Ethylene Glycol) into Protein Solutions: The Effects of Diffusion across Semipermeable Membranes and of Convection. *Cryst. Growth Des.* **2020**, *20* (6), 3927–3936.
(32) Junius, N.; Jaho, S.; Sallaz-Damaz, Y.; Borel, F.; Salmon, J.-B.; Budayova-Spano, M. A Microfluidic Device for Both On-Chip Dialysis Protein Crystallization and in Situ X-Ray Diffraction. *Lab Chip* **2020**, *20* (2), 296–310.
(33) Jaho, S.; Junius, N.; Borel, F.; Sallaz-Damaz, Y.; Salmon, J.-B.; Budayova-Spano, M. Crystallization of Proteins on Chip by Microdialysis for In Situ X-Ray Diffraction Studies. *J. Visualized Exp.* **2021**, No. 170, e61660.
(34) Wallin, E.; Heijne, G. V. Genome-Wide Analysis of Integral Membrane Proteins from Eubacterial, Archaean, and Eukaryotic Organisms. *Protein Sci.* **1998**, *7* (4), 1029–1038.
(35) Fagerberg, L.; Jonasson, K.; Heijne, G. von; Uhlén, M.; Berglund, L. Prediction of the Human Membrane Proteome. *Proteomics* **2010**, *10* (6), 1141–1149.
(36) Bakheet, T. M.; Doig, A. J. Properties and Identification of Human Protein Drug Targets. *Bioinformatics* **2009**, *25* (4), 451–457.
(37) Caffrey, M. Membrane Protein Crystallization. *J. Struct. Biol.* **2003**, *142* (1), 108–132.
(38) Deisenhofer, J.; Epp, O.; Miki, K.; Huber, R.; Michel, H. Structure of the Protein Subunits in the Photosynthetic Reaction Centre of Rhodopseudomonas Viridis at 3Å Resolution. *Nature* **1985**, *318* (6047), 618–624.
(39) Newport, T. D.; Sansom, M. S. P.; Stansfeld, P. J. The MemProtMD Database: A Resource for Membrane-Embedded Protein Structures and Their Lipid Interactions. *Nucleic Acids Res.* **2019**, *47* (D1), D390–D397.
(40) Ostermeier, C.; Michel, H. Crystallization of Membrane Proteins. *Curr. Opin. Struct. Biol.* **1997**, *7* (5), 697–701.
(41) Seddon, A. M.; Curnow, P.; Booth, P. J. Membrane Proteins, Lipids and Detergents: Not Just a Soap Opera. *Biochim. Biophys. Acta Biomembr.* **2004**, *1666* (1), 105–117.
(42) Garavito, R. M.; Picot, D. The Art of Crystallizing Membrane Proteins. *Methods* **1990**, *1* (1), 57–69.
(43) Loll, P. J. Membrane Protein Structural Biology: The High Throughput Challenge. *J. Struct. Biol.* **2003**, *142* (1), 144–153.

(44) Wiener, M. C. A Pedestrian Guide to Membrane Protein Crystallization. *Methods* **2004**, *34* (3), 364–372.
(45) Caffrey, M. A Comprehensive Review of the Lipid Cubic Phase or in Meso Method for Crystallizing Membrane and Soluble Proteins and Complexes. *Acta Crystallogr., Sect. F: Struct. Biol. Commum.* **2015**, *71* (1), 3–18.
(46) le Maire, M.; Champeil, P.; Møller, J. V. Interaction of Membrane Proteins and Lipids with Solubilizing Detergents. *Biochim. Biophys. Acta Biomembr.* **2000**, *1508* (1), 86–111.
(47) Linke, D. Chapter 34 Detergents: An Overview. In *Methods in Enzymology*; *Guide to Protein Purification* (Burgess, R. R., Deutscher, M. P.) Academic Press, **2009**, *463*, 603–617.
(48) Salim, M.; Minamikawa, H.; Sugimura, A.; Hashim, R. Amphiphilic Designer Nano-Carriers for Controlled Release: From Drug Delivery to Diagnostics. *MedChemComm* **2014**, *5* (11), 1602–1618.
(49) Anandan, A.; Vrielink, A. Detergents in Membrane Protein Purification and Crystallisation. In *The Next Generation in Membrane Protein Structure Determination*; Moraes, I., Ed.; Advances in Experimental Medicine and Biology; Springer International Publishing: Cham, **2016**; pp 13–28.
(50) Takeda, K.; Sato, H.; Hino, T.; Kono, M.; Fukuda, K.; Sakurai, I.; Okada, T.; Kouyama, T. A Novel Three-Dimensional Crystal of Bacteriorhodopsin Obtained by Successive Fusion of the Vesicular Assemblies. *J. Mol. Biol.* **1998**, *283* (2), 463–474.
(51) Landau, E. M.; Rosenbusch, J. P. Lipidic Cubic Phases: A Novel Concept for the Crystallization of Membrane Proteins. *PNAS* **1996**, *93* (25), 14532–14535.
(52) Rummel, G.; Hardmeyer, A.; Widmer, C.; Chiu, M. L.; Nollert, P.; Locher, K. P.; Pedruzzi, I.; Landau, E. M.; Rosenbusch, J. P. Lipidic Cubic Phases: New Matrices for the Three-Dimensional Crystallization of Membrane Proteins. *J. Struct. Biol.* **1998**, *121* (2), 82–91.
(53) Briggs, J.; Chung, H.; Caffrey, M. The Temperature-Composition Phase Diagram and Mesophase Structure Characterization of the Monoolein/Water System. *J. Phys. II* **1996**, *6* (5), 723–751.
(54) Qiu, H.; Caffrey, M. The Phase Diagram of the Monoolein/Water System: Metastability and Equilibrium Aspects. *Biomaterials* **2000**, *21* (3), 223–234.
(55) V. Kulkarni, C.; Wachter, W.; Iglesias-Salto, G.; Engelskirchen, S.; Ahualli, S. Monoolein : A Magic Lipid? *Phys. Chem. Chem. Phys.* **2011**, *13* (8), 3004–3021.
(56) Joseph, J. S.; Liu, W.; Kunken, J.; Weiss, T. M.; Tsuruta, H.; Cherezov, V. Characterization of Lipid Matrices for Membrane Protein Crystallization by High-Throughput Small Angle X-Ray Scattering. *Methods* **2011**, *55* (4), 342–349.
(57) Cherezov, V.; Fersi, H.; Caffrey, M. Crystallization Screens: Compatibility with the Lipidic Cubic Phase for in Meso Crystallization of Membrane Proteins. *Biophys. J.* **2001**, *81* (1), 225–242.
(58) Ma, P.; Weichert, D.; Aleksandrov, L. A.; Jensen, T. J.; Riordan, J. R.; Liu, X.; Kobilka, B. K.; Caffrey, M. The Cubicon Method for Concentrating Membrane Proteins in the Cubic Mesophase. *Nature Protoc.* **2017**, *12* (9), 1745–1762.
(59) Aherne, M.; Lyons, J. A.; Caffrey, M. A Fast, Simple and Robust Protocol for Growing Crystals in the Lipidic Cubic Phase. *J. Appl. Crystallogr.* **2012**, *45* (6), 1330–1333.
(60) Caffrey, M.; Cherezov, V. Crystallizing Membrane Proteins Using Lipidic Mesophases. *Nature Protoc.* **2009**, *4* (5), 706–731.

(61) Cherezov, V.; Peddi, A.; Muthusubramaniam, L.; Zheng, Y. F.; Caffrey, M. A Robotic System for Crystallizing Membrane and Soluble Proteins in Lipidic Mesophases. *Acta Crystallogr., Sect. D: Biol. Crystallogr.* **2004**, *60* (10), 1795–1807.
(62) Huang, C.-Y.; Olieric, V.; Ma, P.; Panepucci, E.; Diederichs, K.; Wang, M.; Caffrey, M. In Meso in Situ Serial X-Ray Crystallography of Soluble and Membrane Proteins. *Acta Crystallogr., Sect. D: Biol. Crystallogr.* **2015**, *71* (6), 1238–1256.
(63) S. Khvostichenko, D.; Kondrashkina, E.; L. Perry, S.; S. Pawate, A.; Brister, K.; A. Kenis, P. J. An X-Ray Transparent Microfluidic Platform for Screening of the Phase Behavior of Lipidic Mesophases. *Analyst* **2013**, *138* (18), 5384–5395.
(64) Blake, C. C. F.; Koenig, D. F.; Mair, G. A.; North, A. C. T.; Phillips, D. C.; Sarma, V. R. Structure of Hen Egg-White Lysozyme. *Nature* **1965**, *206*, 757–761.
(65) Phillips, D. C. The Three-Dimensional Structure of an Enzyme Molecule. *Sci. Am.* **1966**, *215* (5), 78–93.
(66) Shugar, D. The Measurement of Lysozyme Activity and the Ultra-Violet Inactivation of Lysozyme. *Biochim. Biophys. Acta* **1952**, *8*, 302–309.
(67) Sauter, C.; Otálora, F.; Gavira, J. A.; Vidal, O.; Giegé, R.; García-Ruiz, J. M. Structure of Tetragonal Hen Egg-White Lysozyme at 0.94 Å from Crystals Grown by the Counter-Diffusion Method. *Acta Crystallogr., Sect. D: Biol. Crystallogr.* **2001**, *57* (8), 1119–1126.
(68) Edens, L.; Heslinga, L.; Klok, R.; Ledeboer, A. M.; Maat, J.; Toonen, M. Y.; Visser, C.; Verrips, C. T. Cloning of CDNA Encoding the Sweet-Tasting Plant Protein Thaumatin and Its Expression in Escherichia Coli. *Gene* **1982**, *18* (1), 1–12.
(69) Vos, A. M. de; Hatada, M.; Wel, H. van der; Krabbendam, H.; Peerdeman, A. F.; Kim, S. H. Three-Dimensional Structure of Thaumatin I, an Intensely Sweet Protein. *PNAS* **1985**, *82* (5), 1406–1409.
(70) Masuda, T.; Taguchi, W.; Sano, A.; Ohta, K.; Kitabatake, N.; Tani, F. Five Amino Acid Residues in Cysteine-Rich Domain of Human T1R3 Were Involved in the Response for Sweet-Tasting Protein, Thaumatin. *Biochimie* **2013**, *95* (7), 1502–1505.
(71) Ko, T.-P.; Day, J.; Greenwood, A.; McPherson, A. Structures of Three Crystal Forms of the Sweet Protein Thaumatin. *Acta Crystallogr., Sect. D: Biol. Crystallogr.* **1994**, *50* (6), 813–825.
(72) McPherson, A.; DeLucas, L. J. Microgravity Protein Crystallization. *Microgravity* **2015**, *1* (1), 1–20.
(73) Dhouib, K.; Malek, C. K.; Pfleging, W.; Gauthier-Manuel, B.; Duffait, R.; Thuillier, G.; Ferrigno, R.; Jacquamet, L.; Ohana, J.; Ferrer, J.-L.; Théobald-Dietrich, A.; Giegé, R.; Lorber, B.; Sauter, C. Microfluidic Chips for the Crystallization of Biomacromolecules by Counter-Diffusion and on-Chip Crystal X-Ray Analysis. *Lab Chip* **2009**, *9* (10), 1412–1421.
(74) Asherie, N.; Ginsberg, C.; Greenbaum, A.; Blass, S.; Knafo, S. Effects of Protein Purity and Precipitant Stereochemistry on the Crystallization of Thaumatin. *Cryst. Growth Des.* **2008**, *8* (12), 4200–4207.
(75) Neilands, J. B. Siderophores: Structure and Function of Microbial Iron Transport Compounds. *J. Biol. Chem.* **1995**, *270* (45), 26723–26726.
(76) Stintzi, A.; Barnes, C.; Xu, J.; Raymond, K. N. Microbial Iron Transport via a Siderophore Shuttle: A Membrane Ion Transport Paradigm. *PNAS* **2000**, *97* (20), 10691–10696.
(77) Ferguson, A. D.; Deisenhofer, J. TonB-Dependent Receptors—Structural Perspectives. *Biochim. Biophys. Acta Biomembr.* **2002**, *1565* (2), 318–332.
(78) Krewulak, K. D.; Vogel, H. J. Structural Biology of Bacterial Iron Uptake. *Biochim. Biophys. Acta Biomembr.* **2008**, *1778* (9), 1781–1804.

(79) Moeck, G. S.; Coulton, J. W. TonB-Dependent Iron Acquisition: Mechanisms of Siderophore-Mediated Active Transport. *Mol. Microbiol.* **1998**, *28* (4), 675–681.
(80) Noinaj, N.; Guillier, M.; Barnard, T. J.; Buchanan, S. K. TonB-Dependent Transporters: Regulation, Structure, and Function. *Annu. Rev. Microbiol.* **2010**, *64* (1), 43–60.
(81) Schauer, K.; Rodionov, D. A.; de Reuse, H. New Substrates for TonB-Dependent Transport: Do We Only See the 'Tip of the Iceberg'? *Trends Biochem. Sci.* **2008**, *33* (7), 330–338.
(82) Burkhard, K. A.; Wilks, A. Characterization of the Outer Membrane Receptor ShuA from the Heme Uptake System of Shigella Dysenteriae: Substrate Specificity and Identification of the Heme Protein Ligands. *J. Biol. Chem.* **2007**, *282* (20), 15126–15136.
(83) Cobessi, D.; Meksem, A.; Brillet, K. Structure of the Heme/Hemoglobin Outer Membrane Receptor ShuA from Shigella Dysenteriae: Heme Binding by an Induced Fit Mechanism. *Proteins: Struct., Funct., Bioinf.* **2010**, *78* (2), 286–294.
(84) Brillet, K.; Meksem, A.; Thompson, A.; Cobessi, D. Expression, Purification, Crystallization and Preliminary X-Ray Diffraction Analysis of the TonB-Dependent Haem Outer Membrane Transporter ShuA from Shigella Dysenteriae. *Acta Crystallogr., Sect. F: Struct. Biol. Cryst. Commun.* **2009**, *65* (4), 402–405.
(85) Okusu, H.; Ma, D.; Nikaido, H. AcrAB Efflux Pump Plays a Major Role in the Antibiotic Resistance Phenotype of Escherichia Coli Multiple-Antibiotic-Resistance (Mar) Mutants. *J. Bacteriol.* **1996**, *178* (1), 306–308.
(86) Yu, E. W.; McDermott, G.; Zgurskaya, H. I.; Nikaido, H.; Koshland, D. E. Structural Basis of Multiple Drug-Binding Capacity of the AcrB Multidrug Efflux Pump. *Science* **2003**, *300* (5621), 976–980.
(87) Tseng, T. T.; Gratwick, K. S.; Kollman, J.; Park, D.; Nies, D. H.; Goffeau, A.; Saier, M. H. The RND Permease Superfamily: An Ancient, Ubiquitous and Diverse Family That Includes Human Disease and Development Proteins. *J. Mol. Microbiol. Biotechnol.* **1999**, *1* (1), 107–125.
(88) Nikaido, H. Multidrug Efflux Pumps of Gram-Negative Bacteria. *J. Bacteriol.* **1996**, *178* (20), 5853–5859.
(89) Deniaud, A.; Goulielmakis, A.; Covès, J.; Pebay-Peyroula, E. Differences between CusA and AcrB Crystallisation Highlighted by Protein Flexibility. *PLoS One* **2009**, *4* (7), e6214.
(90) Murakami, S.; Nakashima, R.; Yamashita, E.; Yamaguchi, A. Crystal Structure of Bacterial Multidrug Efflux Transporter AcrB. *Nature* **2002**, *419* (6907), 587–593.
(91) Yu, E. W.; Aires, J. R.; McDermott, G.; Nikaido, H. A Periplasmic Drug-Binding Site of the AcrB Multidrug Efflux Pump: A Crystallographic and Site-Directed Mutagenesis Study. *J. Bacteriol.* **2005**, *187* (19), 6804–6815.
(92) Das, D.; Xu, Q. S.; Lee, J. Y.; Ankoudinova, I.; Huang, C.; Lou, Y.; DeGiovanni, A.; Kim, R.; Kim, S.-H. Crystal Structure of the Multidrug Efflux Transporter AcrB at 3.1Å Resolution Reveals the N-Terminal Region with Conserved Amino Acids. *J. Struct. Biol.* **2007**, *158* (3), 494–502.
(93) Nakashima, R.; Sakurai, K.; Yamasaki, S.; Nishino, K.; Yamaguchi, A. Structures of the Multidrug Exporter AcrB Reveal a Proximal Multisite Drug-Binding Pocket. *Nature* **2011**, *480* (7378), 565–569.
(94) Eicher, T.; Cha, H.; Seeger, M. A.; Brandstätter, L.; El-Delik, J.; Bohnert, J. A.; Kern, W. V.; Verrey, F.; Grütter, M. G.; Diederichs, K.; Pos, K. M. Transport of Drugs by the Multidrug Transporter AcrB Involves an Access and a Deep Binding Pocket That Are Separated by a Switch-Loop. *PNAS* **2012**, *109* (15), 5687–5692.

(95) Ababou, A.; Koronakis, V. Structures of Gate Loop Variants of the AcrB Drug Efflux Pump Bound by Erythromycin Substrate. *PLoS One* **2016**, *11* (7), e0159154.
(96) Møller, J. V.; Juul, B.; le Maire, M. Structural Organization, Ion Transport, and Energy Transduction of P-Type ATPases. *Biochim. Biophys. Acta Rev. Biomembr.* **1996**, *1286* (1), 1–51.
(97) Bublitz, M.; Morth, J. P.; Nissen, P. P-Type ATPases at a Glance. *J. Cell. Sci.* **2011**, *124* (15), 2515–2519.
(98) Sørensen, T. L.-M.; Hjorth-Jensen, S. J.; Oksanen, E.; Andersen, J. L.; Olesen, C.; Møller, J. V.; Nissen, P. Membrane-Protein Crystals for Neutron Diffraction. *Acta Crystallogr., Sect. D: Struct. Biol.* **2018**, *74* (12), 1208–1218.
(99) Møller, J. V.; Olesen, C.; Winther, A.-M. L.; Nissen, P. The Sarcoplasmic Ca2+-ATPase: Design of a Perfect Chemi-Osmotic Pump. *Q. Rev. Biophys.* **2010**, *43* (4), 501–566.
(100) Hjorth-Jensen, S. J.; Oksanen, E.; Nissen, P.; Sørensen, T. L.-M. Chapter Three - Prospects for Membrane Protein Crystals in NMX. *Meth. Enzymol.* **2020**, *634*, 47–68.
(101) Sørensen, T. L.-M.; Møller, J. V.; Nissen, P. Phosphoryl Transfer and Calcium Ion Occlusion in the Calcium Pump. *Science* **2004**, *304* (5677), 1672–1675.
(102) Olesen, C.; Sørensen, T. L.-M.; Nielsen, R. C.; Møller, J. V.; Nissen, P. Dephosphorylation of the Calcium Pump Coupled to Counterion Occlusion. *Science* **2004**, *306* (5705), 2251–2255.
(103) Toyoshima, C.; Nakasako, M.; Nomura, H.; Ogawa, H. Crystal Structure of the Calcium Pump of Sarcoplasmic Reticulum at 2.6 Å Resolution. *Nature* **2000**, *405* (6787), 647–655.
(104) Tsai, J.-Y.; Kellosalo, J.; Sun, Y.-J.; Goldman, A. Proton/Sodium Pumping Pyrophosphatases: The Last of the Primary Ion Pumps. *Curr. Opin. Struct. Biol.* **2014**, *27*, 38–47.
(105) Luoto, H. H.; Nordbo, E.; Baykov, A. A.; Lahti, R.; Malinen, A. M. Membrane Na+-Pyrophosphatases Can Transport Protons at Low Sodium Concentrations. *J. Biol. Chem.* **2013**, *288* (49), 35489–35499.
(106) Malinen, A. M.; Belogurov, G. A.; Baykov, A. A.; Lahti, R. Na+-Pyrophosphatase: A Novel Primary Sodium Pump. *Biochemistry* **2007**, *46* (30), 8872–8878.
(107) Kellosalo, J.; Kajander, T.; Kogan, K.; Pokharel, K.; Goldman, A. The Structure and Catalytic Cycle of a Sodium-Pumping Pyrophosphatase. *Science* **2012**, *337* (6093), 473–476.
(108) Li, K.-M.; Wilkinson, C.; Kellosalo, J.; Tsai, J.-Y.; Kajander, T.; Jeuken, L. J. C.; Sun, Y.-J.; Goldman, A. Membrane Pyrophosphatases from Thermotoga Maritima and Vigna Radiata Suggest a Conserved Coupling Mechanism. *Nature Commun.* **2016**, *7* (1), 13596.
(109) Patrick Tabeling. *Introduction to Microfluidics*; Oxford University Press, **2005**.
(110) Squires, T. M.; Quake, S. R. Microfluidics: Fluid Physics at the Nanoliter Scale. *Rev. Mod. Phys.* **2005**, *77* (3), 977–1026.
(111) Ghazal, A.; P. Lafleur, J.; Mortensen, K.; P. Kutter, J.; Arleth, L.; V. Jensen, G. Recent Advances in X-Ray Compatible Microfluidics for Applications in Soft Materials and Life Sciences. *Lab Chip* **2016**, *16* (22), 4263–4295.
(112) Kamholz, A. E.; Weigl, B. H.; Finlayson, B. A.; Yager, P. Quantitative Analysis of Molecular Interaction in a Microfluidic Channel: The T-Sensor. *Anal. Chem.* **1999**, *71* (23), 5340–5347.
(113) Knight, J. B.; Vishwanath, A.; Brody, J. P.; Austin, R. H. Hydrodynamic Focusing on a Silicon Chip: Mixing Nanoliters in Microseconds. *Phys. Rev. Lett.* **1998**, *80* (17), 3863–3866.

(114) Brody, J. P.; Yager, P.; Goldstein, R. E.; Austin, R. H. Biotechnology at Low Reynolds Numbers. *Biophys. J.* **1996**, *71* (6), 3430–3441.
(115) Quake, S. R.; Scherer, A. From Micro- to Nanofabrication with Soft Materials. *Science* **2000**, *290* (5496), 1536–1540.
(116) Stroock, A. D.; Dertinger, S. K. W.; Ajdari, A.; Mezić, I.; Stone, H. A.; Whitesides, G. M. Chaotic Mixer for Microchannels. *Science* **2002**, *295* (5555), 647–651.
(117) Song, H.; Chen, D. L.; Ismagilov, R. F. Reactions in Droplets in Microfluidic Channels. *Angew. Chem. Int. Ed.* **2006**, *45* (44), 7336–7356.
(118) van der Woerd, M.; Ferree, D.; Pusey, M. The Promise of Macromolecular Crystallization in Microfluidic Chips. *J. Struct. Biol.* **2003**, *142* (1), 180–187.
(119) Leng, J.; Salmon, J.-B. Microfluidic Crystallization. *Lab Chip* **2009**, *9* (1), 24–34.
(120) Shi, H.; Xiao, Y.; Ferguson, S.; Huang, X.; Wang, N.; Hao, H. Progress of Crystallization in Microfluidic Devices. *Lab Chip* **2017**, *17* (13), 2167–2185.
(121) Sui, S.; Perry, S. L. Microfluidics: From Crystallization to Serial Time-Resolved Crystallography. *Struct. Dyn.* **2017**, *4* (3), 032202.
(122) Laval, P.; Lisai, N.; Salmon, J.-B.; Joanicot, M. A Microfluidic Device Based on Droplet Storage for Screening Solubility Diagrams. *Lab Chip* **2007**, *7* (7), 829–834.
(123) Selimović, Š.; Gobeaux, F.; Fraden, S. Mapping and Manipulating Temperature–Concentration Phase Diagrams Using Microfluidics. *Lab Chip* **2010**, *10* (13), 1696–1699.
(124) Shim, J.; Cristobal, G.; Link, D. R.; Thorsen, T.; Jia, Y.; Piattelli, K.; Fraden, S. Control and Measurement of the Phase Behavior of Aqueous Solutions Using Microfluidics. *J. Am. Chem. Soc.* **2007**, *129* (28), 8825–8835.
(125) Hansen, C. L.; Sommer, M. O. A.; Quake, S. R. Systematic Investigation of Protein Phase Behavior with a Microfluidic Formulator. *PNAS* **2004**, *101* (40), 14431–14436.
(126) Fraser, J. S.; Bedem, H. van den; Samelson, A. J.; Lang, P. T.; Holton, J. M.; Echols, N.; Alber, T. Accessing Protein Conformational Ensembles Using Room-Temperature X-Ray Crystallography. *PNAS* **2011**, *108* (39), 16247–16252.
(127) Kashchiev, D.; Verdoes, D.; van Rosmalen, G. M. Induction Time and Metastability Limit in New Phase Formation. *J. Cryst. Growth* **1991**, *110* (3), 373–380.
(128) Laval, P.; Crombez, A.; Salmon, J.-B. Microfluidic Droplet Method for Nucleation Kinetics Measurements. *Langmuir* **2009**, *25* (3), 1836–1841.
(129) Sauter, C.; Dhouib, K.; Lorber, B. From Macrofluidics to Microfluidics for the Crystallization of Biological Macromolecules. *Cryst. Growth Des.* **2007**, *7* (11), 2247–2250.
(130) Li, L.; Ismagilov, R. F. Protein Crystallization Using Microfluidic Technologies Based on Valves, Droplets, and SlipChip. *Annu. Rev. Biophys.* **2010**, *39* (1), 139–158.
(131) Zheng, B.; Tice, J. D.; Roach, L. S.; Ismagilov, R. F. A Droplet-Based, Composite PDMS/Glass Capillary Microfluidic System for Evaluating Protein Crystallization Conditions by Microbatch and Vapor-Diffusion Methods with On-Chip X-Ray Diffraction. *Angew. Chem. Int. Ed.* **2004**, *43* (19), 2508–2511.
(132) Kisselman, G.; Qiu, W.; Romanov, V.; Thompson, C. M.; Lam, R.; Battaile, K. P.; Pai, E. F.; Chirgadze, N. Y. X-CHIP: An Integrated Platform for High-Throughput Protein Crystallization and on-the-Chip X-Ray Diffraction Data Collection. *Acta Crystallogr., Sect. D: Biol. Crystallogr.* **2011**, *67* (6), 533–539.
(133) Talreja, S.; Kim, D. Y.; Mirarefi, A. Y.; Zukoski, C. F.; Kenis, P. J. A. Screening and Optimization of Protein Crystallization Conditions through Gradual Evaporation Using a Novel Crystallization Platform. *J. Appl. Crystallogr.* **2005**, *38* (6), 988–995.

(134) M. Schieferstein, J.; S. Pawate, A.; J. Varel, M.; Guha, S.; Astrauskaite, I.; B. Gennis, R.; A. Kenis, P. J. X-Ray Transparent Microfluidic Platforms for Membrane Protein Crystallization with Microseeds. *Lab Chip* **2018**, *18* (6), 944–954.
(135) Li, L.; Mustafi, D.; Fu, Q.; Tereshko, V.; Chen, D. L.; Tice, J. D.; Ismagilov, R. F. Nanoliter Microfluidic Hybrid Method for Simultaneous Screening and Optimization Validated with Crystallization of Membrane Proteins. *PNAS* **2006**, *103* (51), 19243–19248.
(136) Du, W.; Li, L.; P. Nichols, K.; F. Ismagilov, R. SlipChip. *Lab Chip* **2009**, *9* (16), 2286–2292.
(137) Khvostichenko, D. S.; Schieferstein, J. M.; Pawate, A. S.; Laible, P. D.; Kenis, P. J. A. X-Ray Transparent Microfluidic Chip for Mesophase-Based Crystallization of Membrane Proteins and On-Chip Structure Determination. *Cryst. Growth Des.* **2014**, *14* (10), 4886–4890.
(138) Zheng, B.; Roach, L. S.; Ismagilov, R. F. Screening of Protein Crystallization Conditions on a Microfluidic Chip Using Nanoliter-Size Droplets. *J. Am. Chem. Soc.* **2003**, *125* (37), 11170–11171.
(139) Zhang, S.; Gerard, C. J. J.; Ikni, A.; Ferry, G.; Vuillard, L. M.; Boutin, J. A.; Ferte, N.; Grossier, R.; Candoni, N.; Veesler, S. Microfluidic Platform for Optimization of Crystallization Conditions. *J. Cryst. Growth* **2017**, *472*, 18–28.
(140) Maeki, M.; Pawate, A. S.; Yamashita, K.; Kawamoto, M.; Tokeshi, M.; Kenis, P. J. A.; Miyazaki, M. A Method of Cryoprotection for Protein Crystallography by Using a Microfluidic Chip and Its Application for in Situ X-Ray Diffraction Measurements. *Anal. Chem.* **2015**, *87* (8), 4194–4200.
(141) Gotthard, G.; Aumonier, S.; De Sanctis, D.; Leonard, G.; von Stetten, D.; Royant, A. Specific Radiation Damage Is a Lesser Concern at Room Temperature. *IUCrJ* **2019**, *6* (4), 665–680.
(142) Chapman, H. N.; Fromme, P.; Barty, A.; White, T. A.; Kirian, R. A.; Aquila, A.; Hunter, M. S.; Schulz, J.; DePonte, D. P.; Weierstall, U.; Doak, R. B.; Maia, F. R. N. C.; Martin, A. V.; Schlichting, I.; Lomb, L.; Coppola, N.; Shoeman, R. L.; Epp, S. W.; Hartmann, R.; Rolles, D.; Rudenko, A.; Foucar, L.; Kimmel, N.; Weidenspointner, G.; Holl, P.; Liang, M.; Barthelmess, M.; Caleman, C.; Boutet, S.; Bogan, M. J.; Krzywinski, J.; Bostedt, C.; Bajt, S.; Gumprecht, L.; Rudek, B.; Erk, B.; Schmidt, C.; Hömke, A.; Reich, C.; Pietschner, D.; Strüder, L.; Hauser, G.; Gorke, H.; Ullrich, J.; Herrmann, S.; Schaller, G.; Schopper, F.; Soltau, H.; Kühnel, K.-U.; Messerschmidt, M.; Bozek, J. D.; Hau-Riege, S. P.; Frank, M.; Hampton, C. Y.; Sierra, R. G.; Starodub, D.; Williams, G. J.; Hajdu, J.; Timneanu, N.; Seibert, M. M.; Andreasson, J.; Rocker, A.; Jönsson, O.; Svenda, M.; Stern, S.; Nass, K.; Andritschke, R.; Schröter, C.-D.; Krasniqi, F.; Bott, M.; Schmidt, K. E.; Wang, X.; Grotjohann, I.; Holton, J. M.; Barends, T. R. M.; Neutze, R.; Marchesini, S.; Fromme, R.; Schorb, S.; Rupp, D.; Adolph, M.; Gorkhover, T.; Andersson, I.; Hirsemann, H.; Potdevin, G.; Graafsma, H.; Nilsson, B.; Spence, J. C. H. Femtosecond X-Ray Protein Nanocrystallography. *Nature* **2011**, *470* (7332), 73–77.
(143) Neutze, R.; Moffat, K. Time-Resolved Structural Studies at Synchrotrons and X-Ray Free Electron Lasers: Opportunities and Challenges. *Curr. Opin. Struct. Biol.* **2012**, *22* (5), 651–659.
(144) Baxter, E. L.; Aguila, L.; Alonso-Mori, R.; Barnes, C. O.; Bonagura, C. A.; Brehmer, W.; Brunger, A. T.; Calero, G.; Caradoc-Davies, T. T.; Chatterjee, R.; Degrado, W. F.; Fraser, J. S.; Ibrahim, M.; Kern, J.; Kobilka, B. K.; Kruse, A. C.; Larsson, K. M.; Lemke, H. T.; Lyubimov, A. Y.; Manglik, A.; McPhillips, S. E.; Norgren, E.; Pang, S. S.; Soltis, S. M.; Song, J.; Thomaston, J.; Tsai, Y.; Weis, W. I.; Woldeyes, R. A.; Yachandra, V.; Yano, J.; Zouni, A.;

Cohen, A. E. High-Density Grids for Efficient Data Collection from Multiple Crystals. *Acta Crystallogr., Sect. D: Struct. Biol.* **2016**, *72* (1), 2–11.

(145) Cohen, A. E.; Soltis, S. M.; González, A.; Aguila, L.; Alonso-Mori, R.; Barnes, C. O.; Baxter, E. L.; Brehmer, W.; Brewster, A. S.; Brunger, A. T.; Calero, G.; Chang, J. F.; Chollet, M.; Ehrensberger, P.; Eriksson, T. L.; Feng, Y.; Hattne, J.; Hedman, B.; Hollenbeck, M.; Holton, J. M.; Keable, S.; Kobilka, B. K.; Kovaleva, E. G.; Kruse, A. C.; Lemke, H. T.; Lin, G.; Lyubimov, A. Y.; Manglik, A.; Mathews, I. I.; McPhillips, S. E.; Nelson, S.; Peters, J. W.; Sauter, N. K.; Smith, C. A.; Song, J.; Stevenson, H. P.; Tsai, Y.; Uervirojnangkoorn, M.; Vinetsky, V.; Wakatsuki, S.; Weis, W. I.; Zadvornyy, O. A.; Zeldin, O. B.; Zhu, D.; Hodgson, K. O. Goniometer-Based Femtosecond Crystallography with X-Ray Free Electron Lasers. *PNAS* **2014**, *111* (48), 17122–17127.

(146) Owen, R. L.; Axford, D.; Sherrell, D. A.; Kuo, A.; Ernst, O. P.; Schulz, E. C.; Miller, R. J. D.; Mueller-Werkmeister, H. M. Low-Dose Fixed-Target Serial Synchrotron Crystallography. *Acta Crystallogr., Sect. D: Struct. Biol.* **2017**, *73* (4), 373–378.

(147) Heymann, M.; Opthalage, A.; Wierman, J. L.; Akella, S.; Szebenyi, D. M. E.; Gruner, S. M.; Fraden, S. Room-Temperature Serial Crystallography Using a Kinetically Optimized Microfluidic Device for Protein Crystallization and on-Chip X-Ray Diffraction. *IUCrJ* **2014**, *1* (5), 349–360.

(148) Pawate, A. S.; Šrajer, V.; Schieferstein, J.; Guha, S.; Henning, R.; Kosheleva, I.; Schmidt, M.; Ren, Z.; Kenis, P. J. A.; Perry, S. L. Towards Time-Resolved Serial Crystallography in a Microfluidic Device. *Acta Crystallogr., Sect. F: Struct. Biol. Commun.* **2015**, *71* (7), 823–830.

(149) Shim, J.; Cristobal, G.; Link, D. R.; Thorsen, T.; Fraden, S. Using Microfluidics to Decouple Nucleation and Growth of Protein Crystals. *Cryst. Growth Des.* **2007**, *7* (11), 2192–2194.

(150) Chen, X.; Shen, J. Review of Membranes in Microfluidics. *J. Chem. Technol. Biotechnol.* **2017**, *92* (2), 271–282.

(151) Jong, J. de; H. Lammertink, R. G.; Wessling, M. Membranes and Microfluidics: A Review. *Lab Chip* **2006**, *6* (9), 1125–1139.

(152) Osada, Y.; Nakagawa, T. Membrane Science and Technology. CRC Press, **1992**.

(153) Sakai, K. Determination of Pore Size and Pore Size Distribution: 2. Dialysis Membranes. *J. Membr. Sci.* **1994**, *96* (1), 91–130.

(154) Váquez, M. I.; Galán, P.; Casado, J.; Ariza, M. J.; Benavente, J. Effect of Radiation and Thermal Treatment on Structural and Transport Parameters for Cellulose Regenerated Membranes. *Appl. Surf. Sci.* **2004**, *238* (1), 415–422.

(155) Leng, J.; Lonetti, B.; Tabeling, P.; Joanicot, M.; Ajdari, A. Microevaporators for Kinetic Exploration of Phase Diagrams. *Phys. Rev. Lett.* **2006**, *96* (8), 084503.

(156) Beebe, D. J.; Moore, J. S.; Bauer, J. M.; Yu, Q.; Liu, R. H.; Devadoss, C.; Jo, B.-H. Functional Hydrogel Structures for Autonomous Flow Control inside Microfluidic Channels. *Nature* **2000**, *404* (6778), 588–590.

(157) Song, S.; Singh, A. K.; Shepodd, T. J.; Kirby, B. J. Microchip Dialysis of Proteins Using in Situ Photopatterned Nanoporous Polymer Membranes. *Anal. Chem.* **2004**, *76* (8), 2367–2373.

(158) Decock, J.; Schlenk, M.; Salmon, J.-B. In Situ Photo-Patterning of Pressure-Resistant Hydrogel Membranes with Controlled Permeabilities in PEGDA Microfluidic Channels. *Lab Chip* **2018**, *18* (7), 1075–1083.

(159) Nguyen, H.-T.; Massino, M.; Keita, C.; Salmon, J.-B. Microfluidic Dialysis Using Photo-Patterned Hydrogel Membranes in PDMS Chips. *Lab Chip* **2020**, *20* (13), 2383–2393.

(160) Eswari, J. S.; Naik, S. A Critical Analysis on Various Technologies and Functionalized Materials for Manufacturing Dialysis Membranes. *Mater. Sci. Energy Technol.* **2020**, *3*, 116–126.
(161) Kornreich, M.; Heymann, M.; Fraden, S.; Beck, R. Cross Polarization Compatible Dialysis Chip. *Lab Chip* **2014**, *14* (19), 3700–3704.
(162) Skou, M.; Skou, S.; Jensen, T. G.; Vestergaard, B.; Gillilan, R. E. In Situ Microfluidic Dialysis for Biological Small-Angle X-Ray Scattering. *J. Appl. Crystallogr.* **2014**, *47* (4), 1355–1366.

Chapter 2

Microfluidic chips

Chapter 2

Microfluidic chips

2.1 Introduction to microfabrication

2.1.1 Designs and masks

Photolithography is one of the standard, conventional methods, along with electron beam or focused ion beam (FIB) lithography, to generate patterned masters[1,2]. Photolithography, usually performed in a clean room, consists of several steps and the basis of the method is to imprint micro-structures on silicon wafers by illumination of a photosensitive resin through a photomask. There are two types of photolithographic masks: the hard masks produced in quartz or borosilicate glass, commonly used in microelectronics, and the soft masks made of plastics as for example, polyethylene terephthalate (PET). In this work, we used soft masks containing transparent and opaque (black) features (Figure 2.1.2 (a) and Figure 2.1.2 (b)). The lateral dimensions of the patterns printed on a soft photomask can reach a limit of 8 µm, whereas for dimensions < 8 µm the patterns are transferred by laser or electron beam on a thin layer of chrome (Cr) metal on a glass slide[3]. Even though hard masks display several advantages such as high resolution, solvent resistance and high transparency, their production is time-consuming and more expensive compared to soft masks that can be printed within a few hours. The physical properties of photolithographic masks can alter with temperature, humidity, mechanical stress and aging. These changes have to be taken into account because they can influence the transfer of the patterns on the photosensitive resin and eventually on the microfluidic device.

Designing the masks is a step that proceeds the microfabrication steps. For this purpose, a vector drawing software (CleWin 3.0) was used to design the motifs of the masks. Two designs of the microfluidic chips are available depending on the volume of the protein reservoir (0.1 µL or 0.3 µL). For each of these chips, two soft photomasks were designed: one outlined with the channels and pillars and one mask outlining only the pillars. Figure 2.1.1 (a) shows the design for the 0.1 µL chip drawn with CleWin and Figure 2.1.2 (a) shows the respective photomasks, while Figure 2.1.1 (b) and Figure 2.1.2 (b) show the design and the photomasks, respectively, for the 0.3 µL chip.

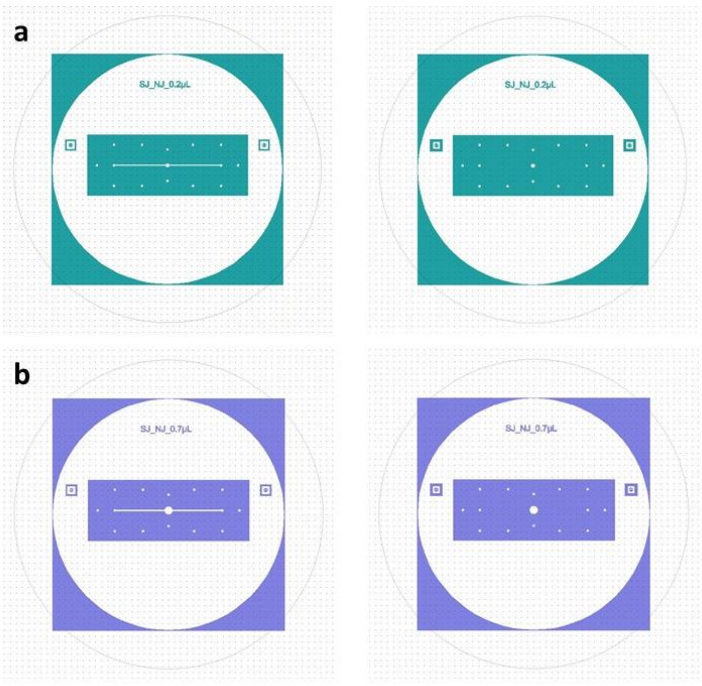

Figure 2.1.1: The patterns of the microfluidic chips as designed with CleWin with (a) 0.1 µL and (b) 0.3 µL volume of the protein reservoir. In both designs, the figure on the left includes the linear fluidic channel and the pillars, while the figure on the right contains only the pillars.

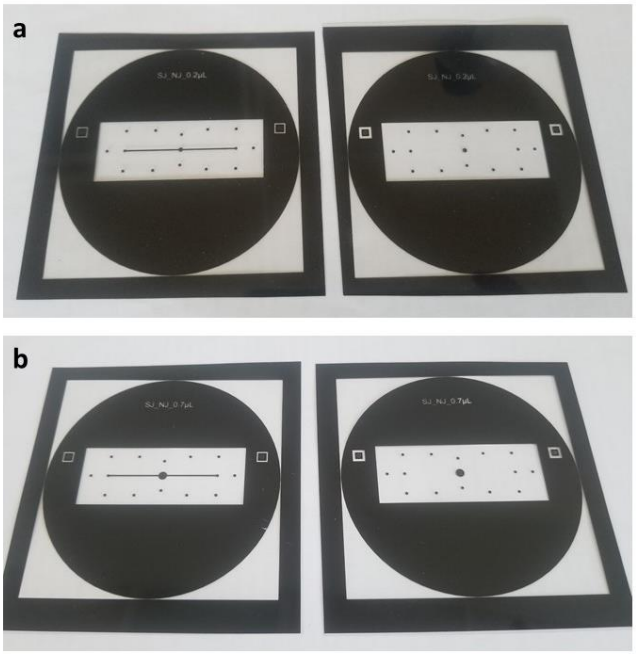

Figure 2.1.2: The soft photomasks of the (a) 0.1 µL and (b) 0.3 µL design containing the channel and the pillars (left) and containing only the pillars (right). The masks feature opaque motifs that remain soluble during the development step when the SU-8 negative photoresist is used for photolithography.

2.1.2 Photolithography

The first step of photolithography is the spin coating of a photosensitive resin on a substrate, as for example a silicon wafer. The photoresist is then exposed to radiation of a specific wavelength in order to transfer the patterns of the photomask on the wafer. There are three ways of pattern transfer from a mask including: i) contact printing, in which the mask is in direct contact with the silicon wafer where the photoresist is deposited, ii) proximity printing which requires short distance between the photoresist and the mask and iii) projection printing where the mask patterns are projected on the photoresist through an optical system. In this work, we used the epoxy-based negative photoresist SU-8 (3000 series, Microchem), the UV illumination source was the mask aligner MJB 4 by SUSS MicroTec and the transfer mode was contact printing. The UV light activates the photoactive components of the resin modifying the local solubility. A photoresist is defined as positive when the exposed parts remain soluble after irradiation, while it is negative if the exposed parts are crosslinked[3,4]. Thus, the black patterns on the photomasks of Figure 2.1.2 (a) and Figure 2.1.2 (b) remain soluble in the developer solvent (PGMEA) after the UV exposure during photolithography and the channels and pillars are engraved on the masters (Figure 2.1.3).

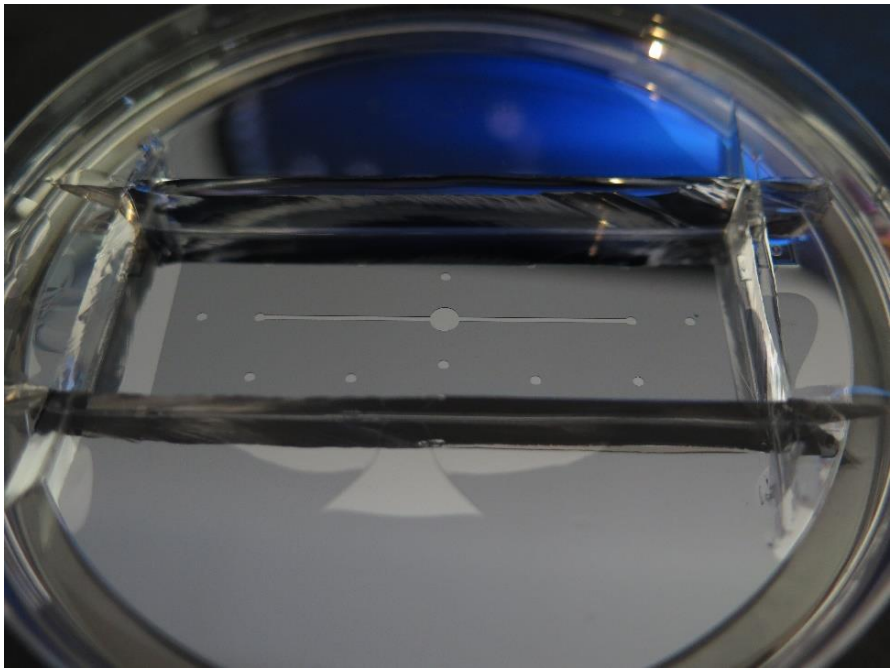

Figure 2.1.3: The SU-8 master of the 0.3 μL design developed during photolithography on a silicon wafer. The opaque features of the photomask are not polymerized during photolithography and the patterns are engraved on the master.

The height of the photoresist on the master depends on the thickness of the layer that is initially deposited on the silicon wafer, while the photomask defines the shape and the lateral dimensions of the patterns[3]. Photoresists can be deposited on silicon wafers with various

techniques such as spin coating, spray coating and electrodeposition. We used the spin coating method and the SPS Spin 150 spin coater. The silicon wafer is placed on the dedicated position of the spin coater and applied vacuum maintains it in place while rotated in high speed. The photoresist is then deposited on the center of the wafer and during acceleration, centrifugal forces spread the photoresist across the surface creating a thin film on the wafer. The thickness and the uniformity of this thin film is very important in microfluidic applications and can be adjusted by the spinning speed and acceleration.

In the case of the SU-8 photoresist, the acceleration ramp and the spinning speed are provided by the manufacturer (Kayaku Microchem) in order to select the appropriate product and the experimental parameters for the desired film thickness. The SU-8 3000 series was developed for improved adhesion, reduced coating stress and high aspect ratio imaging. The thickness of the film after spin coating can range from 4 – 120 μm. SU-8 3000 can be used for UV lithography with a wavelength of 350 – 400 nm, even though in this work we used a wavelength of 365 nm. SU-8 3000 photoresists are provided in five different viscosities. The manufacturer provides graphs of the film thickness (μm) as a function of the spin speed (rpm) for all five SU-8 3000 resists in various temperatures. Figure 2.1.4 shows the film thickness for various spin speeds and SU-8 3000 products at 294 K. To prepare the SU-8 masters, we chose the SU-8 3050 photoresist with a density of 1.153 g mL^{-1} and a viscosity of 13.8 Pa s.

A comprehensive review on SU-8 photolithography is given by Martinez-Duarte and Madou[5]. The general process for producing a SU-8 master on a silicon wafer consists of five steps: the spin coating, the soft baking, the exposure to UV radiation, the post-exposure bake (PEB) and the development. Prior to the application of the photoresist on the substrate, the silicon wafer was treated in an air plasma cleaner (Diener Electronic ZEPTO) for 90 s to promote adhesion. Apart from recommendations on the spin speed and acceleration, the manufacturer provides also information for the time of the soft bake and the PEB at 368 K, the exposure energy and the development time, depending on the film's thickness (Table 2.1.1).

For a thickness of approximately 50 μm, the SU-8 3050 resist was applied as follows (according to Figure 2.1.4 and Table 2.1.1):

- Spin coating: 10 s spin at 500 rpm with acceleration of 100 rpm/s followed by 30 s spin at 3500 rpm with acceleration at 300 rpm/s
- Soft bake: 15 min at 368 K on a hot plate followed by 2 min at room temperature
- UV exposure: 8 s with a power of 41 mW cm^{-2}
- PEB: 5 min at 368 K on a hot plate followed by 2 min at room temperature
- Development: 15 min in PGMEA bath

The silicon wafer with the photoresist structures on it, called the master, is then rinsed with isopropanol until no blurry precipitation is observed, dried with nitrogen gas and stored in Petri dishes. Finally, the surface of the master is treated with a silane to facilitate the detachment of PDMS during the soft lithography steps of the fabrication protocol. The wafers are placed in a tapped hot plate for 10 min at 368 K under the vapor atmosphere of Hexamethyldisilazane (HMDS). The depth measurements of the channels and the pillars engraved on the SU-8 masters prepared for the two chip designs used in this work were performed with a profilometer and the results are provided in Appendix 2.1 (Figure A2.1 and A2.2).

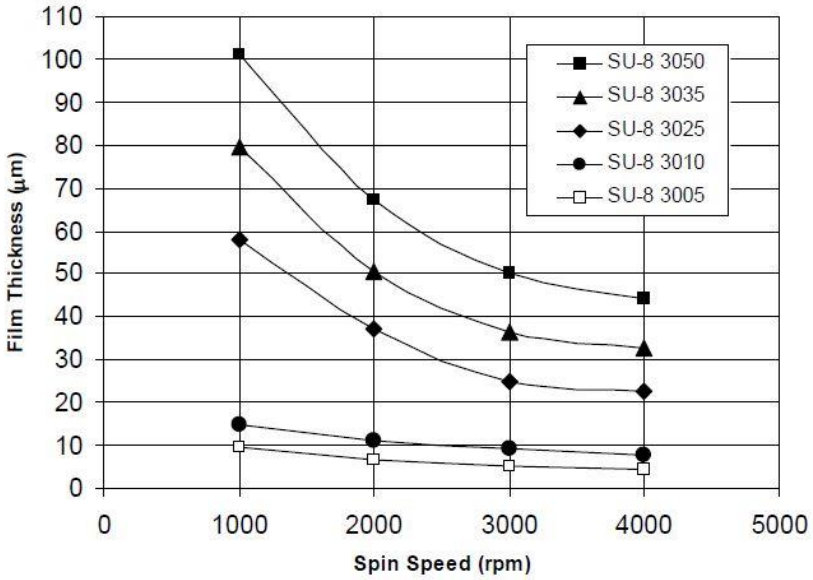

Figure 2.1.4: Film thickness for various spin speeds and SU-8 3000 products at 294 K (Kayaku Microchem).

Table 2.1.1: Recommended time for soft bake, PEB and development and recommended exposure energy depending on the film's thickness for the SU-8 3050 photoresist (Kayaku Microchem).

Thickness (µm)	Soft bake time (min, at 368 K)	PEB (min, at 368 K)	Exposure energy (mJ cm^{-2})	Development (min)
4 – 10	2 – 3	1 – 2	100 – 200	1 – 3
8 – 15	5 – 10	2 – 4	125 – 200	4 – 6
20 – 50	10 – 15	3 – 5	150 – 250	5 – 8
30 – 80	10 – 30	3 – 5	150 – 250	6 – 12
40 – 100	15 – 45	3 – 5	150 – 250	7 – 15

2.1.3 Soft lithography

Soft lithography is a non-photolithographic method where elastomeric materials are used for reproducing micro- and nano-structures (30 nm to 500 µm)[6] on stamps with the patterned relief structures on their surface. There exists a wide variety of soft lithographic techniques[1,6–8] including microcontact printing (µCP)[9], microtransfer molding (µTM)[10], replica molding (REM)[11] and micromolding in capillaries (MIMIC)[12] or other techniques such as solvent-assisted micromolding, cast molding, embossing and injection molding. All soft lithographic techniques have been extensively used in microfabrication due to the low capital cost, the ease in manipulation and reproduction, the diversity of the materials that can be patterned with these methods and the fact that clean room facilities are not required. Soft lithography

techniques use organic (soft) materials such as polymers for transferring and replicating a pattern on stamps or molds. The pattern replication first lies on the fabrication of the patterned silicon masters. Then, the masters are molded with an elastomer (PDMS) to generate the patterned stamps which are subsequently used for generating a replica of the original pattern on a surface or substrate.

PDMS elastomers (or silicone rubbers) are the most widely used materials in soft lithography, exhibiting a plethora of advantageous features. PDMS has low interfacial free energy (19 – 21 mJ m^{-2}), low elastic modulus (2.5 MPa for Sylgard 184[13]) and good thermal stability. It is isotropic and homogeneous material. The elasticity of PDMS and its high permeability to gases[14] make it a suitable candidate for fabricating elastomeric valves and pumps by multilayer soft lithography[15]. The interfacial properties of the elastomer can be modified by air or oxygen plasma treatment. Plasma activation makes a surface more hydrophilic by inducing the generation of Si−OH groups. In the case of PDMS, plasma treatment converts the methyl (−$OSi(CH_3)_2O$−) group to silanol (−$O_nSi(OH)_{4-n}$). The irreversible bonding between two plasma-activated surfaces (as for example PDMS and glass commonly used in microfluidics) is attributed to the formation of the covalent siloxane (Si−O−Si) bond. PDMS is also optically transparent down to 300 nm[6]. Additional properties that make PDMS a good choice are its low cost, biocompatibility, low toxicity and inertness to many chemicals. However, some of the PDMS properties may restrict its application range. PDMS shrinks by approximately 1 % after crosslinking and swells in organic solvents[16]. Moreover, the low elastic modulus limits the working pressure when circulating fluids in PDMS-based microfluidic devices since high pressure values can change the geometry of the fluidic channels. The flexibility of PDMS also limits the aspect ratio of the microstructures that can be patterned on its surface using soft lithography[17]. Finally, distortion of the PDMS stamps, known as stamp collapse, is attributed to adhesive forces between the stamp and the substrate material (SU-8 master) when the former is detached from the latter[18].

PDMS comprises of an inorganic siloxane backbone (Si−O−Si) and organic methyl groups attached to silicon. The repeating monomer group of PDMS is (−$OSi(CH_3)_2$−) terminating with vinyl groups (−$CH=CH_2$), while the periodic group of the curing agent is a silicone hydride (−$OSiHCH_3$−). Due to its low glass transition temperature (148 K[19]), PDMS is liquid in room temperature and can be thermally crosslinked. In this work, we have used the product Sylgard 184 from Dow Corning containing a liquid silicon rubber base and a curing agent. The two components were mixed in a 10:1 (base: curing agent) mass ratio and cured thermally in an oven (Memmert UNE 200-800) for 1 h at 338 K. The mixing ratio of the two PDMS components is defined by the desirable Young's modulus and the higher this ratio the lower is the Young's modulus value of the elastomer[20]. Crosslinking occurs through the hydrosilation reaction between the vinyl groups of the siloxane oligomer and the groups of the curing agent creating (−$Si−CH_2−CH_2−Si$−) bonds. A platinum catalyst contained in the curing agent catalyzes the crosslinking which can take place at room temperature or it can be accelerated at higher temperatures.

2.2 Microfabrication of the dialysis chip

2.2.1 Protocol

The protocol for the fabrication of the microfluidic devices used in this study is a modification of the protocol developed by Niels Junius during his Ph.D. thesis[21]. The original protocol was patented[22] and published in a peer review journal in 2020[23], while the modified protocol, enabling to further reduce the required volume of the protein sample, and a case study of the on chip crystallization of a soluble protein (HEWL) and *in situ* X-ray diffraction data collection were published recently[24]. The fabrication protocol is based on the pioneering work of Bartolo *et al*.[25] who developed "stencil-like" micro-patterned stickers (μPS) made of the thiolene-based resin NOA 81 using soft imprint lithography. Later on, the same group (Morel *et al*.[26]) modified their protocol in order to fabricate microfluidic devices of the NOA resin embedding commercially available polycarbonate membranes. They used the devices to study the diffusion of various components across the membrane under shear free conditions for cell cultures[26,27]. The device consisted of two parts: one layer containing the micro-structures made of the photo-curable resin, embedding a porous membrane and sealed on one side with a glass slide with drilled holes for the circulation of the solutions and the second part was a coverslip patterning open micro-wells for the cell culture. The two parts were bonded in a reversible manner with magnets and the device was used for diffusing the desired molecules from the flow channel, through the membrane to the micro-wells containing the cells or tissues. The porous membranes were made of polycarbonate (Cyclopore) with a 400 nm hole diameter. An innovative modification of the method led to the conception of the dialysis chip used in this work, developed to couple the advantages of the microfluidic technology, such as minute sample consumption per experiment (typically < 1μL), and the microdialysis protein crystallization method allowing for accurate, fine-tuned and reversible control over the experimental parameters of the on chip crystallization. This work is based on the miniaturization of a macro-scale bench (typical volume > 20 μL), previously developed in our laboratory, using a dialysis flow cell for screening and optimizing protein crystallization by mapping temperature or precipitant concentration phase diagrams[28,29].

The fabrication protocol is shown schematically in Figure 2.2.1 as a transverse view and in Figure 2.2.2 as a 3D representation. The preparation of the SU-8 masters was performed at the Laboratory of the Future (LOF, Bordeaux) and the microfluidic chips were fabricated at the Laboratoire Interdisciplinaire de Physique (LiPhy, Grenoble). The first step of the fabrication procedure is to prepare two masters on silicon wafers (Si wafers, (100) orientation, 76.2 mm diameter, 500 ± 20 μm thickness) with the desirable patterns by photolithography using a negative photoresist in a clean room. Before use, the surface of the two Si wafers was treated with air plasma for 90 s to facilitate the deposition and attachment of the negative photoresist. Once treated, the Si wafer was placed on a spin coater and roughly 3 mL of the photoresist was poured in the middle of the wafer. In order to obtain a layer of 50 μm nominal thickness, the SU-8 3050 negative photoresist was spin coated for 10 s at 500 rpm and successively for 30 s at 3500 rpm (Figure 2.2.2 (A)). After the deposition, the photoresist was placed on a hot plate (Sawatec HP-200-Z-HMDS BM) for 15 min at 368 K. This step is called soft baking (pre-exposure baking) and it allows the evaporation of the solvent contained in SU-8 and the partial solidification of the resin. This way, the masters don't stick on the photomasks during the following steps of the protocol. Then, the masters are left at room

temperature for 2 min. The next step of photolithography lies on the production of the geometrical patterns designed for the chip on the silicon wafers. Therefore, the silicon master covered with the partially solidified SU-8 photoresist is placed on a mask aligner with a power of 41 mW cm^{-2} and exposed to UV light for 8 s (Figure 2.2.2 (B)). Subsequently, the master is placed again on the hot plate for 5 min at 368 K for the post-exposure baking to complete the photoreaction initiated by the UV exposure. Next, the wafer is immersed in a bath of PGMEA and stirred gently for approximately 15 min in order to remove all the SU-8 resist that was not crosslinked during the UV exposure. The wafer is then rinsed with isopropanol and dried with nitrogen gas. Two designs of the microfluidic chips are available depending on the volume of the compartment dedicated to be the protein reservoir. The respective volume values can be 0.1 µL or 0.3 µL. For each of these two designs, two silicon masters are necessary for the fabrication process. After photolithography, one master contains the linear, fluidic channel and the pillars (Figure 2.2.1 (A) left, Figure 2.2.2 (B) left) and the second master contains only the pillars (Figure 2.2.1 (A) right, Figure 2.2.2 (B) right). Therefore, the steps of photolithography detailed above are applied twice in order to produce two silicon masters for each chip design. Finally, the surface of both masters is treated with a silane to facilitate the detachment of PDMS during the following steps of the fabrication protocol. The wafers are placed in a tapped hot plate for 10 min at 368 K under the vapor atmosphere of HMDS. The silicon masters can be stored in Petri dishes and used indefinitely if the patterned micro-structures are not damaged. Moreover, the surface of the masters can be treated with HMDS vapor whenever the detachment of PDMS becomes difficult after several uses.

The second part of the fabrication protocol is based on soft lithography techniques[6,7] and specifically, on soft imprint lithography[30]. For each design, two PDMS molds were generated by replica molding of the two masters. The PDMS silicone base was mixed with its curing agent in a 10:1 mass ratio. Then, the mixture was degassed in a vacuum desiccator to remove all air bubbles. The mixture was then poured on the two masters up to a height of approximately 5 mm (Figure 2.2.1 (B), Figure 2.2.2 (C)) and PDMS was cured thermally in an oven for 1 h at 338 K. Once the PDMS molds were hardened (Figure 2.2.2 (D)), they were cut with a scalpel around the patterns of the SU-8 masters (Figure 2.2.2 (E)). The first PDMS mold consists of a layer including the linear fluidic channel and the pillars for the inlet/outlet ports and the protein reservoir (Figure 2.2.2 (E) left) and the second mold includes only a layer of pillars (Figure 2.2.2 (E) right). The patterns exceed vertically from the horizontal surface of the PDMS molds by approximately 45 µm which is the height of the patterns produced on the SU-8 masters during photolithography. It should be mentioned that during photolithography, the nominal height of the patterns engraved on the two masters was 50 µm but, once the procedure was completed, profilometer measurements showed that the experimental value was approximately 48 or 44 µm (Appendix 2.1).

The third part of the protocol is the fabrication of the dialysis chips. The PDMS mold containing both the channel and pillars is placed on a rigid microscope glass slide (3 x 1 in. standard size) with the patterns facing upwards (Figure 2.2.1 (C), Figure 2.2.2 (F)). A dry piece of the RC dialysis membrane with the appropriate MWCO is deposited on the PDMS mold right above the central pillar which is the protein reservoir. The size of the RC membrane piece is 2 x 2 mm^2 for the 0.1 µL chip and 4 x 4 mm^2 for the 0.3 µL chip. Then, the second PDMS mold containing only the pillars is placed and aligned with its micro-structures facing downwards. The alignment can be accomplished by visual inspection or with the aid of an optical microscope. The main goal is to align the two central pillars and the respective inlet/outlet

points (at the edges of the fluidic channel) of the two PDMS molds. The piece of the RC dialysis membrane is “sandwiched” in between the two PDMS molds (shown in red color in Figure 2.2.1 (D) and Figure 2.2.2 (G)). Once the alignment is achieved, the assembly is desiccated for 30 min in a vacuum chamber in order to remove all the trapped air in the PDMS molds and facilitate the insertion of the resin during the next step in the protocol. The two PDMS molds are held together by solid-solid (PDMS-PDMS) adhesion and there is no need for pressure or other external way of temporary bonding. The empty space between the two PDMS molds is then filled with the photocurable, thiolene-based resin NOA 81 by capillary imbibition (Figure 2.2.1 (E), Figure 2.2.2 (H)) and the adhesion between the two PDMS molds prevents the filling of the pillars by the liquid resin. NOA 81 has a viscosity of 300 mPa s at 298 K and it takes a few minutes to fill in the space between the two PDMS molds by capillarity. Once the filling is complete, the resin is cured by UV (365 nm) exposure for 10 s using a collimated UV lamp with a power of 35 mW cm^{-2} (UVITec Crosslinker CL-508) (Figure 2.2.1 (F), Figure 2.2.2 (I)). This short exposure allows NOA 81 resin to be partially crosslinked leaving a thin layer of the liquid precursor in contact with the two PDMS molds uncured due to the gas permeability of PDMS and the inhibition of polymerization by oxygen. The upper PDMS mold with the partially crosslinked layer of NOA is separated from the bottom PDMS mold supported on the glass slide and, it is gently pressed on a 175 µm thick PMMA (Goodfellow) foil (Figure 2.2.1 (G), Figure 2.2.2 (J)). The new assembly (upper PDMS mold + NOA + PMMA) is exposed again to UV light for 60 s. The second exposure allows the resin to be fully crosslinked and facilitates the adhesion of NOA to the PMMA substrate without any further treatment or manipulation. Finally, the upper PDMS mold is carefully removed from the NOA 81 sticker (Figure 2.2.1 (H), Figure 2.2.2 (K)). The two PDMS molds can be reused a few times once washed with isopropanol and acetone, as long as they are not damaged or bent. Damage of the PDMS molds can lead to un-desirable leakage of the liquid NOA resin in between the pillars.

A side view schematic of the dialysis chip is given in Figure 2.2.1 (I) and Figure 2.2.2 (L). The piece of the RC dialysis membrane is directly incorporated within the NOA 81 crosslinked resin, separating the protein reservoir from the linear fluidic channel located at the bottom layer of the chip. No mechanical clamping or further manipulation was necessary to fix the membrane. The height of the micro-structures imprinted on the bottom layer of the chip (fluidic channel) is approximately 45 µm and the height of the protein reservoir is 45 µm, while the height of the inlet and outlet port is 90 µm. The volume of the protein reservoir is 0.1 or 0.3 µL (two different designs), while the respective values for the chips developed by Junius *et al*.[23] were 0.2 and 0.7 µL.

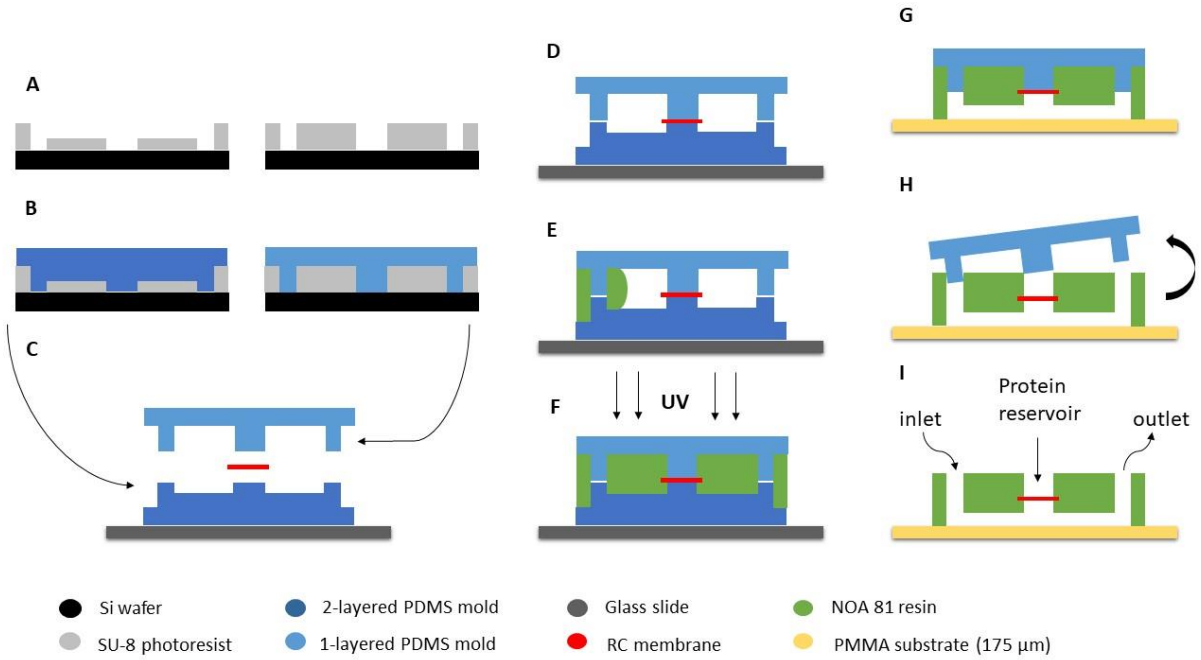

Figure 2.2.1: Schematic representation of the dialysis chip fabrication process (side view). (A) Two SU-8 masters on silicon wafers containing the channel and pillars are produced with photolithography and (B) two PDMS molds are produced by soft lithography containing the reverse patterns of the SU-8 masters. (C, D) The two PDMS molds are supported on a glass slide and a piece of the RC dialysis membrane is "sandwiched" between the molds. (E) The space between the molds is filled by capillarity with the photo-curable resin NOA 81 and (F) the resin is exposed to UV light. (G) The bottom PDMS mold is removed and the assembly containing the upper PDMS mold and the partially cured NOA 81 resin is pressed on a PMMA substrate. (H) A second UV exposure follows to fully polymerize the resin and the upper PDMS mold is removed. (I) Side view of the dialysis chip showing the protein reservoir and the inlet/outlet ports of the fluidic channel. Modified by Junius *et al*.[23]

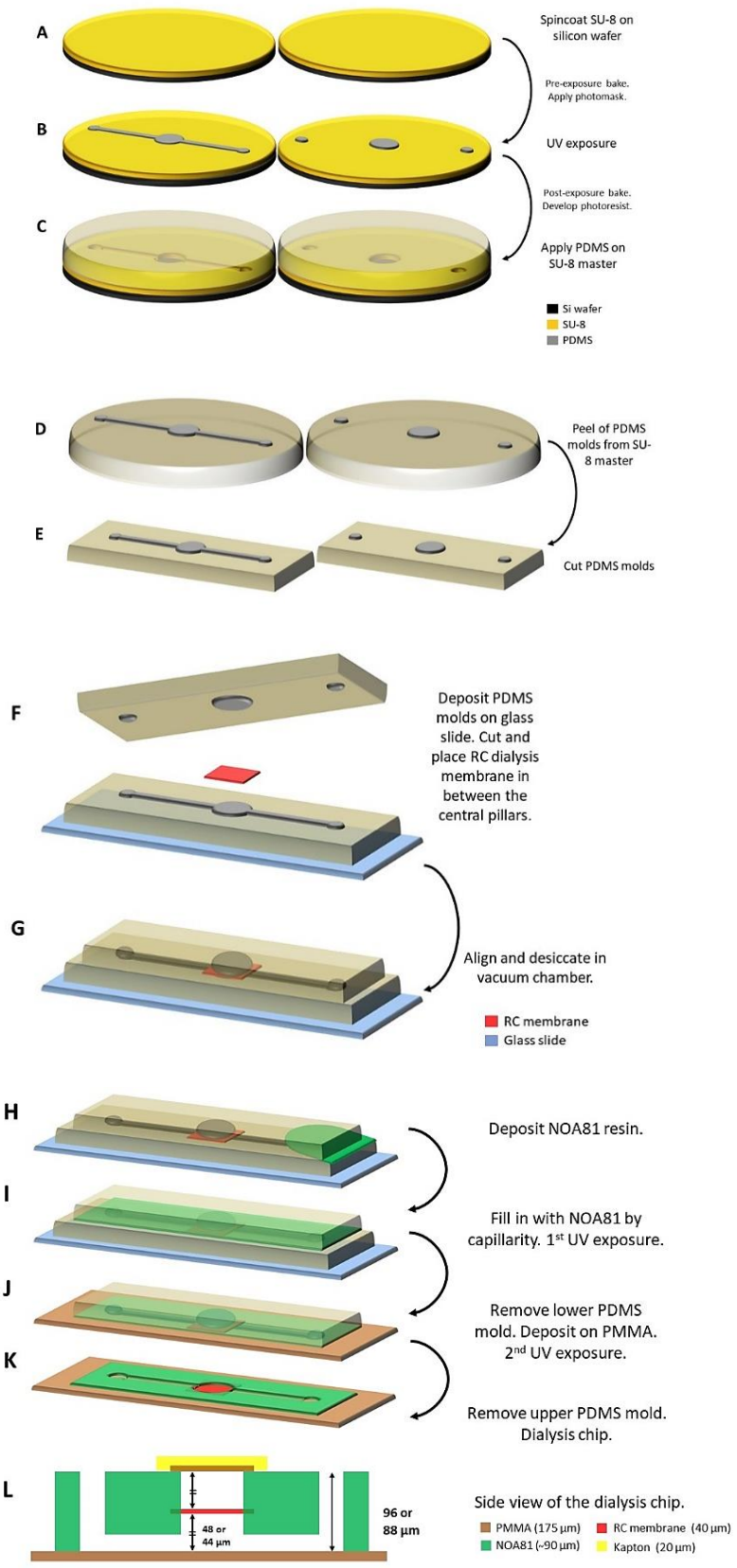

Figure 2.2.2: 3D schematic representation of the dialysis chip fabrication protocol. (A) The SU-8 resist is spin coated on two silicon wafers and (B) two masters containing the channels and pillars are prepared during photolithography. (C) PDMS is poured on the silicon masters and after being cured for 1 h at 338 K, (D) the two PDMS molds produced by soft

lithography are peeled of the SU-8 masters. (E) The two PDMS molds featuring the micro-patterns are cut to an appropriate size and (F) supported on a glass slide. The RC dialysis membrane is "sandwiched" between the two central pillars of the PDMS molds and (G) the molds are placed in desiccator for approximately 30 min. (H, I) The space between the molds is filled by capillarity with the photo-curable resin NOA 81 and exposed to UV light for 10 s. (J) After the first exposure, the bottom PDMS mold is removed and the assembly with the partially cured NOA 81 layer and the upper PDMS mold is supported on a PMMA substrate. (K) The new assembly is exposed again to UV light (60 s) and the upper PDMS mold is removed. (L) Side view schematic of the dialysis chip including the thickness of the materials and the height of the micro-patterns. Modified by Jaho *et al*.[24]

2.2.2 Connectors and protein encapsulation

Pictures of the microchips, the fluidic channels, the protein reservoir and the connectors used for setting up crystallization experiments are shown in Figures 2.2.3 – 2.2.5. Two designs were developed for the on chip crystallization of proteins via microdialysis depending on the maximum volume capacity of the protein reservoir. Microchips with 0.3 µL and 0.1 µL maximum volume of the protein reservoir are shown in Figure 2.2.3 (a) and Figure 2.2.3 (b), respectively. The protein reservoirs and the linear fluidic channels are indicated in Figure 2.2.3 (c) for two different microchips. For both designs, the length of the fluidic channel is approximately 36 mm and its width is 0.5 mm. However, the height of the channels depends on the thickness of the deposited SU-8 resin on the silicon master during photolithography. As explained in Appendix 2.1, the nominal thickness value during photolithography was 50 µm but the experimental values measured with a profilometer were 48 µm of thickness for the 0.1 µL design and 44 µm for the 0.3 µL design. Assuming a rectangular cross section for the fluidic channels, the volume was calculated to be approximately 0.9 µL for the two chip designs. Thus, one chip requires merely 0.1 µL of protein sample and 0.9 µL of precipitant solution to fill the fluidic channel and start a crystallization experiment, whereas the other chip requires 0.3 µL of protein sample and 0.9 µL of precipitant solution.

As explained in the fabrication protocol (Section 2.2.1), a 175 µm thick PMMA foil is used as a substrate for the NOA 81 chip (Figure 2.2.3 (a)). During the second UV exposure, the NOA 81 resin gets fully polymerized and is attached on the PMMA substrate by adhesion. COC was also tested as a potential substrate for the NOA 81 chips considering its widespread application in microfluidic devices compatible for *in situ* X-ray diffraction experiments. Figure 2.2.3 (b) shows a NOA 81 chip on a 50 µm thick COC foil (Microfluidic ChipShop). The fabrication protocol is the same as the one used to fabricate NOA on PMMA chips with a few modifications. The time for the first UV exposure of the NOA 81 resin is 5 s (as opposed to 10 s for the standard protocol) and for the second UV exposure is 45 s (as opposed to 60 s for the standard protocol). Moreover, the hydrophobic surface of the COC foil was treated with air plasma for 3 min prior to its use in order to enhance the adhesive bonding with the NOA 81 resin. Once the UV exposure time and the plasma treatment time were established, several chips were fabricated on a COC substrate. However, the COC foil is more flexible than PMMA. Thus, PMMA was the preferred substrate for fabricating chips for crystallization experiments and *in situ* X-ray diffraction studies.

The on chip crystallization experiments can be performed in two different modes, the static and the continuous circulation mode. For the static mode operation, the fluidic channel is filled with the precipitant solution manually or automatically with the aid of a syringe pump or a pressure-driven system and then, it is set aside, under proper temperature and humidity conditions, for crystallization. For the continuous circulation mode, the precipitant solution is flowing within the fluidic channel continuously under constant flow or under constant differential pressure (ΔP) between the inlet and the outlet port of the fluidic channel. The pressure at the outlet port is equal to the atmospheric pressure, while the inlet pressure value can be adjusted by a pressure-driven system (Chapter 3). Junius *et al*.[23] suggested that the inlet pressure value varies between 20 – 60 mbar for solutions with viscosity close to water viscosity and between 50 – 150 mbar for more viscous solutions. In the case of the on chip crystallization of membrane proteins where the crystallization solution often contains PEG or glycerol, we used an injection pressure of 50 – 100 mbar. Moreover, the continuous circulation mode offers the advantage to exchange the precipitant solution with another one without wasting the protein sample and the device itself. 400 µL is the total volume required in order to completely exchange a solution flowing within the channel with another one[23]. This approach is recommended for screening crystallization conditions and mapping the phase diagram of the protein with reduced sample consumption. The instrumental developments related to the automation and control of the on chip protein crystallization via microdialysis are discussed in detail in Chapter 3.

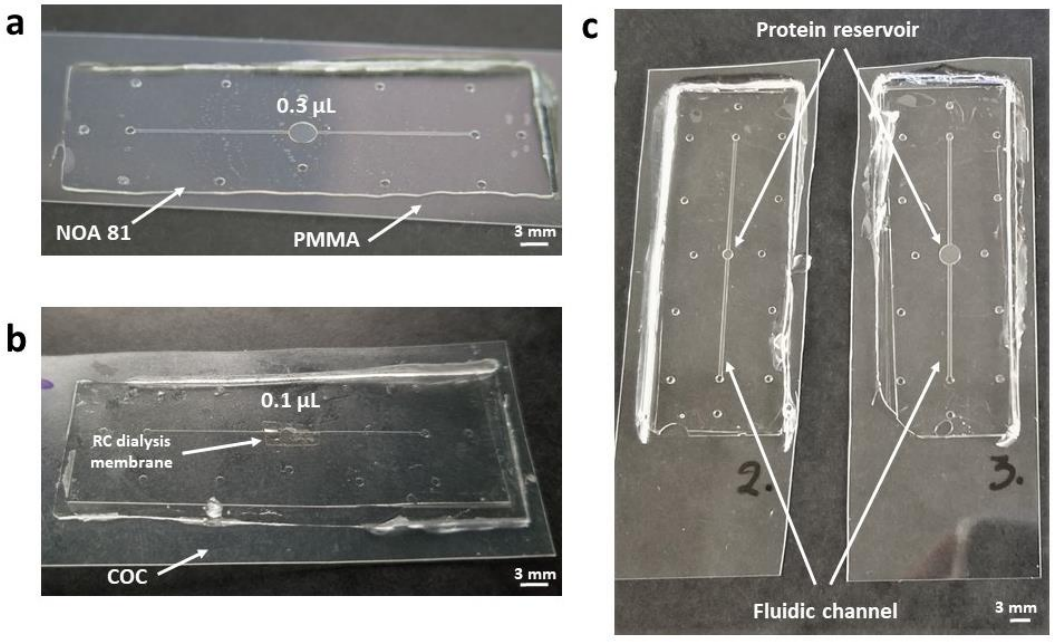

Figure 2.2.3: Microfluidic chips embedding a RC dialysis membrane for on chip protein crystallization. (A) NOA 81 chip with a 0.3 µL protein reservoir on a 175 µm thick PMMA substrate. (B) NOA 81 chip with a 0.1 µL protein reservoir on a 50 µm thick COC substrate. (C) Top view of NOA 81 chips with 0.1 µL (left) and 0.3 µL (right) protein reservoir on PMMA. The fluidic channels and the protein reservoirs are indicated.

A close-up view of the 0.3 µL protein reservoir under a bright field optical microscope (Leica) is shown in Figure 2.2.4. As described in the fabrication protocol, the piece of the RC dialysis membrane is directly embedded within the NOA 81 crosslinked resin (Figure 2.2.4 (a)). The protein reservoir is the compartment located right above the dialysis membrane and corresponds to the central pillar of the upper PDMS mold as illustrated in Figure 2.2.2 (F) of the fabrication protocol. The other two pillars of the same PDMS mold correspond to the inlet and outlet ports of the fluidic channel. The protein reservoir and the inlet/outlet ports resemble holes on the various photographs of chips shown in Figure 2.2.3. The height of the protein reservoir is determined by the thickness of the SU-8 resin deposited on the silicon master during photolithography. For the design with 0.1 µL volume of the protein reservoir, the height was measured to be 48 µm and for the 0.3 µL design, the height was 44 µm. The heights of the protein reservoir (48 or 44 µm), the fluidic channel (48 or 44 µL) and the inlet/outlet ports (96 or 88 µm) are shown in a schematic side view of the chip in Figure 2.2.2 (L).

It is worth noting that several studies have been conducted to estimate the effect of UV radiation on PDMS and polymeric membranes. UV radiation can change the surface chemistry of PDMS[31] and it can be used for direct photo-patterning of PDMS mixtures containing photo-initiators like benzophenone[32]. However, in this work, we use PDMS molds only as intermediates for the fabrication of the NOA 81 sticker. The PDMS molds are used several times but they are disposed when they are damaged and hinder the fabrication process. In the case of polymeric membranes, it has been shown that UV irradiation increases the water permeability of poly(ether sulfone) and sulfonated poly(sulfone) membranes[33,34] or the salt permeability of the RC dialysis membrane[35]. Specifically, Váquez *et al*.[35] treated a sample of RC membrane with UV light at 317 nm and 40 W for 48 h and they measured 5 % increase in NaCl permeability of the UV treated membrane compared to the permeability of the untreated membrane. This change was related to changes in the packing of the polymer chains resulting in increased fractional void volume after UV irradiation. Nevertheless, the exposure time and energy used during the fabrication of the dialysis chip (10 and 60 s at 35 mW cm^{-2}) can be considered negligible to induce any alteration on the functionality of the RC dialysis membrane.

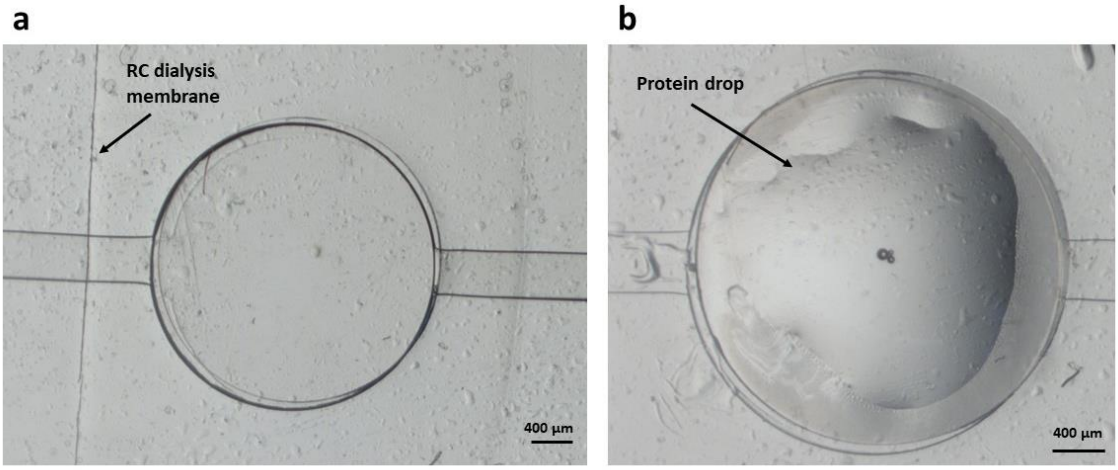

Figure 2.2.4: Top view of the 0.3 µL protein reservoir through an optical microscope. (a) The RC dialysis membrane, embedded within the NOA 81 chip, is indicated. (b) The droplet of the protein sample is pipetted in the protein reservoir located right above the RC dialysis membrane.

As described so far, the central pillar of the chip designed to being used as the protein reservoir remains open and exposed to the atmosphere. First, the protein droplet is manually pipetted within the protein reservoir right upon the RC dialysis membrane, as shown in Figure 2.2.4 (b). Then, a thin layer of high-vacuum silicone grease is applied all around the protein reservoir and a small piece of PMMA is placed gently right above covering the whole surface of the protein compartment. PMMA is impermeable to air[36]. The thickness of the PMMA piece is 175 µm and it is the same material used as substrate for the NOA 81 chip (Figure 2.2.3 (a)). The contact between the PMMA piece and the NOA 81 chip is not an irreversible bonding but merely a solid/solid interface. The thin layer of silicone grease between them is used to prevent the spreading of the protein droplet outside the limits of the protein reservoir. In order to ensure an overall air-tight sealing of the protein reservoir, a piece of a 20 µm thick Kapton tape (DuPont) is set above the PMMA piece, sticking on the NOA 81 chip as shown in Figure 2.2.5 (b). Once the protein sample is encapsulated within the protein reservoir, the dialysis chip is ready to be used for crystallization experiments as discussed in detail in Chapter 4. The chips can be reused if the RC membrane and the adhesion of the NOA 81 sticker on the PMMA substrate are not damaged, otherwise, leaks are observed when injecting the crystallization solution into the fluidic channel. Distilled water is used to wash the channels and the protein reservoir in the case of low viscosity solutions (salts, buffers), while for more viscous solutions (PEGs or glycerol) reusing the chips is not recommended.

While the protein sample is manually pipetted in the protein reservoir, connectors must be bonded on the inlet and outlet ports of the fluidic channel for handling the precipitant solution. Commercially available PEEK connectors (NanoPort) can be bonded using fast epoxy glue, as shown in Figure 2.2.5 (b). PTFE tubes are used for the injection of the precipitant solution within the fluidic channel either manually with a disposable syringe or automatically with the aid of a syringe pump or a pressure-driven system. The diameter of the PTFE tubes is chosen according to the inner diameter of the connectors. Even though commercially available kits are recommended for easy and precise manipulation, disposable laboratory

pipette tips can also be used as connectors (Figure 2.2.5 (a)). The tips must be cut in one side so that the diameter fits the outer diameter of the PTFE tubes.

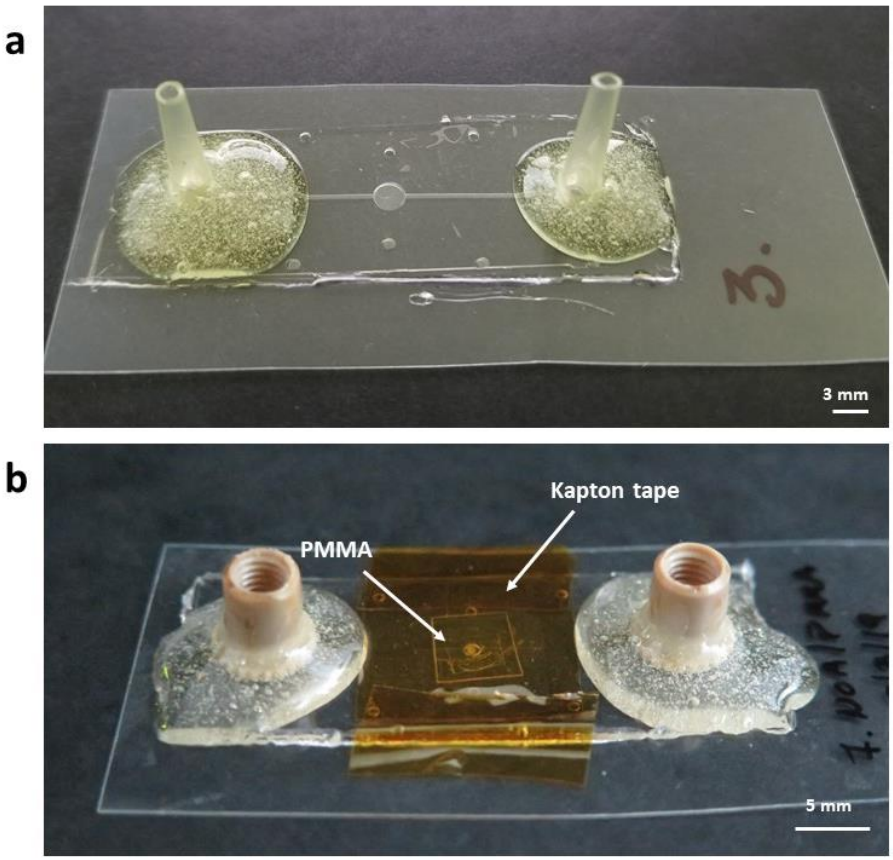

Figure 2.2.5: (a) Dialysis chip with pipette tips glued as connectors on the inlet and outlet ports of the linear fluidic channel. (b) A dialysis chip ready for crystallization experiments. Commercially available connectors are glued on the ports of the fluidic channel and the protein sample is encapsulated within the protein reservoir by a piece of PMMA foil and Kapton tape.

2.3 A chip for *in situ* fabrication of hydrogel membranes

2.3.1 Designs and photolithography masks

The dialysis chip described in Section 2.2 has been designed to integrate the microdialysis crystallization method for proteins in a microfluidic device compatible with *in situ* X-ray diffraction studies. The device is fabricated based on soft imprint lithography techniques by the UV-induced polymerization of the photo-curable resin NOA 81. The RC dialysis membrane is embedded within the layer of the NOA 81 resin and its MWCO is chosen accordingly to the

molecular weight of the protein sample and the precipitant molecules. The protein sample must be retained within the protein reservoir of the device, while the precipitant agents diffuse across the membrane to induce nucleation. In order to avoid the manual handling and alignment during the integration of the dialysis membrane, I had the opportunity, during my first secondment (2018) in the group of Dr. Jean-Baptiste Salmon at the Laboratory of the Future (LOF), to implement the method of *in situ* fabrication of hydrogel membranes. They use maskless UV projection for *in situ* photo-patterning hydrogel membranes in microfluidic devices made of PEGDA 250[37] or PDMS[38]. I have designed a chip that could be compatible with on chip microdialysis crystallization of proteins made of PEGDA 250. The design of this preliminary chip was subsequently improved by Camille Keita and used for the study of colloidal dispersions during her Ph.D. thesis entitled "Microfluidic osmotic compression: colloidal dispersions and industrial formulations characterization"[39]. In this section, the design of the preliminary chip, its fabrication protocol as well as some droplet tests are described.

The design of the chip is divided in two layers: the first layer contains the channels and the pillars, and the second layer contains only the pillars. The pillars connected to the channels are, in fact, the inlet and outlet ports of the microfluidic device where suitable connectors can be placed after the development of the chip for the injection of the protein solution and the crystallization agents. CleWin 3.0 was used to design the motifs of the masks. Figure 2.3.1 (a) shows the design of the first layer containing the channels and pillars on the left and the second layer patterning only the pillars on the right. The masks used for photolithography are illustrated in Figure 2.3.1 (b), where the first layer is located on the left of the figure and the second layer on the right. During photolithography, when the SU-8 photoresist is exposed to UV radiation, the transparent patterns of the photomasks are crosslinked while the opaque features of the masks remain soluble in the PGMEA developer.

It is worth noting that the design illustrated in Figure 2.3.1 (a) is the final design that was used to develop the microfluidic chips for *in situ* photo-patterning of hydrogel membranes. Two more masks were tested before the final one ("SJ_mask 4") and the designs are provided in Appendix 2.2.1 (Figure A2.3). Moreover, during my second secondment at LOF (2019), I designed another device for on chip microdialysis crystallization via *in situ* fabrication of hydrogel membranes (named "SJ_1 µL") and the respective design, masks and protocols are included in Appendix 2.2.2.

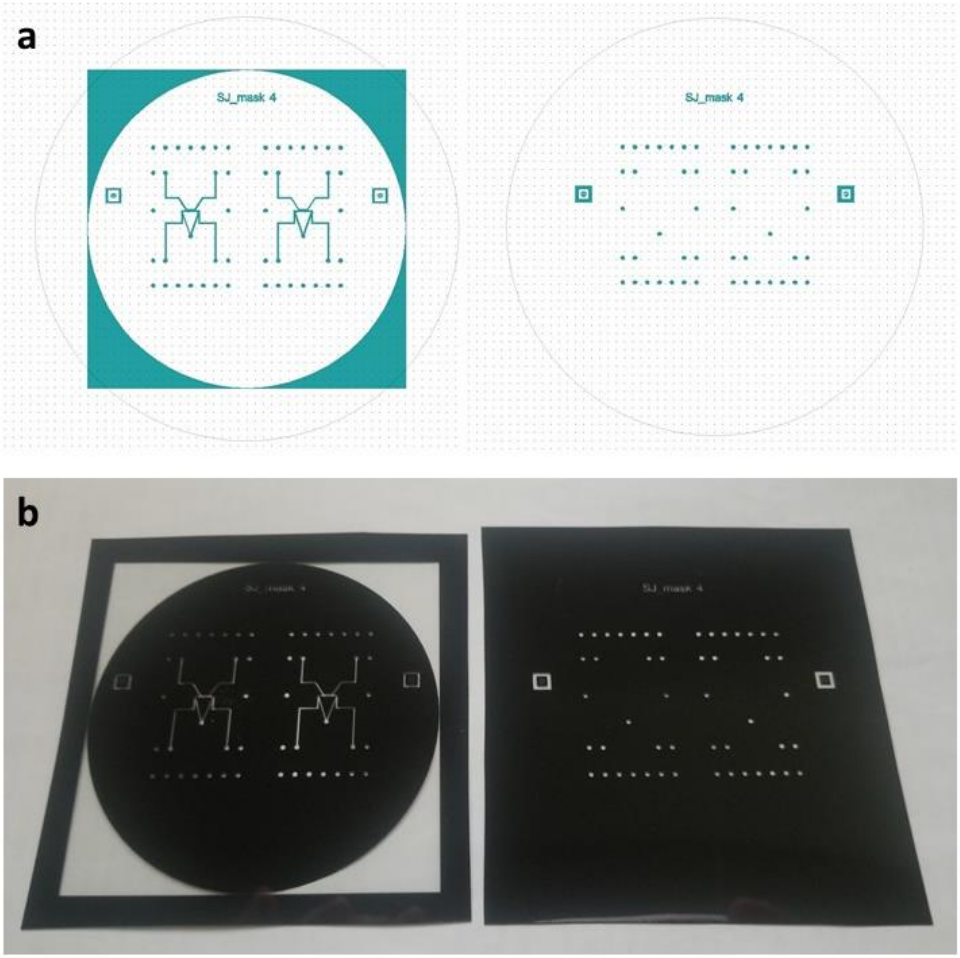

Figure 2.3.1: (a) The patterns of the microfluidic chip ("SJ_mask4") for *in situ* photo-patterning of hydrogel membranes as designed with CleWin and (b) the respective masks for photolithography.

The width of the channels and diameter of the pillars are given in Figure 2.3.2 (a). The central reservoir for the protein sample is given in magnification in Figure 2.3.2 (b). The interface between the two colored areas (purple and blue) is the location where the hydrogel membranes are fabricated *in situ* by maskless UV projection. The height of the channels and the height of the pillars is defined during photolithography by the thickness of the SU-8 resin (Section 2.1.2). For the final design ("SJ_mask 4"), the thickness of the SU-8 photoresist and subsequently the height of the channels is approximately 8 µm. So, considering a rectangular cross-section for the protein reservoir, the volume can be calculated and its value is 7.2 nL.

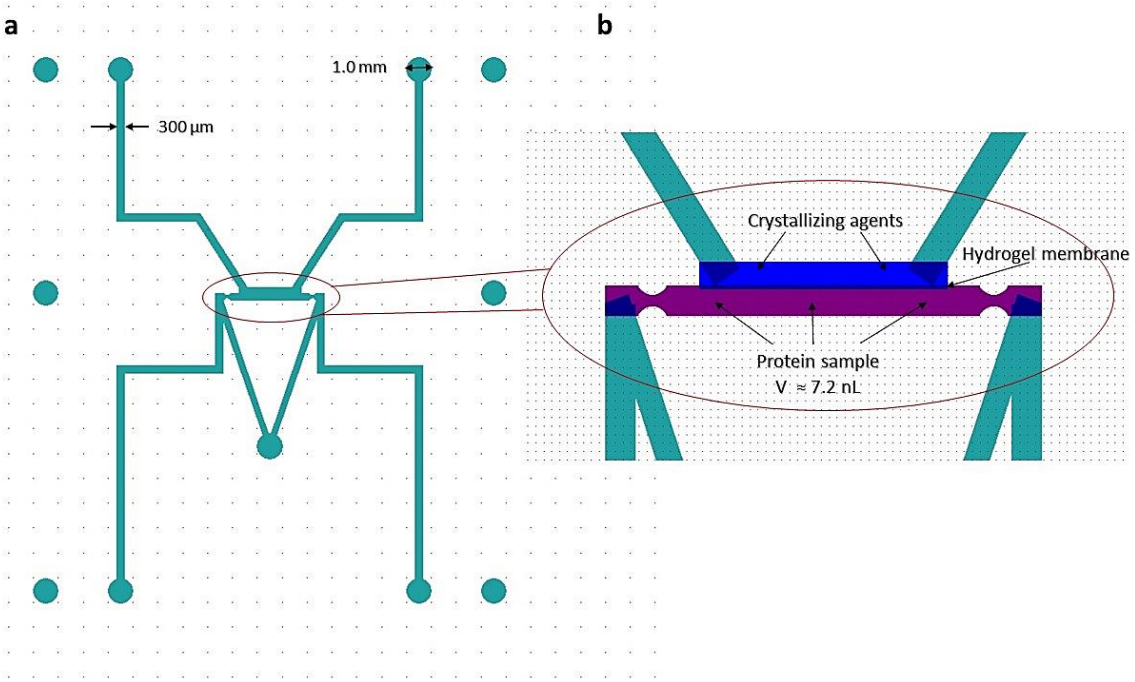

Figure 2.3.2: (a) The width of the channels and the diameter of the pillars for the chip designed for *in situ* photo-patterning of hydrogel membranes ("SJ_mask4"). (b) Magnification of the central reservoir where the location of the membrane is indicated.

2.3.2 Photolithography

Photolithography was implemented to acquire the masters for the designs named "SJ_mask 4" (Figure 2.3.1) and "SJ_1 µL" (Appendix 2.2, Figure A2.4). The protocol for the "SJ_mask 4" master is described in the following section, while the protocol for the "SJ_1 µL" design is provided in Appendix 2.2.2. The SU-8 3000 series negative photoresist was used on silicon wafers (76.2 mm diameter and 500 ± 20 µm thickness). The equipment used for plasma treatment, spin coating, soft baking and the mask aligner are the same as described in Section 2.1. Moreover, the surface measurements of the SU-masters of all the designs tested for *in situ* photo-patterning of hydrogel membranes are included in Appendix 2.2.3.

2.3.2.1 Protocol for "SJ_mask 4"

Two-layer photolithography was implemented for the "SJ_mask 4" design. The nominal thickness of the first layer patterning the channels and the pillars (Figure 2.3.1 (b) left) was approximately 12 µm and the thickness of the second layer patterning only the pillars (Figure 2.3.1 (b) right) was approximately 100 µm. It is noteworthy that for the fabrication of the PEGDA chips based on the "SJ_mask 4" design, only one master is required and it should not be confused with the protocol described in Section 2.1 where two masters were necessary for each design for the fabrication of the dialysis chip. Therefore, the two photomasks shown in

Figure 2.3.1 (b) are used to develop one master by multi-layer photolithography. Each layer of the SU-8 photoresist is deposited above the previous layer on the same silicon wafer to fabricate a multi-layered device.

Prior to photolithography, the silicon wafer was rinsed with isopropanol and acetone, dried with nitrogen gas and its surface was treated with air plasma for 90 s, in order to facilitate the adhesion of the SU-8 photoresist. The wafer was then placed on the spin coater. For the first layer of photolithography, the SU-8 3005 photoresist was chosen. For a thickness of approximately 10 μm, the SU-8 3005 resist was applied as follows (according to data provided by Microchem, Figure 2.1.4):

- Spin coating: 10 s spin at 500 rpm with acceleration of 100 rpm/s followed by 30 s spin at 500 rpm with acceleration at 300 rpm/s
- Soft bake: 10 min at 368 K on a hot plate followed by 3 min at room temperature
- UV exposure: 8 s with a power of 41 mW cm^{-2}
- PEB: 5 min at 368 K on a hot plate followed by 3 min at room temperature

SU-8 3050 was chosen for the second layer of photolithography. The wafer was centered again on the spin coater. SU-8 3050 is more viscous than SU-8 3005 and it is crucial to cover all the patterns of the first layer before starting the spinning process. For a thickness of approximately 100 μm, the SU-8 3050 resist was applied as follows (Figure 2.1.4):

- Spin coating: 10 s spin at 500 rpm with acceleration of 100 rpm/s followed by 30 s spin at 2000 rpm with acceleration at 300 rpm/s
- Soft bake: 30 min at 368 K on a hot plate followed by 3 min at room temperature
- UV exposure: 8 s with a power of 41 mW cm^{-2}
- PEB: 5 min at 368 K on a hot plate followed by 3 min at room temperature
- Development: 15 min in PGMEA bath

The master with the photoresist structures on it was then rinsed with isopropanol, dried with nitrogen gas and stored in Petri dishes. If blurry white precipitate is visible after rinsing with isopropanol, the master must be immersed again in the PGMEA bath as the development step is not completed. Finally, the surface of the master is treated with a silane to facilitate the detachment of the PEGDA 250 hydrogel used for the fabrication of the microchips. The wafer is placed in a tapped hot plate for 10 min at 368 K under the vapor atmosphere of HMDS. Figure 2.3.3 shows the SU-8 masters developed at LOF for the “SJ_mask 4” design.

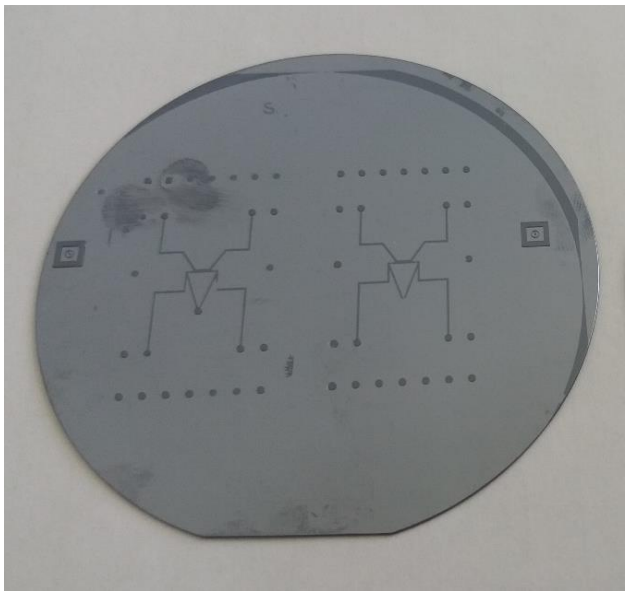

Figure 2.3.3: The SU-8 masters developed by two-layer photolithography for the "SJ_mask4" design.

The alignment of the separate layers is crucial when using multi-layer photolithography. In this case, the pillars of the second layer (Figure 2.3.1 (b)) must be perfectly aligned with the pillars of the first layer (Figure 2.3.1 (a)). For this purpose, alignment marks, shown on the left and right edges of each photomask, are used. The alignment marks are illustrated in Figure 2.3.4: when combined, the motifs of the mark of the first layer (Figure 2.3.4 (a)) and the marks of the second layer (Figure 2.3.4 (b)), should fit perfectly (Figure 2.3.4 (c)).

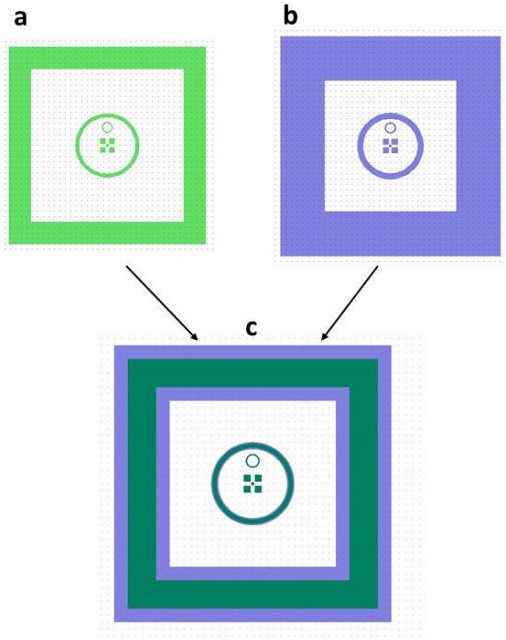

Figure 2.3.4: Alignment marks for two-layer photolithography. The features of the first layer (a) and the features of the second layer (b) must fit perfectly (c).

2.3.3 Microfabrication of PEGDA chips

Two methods were used for fabricating PEGDA chips. The first method is described by Decock *et al*.[37] and involves the fabrication of two PDMS molds from the SU-8 master, whereas, with the second method, the chips are fabricated directly on the SU-8 master. The protocol for the first method is provided in Appendix 2.3.1, while the protocol for the second method is described in Section 2.3.3.1. The solution used to fabricate the PEGDA chips contains 95 % v/v of PEGDA 250 (average Mn, Sigma-Aldrich) and 5 % v/v of the photo-initiator 2-Hydroxy2-methylpropiophenone (Darocur 1173, Sigma-Aldrich). For PEGDA, the number 250 refers to the average molecular weight, Mn, defined as the weight of the polymer molecules in a sample divided by the total number of polymer molecules in the sample.

2.3.3.1 Direct fabrication on the master

The second method of fabricating PEGDA stickers on a glass substrate is less time-consuming than the first method (Appendix 2.3.1) because there is no necessity to prepare PDMS stamps. The procedure is schematically described in Figure 2.3.5 from top to bottom. First, a microscope glass slide was set above the patterned SU-8 master which was previously treated with HMDS vapor for 10 min at 368 K. The empty space between the glass slide and the master was filled by capillarity with the PEGDA 250 solution. The assembly was exposed to UV light for 1 s and the thin PEGDA layer was partially crosslinked. Then, the PEGDA sticker was peeled off the glass slide and was pressed gently on another glass slide, previously silanized with 3-(trimethoxysilyl) propyl acrylate in a closed environment at 338 K for 24 h. The assembly was exposed again to UV light for 180 s. During the deposition of the partially crosslinked PEGDA sticker on the silanized glass slide, the risk of entrapping air bubbles was increased. This would happen frequently with the first two designs (“SJ_pattern 1” and “SJ_mask 3” shown in Appendix 2.2.1) due to the complexity of the design and the large dimensions of the channels. Specifically, the length of the channels (a few mm) was quite large compared to their height (less than 10 µm) and this could lead to entrapped air bubbles or the channels could collapse during microfabrication. However, the “SJ_mask 4” design gave more satisfactory results. PEGDA chips were fabricated by using this mask where less air bubbles were trapped and the channels were well-shaped and well-suited for the application. A chip prepared with this method is shown in Figure 2.3.6 (a).

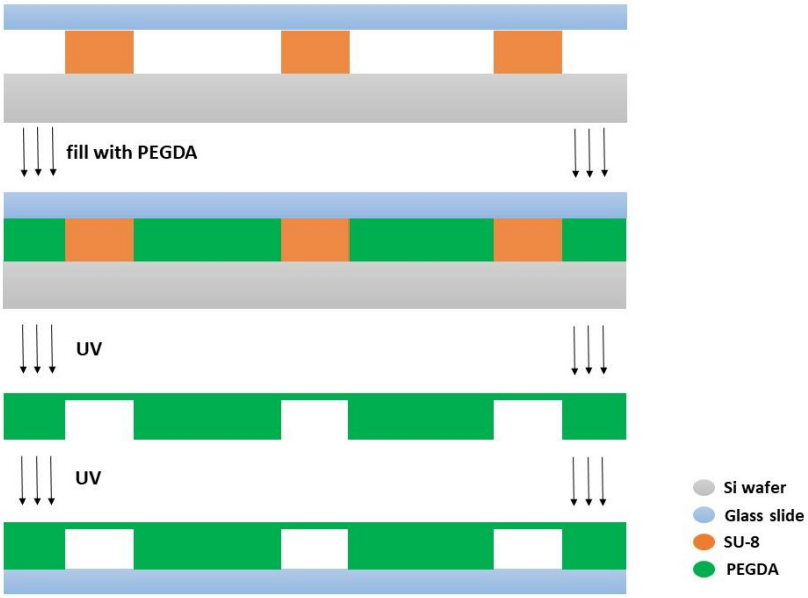

Figure 2.3.5: Schematic representation of the second method for fabricating PEGDA chips. From top to bottom: a glass slide is placed above the patterns of the SU-8 master. The PEDGA 250 solution fills in the space between the master and the glass slide by capillarity and it is exposed to UV light (1 s). The partially crosslinked PEGDA layer is detached from the master and pressed on a silanized glass slide. The polymerization is completed by a second UV exposure (180 s).

Once the chips were fabricated, micropipette tips were used as connectors. They were attached on the inlet and outlet ports by using an epoxy glue. PTFE tubing with inner diameter of 1 mm were plugged on the connectors to test the flow within the channels. The chips that were made from the "SJ_mask 4" master gave satisfactory results concerning the flow, since no leaks were observed for pressure values up to nearly 600 mbar. Figure 2.3.6 (b) illustrates a PEGDA chip on a glass slide with its connectors.

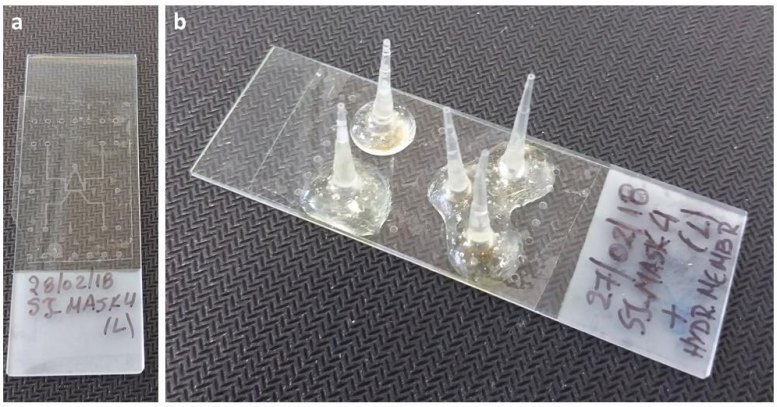

Figure 2.3.6: (a) PEGDA chip fabricated directly from the SU-8 master and (b) the pipette tips used as connectors on the inlet and outlet ports.

2.3.4 *In situ* photo-patterning of hydrogel membranes

Once the PEGDA chips were fabricated by using the "SJ_mask 4" wafer and the connectors were glued, the proceeding step was the *in situ* photo-patterning of the hydrogel membrane at the interface between the protein reservoir and the reservoir of the crystallizing agent, as shown in Figure 2.3.2 (b). This was achieved with a maskless UV projection setup (Primo, Alvéole) able to project patterns at the focal plane of a microscope. The optical apparatus uses a UV laser with a wavelength of 375 nm combined with a digital micro-mirror device (DMD) for the projection of the patterns. The lateral resolution of the projected patterns can be approximately 1.2 µm over a field of view of 500 x 300 μm^2 with a 20x objective. The software (Leonardo) allowing the control of several parameters, such as the power of the laser source and the illumination, is a product of the same company.

The aqueous solution for the *in situ* polymerization of hydrogel membranes contains PEGDA 700 (average Mn, Sigma Aldrich) as a precursor, 2-hydroxy-2-methylpropiophenone (Darocur 1173, Sigma Aldrich) as photo-initiator, PEG 1000 (Sigma Aldrich) as porogen and water as the solvent. Specifically, the PEGDA 700/photo-initiator solution (with a 90: 10 % per volume ratio), was mixed with PEG 1000 and water in a 25 % : 25 % : 50 % volume fraction. First of all, the hydrogel formulation was stirred before use to homogenize the mixture. Then, a droplet of the mixture was injected within the channels of the chip from one of the five inlets (Figure 2.3.7 (b)). The injection of the hydrogel formulation can be done either manually with the aid of a disposable syringe or with the aid of an automated pressure-driven fluidic system (Fluigent). If air bubbles are trapped within the microfluidic channels, then a new quantity of the hydrogel formulation is injected from one of the chip's inlets and simultaneously air is pressurized from the opposite inlets with the aid of the pressure-driven system. It is important to avoid air bubbles close to the area where the hydrogel formulation will be photo-polymerized to create the membrane. Once the channels are filled with the hydrogel solution, a suitable pattern is chosen to be projected with the maskless UV projection setup. Then, the UV photo-polymerization of the hydrogel solution takes place at the desired position. An example of a photo-patterned hydrogel membrane within a chip made from "SJ_mask 4" is shown in Figure 2.3.7 (a) (yellow arrow). The red and green arrows indicate the protein reservoir and the flow of the crystallizing agents, respectively.

Once the hydrogel solution was polymerized, the chip was rinsed with distilled water in order to remove the non-polymerized hydrogel solution from the microfluidic channels. This step should be implicated fast and sufficient amount of water should be used to wash the channels, otherwise the non-polymerized hydrogel solution remaining in the channels can be polymerized by the UV light present in the environment and block the fluidic channels. The chip is ready for use or it can be stored for future use, while the channels remain filled with water. It should be mentioned that the porosity of the membrane depends on the composition of the hydrogel formulation.

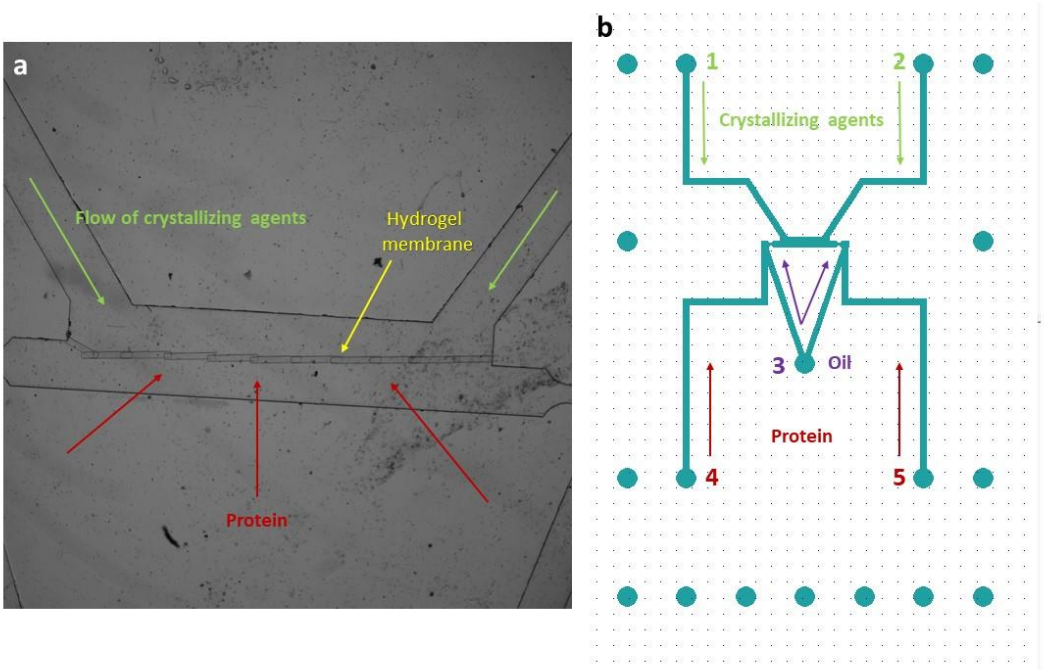

Figure 2.3.7: (a) The hydrogel membrane fabricated by *in situ* photo-patterning on a PEGDA chip. (b) The inlet/outlet ports of the PEGDA chip dedicated for the circulation of the crystallization solution (green color), the protein solution (red color) and the fluorinated oil (purple color).

2.3.5 Droplet tests

The main purpose of designing the "SJ_mask 4" chip is to entrap a small volume (nL scale) of protein sample within the central channel of the chip, surrounded by a droplet of biocompatible oil. This idea is described schematically in Figure 2.3.7 (b) where the flow of the various solutions within the different channels of the chip is indicated with colored arrows. Inlets 1 and 2 (green color) can be used for the circulation of the crystallization solution, inlets 4 and 5 (red color) for the protein solution and inlet 3 (V-shape, purple color) can be used for the injection of fluorinated oil to entrap a droplet of the protein solution within the central channel. Once the oil is injected within the channels, it creates an interface with the aqueous phase, as shown in Figure 2.3.8. In order to maintain the oil/water interface in a standard position, constant pressure is applied from both inlets 4 and 5. This way, both inlets 4 and 5 are blocked and neither oil nor the protein sample can flow back through these inlets (backward flow) and everything is trapped within the central channel. The hydrogel membrane which is fabricated in the central channel, allows the diffusion of molecules from the side where the crystallizing agents flow to the side where the protein sample is trapped by the oil droplet.

Some tests were performed at LOF to realize the idea of entrapping a small volume of an aqueous solution by an oil droplet. For this experiments, distilled water and fluorinated oil were used. The outcome of one of the tests is shown in Figure 2.3.8. An oil/water interface,

indicated with red arrows, was created on both sides of the central channel. On the left side, however, the interface is not well-formed, as an air bubble is trapped inside the channel. As may be seen from Figure 2.3.7 (a), the hydrogel membrane is not well-defined on the left edge of the central channel allowing water and air molecules to diffuse easily from one side of the channel to the other. Nevertheless, the membrane remained functional despite of the high pressure values applied during the tests (up to 600 mbar).

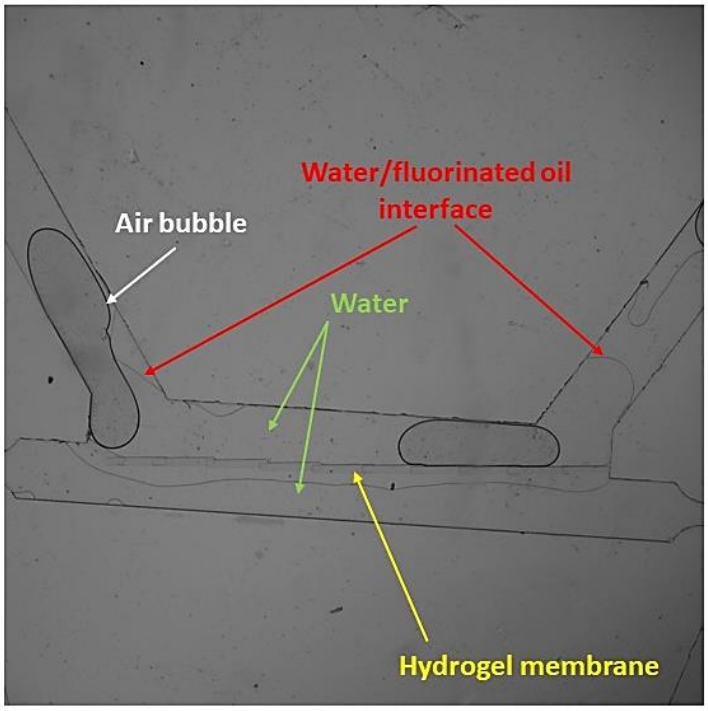

Figure 2.3.8: The water/fluorinated oil interface and the diffusion of water through the hydrogel membrane in PEGDA chip fabricated from the "SJ_mask 4" master.

2.4 Microfluidic devices for *in situ* serial X-ray crystallography

2.4.1 Introduction

Microfluidic technology has been proven a valuable tool for X-ray crystallography, exhibiting numerous advantages for the crystallization of biological macromolecules and their structural studies. The novel approach of on chip and *in situ* X-ray diffraction data collection has been proposed and used by several groups working in the field of structural biology [40,41], as it eliminates the manual manipulation of the fragile macromolecular crystals and the potential deterioration of the crystal quality prior to diffraction experiments. A wide range of microfluidic devices for *in situ* X-ray protein crystallography studies have been designed and developed by various research groups, choosing fabrication materials and techniques compatible with the restrictions posed by the interactions of the fabrication materials with X-

rays. The fabrication materials must be optically transparent, biologically inert and demonstrate high transparency to X-ray radiation and optimal signal-to-noise ratio during the *in situ* data collection.

PDMS-based devices have been developed for the crystallization of model soluble protein targets and their structural investigation via *in situ* X-ray diffraction. Hansen *et al*.[42] used the permeability of PDMS membranes in combination with the FID crystallization method for growing lysozyme, glucose isomerase, thaumatin and catalase crystals and collecting *in situ* diffraction data at 100 K by diffusing cryoprotectant solutions directly into the chip's chambers over a period of 24 – 72 h. A composite PDMS and glass capillary device was fabricated by Zheng *et al*.[43] using microbatch or vapor diffusion droplet-based crystallization. Lysozyme and thaumatin crystals were grown for *in situ* data collection at room temperature and diffracted close to 1.8 Å resolution. Microchips made of PDMS by replica casting, PMMA by direct laser ablation or COC by hot embossing were used by Dhouib *et al*.[44] for the *in situ* X-ray diffraction of lysozyme and thaumatin crystals grown on the chips by counter-diffusion. The background noise generated by the various fabrication materials was evaluated and the differences in the quality of the diffraction data were extensively explained based on the choice of the chips' materials and their thickness. The scattering background was measured at two different wavelengths showing that PMMA and COC provide a good compromise between the device thickness and the absorption of X-rays. A similar study on the characterization of the X-ray transparency of materials based on their linear attenuation coefficient and the transmission factor was performed by Guha *et al*.[45]. A thin hybrid microfluidic chip consisting of one thin layer of PDMS (20 μm) and two layers of COC (100 μm and 50 μm) was used to collect X-ray diffraction data of lysozyme crystals at room temperature and the mosaicity of the merged data set was an order of magnitude lower than the mosaicity of the respective data collected at cryogenic conditions.

Moreover, the *in situ* data collection strategy on microfluidic chips has been also applied in more challenging protein targets. Kisselman *et al*.[46] developed the X-CHIP for high-throughput, microbatch crystallization and *in situ* diffraction of the protein kinase domain of human ephrin receptor tyrosine kinase A3 (EphA3) and the *Pseudomonas aeruginosa* alkylhydroperoxidase D protein (PA0269). On chip anomalous diffraction *de novo* structure determination at room temperature was performed by Perry *et al*.[47] for the selenomethionine (SeMet) derivative of the phosphonoacetate hydrolase (PhnA) from *Sinorhizobium meliloti* at 2.11 Å resolution. The 24- or 96-well microfluidic array chips were made of COC, PDMS and Duralar®. More recently, *in situ* structural analysis has been used with membrane protein crystals of cytochrome bo_3 oxidase, grown with microseeds on microfluidic assemblies made of PDMS and COC layers with a total thickness of 200 μm[48].

Microfluidic chips have been designed to couple the *in situ* and the serial data collection strategies in a single device for X-ray crystallography experiments at synchrotrons and X-ray free-electron lasers (XFEL). Heymann *et al*.[49] developed X-ray semi-transparent chips of a total 155 μm thickness by bonding COC or Kapton films on a thin PDMS layer containing the microfluidic channels. Nanoliter-sized droplets of glucose isomerase were encapsulated in oil within the chips and stabilized by surfactants. Several partial data sets were collected from 152 randomly orientated glucose isomerase crystals at room temperature using a synchrotron source and they yielded 93 % completeness of the merged data sets and a structure at 2.1 Å resolution. More innovative materials were used by Sui *et al*.[50] for fixed-target on chip serial synchrotron crystallography. Single-layer graphene on PMMA substrate was incorporated into

ultra-thin microfluidic devices made of 100 µm thick COC. An extensive study was performed to fully characterize the compatibility of the chips for *in situ* experiments by calculating the transmission factor (I/I_0) as a function of the materials' thickness at a fixed energy value or as a function of energy for various thickness values of the materials or by measuring the background scattering and estimating the signal-to-noise when diffraction data were collected from HEWL crystals at room temperature. Gicquel *et al*.[51] fabricated devices patterned from epoxy glue that were lidded on both sides with polyimide foils windows allowing goniometer based fixed target serial data collection with low background noise. Small crystals (size 10 – 20 µm) of thaumatin, glucose isomerase and thioredoxin were used to evaluate the compatibility of the chips for *in situ* X-ray serial crystallography at room temperature. More recently, ChipX3, a microchip made entirely of COC, was used for the on chip crystallization of several bio macromolecules via counter-diffusion[52]. The characteristic diffusive scattering ring of COC at 4 – 6 Å resolution had no significant impact on the diffraction data quality. The structure of 4 proteins (protease 1 from *Pyrococcus horikoshii* (PhP1), lipase from *Thermomyces lanuginosus* (Lip), CCA-adding enzyme from *Planococcus halocryophilus* (CCA), Ilama nanobody PorM_02 (Nb02)) and an RNA duplex were successfully determined within the resolution range of 1.5 – 2.5 Å by collecting partial data sets from several different crystals or from several volume wedges of the same crystal. Another interesting approach for serial synchrotron crystallography (SSX) is the in-flow SSX where diffraction data can be collected from a slurry of microcrystals under flowing conditions. Monteiro *et al*.[53] developed a metal-polyimide (Kapton) flow-focusing device and determined the lysozyme structure at 2.1 Å from multiple data sets collected at room temperature. Unlike the devices described so far where the macromolecular crystals grew on chip, for the metal-polyimide flow-focusing device, the lysozyme crystals were not grown directly on the chip but were transferred to the sample chamber right before the *in situ* diffraction data collection.

2.4.2 Characterization of materials for *in situ* X-ray diffraction studies

When microfluidic devices are used for *in situ* X-ray crystallography, the diffraction signal from the macromolecular crystals is added to the signal generated by the interactions between the materials composing the chip and the X-rays, known as background noise. The background noise is generated by scattering or attenuation of X-rays through mater when the X-ray beam interacts with the chip's materials or any other material interfering between the chip and the detector, as for example the surrounding air or the mother liquor surrounding the crystal. During data collection, the signal-to-noise ratio between the diffraction signal of the macromolecular crystal and the background noise of the microfluidic device should be maintained as high as possible. Therefore, it is important to characterize the materials composing the microfluidic device and minimize parameters leading to the degradation of the signal-to-noise ratio. The density and the thickness of each material should be chosen accordingly in order to generate as low background noise as possible, while remaining biocompatible and compatible with the mechanical restrains of the experiment.

2.4.2.1 Measurements of background noise

The measurements for the material characterization were performed at BM30A-FIP beamline at ESRF equipped with an ADSC Quantum 315r detector with a matrix of 3 × 3 CCD (charged-coupled device) for an active surface of 315 × 315 mm and a resolution of 9.4 mega pixels. Monochromatic X-rays of 0.98 Å wavelength or 12.656 keV energy (Selenium K edge) were used and the beam slit size was 250 × 250 µm. The photon flux was 3.32×10^{10} ph s^{-1} with 200 mA in the storage ring at ESRF. The distance between the sample material and the detector was 200 mm and each sample was exposed for 20 s while remaining perpendicular to the X-ray beam during the data collection. Each measurement was followed by an exposure of 20 s to the surrounding environment. For example, the exposure of the 175 µm thick PMMA sheet was followed by an exposure to empty space, where no material apart from air interfered between the beam output and the detector. However, the amplitude of X-ray scattering contribution increases with the elemental atomic number, Z. Thus, instead of atmospheric air (a mixture of mainly nitrogen with $Z_N = 7$ and oxygen with $Z_O = 8$), helium (He, $Z_{He} = 2$) flux (a feature provided at BM30A-FIP beamline, currently rebuilt on a new position as BM07-FIP2 at ESRF) was chosen during data collection for material characterization and protein diffraction experiments. Scattering images were viewed using Adxv and radial intensity plots were designed using ROOT.

The scattering signal of each material comprising the microfluidic chip was measured in He atmosphere. The part of the microchip that is exposed to the beam during *in situ* X-ray diffraction experiments is the protein reservoir where the macromolecular crystals grow. The protein reservoir consists of a layer of Kapton tape (~ 20 µm thickness), two layers of PMMA (175 µm thickness each), one used below the Kapton tape to encapsulate the protein sample within the protein compartment and one used as the substrate of the microchip, and the RC dialysis membrane (~ 40 µm thickness). The total thickness of the materials interacting with the X-rays is ~ 410 µm. Figure 2.4.1 illustrates the intensity of background scattering generated by the materials comprising the protein reservoir (Kapton, PMMA, RC membrane) and their assembly (microchip) plotted against resolution (Å). In the case of the PMMA sheet, a wide peak can be observed between 4 – 8 Å, corresponding to the diffusion of the X-rays in the material and then the intensity decreases, while for the Kapton tape a diffuse peak is present at a resolution lower than 4 Å. The RC dialysis membrane contributes little to the background noise with a peak spotted at 4 – 5 Å resolution owing the lowest intensity of all the materials measured in Figure 2.4.1. The diffusive peaks are characteristic of amorphous materials. However, polymers are not totally amorphous. For example, they contain groups like the benzene group and they behave as randomly orientated crystals. The background noise generated by the microchip (the assembly of Kapton tape, RC membrane and 2 layers of PMMA) is maximum (peak) at a relatively low resolution (6 – 7 Å), which is less critical for processing diffraction data at higher resolution. Figure 2.4.2 shows the scattering images recorded for each material at 0.98 Å containing 3072 × 3072 pixels. The grayscale shown on the left of Figure 2.4.2 has been adjusted and is the same for all images. The background of He is also shown and it can be seen that the background of thinner materials, like Kapton and PMMA, is less significant than the noise generated by thicker or denser materials. In the measurements presented in this section, the dialysis chip was empty of any solution (protein or precipitant solution) and the contribution of the presence of solution to the background noise has not been measured.

Apart from the materials comprising the protein reservoir of the microfluidic chip, Figure 2.4.1 includes the intensity plots for three more materials studied in this thesis. COC is a material widely used in the literature[44,45,49,50,52] for the fabrication of microfluidic devices compatible with *in situ* X-ray macromolecular crystallography (MX). A 50 µm thick COC foil was considered as an alternative to substitute the 175 µm thick PMMA sheet used as a substrate of the NOA 81 dialysis chip. The background scattering intensity of the COC foil was also measured under the same experimental conditions (200 mm sample-to-detector distance, 20 s exposure time, He atmosphere) at BM30A-FIP. The characteristic peaks of COC (Figure 2.4.1) can be distinguished in a resolution range from 4 – 6 Å and the respective rings are shown in the scattering image in Figure 2.4.2. On the other hand, PMMA shows a wider peak owing roughly the same intensity value, shifted towards a lower resolution range (4 – 8 Å), rendering the PMMA sheets a more suitable candidate for the fabrication of the dialysis chip. Moreover, the PMMA sheets are more robust and mechanically stable than the COC foil, minimizing the potential risks rising when transferring and setting up the chips in the beamline. Another material tested was the PEGDA 250 hydrogel, considered to replace the NOA 81 resin during the fabrication of the microchips. Moreover, hydrogels were considered to replace the RC dialysis membrane. As described in the protocol for the device fabrication (Section 2.2), the RC membrane is incorporated between two layers of the chip, adding more steps on the fabrication protocol. Instead, hydrogel membranes can be fabricated directly within the microfluidic channels of the chip by *in situ* photo-patterning[37,38], simplifying the fabrication protocol and reducing the total thickness of the chip which would be a one-layered device (Section 2.3). From Figure 2.4.1 and Figure 2.4.2, it can be seen that the polymerized layer of PEGDA 250 has a peak within 4 – 6 Å resolution, whereas the intensity peak of the RC membrane lies within 4 – 5 Å. However, the maximum background intensity caused by the interaction of the PEGDA 250 hydrogel is 3 times higher than the respective value for the RC dialysis membrane. Finally, the background noise generated by the NOA 81 resin was also measured. Even though the NOA 81 resin is not part of the protein reservoir that is directly exposed to X-rays during the *in situ* data collection, it forms the main body of the microchip. For NOA 81, a peak is present between 3 – 6 Å (Figure 2.4.1 and Figure 2.4.2). An interesting concluding remark after the analytical inspection of the intensity plots is that all the polymeric materials (PMMA, COC, NOA 81 and PEGDA 250) present a scattering peak at approximately the same resolution range and intensity value.

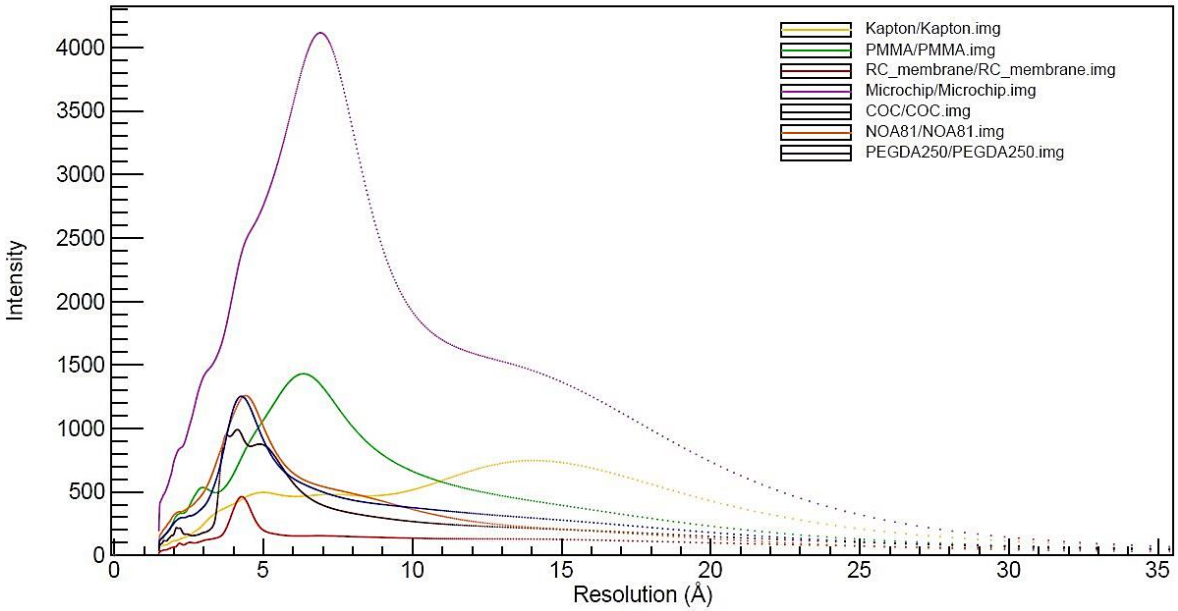

Figure 2.4.1: Background scattering intensity as a function of resolution (Å) for the materials comprising the protein reservoir of the dialysis chip (PMMA, Kapton, RC membrane), the microchip, NOA 81 and other materials studied in this work (COC, PEGDA 250).

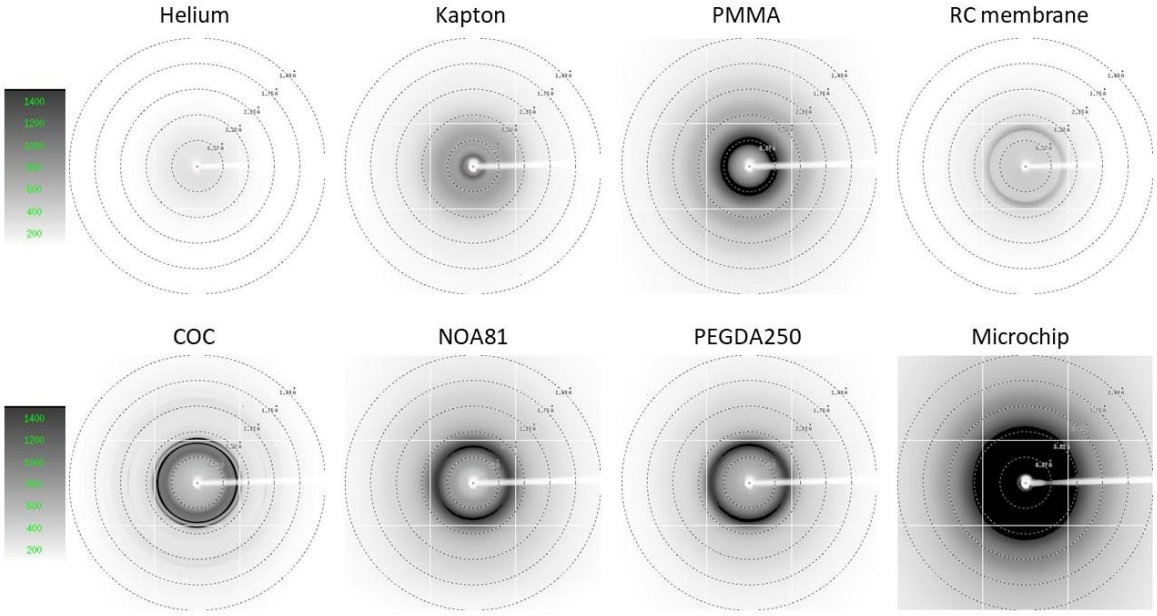

Figure 2.4.2: Scattering images showing the background noise generated by the materials used in this work (Kapton, PMMA, RC membrane, COC, NOA 81, PEGDA 250), the microchip and helium. The gray scale has been adjusted to the same level for all images.

The background scattering of the dialysis chip was then compared to the background noise generated by two commercial plates for crystallization screening and *in situ* X-ray diffraction experiments, the 96-well plate CrystalQuickX by Greiner made of low birefringent COC and the 96-well plate CrystalCube designed by Cube Biotech for *in meso* crystallization. Figure 2.4.3 illustrates the background scattering intensity *versus* resolution (Å) graphs for the dialysis chip and the commercial crystallization plates. As described previously, the intensity corresponds to the value recorded by the detector for the chip or the plates, after subtracting the measurement performed without any sample between the beam and the detector. All measurements were done in He atmosphere, the sample to detector distance was 200 mm and the exposure time 20 s. During data collection, all samples were perpendicular to the X-ray beam. The two commercial plates have a high intensity peak close to 5 Å resolution and the dialysis chip shows a maximum intensity at a resolution lower than 5 Å. However, the background noise intensity obtained by the microchip is approximately 8 to 15 times lower than the background noise generated by the commercial plates for *in situ* X-ray crystallography. Practically, this means that for a given protein sample and volume, the quality of the diffraction image will be less impacted by the background noise in the case of the dialysis chips. Choosing materials with relatively high X-ray transparency and reducing their thickness are key parameters for *in situ* data collection. Nevertheless, very low thickness values can compromise the rigidity of the microfluidic device and has been associated with sample evaporation issues[50].

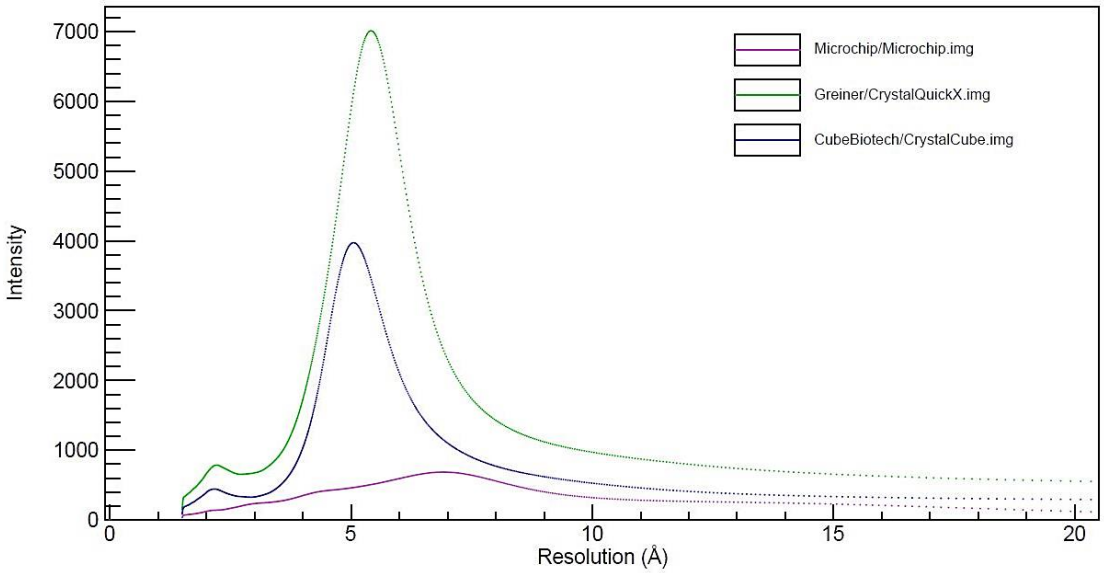

Figure 2.4.3: Background scattering intensity as a function of resolution (Å) for the dialysis chip and the commercial crystallization 96-well plates CrystalQuickX and CrystalCube.

Giving a graphical representation of the scattering images shown in Figure 2.4.2, would lead to intensity graphs plotted against the image pixels, as shown in Figure 2.4.4, where scattering measurements were performed for a sample to detector distance of 200 mm and

an exposure time of 20 s. The samples shown in Figure 2.4.4 were a layer of polymerized PEGDA 250, a COC foil and polymerized NOA 81 resin on COC substrate. However, Figures 2.4.1 and 2.4.3 show intensity graphs plotted as a function of resolution (Å). The pixel value of each scattering image read directly by the detector was converted to resolution values using Bragg's law:

$$d = \frac{\lambda}{2\sin\theta} \quad (2.1)$$

Where d is the resolution value (Å), λ is the wavelength (0.98 Å) and θ is the scattering angle (°).

Moreover, by inspecting Figure 2.4.4 and comparing with Figures 2.4.1 or 2.4.3, it is obvious that the intensity data are quite noisy and the respective graph doesn't appear smooth. In order to improve the representation of the data, a window function was used. The intensity data represented on the y axis of Figures 2.4.1 and 2.4.3 were filtered with a low-pass filter. Specifically, a Hamming window of 49 values was applied:

$$h(n) = 0.54 - 0.46\cos\left(\frac{2\pi n}{N}\right), n \in [0, N] \quad (2.2)$$

Where N is the order of the filter, which is equal to the filter length -1.

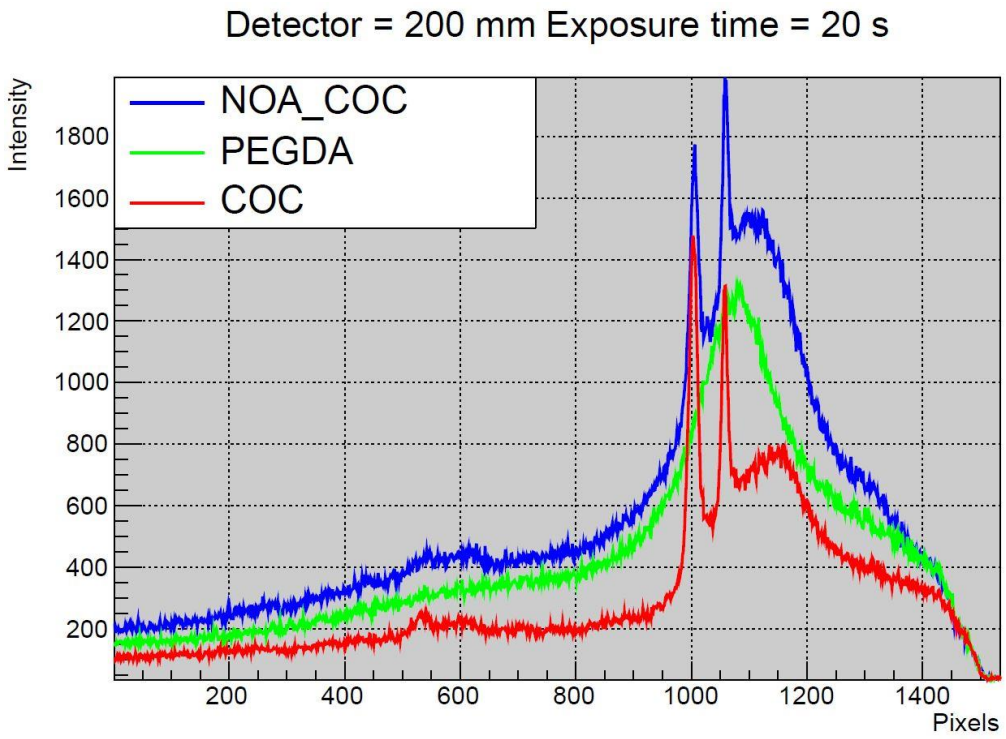

Figure 2.4.4: Background scattering intensity as a function of the image pixels for various materials (NOA 81 on COC, PEGDA 250, COC).

2.4.2.2 Impact of the sample-detector distance and exposure time on the background noise

Two parameters considered during the measurements for the material characterization were the distance between the sample and beamline detector and the exposure time. Several tests were performed to examine the impact of the detector to sample distance and the exposure time on the intensity of the background noise and two examples are shown in Appendix 2.4.1 for a 50 μm thick COC foil and a polymerized PEGDA 250 layer. Moreover, in order to evaluate the impact of a long exposure time on the background noise generated by various materials (Kapton, PMMA, RC dialysis membrane, microchip), a supplementary study was performed at BM30A-FIP and the results are provided in Appendix 2.4.2.

2.4.3 Considerations for X-ray compatibility

The design and fabrication of microfluidic devices compatible with *in situ* X-ray diffraction experiments lies on the optimization between the observed sample signal (diffraction spots of the protein crystal) and the background noise. The background noise can be attributed to the attenuation of the incident or diffracted beam, especially if the beam size and the sample size are different or can be the result of X-ray scattering due to the presence of the chip's materials, the surrounding air and the presence of liquid within the protein crystal or around it (crystallization solution). Attenuation arises from the absorption of photons by the materials, resulting to the loss of intensity of both the incident and diffracted beam, while scattering refers to the elastic re-direction of the incident photons by the internal structure of the material. Therefore, the nature of the material and its thickness contribute significantly to scattering, while the crystalline order, the crystal size and packing density contribute to the diffraction. So far, the evaluation of the materials' diffusion when exposed to X-ray radiation has been presented. However, for this evaluation the transmission of the materials should be considered too.

For a given energy value, attenuation can be calculated by the exponential decay of the intensity of monochromatic photons from the incident intensity, I_0, as the beam traverses the material of thickness χ and density ρ[40,45,50,54,55]:

$$I = I_0 \exp\left[\left(-\mu/\rho\right)\chi\right] \quad (2.3)$$

The mass attenuation coefficient, μ, can be calculated for a compound or a mixture as the sum of the contribution to attenuation of each elemental material, i, weighted according to their mass fraction, w_i:

$$\mu = \sum_i \mu_i w_i \quad (2.4)$$

Eq. (2.3) shows that the thickness of the material contributes significantly to the background noise and reducing its value can mitigate both attenuation and scattering effects. This is the main reason why X-ray diffraction experiments are performed under vacuum in order to reduce the air density between the crystalline sample and the detector. He flux is used instead of air, since the lower atomic number of He decreases significantly attenuation effects. The attenuation coefficient varies as a function of photon energy, with soft X-rays (100 eV – 10 keV) resulting in stronger attenuation, and has been well-studied for all elemental materials[55]. In general, the mass attenuation coefficient is lower for higher photon energies. An example for the dependence of the attenuation coefficient on the photon energy is given in Figure 2.4.5 for carbon (https://physics.nist.gov/PhysRefData/XrayMassCoef/tab3.html).

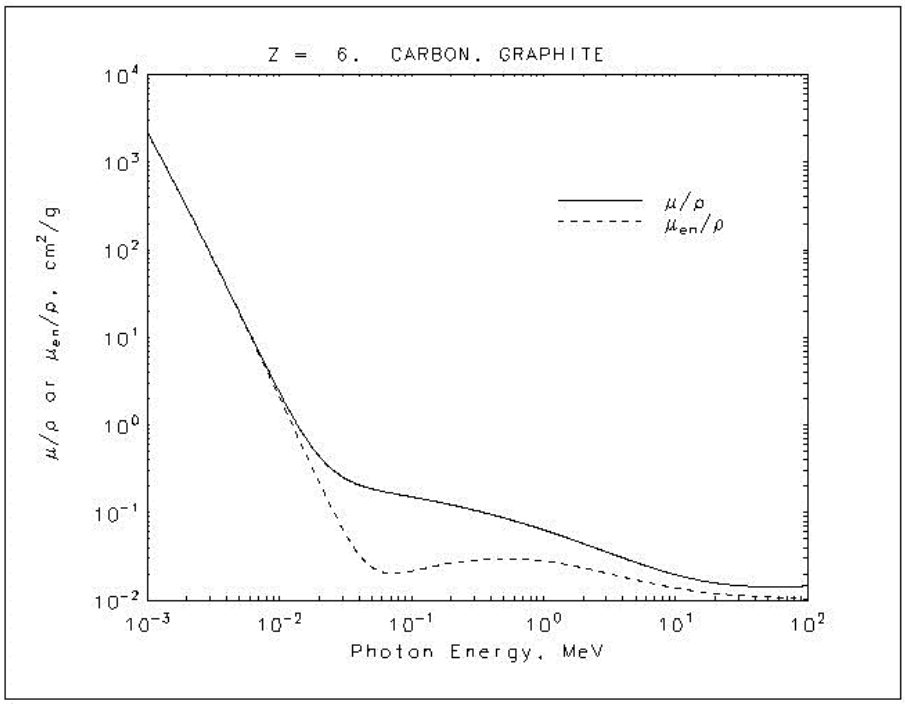

Figure 2.4.5: Dependence of the attenuation coefficient (μ) on the photon energy for carbon.

The attenuation coefficient for the materials used in this study were calculated according to Eq. (2.4) and the results are summarized in Table 2.4.1. The list of materials includes Kapton or polyimide ($(C_{22}H_{10}O_5N_2)_n$), PMMA ($(C_5H_8O_2)_n$), cellulose ($(C_6H_{10}O_5)_n$), COC ($(C_9H_{14})_n$), PEGDA 250 ($(C_8H_{10}O_4)_n$) and NOA 81. For NOA 81, according to the producing company (Norland Products Inc.), the resin is a mixture of 50 – 70 % mercapto-ester ($C_3H_6O_2S$) and 50 – 70 % triallyl isocyanurate ($C_{12}H_{15}N_3O_3$). In order to calculate the linear attenuation coefficient, a mixture of 50 % mercapto-ester and 50 % triallyl isocyanurate was assumed for the NOA 81 composition. Table 2.4.1 includes the atomic mass fraction of each element composing the material (w_i) and the mass attenuation coefficient (μ/ρ in $cm^2\ g^{-1}$) calculated at 0.98 Å (12.65 keV). Values for the X-ray mass attenuation coefficient of each element (H, C, O, N, S) were taken by NIST tables (https://physics.nist.gov/PhysRefData/XrayMassCoef/tab3.html) for X-ray energies of 10 and 15 keV, while the value at 12.65 keV was calculated by linear

interpolation. Then, the attenuation coefficient of the mixture was calculated by Eq. (2.4), using the elemental atomic mass fraction and the elemental mass attenuation coefficient at 12.65 keV, and is given in Table 2.4.1. The attenuation coefficients of Kapton, PMMA, cellulose and PEGDA have similar values. The lowest value is acquired for COC which contains only carbon and hydrogen atoms and the highest value corresponds to NOA 81 which contains nitrogen (N) and sulfur (S) atoms. Heavier atoms, like N or S, have a larger cross-section of interaction with the photons and cause a larger degree of attenuation[40].

Table 2.4.1: The atomic mass fraction (w) of the elements composing the materials used in this work and the mass attenuation coefficient (μ/ρ in $cm^2\ g^{-1}$) calculated at 12.65 keV.

Element	Kapton	PMMA	Cellulose	COC	PEGDA	NOA 81
H	0.0263	0.0805	0.0621	0.1154	0.0592	0.0595
C	0.6911	0.5998	0.4444	0.8845	0.5646	0.5069
O	0.2092	0.3196	0.4933	-	0.3760	0.2250
N	0.0732	-	-	-	-	0.1182
S	-	-	-	-	-	0.0902
μ/ρ at 0.98Å ($cm^2\ g^{-1}$)	2.0470	2.4546	2.5697	1.4088	2.3119	4.8129

From Eq. (2.3) - (2.4), the transmission factor (I/I_0) can be calculated and plotted against the thickness (χ in μm) of any material, as shown in Figure 2.4.6 for 12.65 keV photon energy (0.98 Å). At a given thickness value, the transmission factor is higher and therefore the transmission is better for the lower density, thin COC foil, while the NOA 81 resin has the lowest transmission. The transmission curves for the other organic polymers (Kapton, PMMA, cellulose, PEGDA) show a similar tendency. Sui and Perry[40], calculated and plotted the transmission factor against the thickness value (μm) for several materials used in the fabrication of microfluidic devices (COC, Graphene, PMMA, PDMS, SiO_2, Si_3N_4, Silicon), as well as air, water and He. In this plot[40], the transmission factor was calculated at an energy of 12.4 keV (1 Å). The authors showed that the transmission is higher for low density gases (air, He), while thin films of organic polymers (COC and PMMA) and graphene show lower attenuation than silicon-based elastomers (PDMS) or hard materials (quartz, SiO_2, silicon nitride, Si_3N_4). Moreover, they showed that water, majorly present in protein crystallography experiments, attenuates X-rays to a similar manner as most organic polymers. Studies on the transmission factor of various fabrication materials have also been conducted by other groups[45,50,54,56]. Therefore, decreasing the thickness of the device and choosing materials with low atomic numbers are strategies commonly encountered in the fabrication of X-ray compatible microchips. However, it should be noted that the thickness of the materials should be chosen carefully, as even though ultra-thin polymeric films are available, they tend to provide poor mechanical stability and increased sample dehydration in microfluidic applications in protein crystallography[40]. In conclusion, both material thickness and composition contribute to the signal attenuation.

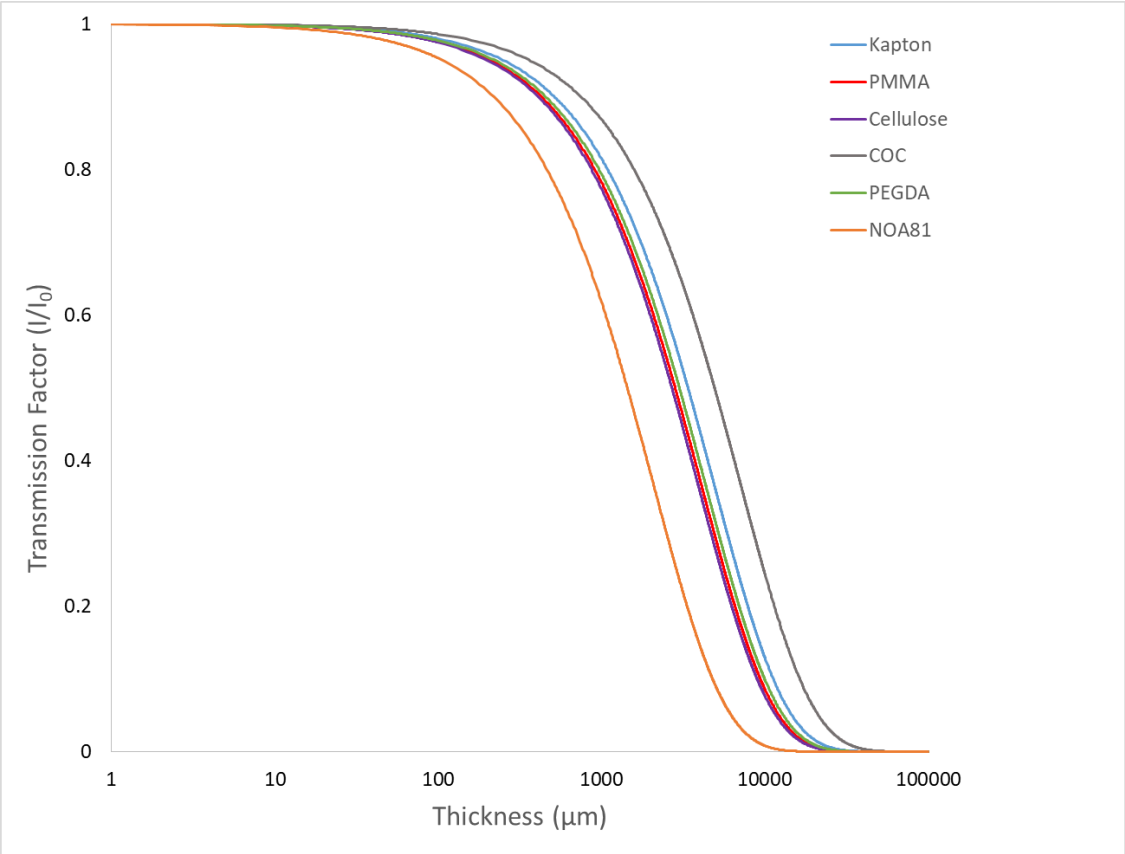

Figure 2.4.6: The transmission factor (I/I_0) plotted against the thickness (χ in µm) of various materials (Kapton, PMMA, Cellulose, COC, PEGDA 250, NOA 81) at 12.65 keV photon energy.

2.5 Conclusions

A microfluidic chip has been developed for the on chip crystallization of protein samples using the microdialysis method. The RC dialysis membrane is incorporated directly on the chip during the fabrication process and no chemical bonding, clapping or any other mechanical manipulation is required to fix the membrane. The MWCO of the membrane can be chosen according to the molecular weight of the protein sample and the precipitant solution. In fact, the protocol for the device fabrication can be upgraded in order to incorporate any kind of polymeric membrane, as for example poly(ether sulfone) (PES) membranes, with various MWCO values. Two devices have been designed depending on the maximum volume capacity of the protein reservoir which can be 0.1 µL or 0.3 µL. The rapid prototyping of the chips, the flexibility of choosing a RC membrane with appropriate MWCO for the application and the relatively inexpensive materials enable the fabrication of numerous chips. Moreover, the chips can be washed and reused as long as the dialysis membrane or the adhesion of the NOA 81 sticker on the PMMA substrate are not damaged. The same applies to the PDMS molds used during intermediate steps of the fabrication protocol. The PDMS molds can be washed with acetone and isopropanol and used several times.

The chips have been designed for injecting and continuously circulating the crystallization solution within the fluidic channel with the aid of an automated pressure-driven system or syringe pump. The maximum values of pressure have been defined in order to avoid deformation of the channels or the RC membrane, which is not firmly bonded on the layers of the NOA 81 sticker. In order to address issues raised by the integration of the membrane and potential leaks while circulating the crystallization solution, two prototypes were designed for fabricating hydrogel membranes in the chips by *in situ* photo-patterning. Different fabrication (PEGDA 250, NOA 81) and substrate (glass, COC) materials were used and the flow in the channels was tested. Even though, these two designs constitute a potential alternative to the dialysis chip, more experiments should be conducted to establish a well-functioning protocol for their use with on chip protein crystallization via microdialysis. Further work is also required on the characterization of the hydrogel membranes based on the molecular weight cut-off and their resistance to applied external pressure.

Finally, the dialysis chips have been developed for *in situ* X-ray diffraction studies at room temperature. The *in situ* data collection approach at room temperature addresses issues associated with cryo cooling, manual harvesting and radiation damage (Chapter 4) of the protein crystals. Once protein crystals are grown on the dialysis chip, the chip can be mounted directly on synchrotron beamlines compatible with in plate X-ray diffraction experiments, with the aid of a 3D printed support (Chapter 4). The background noise generated by the interaction of X-rays with the materials comprising the dialysis chip (PMMA, Kapton, RC membrane) has been evaluated, rendering the chips compatible with *in situ* X-ray data collection.

2.6 References

(1) Xia, Y.; Rogers, J. A.; Paul, K. E.; Whitesides, G. M. Unconventional Methods for Fabricating and Patterning Nanostructures. *Chem. Rev.* **1999**, *99* (7), 1823–1848.

(2) Skinner, J. G.; Groves, T. R.; Novembre, A.; Pfeiffer, H.; Singh, R. Photomask Fabrication Procedures and Limitations. In *Handbook of Microlithography, Micromachining, and Microfabrication. Volume 1: Microlithography* SPIE PRESS, **1997**.

(3) Weibel, D. B.; DiLuzio, W. R.; Whitesides, G. M. Microfabrication Meets Microbiology. *Nat. Rev. Microbiol.* **2007**, *5* (3), 209–218.

(4) Levinson, H. J. Principles of Lithography. SPIE PRESS, **2010**.

(5) Martinez-Duarte, R.; Madou, M. J. SU-8 Photolithography and Its Impact on Microfluidics. In *Microfluidics and Nanofluidics Handbook* CRC Press, **2016**, 231–268.

(6) Xia, Y.; Whitesides, G. M. Soft Lithography. *Annu. Rev. Mater. Sci.* **1998**, *28* (1), 153–184.

(7) Gates, B. D.; Xu, Q.; Love, J. C.; Wolfe, D. B.; Whitesides, G. M. Unconventional Nanofabrication. *Annu. Rev. Mater. Res.* **2004**, *34* (1), 339–372.

(8) Qin, D.; Xia, Y.; Whitesides, G. M. Soft Lithography for Micro- and Nanoscale Patterning. *Nat. Protoc.* **2010**, *5* (3), 491–502.

(9) Kumar, A.; Whitesides, G. M. Features of Gold Having Micrometer to Centimeter Dimensions Can Be Formed through a Combination of Stamping with an Elastomeric Stamp and an Alkanethiol ‘“Ink”’ Followed by Chemical Etching. *Appl. Phys. Lett.* **1993**, *63* (14), 2002–2004.

(10) Zhao, X.-M.; Xia, Y.; Whitesides, G. M. Fabrication of Three-Dimensional Micro-Structures: Microtransfer Molding. *Adv. Mater.* **1996**, *8* (10), 837–840.

(11) Xia, Y.; Kim, E.; Zhao, X.-M.; Rogers, J. A.; Prentiss, M.; Whitesides, G. M. Complex Optical Surfaces Formed by Replica Molding Against Elastomeric Masters. *Science* **1996**, *273* (5273), 347–349.

(12) Kim, E.; Xia, Y.; Whitesides, G. M. Polymer Microstructures Formed by Moulding in Capillaries. *Nature* **1995**, *376* (6541), 581–584.

(13) Bietsch, A.; Michel, B. Conformal Contact and Pattern Stability of Stamps Used for Soft Lithography. *J. Appl. Phys.* **2000**, *88* (7), 4310–4318.

(14) Firpo, G.; Angeli, E.; Repetto, L.; Valbusa, U. Permeability Thickness Dependence of Polydimethylsiloxane (PDMS) Membranes. *J. Membr. Sci.* **2015**, *481*, 1–8.

(15) Unger, M. A.; Chou, H.-P.; Thorsen, T.; Scherer, A.; Quake, S. R. Monolithic Microfabricated Valves and Pumps by Multilayer Soft Lithography. *Science* **2000**, *288* (5463), 113–116.

(16) Lee, J. N.; Park, C.; Whitesides, G. M. Solvent Compatibility of Poly(Dimethylsiloxane)-Based Microfluidic Devices. *Anal. Chem.* **2003**, *75* (23), 6544–6554.

(17) Delamarche, E.; Schmid, H.; Michel, B.; Biebuyck, H. Stability of Molded Polydimethylsiloxane Microstructures. *Adv. Mater.* **1997**, *9* (9), 741–746.

(18) Huang, Y. Y.; Zhou, W.; Hsia, K. J.; Menard, E.; Park, J.-U.; Rogers, J. A.; Alleyne, A. G. Stamp Collapse in Soft Lithography. *Langmuir* **2005**, *21* (17), 8058–8068.

(19) Lötters, J. C.; Olthuis, W.; Veltink, P. H.; Bergveld, P. The Mechanical Properties of the Rubber Elastic Polymer Polydimethylsiloxane for Sensor Applications. *J. Micromech. Microeng.* **1997**, *7* (3), 145–147.

(20) Lorenz, H.; Laudon, M.; Renaud, P. Mechanical Characterization of a New High-Aspect-Ratio near UV-Photoresist. *Microelectron. Eng.* **1998**, *41–42*, 371–374.

(21) Niels Junius. Développements Instrumentaux Pour Le Contrôle de La Cristallisation Par La Dialyse : Approche Microfluidique et Analyse Aux Rayons X, Université Grenoble Alpes, Grenoble, **2016**.
(22) M. Spano; J.-B. Salmon; N. H. Junius. Puce Microfluidique Pour La Cristallisation de Molecules, Procede de Preparation, Dispositif La Comprenant et Procede de Cristallisation de Molecules. FR3044685A1.
(23) Junius, N.; Jaho, S.; Sallaz-Damaz, Y.; Borel, F.; Salmon, J.-B.; Budayova-Spano, M. A Microfluidic Device for Both On-Chip Dialysis Protein Crystallization and in Situ X-Ray Diffraction. *Lab Chip* **2020**, *20* (2), 296–310.
(24) Jaho, S.; Junius, N.; Borel, F.; Sallaz-Damaz, Y.; Salmon, J.-B.; Budayova-Spano, M. Crystallization of Proteins on Chip by Microdialysis for In Situ X-Ray Diffraction Studies. *J. Visuaalized Exp.* **2021**, No. 170, e61660.
(25) Bartolo, D.; Degré, G.; Nghe, P.; Studer, V. Microfluidic Stickers. *Lab Chip* **2008**, *8* (2), 274–279.
(26) Morel, M.; Galas, J.-C.; Dahan, M.; Studer, V. Concentration Landscape Generators for Shear Free Dynamic Chemical Stimulation. *Lab Chip* **2012**, *12* (7), 1340–1346.
(27) Morel, M.; Shynkar, V.; Galas, J.-C.; Dupin, I.; Bouzigues, C.; Studer, V.; Dahan, M. Amplification and Temporal Filtering during Gradient Sensing by Nerve Growth Cones Probed with a Microfluidic Assay. *Biophys. J.* **2012**, *103* (8), 1648–1656.
(28) Junius, N.; Oksanen, E.; Terrien, M.; Berzin, C.; Ferrer, J.-L.; Budayova-Spano, M. A Crystallization Apparatus for Temperature-Controlled Flow-Cell Dialysis with Real-Time Visualization. *J. Appl. Crystallogr.* **2016**, *49* (3), 806–813.
(29) Junius, N.; Vahdatahar, E.; Oksanen, E.; Ferrer, J.-L.; Budayova-Spano, M. Optimization of Crystallization of Biological Macromolecules Using Dialysis Combined with Temperature Control. *J. Appl. Crystallogr.* **2020**, *53* (3), 686–698.
(30) Rolland, J. P.; Hagberg, E. C.; Denison, G. M.; Carter, K. R.; Simone, J. M. D. High-Resolution Soft Lithography: Enabling Materials for Nanotechnologies. *Angew. Chem. Int. Ed.* **2004**, *43* (43), 5796–5799.
(31) Efimenko, K.; Wallace, W. E.; Genzer, J. Surface Modification of Sylgard-184 Poly(Dimethyl Siloxane) Networks by Ultraviolet and Ultraviolet/Ozone Treatment. *J. Colloid Interface Sci.* **2002**, *254* (2), 306–315.
(32) S. Bhagat, A. A.; Jothimuthu, P.; Papautsky, I. Photodefinable Polydimethylsiloxane (PDMS) for Rapid Lab-on-a-Chip Prototyping. *Lab Chip* **2007**, *7* (9), 1192–1197.
(33) Kilduff, J. E.; Mattaraj, S.; Pieracci, J. P.; Belfort, G. Photochemical Modification of Poly(Ether Sulfone) and Sulfonated Poly(Sulfone) Nanofiltration Membranes for Control of Fouling by Natural Organic Matter. *Desalination* **2000**, *132* (1), 133–142.
(34) Pieracci, J.; Crivello, J. V.; Belfort, G. Increasing Membrane Permeability of UV-Modified Poly(Ether Sulfone) Ultrafiltration Membranes. *J. Membr. Sci.* **2002**, *202* (1), 1–16.
(35) Váquez, M. I.; Galán, P.; Casado, J.; Ariza, M. J.; Benavente, J. Effect of Radiation and Thermal Treatment on Structural and Transport Parameters for Cellulose Regenerated Membranes. *Appl. Surf. Sci.* **2004**, *238* (1), 415–422.
(36) Tan, H. Y.; Loke, W. K.; Nguyen, N.-T. A Reliable Method for Bonding Polydimethylsiloxane (PDMS) to Polymethylmethacrylate (PMMA) and Its Application in Micropumps. *Sens. Actuators B Chem.* **2010**, *151* (1), 133–139.
(37) Decock, J.; Schlenk, M.; Salmon, J.-B. In Situ Photo-Patterning of Pressure-Resistant Hydrogel Membranes with Controlled Permeabilities in PEGDA Microfluidic Channels. *Lab Chip* **2018**, *18* (7), 1075–1083.

(38) Nguyen, H.-T.; Massino, M.; Keita, C.; Salmon, J.-B. Microfluidic Dialysis Using Photo-Patterned Hydrogel Membranes in PDMS Chips. *Lab Chip* **2020**, *20* (13), 2383–2393.
(39) Camille Keita. Compression Osmotique Microfluidique: Caractérisation Rapide de Dispersions Colloïdales et de Formulations Industrielles, Université Bordeaux, Bordeaux, **2021**.
(40) Sui, S.; Perry, S. L. Microfluidics: From Crystallization to Serial Time-Resolved Crystallography. *Struct. Dyn.* **2017**, *4* (3), 032202.
(41) Sauter, C.; Dhouib, K.; Lorber, B. From Macrofluidics to Microfluidics for the Crystallization of Biological Macromolecules. *Cryst. Growth Des.* **2007**, *7* (11), 2247–2250.
(42) Hansen, C. L.; Classen, S.; Berger, J. M.; Quake, S. R. A Microfluidic Device for Kinetic Optimization of Protein Crystallization and In Situ Structure Determination. *J. Am. Chem. Soc.* **2006**, *128* (10), 3142–3143.
(43) Zheng, B.; Tice, J. D.; Roach, L. S.; Ismagilov, R. F. A Droplet-Based, Composite PDMS/Glass Capillary Microfluidic System for Evaluating Protein Crystallization Conditions by Microbatch and Vapor-Diffusion Methods with On-Chip X-Ray Diffraction. *Angew. Chem. Int. Ed.* **2004**, *43* (19), 2508–2511.
(44) Dhouib, K.; Malek, C. K.; Pfleging, W.; Gauthier-Manuel, B.; Duffait, R.; Thuillier, G.; Ferrigno, R.; Jacquamet, L.; Ohana, J.; Ferrer, J.-L.; Théobald-Dietrich, A.; Giegé, R.; Lorber, B.; Sauter, C. Microfluidic Chips for the Crystallization of Biomacromolecules by Counter-Diffusion and on-Chip Crystal X-Ray Analysis. *Lab Chip* **2009**, *9* (10), 1412–1421.
(45) Guha, S.; Perry, S. L.; Pawate, A. S.; Kenis, P. J. A. Fabrication of X-Ray Compatible Microfluidic Platforms for Protein Crystallization. *Sens. Actuators B Chem.* **2012**, *174*, 1–9.
(46) Kisselman, G.; Qiu, W.; Romanov, V.; Thompson, C. M.; Lam, R.; Battaile, K. P.; Pai, E. F.; Chirgadze, N. Y. X-CHIP: An Integrated Platform for High-Throughput Protein Crystallization and on-the-Chip X-Ray Diffraction Data Collection. *Acta Crystallogr., Sect. D: Biol. Crystallogr.* **2011**, *67* (6), 533–539.
(47) L. Perry, S.; Guha, S.; S. Pawate, A.; Bhaskarla, A.; Agarwal, V.; K. Nair, S.; A. Kenis, P. J. A Microfluidic Approach for Protein Structure Determination at Room Temperature via On-Chip Anomalous Diffraction. *Lab Chip* **2013**, *13* (16), 3183–3187.
(48) M. Schieferstein, J.; S. Pawate, A.; J. Varel, M.; Guha, S.; Astrauskaite, I.; B. Gennis, R.; A. Kenis, P. J. X-Ray Transparent Microfluidic Platforms for Membrane Protein Crystallization with Microseeds. *Lab Chip* **2018**, *18* (6), 944–954.
(49) Heymann, M.; Opthalage, A.; Wierman, J. L.; Akella, S.; Szebenyi, D. M. E.; Gruner, S. M.; Fraden, S. Room-Temperature Serial Crystallography Using a Kinetically Optimized Microfluidic Device for Protein Crystallization and on-Chip X-Ray Diffraction. *IUCrJ* **2014**, *1* (5), 349–360.
(50) Sui, S.; Wang, Y.; W. Kolewe, K.; Srajer, V.; Henning, R.; D. Schiffman, J.; Dimitrakopoulos, C.; L. Perry, S. Graphene-Based Microfluidics for Serial Crystallography. *Lab Chip* **2016**, *16* (16), 3082–3096.
(51) Gicquel, Y.; Schubert, R.; Kapis, S.; Bourenkov, G.; Schneider, T.; Perbandt, M.; Betzel, C.; Chapman, H. N.; Heymann, M. Microfluidic Chips for In Situ Crystal X-Ray Diffraction and In Situ Dynamic Light Scattering for Serial Crystallography. *J. Visualized Exp.* **2018**, No. 134, e57133.
(52) de Wijn, R.; Hennig, O.; Roche, J.; Engilberge, S.; Rollet, K.; Fernandez-Millan, P.; Brillet, K.; Betat, H.; Mörl, M.; Roussel, A.; Girard, E.; Mueller-Dieckmann, C.; Fox, G. C.; Olieric, V.; Gavira, J. A.; Lorber, B.; Sauter, C. A Simple and Versatile Microfluidic Device for

Efficient Biomacromolecule Crystallization and Structural Analysis by Serial Crystallography. *IUCrJ* **2019**, *6* (3), 454–464.
(53) Monteiro, D. C. F.; Vakili, M.; Harich, J.; Sztucki, M.; Meier, S. M.; Horrell, S.; Josts, I.; Trebbin, M. A Microfluidic Flow-Focusing Device for Low Sample Consumption Serial Synchrotron Crystallography Experiments in Liquid Flow. *J. Synchrotron Radiat.* **2019**, *26* (2), 406–412.
(54) D. Greaves, E.; Manz, A. Toward On-Chip X-Ray Analysis. *Lab Chip* **2005**, *5* (4), 382–391.
(55) Hubbell, J.H. Bibliography of Photon Total Cross Section (Attenuation Coefficient) Measurements 10 EV to 13.5 GeV, 1907-1993. *NISTIR 5473* **1994**.
(56) Catalano, R.; Perozziello, G.; Simone, G.; Candeloro, P.; Gentile, F.; Coluccio, M. L.; Pardeo, F.; Burghammer, M.; Cuda, G.; Riekel, C.; Di Fabrizio, E. Optimized Fabrication Protocols of Microfluidic Devices for X-Ray Analysis. *Microelectron. Eng.* **2014**, *124*, 13–16.

Chapter 3

Instrumental developments

Chapter 3

Instrumental developments

3.1 Introduction

In Chapter 1, several conventional methods (vapor diffusion, batch, dialysis, FID) for protein crystallization were described along with their benefits or drawbacks and their range of applicability. Crystallization is the first major step in X-ray protein crystallography applied to elucidate the atomic structure of protein targets and their mechanism of action in living organisms. However, finding the optimal crystallization conditions for each protein target is a demanding, time-consuming task adding extra cost, time and labor to the study of these high-valued biological macromolecules. The knowledge of the phase diagram of each protein is a fundamental necessity for rationalizing protein crystallization and facilitating the screening for favorable crystallization conditions. The kinetic trajectory of the dialysis crystallization method (Figure 1.1.3) allows the exploration of the phase diagram through a precise and reversible control over the crystallization conditions. The dialysis kinetics can be modulated by the MWCO of the membrane, the volume of the system and the precipitant concentration, while multiple crystallization conditions can be explored by using the same protein sample. Apart from searching for crystallization conditions, optimizing these conditions to yield well-diffracting protein crystals is an additional step in the query of unraveling the 3D protein structure. Developing techniques to adjust the uniformity of the crystal population and tailor their size and morphology is significant for growing well-diffracting crystals. Dialysis combined with temperature control can be used to decouple nucleation and crystal growth and facilitate the investigation of the phase diagram[1,2].

In Chapter 2, I described the development of microfluidic chips for the on chip crystallization of soluble and membrane proteins with the microdialysis method compatible with *in situ* X-ray diffraction experiments[3,4]. The dialysis chip was designed to combine the advantages of the microfluidic technology, such as minute sample consumption (< 1 µL) and fine control over transport phenomena, and the dialysis protein crystallization method allowing an accurate tuning of the experimental parameters. A small piece of RC dialysis membrane with various MWCOs is incorporated within the two layers of the chip separating the fluidic channel for circulating the crystallization solution from the protein reservoir. The MWCO of the membrane is chosen accordingly to enable the diffusion of the precipitant's molecules from the fluidic channel towards the protein reservoir and to retain the protein sample in the reservoir. The diffusion of the precipitant across the membrane is driven by a concentration difference (Δc) and results in increasing the supersaturation of the protein solution and inducing nucleation. Several model soluble and membrane proteins were crystallized on chip via microdialysis and used for *in situ* X-ray diffraction experiments at room temperature in various synchrotron sources and the results will be discussed in Chapter 4.

In the current chapter, I am going to elaborate on the development of a visualization platform (MicroCrys), one of the main goals of this project whose overall ambition is to optimize and rationalize protein crystallization. MicroCrys has been developed to automate

the on chip protein crystallization via microdialysis for the investigation of phase diagrams, integrating chemical composition and temperature control. The MicroCrys platform is a miniaturization of two other macro-scale pipelines developed and operating in our laboratory over the past years, for screening and optimizing protein crystallization by mapping temperature or precipitant concentration phase diagrams[2,5]. The first generation apparatus consists of temperature-controlled, multiple wells designed to grow large crystals for neutron crystallography with the batch crystallization method[5]. Quartz cells of 25 - 1000 µL volume are used in a single-well or multiple-well motorized carousel attached on a brass support. The temperature is regulated with Peltier elements reaching a range of 233 – 353 K with an accuracy of ± 0.1 K. The apparatus can be mounted in a microscope table with an adapted support facilitating real-time visualization and recording. Later on, temperature-controlled dialysis buttons with a volume of 25 – 200 µL were designed for the same instrument[2]. The stainless steel dialysis buttons include a polycarbonate window at the bottom for visualization and they are attached on brass supports fitting in wells of the motorized carousel. This instrument is a semi-automated approach in the sense that the precipitant solution is introduced manually with a pipette in the dedicated reservoir. In order to fully automate the procedure, a dialysis setup with a flow cell was designed[2]. The protein chamber (15 µL) is separated from the reservoir by a dialysis membrane of the appropriate MWCO, featuring a polycarbonate window for real-time visualization. The reservoir is connected to a pressure-driven system for automated mixing and circulation of the crystallization solution, functioning as a flow cell. The dialysis setup is supported on a platform (OptiCrys) where thermal regulation is achieved with two Peltier modules. A graphical user interface was designed with LabVIEW for visualization and recording and for control over the experimental parameters (temperature, chemical composition, mixing and flow of the crystallization solution)[6]. This instrument has been used to explore the temperature – precipitant concentration phase diagram and control the crystal size and morphology of various proteins[7]. Crystals of several proteins grown with these two instruments have been used for neutron and X-ray diffraction measurements.

3.2 MicroCrys: a platform to automate on chip crystallization

The MicroCrys platform includes a support for the chips compatible with the dimensions and the mechanical constraints of the flexible, polymeric materials composing the microfluidic devices, a digital camera with automated focus for real-time monitoring and image recording during the evolution of the crystallization process and a fluidic system for mixing and circulating the crystallization solution within the chips under constant flow or under constant differential pressure (ΔP) between the inlet and the outlet port of the fluidic channel. The support is motorized and allows stepwise movement along all three axes in a Cartesian coordinate system (x, y, z) enabling the scanning of the microchips for detecting the protein crystals within the protein reservoir. Moreover, the parts of the platform are controlled by a custom-built software designed to manipulate the movement of the support and the focus of the camera, to record images and to initialize or stop the mixing and the flow of the crystallization solution within the fluidic channel of the chips. A bench, provided by Dr. Jean-Luc Ferrer (Synchrotron Group, IBS, Grenoble), has been manufactured by NatX-ray to support

commercial 96-well crystallization plates (SBS standard) for real-time visualization of the drops within the wells. We were allowed to modify it and expand its use for crystallization experiments on microchips. The developments of the instrumentation and the software were accomplished in collaboration with Dr. Yoann Sallaz-Damaz (Synchrotron Group, IBS and BM07-FIP2, ESRF, Grenoble). The visualization platform is shown in Figure 3.2.1.

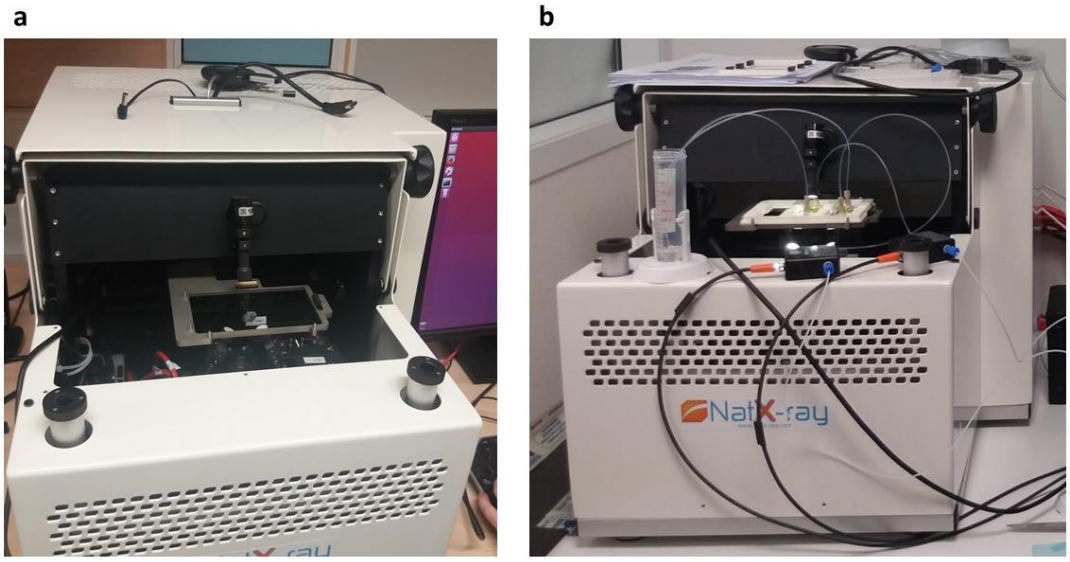

Figure 3.2.1: (a) The visualization bench manufactured by NatX-ray for on plate protein crystallization. (b) The MicroCrys platform developed for automated on chip protein crystallization. The 3D printed white support for the microchips is positioned on the metallic sample holder of the bench.

Specifically, the platform contains a metallic support for 96-well plates or the microfluidic chips (Figure 3.2.2 (a)). The dimensions of this unit are suitable for supporting a typical 127 mm × 85 mm CrystalQuickX crystallization plate (Greiner). Two M-404 precision linear stages and one M-232 high-resolution linear actuator with direct current (DC) motor (Physik Instrumente, PI) are used for the spatial movement of the metallic support along the three axes. The M-404 linear stages have a travel range from 25 – 200 mm and minimum incremental motion of 0.1 µm, while the M-232 actuator has a travel range of 17 mm and minimum incremental motion of 0.1 µm. The linear stages and the DC motor are controlled by three 1-axis C-863 Mercury servo controllers (PI). The linear stages and the Mercury controllers are shown in Figure 3.2.2 (a) and Figure 3.2.2 (c), respectively. The unit of the platform adjusted for visualization is an inverted UEye color, Internet camera (IDS) with a resolution of 1280 × 1024 pixels (Figure 3.2.2 (b)). The camera is placed under the metallic support for the microfluidic chips. A stepper motor controls the microscope zoom of the camera. A 1-axis networkable C-663 Mercury controller (PI,) is used for the stepper motor. Two LED (light emitting diode) lights (CCS HLV2 series, white LED) are attached beneath the metallic support of the platform, near the UEye camera (Figure 3.2.2 (b)), and one LED light is

located above the support, as shown in Figure 3.2.2 (a). The two front lights allow visualization through reflection and the back light visualization through transparency.

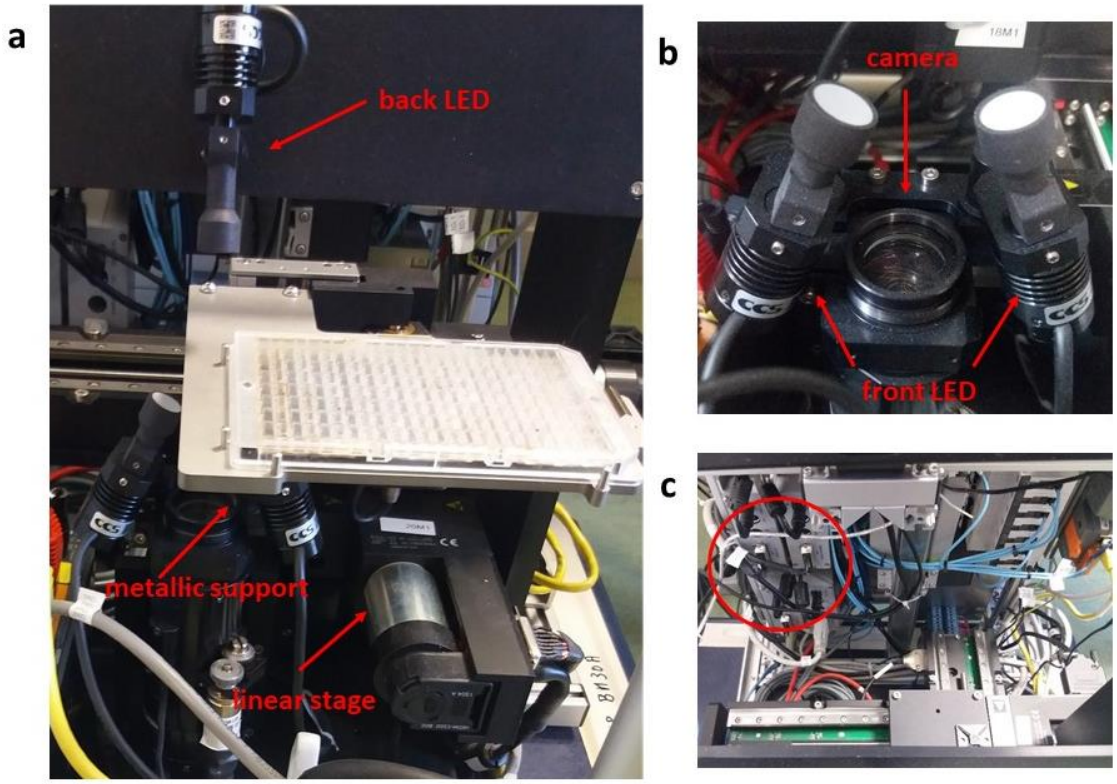

Figure 3.2.2: Components of the visualization platform. (a) The metallic support for 96-well plates or microfluidic chips, the M-404 linear stage and the back LED light, (b) the inverted UEye color camera with the two front LED lights and (c) the C-863 Mercury servo controllers.

In Figure 3.2.1 (b) the platform is shown while being used for on chip protein crystallization experiments. For the on chip crystallization experiments, a sample support has been designed with SolidWorks and was printed using 3D printing. The 3D printed sample support can be mounted directly on the metallic support of the platform and it can carry up to three microchips simultaneously[3]. In Figure 3.2.1 (b) two microchips are mounted on the sample support (white color polymeric support) bearing the appropriate connectors and PTFE tubes for fluid handling with the external pressure-driven system. The external dimensions of the support are equal to the dimensions of the commercial 96-well crystallization plates CrystalQuickX (SBS standard), as shown in Figure 3.2.3 (b), while each one of the three slots (Figure 3.2.3 (a)) designed for the placement of the chips has the standard dimensions of a microscope glass slide (3 x 1 in). It should be reminded at this point, that the PMMA foil used as a substrate for the NOA 81 sticker during the fabrication of the devices (Section 2.2.1) has the same dimensions as a microscope glass slide. The same sample support can be mounted in macromolecular crystallography beamlines compatible with in plate crystallography measurements and can be used to hold the chips in front of the X-ray beam for *in situ* X-ray

diffraction experiments (Chapter 4). The use of the 3D printed sample support contributes significantly to the automation of the entire procedure, from the on chip crystallization experiments performed with the MicroCrys platform to the *in situ* X-ray diffraction experiments at synchrotron beamlines because the sample changers of the beamlines are designed to manage crystallization plates.

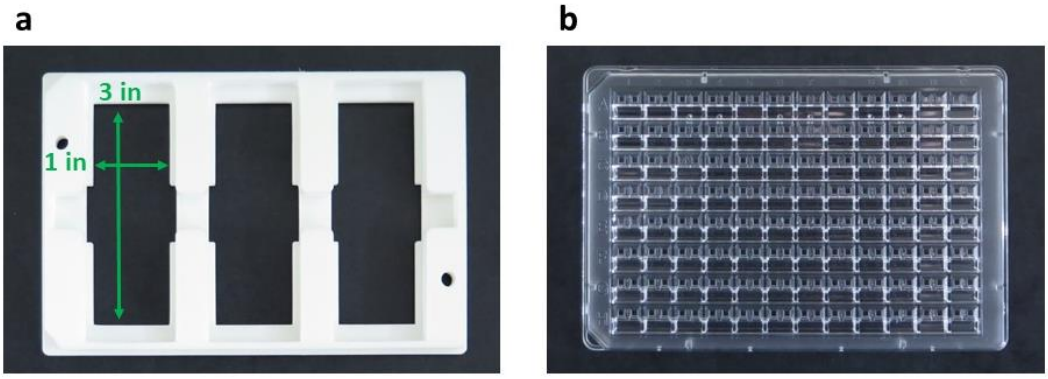

Figure 3.2.3: The 3D printed support for microchips (a) has the same external dimensions as the 96-well crystallization plate CrystalQuickX (b). The support can carry up to three chips simultaneously and each position has the dimensions of a microscope glass slide (3 x 1 in).

3.2.1 Electronics and programming

The three C-863 and the C-663 Mercury motor controllers are connected in serial connection to an Ethernet convertor. An Ethernet Modbus controller controls the three LED lights. The operational system (OS) of the visualization platform is Windows 10. The bench designed by NatX-ray was operating in Linux. However, in order to operate the bench with the requirements and specifications of the MicroCrys platform, the original control system had to be changed completely and all units were re-programmed to run in Windows 10. Currently, a program developed in LabVIEW (National Instruments, NI) controls all the units of the platform (inverted camera, LED lights and motorized controllers). The objective of developing the LabVIEW program was to create a user-friendly interface where all the separate units of the MicroCrys platform can be adjusted and controlled in an easy and automated way, while permitting further manipulations or additions without interfering on the functionality of the main program.

The main VI (Virtual Instrument) of the LabVIEW software includes three windows, each one dedicated to a specific manipulation. The front panel of the main VI is illustrated in Figure 3.2.4 where the interface windows named “Display”, “Image Record” and “μfluidic” are distinguished. The specific screenshot relates to the “Display” interface dedicated to manipulating the parameters of visualization. The user can adjust the intensity of the front and back LED lights to the desired luminosity, as well as the zoom of the inverted camera. In

the example shown in Figure 3.2.4, the camera has been zoomed up to 75 % in order to inspect the fluidic channel and part of the protein reservoir of a 0.1 µL dialysis chip. The focus is adjusted externally by rolling the central wheel of the computer's mouse. Adjusting the focus can take up to several seconds especially when trying to accurately locate the micro-patterns of the chips, because the zoom level used for the experiments renders the depth of field very low. For this reason, an "off/on" button has been added on the "Display" interface for controlling the focus with higher accuracy. When the button is clicked (as in Figure 3.2.4), the accurate focus mode is "on" and rolling the mouse wheel allows for a precise control. On the contrary, when the button is not clicked, the accurate focus mode is "off" and a single roll of the mouse wheel can change the focus rapidly. This operation is very useful when screening the entire surface of the microchip or when localizing in a specific compartment, as for example the protein reservoir. Finally, the spatial movement of the metallic support along the x- and y-axes is achieved by clicking the mouse on the targeted direction on the image displayed on the "Display" interface. For example, by clicking on the upper most point of the image displayed in Figure 3.2.4, the motorized stage will move accordingly and the view of the whole protein chamber will be revealed. If the user needs to examine the fluidic channel across all its length, clicking successively on the lower point of the image moves the stage accordingly. The same procedure is applied for investigating the image on the left or right direction.

The "Image Record" interface of the main VI, shown in Figure 3.2.5, is designed for handling the recording parameters. First, the user has to define the directory for image recording and then choose the frequency (in seconds) at which images are recorded in the pre-defined directory. In the example shown in Figure 3.2.5, one image is recorded every 1000 s. Moreover, the software offers the possibility to turn on the LED lights only during recording to prevent overheating the solution within the protein reservoir from continuous lighting. This can be achieved by selecting the "Light on only during recording" button. With this functionality, even if the front- and back-lights are set to zero value in the "Display" panel, they will be turned on while recording an image. Finally, once all the parameters for recording are regulated, the user has to press the "Start" button to initiate the image recording at the desired time intervals. If recording is no longer required during the course of the experiment, pressing the "Stop" button can cease it.

Figure 3.2.4: The front panel of the main VI of the LabVIEW software developed to control all the separate units of the MicroCrys platform. The main interface includes three windows named “Display”, “Image Record” and “µfluidic”, each designated to specific functionalities of the platform. The “Display” interface shown here is dedicated to manipulating the parameters of visualization.

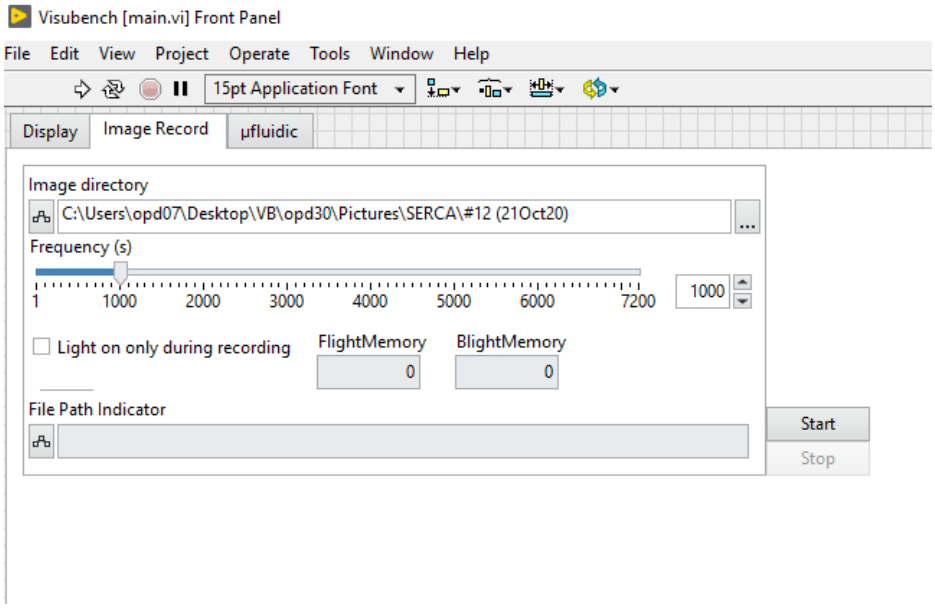

Figure 3.2.5: The “Image Record” interface of the main VI designed for handling the recording parameters with MicroCrys.

A flowchart of the LabVIEW code divided in three modules is shown in Figure 3.2.6. The first module (INIT) initializes the communications of all the units of the platform. The lights and the motors are initialized with an Ethernet Modbus communication protocol and the camera with a proprietary protocol requiring a driver supplied by the manufacturer. Once the communication is initialized properly, the second module (RUN) is activated. This module is related to the operation of the camera, the recording and lighting parameters as well as the spatial displacement of the metallic support through the motorized stepper controllers. Within the operations of this module the motors are controlled by the computer's mouse (left click on the screen or rotation of the mouse wheel), the intensity level of all the LED lights is adjusted through the front panel of the main VI on the "Display" interface and the recording parameters are set on the "Image Record" interface. In the block diagram of the LabVIEW code, all the functions of the main code are running in a loop with event check. When the "Exit" button on the graphical user interface is clicked, the third module of the flowchart is activated, terminating the communication for each sub-task of the main program.

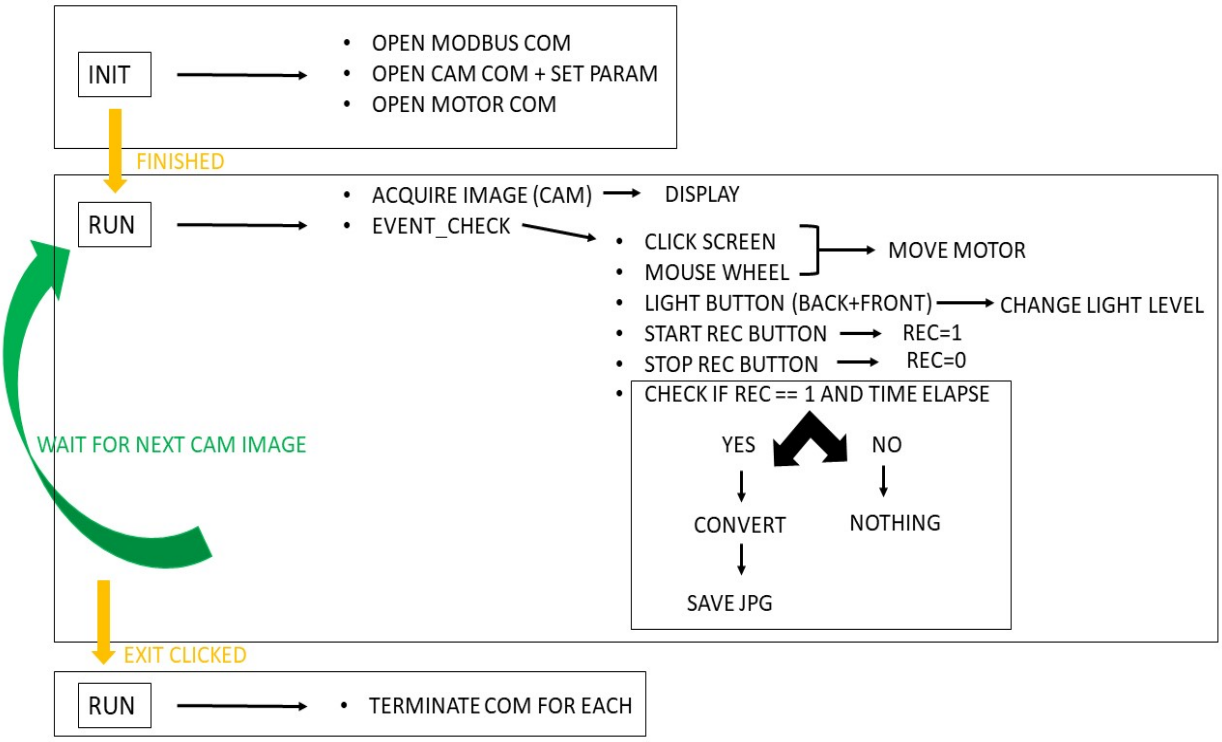

Figure 3.2.6: A flowchart of the LabVIEW program developed for automated operation of the visualization and recording functionalities with the MicroCrys platform.

3.2.2 System for fluid handling

For mixing and circulating the crystallization solution within the channel of the microchip, a pressure-driven flow controller from Elveflow has been incorporated in the MicroCrys platform. The OB1 pressure controller consists of the OB1 base MkIII and the two OB1 MkIII

pressure channels that are used to drive the solutions from pressurized containers into the PTFE tubes connected to the inlet and outlet ports of the microfluidic device. The maximum inlet pressure for the OB1 channels is 2000 mbar. The OB1 controller supports up to four pressure channels. The setup also includes two thermal-based digital MFS4 flow sensors for measuring the flow rate in a range of 1 µL min^{-1} to 1 mL min^{-1}. The flow sensors are bi-directional, and their working principle is based on measuring the temperature through a glass capillary due to the local heating of the flowing solution[8]. One of the flow sensors can be connected prior to the inlet of the microfluidic chip to regulate the flow of the solution as imposed by the pressure-driven controller and the second flow sensor can be connected right after the outlet port of the chip. If knowing the outlet flow rate is not essential for the experiment, the second flow sensor can be used to regulate the inlet flow rate of a second chip allowing multiple on chip crystallization experiments to be performed simultaneously. In fact, flow sensors can be added at any point along the direction of the flow where the accurate measurement or regulation is necessary. This equipment is sufficient to perform experiments when the crystallization solution is prepared manually by mixing the buffer and precipitant solutions in advance and the pressure channels are used to circulate the solution from the pressurized container (50 mL Falcon tubes) into the fluidic channel of the chip. A schematic illustration of this operation is shown in Figure 3.2.7. In our case, the OB1 controller has two pressure channels that can be used independently to circulate a solution in two different chips; therefore, two crystallization experiments can be performed simultaneously.

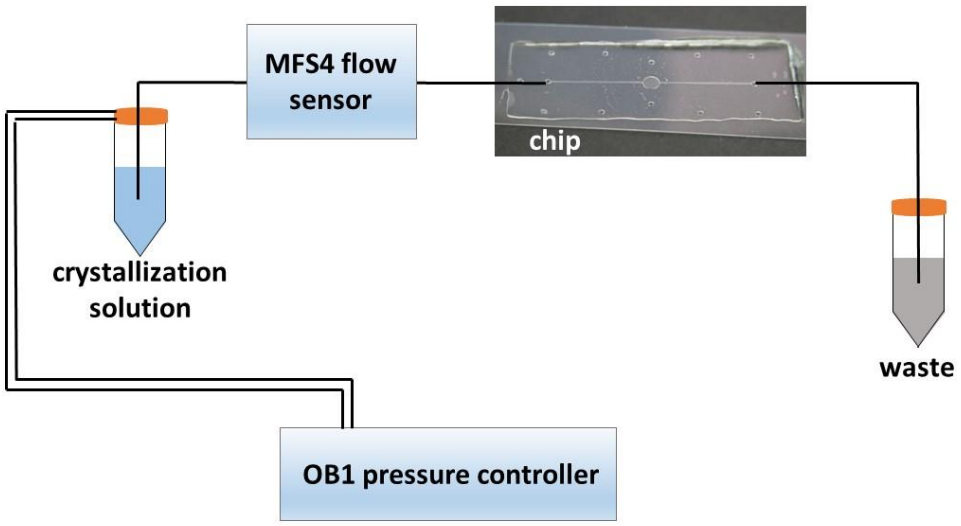

Figure 3.2.7: Operation of the OB1 pressure controller (Elveflow) for injecting a pre-mixed crystallization solution in the channel of the microfluidic chip. A flow sensor is added prior to the inlet point of the chip.

Apart from manually preparing the crystallization solutions by mixing all the components in advance, there is the possibility to automate the procedure with the MUX Distributor (Elveflow). The distributor of our choice was the 6 to 1 model including six inlets and one outlet port. The device has been designed to add sequentially solutions in a mixing reservoir. A

flowchart of the procedure is illustrated in Figure 3.2.8. Solutions (salts, buffers, etc.) are shown in Figure 3.2.8 with numbers 1 – 4 inside the reservoirs. The solutions are injected one by one through the MUX Distributor and a microfluidic valve (MPV 3/2 from Elveflow) into an intermediate reservoir, in order to prepare the crystallization solution. A flow sensor (MFS4) is regulating the flow rate of the solutions prior to their injection within the intermediate reservoir. The crystallization solution within the intermediate reservoir is then pressurized through the OB1 pressure controller to flow towards the inlet of the microfluidic chip. Prior to the inlet of the microfluidic chip, another flow sensor (MFS4) is connected to regulate the flow rate of the crystallization solution. Figure 3.2.9 shows all the parts of the fluidic system as have been set next to the MicroCrys platform.

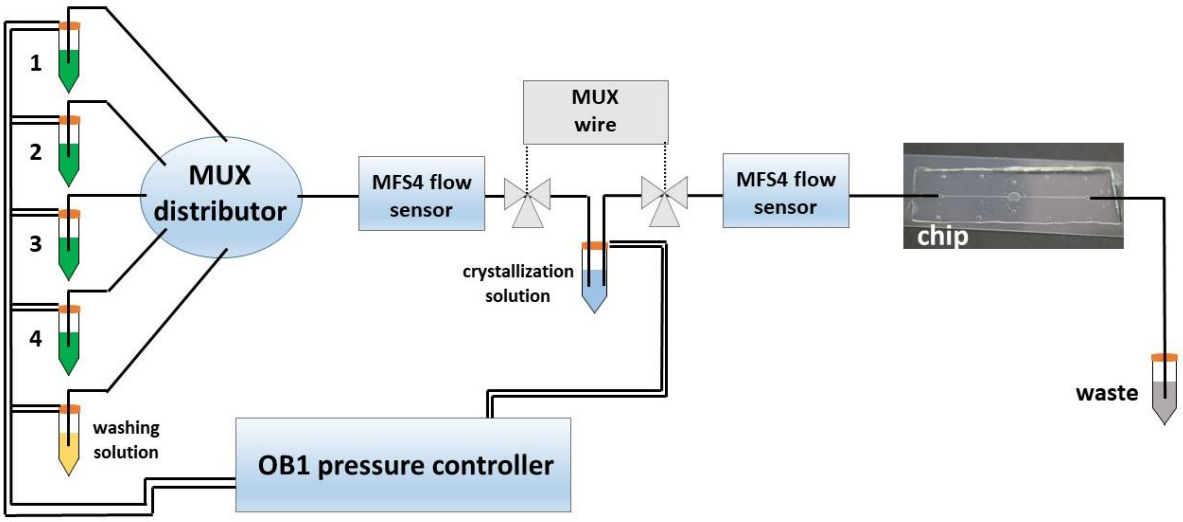

Figure 3.2.8: Schematic illustration of the OB1 pressure controller and the MUX distributor (Elveflow) for mixing components (salts, buffers, etc.) of the crystallization solution by sequential injection into a mixing reservoir. Flow sensors are added at points along the direction of the flow where the accurate measurement or regulation is necessary.

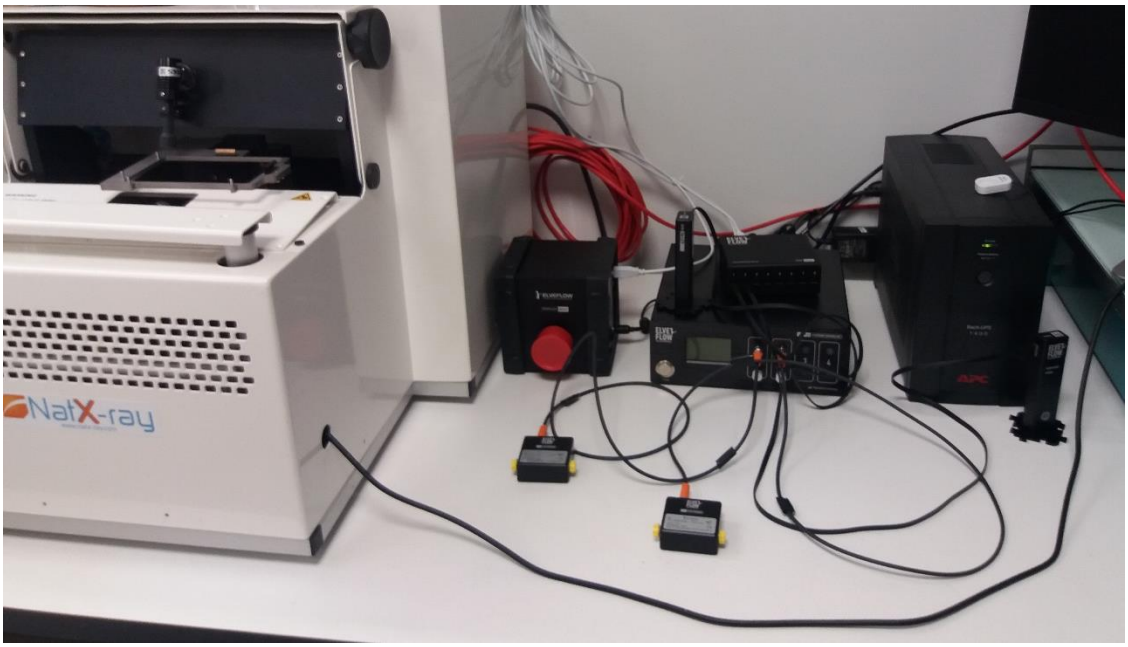

Figure 3.2.9: Next to the MicroCrys platform, from left to right, are shown the MUX distributor, the OB1 pressure controller and the two MFS4 flow sensors of the Elveflow fluidic system.

Elveflow has developed the ESI (Elveflow Smart Interface) software for an interactive, user-friendly control of all the instruments. The software allows the user to connect up to sixteen different instruments and manipulate their functional parameters through the user interface, such as flow rate, pressure value, acquisition time and frequency, units, or recording parameters, such as graphical display and data recording path. A screenshot of the two pressure channels used for the experiments conducted with the MicroCrys platform as displayed on the ESI user interface is shown in Figure 3.2.10. The panel of the pressure channels can be used to set a pressure (in mbar) or flow rate (in µL min^{-1}) and displays the actual pressure and sensor value. Each pressure channel can be configured independently, while the values of the pressure regulators and the flow sensors are shown in real time in the ESI Graph window (Figure 3.2.10, bottom right side). Moreover, the pressure of the regulator and the flow rate of the sensor can be constant at the set value or it can be adjusted using several built-in profiles, like the ramp profile where the pressure increases linearly to reach the set value in a defined time interval. In fact, a PID (Proportional – Integral – Derivative) algorithm is used to adapt the actual pressure to the set value and custom profiles can be made by tuning the parameters of the PID regulation. A PID algorithm calculates an error value defined by the difference between a set point and a measured value and applies a correction based on proportional, integral or derivative terms. For example, the proportional or gain parameter of a PID algorithm of the flow sensor improves the response time of the system and the integral parameter can regulate the instabilities of the flow rate. However, each one of the PID parameters may induce instabilities on the others, therefore, fine-tuning the PID parameters is crucial for the optimal response of the system (controller, regulator, sensor, etc.).

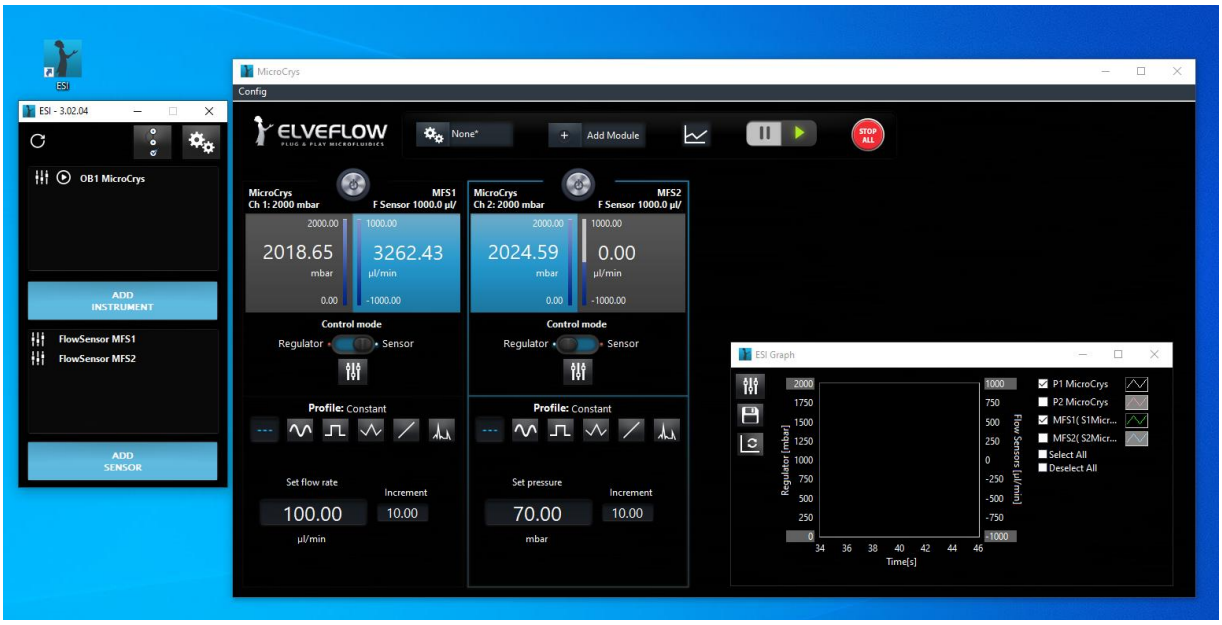

Figure 3.2.10: The ESI (Elveflow Smart Interface) software illustrating the two pressure channels used for the on chip crystallization experiments conducted with the MicroCrys platform.

Our aim has been to integrate the feature functionalities of the ESI software in the LabVIEW program developed for MicroCrys. The “µfluidic” interface of the main VI (Figure 3.2.4) has been dedicated to the integration of the Elveflow fluidic system. Elveflow provides SDK (Software Development Kit) packages in various programming languages (C++, MATLAB, Python or LabVIEW) for Windows OS only, containing all the functions for a customized software development. The LabVIEW libraries contain example VIs for the OB1 pressure controller, the MFS flow sensors and the MUX distributor. The VI of the OB1 pressure controller has been added to the “µfluidic” interface and a screenshot is shown in Figure 3.2.11. The workflow of the OB1 VI is summarized in four modules related to the configuration of the controller, the calibration, the main working loop and the termination of the operation. First, the instrument is initialized and the flow sensors are connected to each one of the four pressure channels. Then the controller is calibrated and the execution of the main working loop starts. In the main loop, the user can set the pressure value to all the channels at once or to each channel separately. The main working loop includes also operations related to data acquisition, displaying and recording. A “STOP” button in the front panel ensures the proper termination of the working loop. Once the VIs for the MFS flow sensors and the MUX distributor are incorporated in the LabVIEW program of MicroCrys, then all the actions related to visualization and fluid handling can be accomplished through a single graphical user interface.

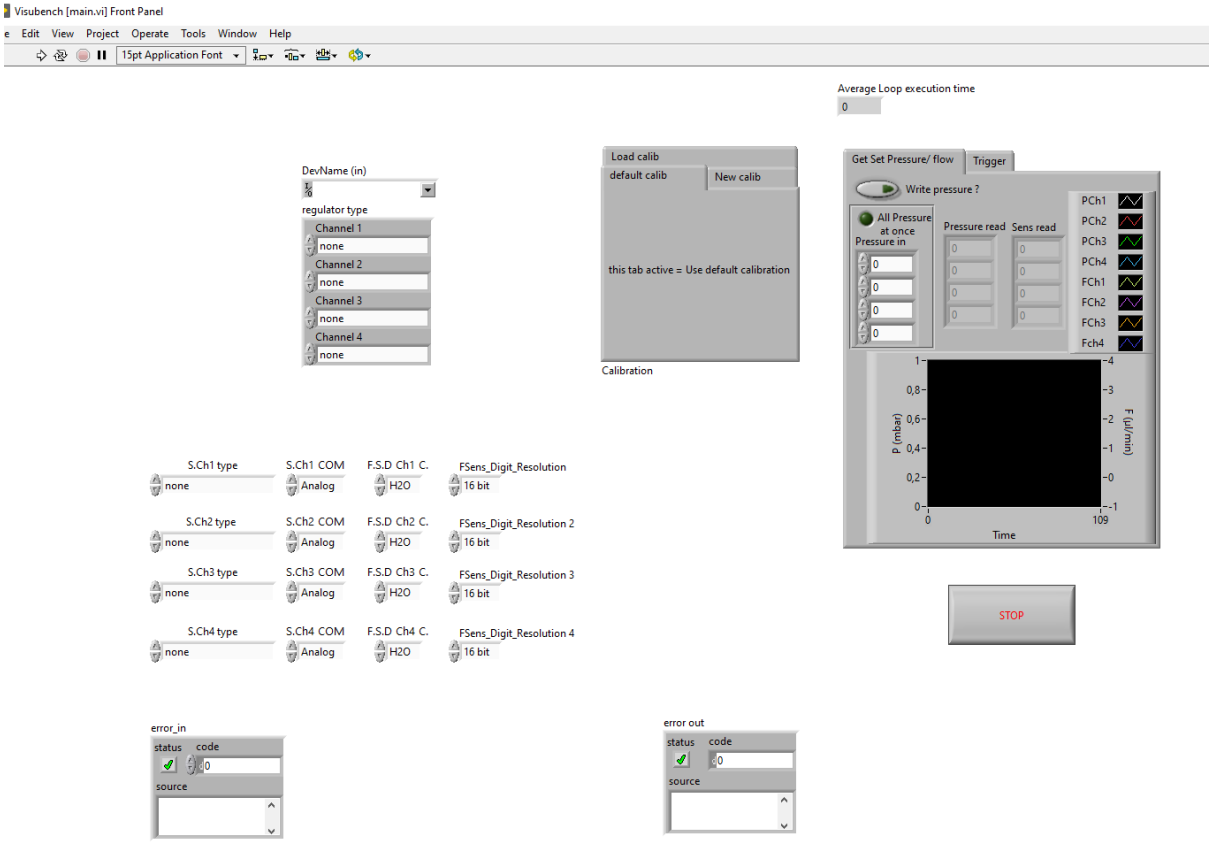

Figure 3.2.11: The LabVIEW VI of the OB1 pressure controller added to the "µfluidic" interface of the main LabVIEW program developed for MicroCrys.

3.3 Thermal regulation

3.3.1 Thermal transfer in microfluidics

Temperature is an important parameter in the crystallization of biological macromolecules affecting the solubility of the protein sample, as explained in Chapter 1 (Section 1.1.3). Temperature control combined with the dialysis method can be used to decouple nucleation and crystal growth and facilitate the investigation of temperature and/or precipitant concentration phase diagrams. However, exploring the full potential of precise temperature control as a crystallization variable in the microfluidic scale is quite challenging. Heat transfer mechanisms, in the macro- or micro-scale, are ruled by complex physical and thermodynamic concepts, especially when combined with the presence of fluid flow or electronic components. The fundamental notions on thermal transfer in microfluidics are provided in the book of P. Tabeling[9].

A review by Miralles *et al*.[10] on thermal regulation in microfluidic systems designates the developed applications in three main categories: external heating, integrated heating or heating through electromagnetic radiation[11]. For the two first approaches, a heating source is

used for thermal transfer towards the fluid, while for the third approach the fluid is heated in the bulk without using any source. Thermal regulation and control in microfluidic applications can be described either in terms of temperature profile or in terms of temperature range. External heating techniques operate with commercial heaters for pre-heating a fluid prior to its use in microfluidic devices or the thermal components are integrated in the microfluidic application. A widely applied technique is the use of thermoelectric components, such as the Peltier modules[12]. The temperature profile achievable with these techniques can be homogeneous throughout the position of interest or a constant temperature gradient can be generated with high accuracy. For example, Khandurina *et al*.[13] developed an integrated system for rapid PCR (polymerase chain reaction) analysis based on the thermal cycle of two Peltier modules coupled with microchip gel electrophoresis device achieving a heating or cooling ramp rate of 20 – 30 °C s^{-1}. Apart from PCR applications, Peltier junctions have been used with PDMS microfluidic devices for high resolution imaging of cells[14]. Fast (10 s) temperature switching between 5 and 45 °C was used to study temperature-sensitive gene mutations of the fission yeast *Schizosaccharomyces pombe*. The heat produced by the Peltier elements was dissipated by water circulation in the top layer of the multi-layered chip. Instead of using water cooling, Yang *et al*.[15] developed a system for dissipating the heat from the Peltier elements through aluminium cooling fins and two cooling fans achieving heating and cooling rates of 7 – 8 °C and 5 – 6 °C, respectively.

Linear temperature profiles in PDMS-based microfluidic devices were generated either with pre-heated liquids through standard laboratory water bath circulators (5.8 °C mm^{-1} gradient)[16] or Peltier elements and a copper block for heat dissipation (13.75 °C mm^{-1} gradient)[17]. Laval *et al*.[18] used temperature gradients generated through external Peltier elements located below a silicon wafer to screen two-dimensional solubility phase diagrams. They fabricated a PDMS device to store hundreds of droplets of nL volume containing a solution with gradual variation of the solute concentration. Crystallization in the droplets was induced by rapid cooling and a temperature gradient (0.7 °C mm^{-1}) along the channel of the chip was used to eventually dissolve the crystals and map-out a concentration vs. temperature phase diagram and localize the solubility curve. However, temperature gradients can be produced by integrating resistive thermal components in the microfluidic device[19] or by injecting and polymerizing a conductive silver-filled epoxy within a microfluidic channel dedicated only to cooling[20].

Integrated heating or cooling techniques are based on the thermal transfer from a system integrated within the microfluidic device towards the fluid under study. Joule heating is applied through conductive materials, as for example the silver-filled epoxy mentioned above, being part of the microfluidic device or separate thermal components or metal wires[21] can be assembled with the chip. Moreover, endothermic or exothermic chemical reactions within the microfluidic channels are characterized as integral processes for temperature control. Guijt *et al*.[22] used the endothermic evaporation of acetone to cool down a microchannel and the exothermic dissolution of sulfuric acid in water for heating.

Astier and Veesler[23] highlighted the significance of temperature as a crystallization variable with practical examples on the impact of temperature on protein phase separation and crystallization. HEWL was crystallized on chips fabricated from silicon wafers with chamber arrays[24]. A constant temperature gradient between 12 – 40 °C was maintained across the silicon substrate with two Peltier modules and a heat sink with cooling fins was used for heat dissipation. The HEWL crystals grown on chip with temperature control were used for X-

ray diffraction data collection at room temperature and diffracted at 1.78 Å resolution. Teychené and Biscans[25] developed glass microfluidic devices for on chip crystallization of organic molecules in organic solvents and relative studies on the nucleation kinetics. Supersaturation was achieved either through mass transfer or thermal gradient generated with two Peltier elements. The authors studied the crystallization of eflucimibe in droplets of octanol generated in water[25,26] and the liquid-liquid phase separation of ibuprofen in organic solvents partially miscible with water[25].

In this study, we used the external approach based on thermoelectric Peltier modules for the thermal regulation and control of the protein reservoir of the microchip where crystallization occurs. The two prototypes, the separate components involved in thermal regulation and a graphical user interface designed for automation and integration of the thermal system into the MicroCrys platform are described in the following sections.

3.3.2 Components for thermal regulation

3.3.2.1 The programmable controller

The TC-XX-PR-59 (Laird Technologies) is a programmable temperature controller designed for reversible control of thermoelectric assemblies (like Peltier elements) that require accuracy and precise control of the temperature. The controller can regulate the temperature in cooling and heating modes, while the user can configure the regulation mode that can be selected among several options (power, PID, on/off or algorithm mode). The temperature range for thermal regulation is from -20 °C to + 100 °C with the standard NTC (negative temperature coefficient) type sensor and the accuracy is 0.05 °C. The TC-XX-PR-59 controller can be configurated and used with RS–232 interface, a standard for serial communication and transmission of data. The controller features two programmable fan outputs, an alarm output relay, as well as outputs for LEDs, thermoelectric modules and NTC thermistors or PT1000 sensors (platinum resistance thermometer with a resistance of 1000 Ω at 0 °C). A minimum power supply of 450 W can supply 11 – 30 V voltage to the controller. Moreover, the same company has designed computer software for Windows OS and a graphical user interface can be used to set input parameters and visualize output parameters in real time. The user can also adjust the set point of the controller with an external potentiometer within the range of 0 – 5 V, while the outputs and the alarms are configurable.

The TC-XX-PR-59 controller is operating with a pulse-width modulation (PWM) of the output. PWM is a method of digitally encoding the average power delivered by an electrical signal into discrete quantities[27,28]. The base frequency of the controller is 10 kHz. In fact, PWM techniques are algorithms generating a repeated switching function. The average voltage or current is supplied to the load via the PWM algorithm with repeating on and off pulses with different duration. The duration of the on pulses defines the total power supplied to the load, while the frequency of the switching function can be adjusted according to the load and the application. This switching frequency is described by the duty cycle defined as the time percentage during which the signal is active (on status) in one period[29]. The period (T) of the repetitive signal is the time interval necessary to complete a cycle and it is defined as the reciprocal of the frequency (f): $T = 1/f$. The duty cycle is expressed in a percentage of the pulse

width during active time divided by the period (Eq. (3.1)). For example, a digital signal with a duty cycle of 50 % is half of the time “on” and half of the time “off”. This can be expressed graphically by a wave function (Figure 3.3.1 (a)). A duty cycle of 25 % is shown in Figure 3.3.1 (b) where the pulse is “on” only 25 % of the period.

$$\text{Duty cycle} = \frac{\text{pulse width}}{\text{T}} \cdot 100\ \% \quad (3.1)$$

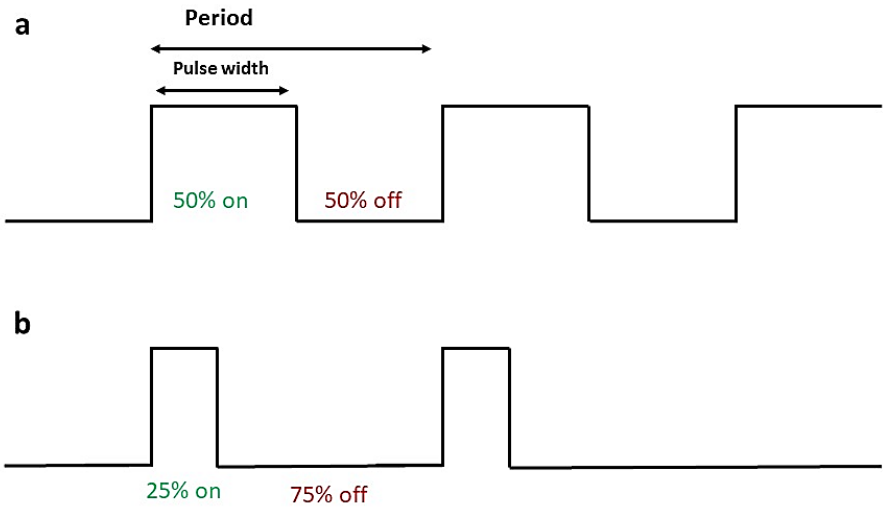

Figure 3.3.1: A duty cycle of (a) 50 % and (b) 25 % for pulse-width modulation algorithms.

Figure 3.3.2 features the connections on the output relays of the TC-XX-PR-59 controller, as specified by the manufacturer. The DC power supply and the thermoelectric (Peltier) module are connected in four flat pin terminals. The NTC temperature sensor is connected in a three-wire KK type Molex terminal. The controller also features three more KK type Molex terminals for two-wire connections available for an alarm, an external potentiometer or a second temperature sensor. Screw terminals are used to connect the RS-232 standard and the fan.

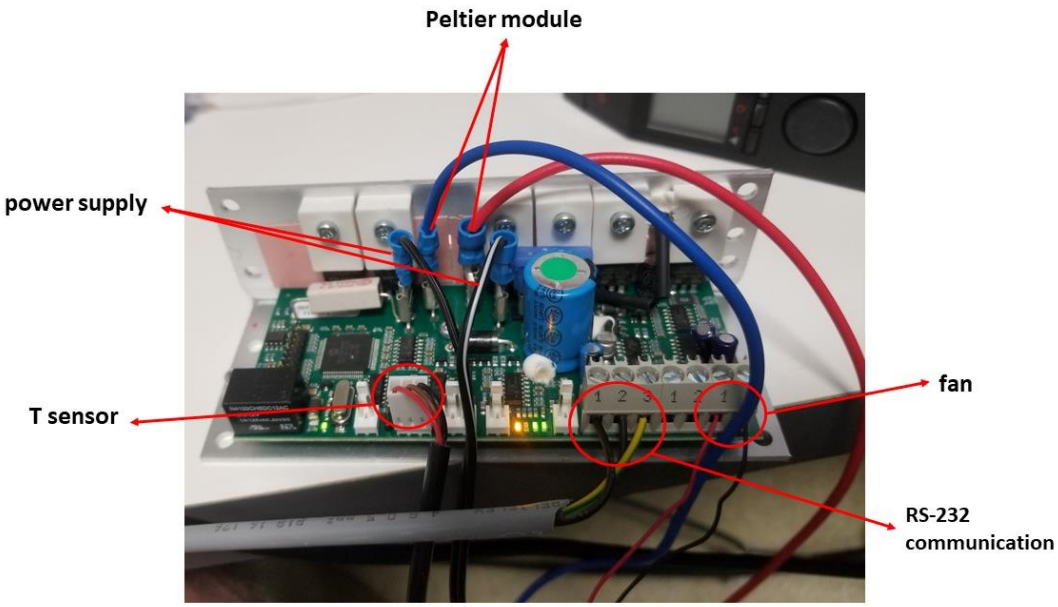

Figure 3.3.2: The output relays for the DC power supply, the Peltier module, the temperature sensor, the fan and the RS-232 communication on the TC-XX-PR-59 reversible controller.

3.3.2.2 The temperature sensor

The first temperature measurements were conducted with the 3 kΩ NTC thermistor manufactured by Vishay. This NTC thermistor consists of a chip soldered between two insulated 0.3 mm nickel leads and it is coated with a solid epoxy lacquer. The thermistor is mounted on the Molex terminal of the controller by soldering its cables. It can operate from 0 °C to 50 °C with an accuracy of ± 0.5 °C. This thermistor didn't respond well to the system developed for thermal regulation of the microfluidic chips, while its head diameter of 2.4 mm is relatively large and comparable to the dimensions of the protein reservoir where the temperature sensor must be fixed.

In order to improve the response time and decrease the dimension of the probe head, we connected a second temperature sensor on the two-wire Molex terminal of the controller. For this application, the J type thermocouple by RS Components was chosen (Figure 3.3.3 (a)), with a head diameter of 2 mm, equipped with a soldered junction connected to earth for fast response time and wires with PTFE insulation. It can measure temperatures in the range of -50 °C to 250 °C with a ± 1.5 °C accuracy and a response time of 5 s. A thermocouple is a temperature sensor consisting of two wires made from different metals, joined together at one end to form an electrical junction. The J type thermocouple is made of one positive, iron wire and one negative, constantan alloy (copper-nickel) wire. The thermocouple produces a voltage as result of the Seebeck effect that can be interpreted to measure temperature. For the case of the J type thermocouple by RS Components, a 5.269 mV output voltage corresponds to 100 °C. The Seebeck effect describes that if two conductive materials are joined together at a point, declared hot point, and there is a temperature difference (ΔT) between the hot point and the tail of the two conductive wires (cold point), then an open

circuit voltage (ΔV) is developed at the cold point[30]. This correlation is expressed in Eq. (3.2) and illustrated in Figure 3.3.3 (b).

$$\Delta V = \alpha_S \Delta T \quad (3.2)$$

Where α_S (V K^{-1}) is the Seebeck coefficient, a temperature-dependent property of conductive materials. According to NIST data, the Seebeck coefficient for the J thermocouple at 20 °C is 51.502 µV $°C^{-1}$ [31].

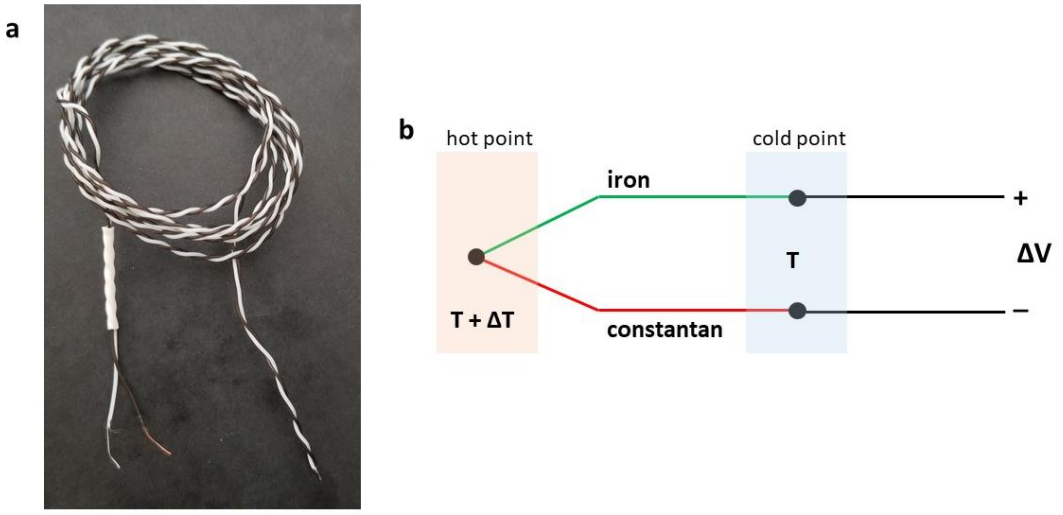

Figure 3.3.3: (a) The J type thermocouple (RS) made of an iron and a copper-nickel alloy wire. (b) Schematic illustration of the Seebeck effect as developed in the J type thermocouple.

There are several types of thermocouples depending on the semiconductive materials of the wires. For example, the J thermocouple used in this study has an iron and a copper-nickel alloy wire, the E thermocouple has a nickel-chromium and a copper-nickel wire and the K type has a nickel-chromium and a nickel-aluminium wire. The various types of thermocouples exhibit different range of temperature and accuracy. For protein crystallization, the temperature range is not very wide as the minimum temperature value required would be approximately 4 °C and the maximum approximately 25 °C. The crucial parameters are the accuracy of the measurement and the response time. For this reason, we chose the J thermocouple having an accuracy of ± 1.5 °C compared to ± 2.2 °C for the K thermocouple (data by RS Components). Figure 3.3.4 shows the graph of voltage (mV) to temperature (°C) for a reference junction at 0 °C, for the J, K and E types as calculated from data acquired from NIST tables based on the ITS-90 standard (The International Temperature Scale of 1990)[31].

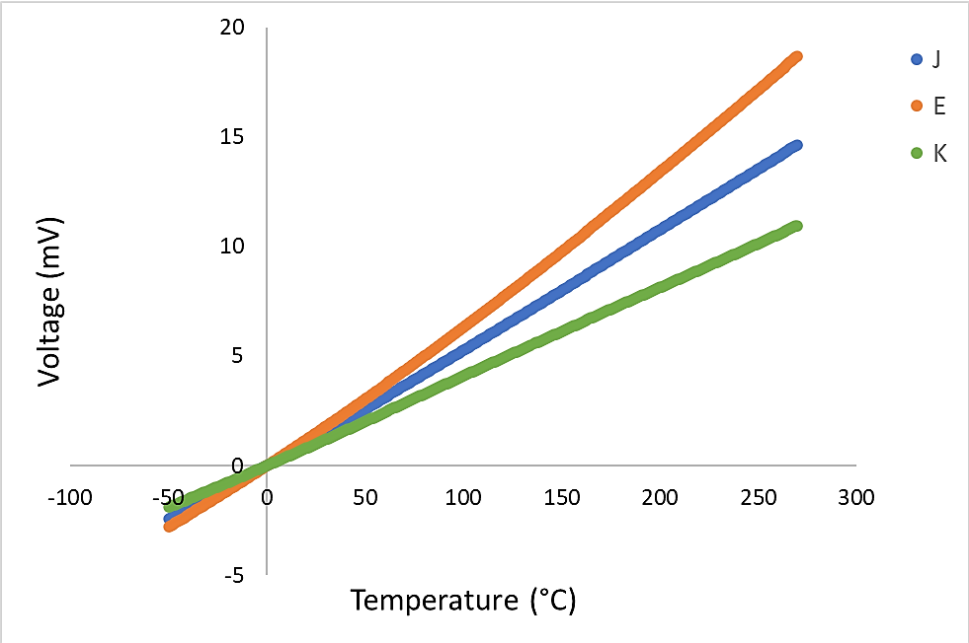

Figure 3.3.4: Voltage (mV) versus temperature (°C) graph for the J, E and K type thermocouples based on the ITS-90 standard.

3.3.2.3 The thermoelectric Peltier module

Apart from the Seebeck effect, another thermoelectric effect implemented in the thermal regulation of the dialysis chips is the Peltier effect. The Peltier effect describes the absorption or release of heat to the environment when an electrical current flows through the junction of two different semiconductive materials[30,32]. This heat exchange is associated to the thermal energy produced by an electrical current being different depending on the material. Thus, when an electrical current flows through the junction of two materials, the difference in their thermal energy is released or absorbed at the junction depending on the direction of the electric current. Typical Peltier modules are doped with n-type (negative) and p-type (positive) semiconductors. In this case, energy is released from the junction when the current flows from the n-type to the p-type doped material or the junction is heated when the current flows the opposite way. This correlation is expressed in Eq. (3.3) and illustrated in Figure 3.3.5 (b).

$$Q = -\Pi_{NP} I \quad (3.3)$$

Where Q (J) is the heat generated at the junction, Π_{NP} (V) is the Peltier coefficient of the junction calculated from the respective Peltier coefficients of the n-type and p-type semiconductors and I (A) is the electric current flow through the junction.

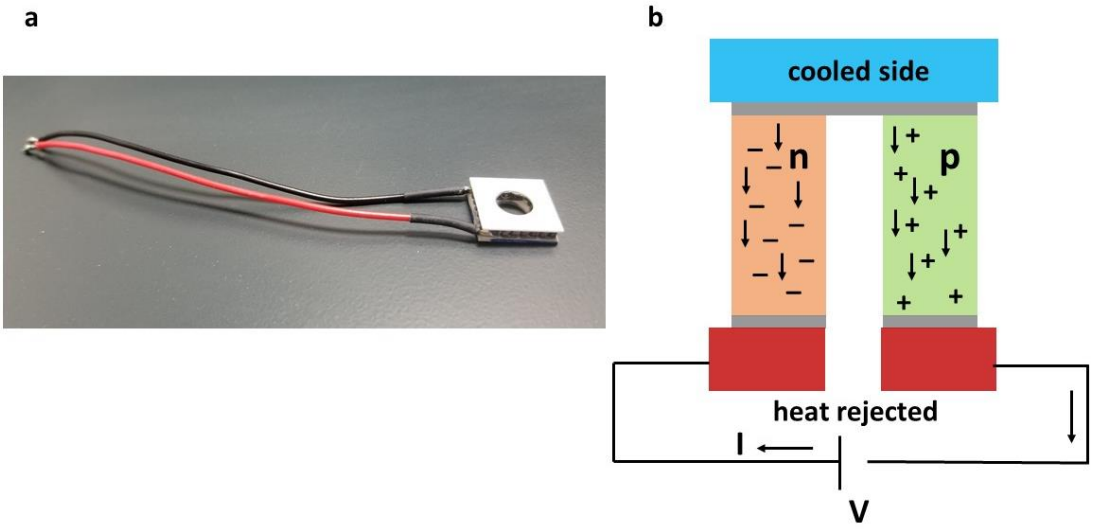

Figure 3.3.5: (a) The Peltier element (Laird Thermal Systems) used for thermal regulation features a 7.21 mm diameter hole allowing visualization of the protein reservoir of the dialysis chip with the MicroCrys platform. (b) Schematic illustration of the Peltier thermoelectric effect for modules doped with n-type and p-type semiconductors.

The thermoelectric module that we chose for temperature control of the protein reservoir of the dialysis chip is the SH10-23-06-L1-W4.5 annular thermoelectric cooler (Laird Thermal Systems), shown in Figure 3.3.5 (a). The ceramics (alumina, Al_2O_3) of the hot and cold side have a circular hole in the center. This design facilitates light protrusion for visualization of the protein reservoir with the MicroCrys platform. The thermoelectric cooler can be placed right below the chip and the hole of the module can be aligned with the protein reservoir allowing visualization and precise thermal regulation. The diameter of the hole is 7.21 mm and the diameter of the protein reservoir for the 0.1 µL and the 0.3 µL chip is 1.5 mm and 2.8 mm, respectively. While in most applications two thermoelectric modules are used to allocate a temperature difference between the hot and cold side, the TC-XX-PR-59 controller is used for reversible control of the thermoelectric assembly. Thus, one module is sufficient in our system since the controller can reverse the side of the module that is in contact with the chip depending on whether we heat the protein reservoir or cool it down. According to the manufacturer, the maximum power (Q) of the SH10-23-06-L1-W4.5 module is 4.6 W when the temperature difference is $\Delta T = 0$ °C, while the power is zero for $\Delta T = 70.5$ °C. The specifications for the optimal operation of the thermoelectric module are given by the company and are summarized in Table 3.3.1. A graph for the operating performance of the Peltier module is provided by the manufacturer in the datasheet (Figure 3.3.6), showing the current (I) versus voltage (V) profiles for various temperature difference (ΔT) values between the hot and cold side.

Table 3.3.1*:* Specifications for the optimal operation of the Peltier module used in this study as provided by the manufacturer (Laird Thermal Systems).

Specifications			
Hot side T	27 °C	35 °C	50 °C
Q_{max} ($\Delta T = 0$)	4.6 W	4.8 W	5.0 W
ΔT_{max} ($Q = 0$)	70.5 °C	73.5 °C	78.8 °C
I_{max} (at ΔT_{max})	3.1 A	3.1 A	3.0 A
V_{max} (at ΔT_{max})	2.5 V	2.6 V	2.8 V
Resistance	0.76 Ω	0.79 Ω	0.85 Ω
Operating T_{max}	80 °C		

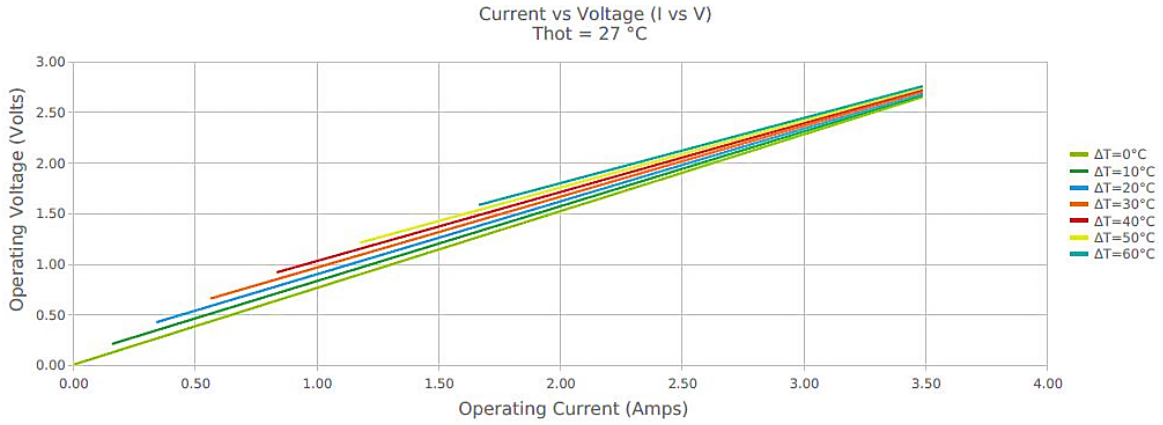

Figure 3.3.6: Current (I) versus voltage (V) profiles for various temperature difference (ΔT) values between the hot and cold side of the Peltier module used in this study.

The maximum values for the current, the voltage and the temperature should not be exceeded when operating the Peltier module. One of the major challenges that we encountered when setting up the thermoregulation system was the different operating voltage of the controller (12 V) and the Peltier module (3 V, as measured with an external voltmeter at room temperature). To address this issue, a resistance (R) had to be added in serial connection to the Peltier module. An external oscilloscope (ISO-TECH Kunststoff) was used to measure the voltage of the controller, the resistance and the Peltier module in order to calculate the final value of the resistance that had to be added to make the operating voltage of the Peltier module 3 V. First, two resistances R_1 (3.3 Ω) and R_2 (4.7 Ω) were connected in parallel resulting in a total resistance, R, of approximately 1.9 Ω, according to Eq.

(3.4). The voltage of the resistance was measured at 7 V (Figure 3.3.7 (c)) and the current flowing through the resistance and the overall circuit was calculated according to Eq. (3.5) to be 3.6 A. It should be noted that the vertical axis of the oscilloscope is the voltage and the increment is 2 V, while the horizontal axis is the time and the increment is 10^{-5} s. The voltage of the Peltier was measured at 4.8 V (Figure 3.3.7 (b)) and the voltage of the overall circuit was 11.8 V (Figure 3.3.7 (a)) being in compliance with the operating voltage of the controller. However, in order to have 3 V at the Peltier module, the voltage of the resistance should be 11.8 V – 3 V = 8.8 V. For 8.8 V and 3.6 A current, the resistance is calculated according to Eq. (3.5) at approximately 2.5 Ω. A circuit with a serial connection of two elements and the relationships among the voltages, the current and the resistances are shown in Figure 3.3.8.

$$R = \frac{R_1 \cdot R_2}{R_1 + R_2} \quad (3.4)$$

$$I = \frac{V}{R} \quad (3.5)$$

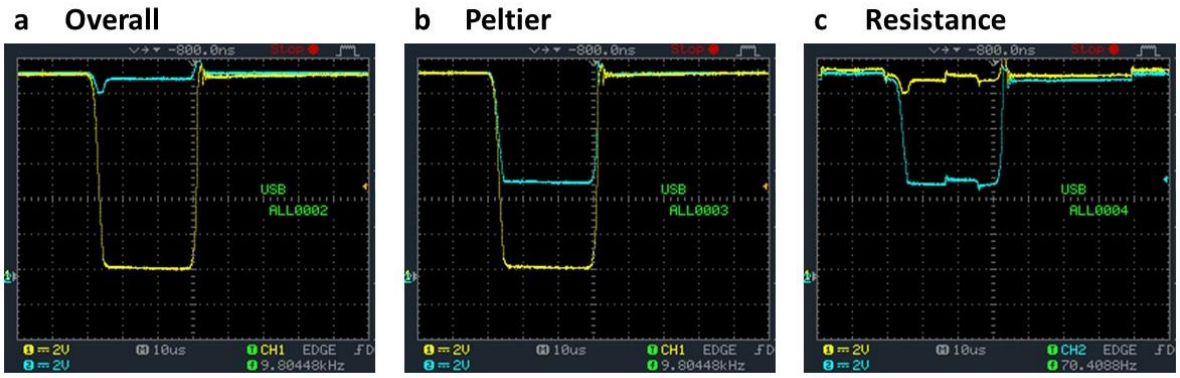

Figure 3.3.7: Voltage measurements of (a) the overall circuit, (b) the Peltier module and (c) the resistance with an external oscilloscope. The increment of the vertical axis is 2 V and the horizontal axis is 10^{-5} s.

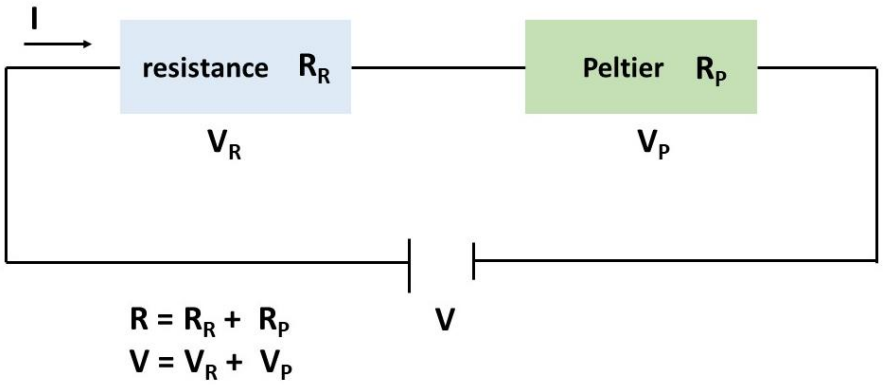

Figure 3.3.8: An electrical circuit with serial connection of two elements (resistance and Peltier module).

In the final version of the thermal regulation system, we used a 2.7 Ω coil resistance from the RS100 series by RS Components covered by aluminium envelope (Figure 3.3.18). The resistance is able to deal with a power of 100 W. With this resistance value, the voltage of the Peltier element is 2.3 V and lies within the operating specifications of the manufacturer.

3.3.2.4 The heat dissipater

Thermoelectric modules require a heat sink or other heat exchanger to dissipate the excess of heat. Typically, in these applications, a water circulating system (chiller) is used to dissipate the heat. However, our goal has been to integrate the thermal regulation system into the MicroCrys platform avoiding voluminous equipment. For this, a heat sink for IC (integrated circuit) processors with cooling fins was combined with an axial ventilator. The aluminium dissipater, purchased by RS Components, features a black anodized surface with dimensions of 43.6 x 43.6 x 12.3mm. Its thermal resistance is 9 K W^{-1} and the installation is implemented by thermal conductive adhesive. For all the thermal contacts in our system, the silicone thermal grease by RS Components is used with a thermal conductivity value of 5.2 W m^{-1} K^{-1} and operational temperature range of - 30 °C to 300 °C. The axial fan was also purchased by RS Components and operates at 12 V DC supply voltage. The dimensions of the fan are 40 x 40 x 20 mm and the speed is 7800 rpm. Axial ventilators operate by dissipating hot air from the surface to cool down the surface. The airflow for the axial ventilator used in this study is 15.3 m^3 h^{-1}. The heat dissipater and the axial ventilator are shown in Figure 3.3.9 (a) and Figure 3.3.9 (b), respectively.

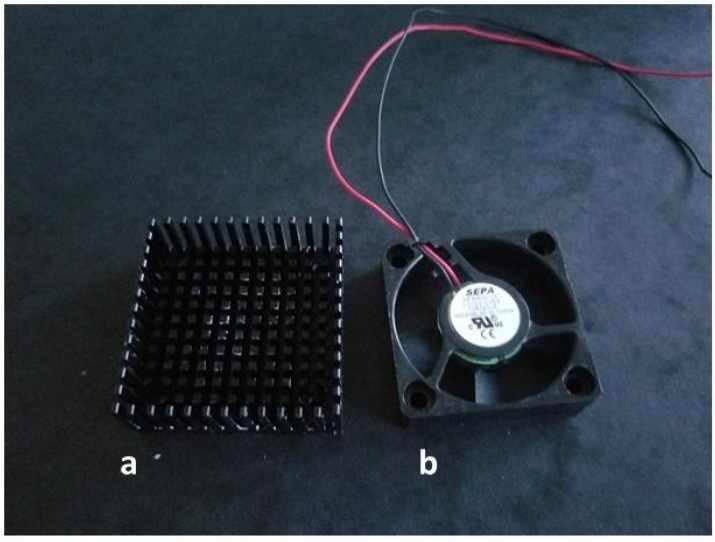

Figure 3.3.9: (a) The heat sink with integrated cooling fins (RS) and (b) the axial ventilator (RS) used for dissipating the heat produced by the Peltier module.

3.3.3 Data acquisition

The TC-XX-PR-59 reversible controller can be manipulated by user-friendly PC software, the LT-Interface, developed by Laird Technologies, described in more detail in Appendix 3.1.

3.3.3.1 The LabVIEW program

In order to automate the use of the controller and to integrate the thermal system to the LabVIEW based interface of MicroCrys, an assembly of input/output electronic WAGO cards has been developed. The J type thermocouple is connected to a two-channel analog input card WAGO 753-469 and a two-channel analog output card WAGO 753-550 is connected to the KK type Molex terminal of the controller for two-wire connections. The communication between the WAGO cards and the computer is achieved by the MODBUS TCP/IP communication protocol through a Fieldbus Ethernet coupler WAGO 750-352 card, while an end module WAGO 750-600 card is added at the end. The fieldbus coupler connects Ethernet to the modular WAGO I/O (WAGO 753-469 and WAGO 753-550) system and creates a local memory map with mixed arrangements of analog and digital modules. According to the manufacturer, the coupler is designed for communication in both Ethernet/IP and MODBUS networks and supports various standard Ethernet protocols (HTTP, FTP, etc.). A power supply WAGO 787-602 card with 24 V DC output voltage and 1.3 A output current is connected prior to the fieldbus coupler. Once the fieldbus node is assembled, the end module is added to complete the internal data circuit and to ensure a correct data flow within the system. The WAGO system is shown in Figure 3.3.10.

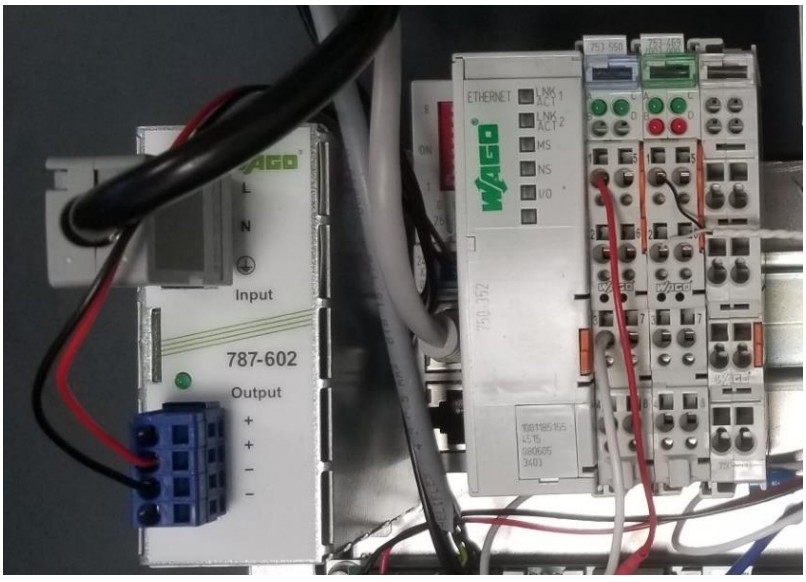

Figure 3.3.10: The WAGO system assembled to automate the use of the reversible controller and integrate the thermal system to the LabVIEW based interface of MicroCrys. The electronic cards are the switched-mode power supply 787-602, the fieldbus Ethernet coupler 750-352, the analog input 753-469, the analog output 753-550 and the end module 750-600 (from left to right).

A program written in LabVIEW accomplishes the recording of the data at the computer. The Serial Command Interface of the controller (Laird Technologies) is a serial communication protocol for taking full command of the controller. In this case, the communication is done by ASCII chars. When initiating the controller, the parameters of the internal EERROM memory are copied to the runtime registers. With the RW command, the master can write the runtime registers to EEPROM after ensuring that all runtime registers have been changed. This communication is integrated in the main VI of the LabVIEW software developed for thermal regulation and it is initialized when the “Init Peltier CTRL” button is clicked on the front panel (Figure 3.3.11). The block diagram of the main VI for thermal regulation is provided in Appendix 3.2.

The temperature of the J thermocouple is read with the WAGO cards and the MODBUS protocol via the LabVIEW program. The “Init WAGO” button has been added to the front panel of the main VI for this purpose. A user-friendly graphical interface allows recovering the numerical value of the thermocouple and displaying the corresponding data. The front panel (Figure 3.3.11) includes a waveform chart window to visualize temporal (s) variations of the temperature (°C) as measured by the J type thermocouple. The power supply of the Peltier module is realized directly with a PID control integrated in the LabVIEW program. The controller is set to power regulation mode allowing to regulate the output power from - 100 % to + 100 % depending on the voltage value. A sliding bar named “Voltage from WAGO to Peltier CTRL” has been added to the main VI with a value range from 0 – 5 V. 0 V correspond to - 100 % power, 2.5 V to 0 % power and 5 V to 100 % output power. When performing an experiment, the temperature in °C is set in the “Set point in degree” box and the “Start Peltier” and “Start Regulation” switches are turned on (Figure 3.3.11). The PID algorithm will regulate the voltage to adjust the temperature. This temperature value is adjusted in real time by comparing the temperature set point to the actual temperature through the PID control. Finally, a “STOP” button allows terminating the “while” loop operating in the block diagram that includes all the above-mentioned functions.

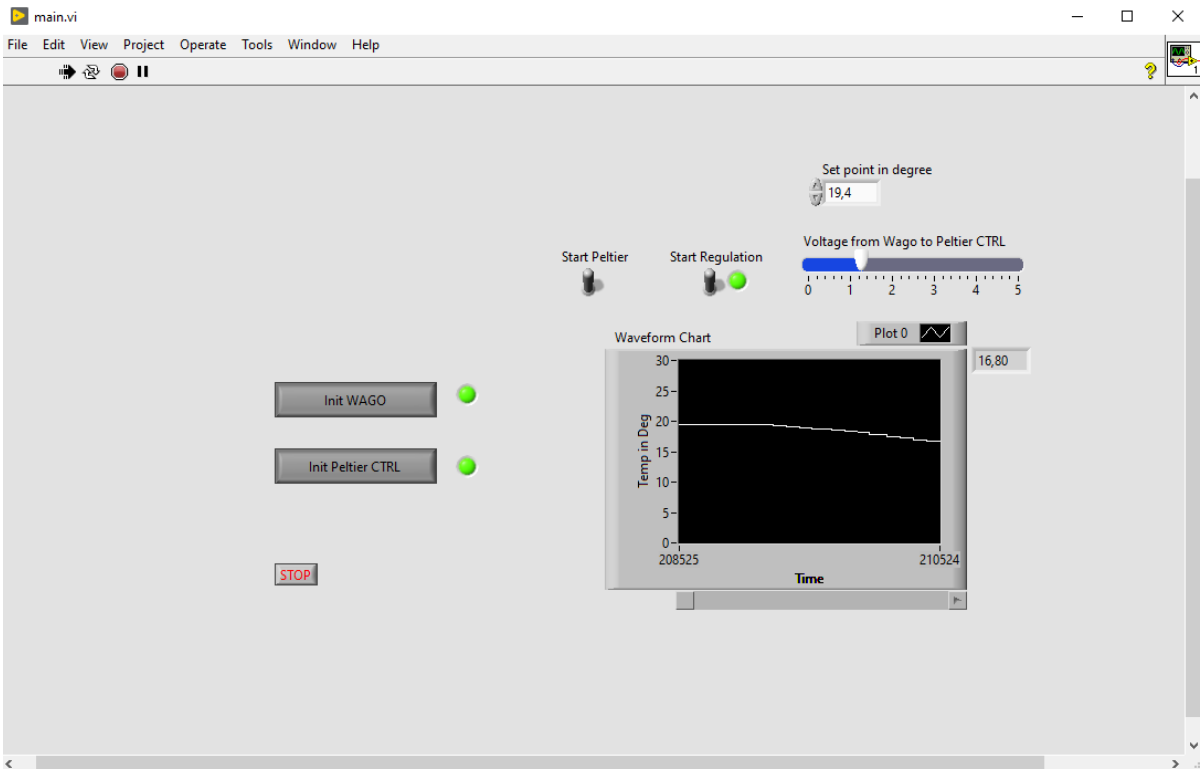

Figure 3.3.11: The front panel of the main VI of the LabVIEW software developed for thermal regulation. The interface includes buttons to initialize the controller and the WAGO system, to set the temperature and start the regulation of the Peltier module. The temporal variations of the temperature (°C) in real time are shown in a graph.

3.3.4 Support for on chip thermal regulation

3.3.4.1 First prototype

In order to promote thermal transfer from the Peltier module to the microchip, a conductive system is necessary to connect these two elements. A support was designed with the CAD (Computer Aided Design) software Solidworks and was 3D printed at the SERAS platform (Institut Néel, Grenoble). The resin support with 12.7 x 8.6 cm external dimensions has the exact size of a SBS standard 96-well crystallization plate (Figure 3.2.3 (b)) and it can fit on the metallic sample support of the OptiCrys platform (Figure 3.2.2 (a)). The CAD design of the support is shown in Figure 3.3.12 (a), where the cavities and the pockets for incorporating the various parts (thermocouple, Peltier element, microchip, copper lamella and heat dissipater) for the thermal regulation are visible. A top and a bottom view of the design are illustrated in Figure 3.3.13 (a) and Figure 3.3.13 (b), respectively. The microchip is positioned horizontally on the support and the protein reservoir is aligned with the central hole of the Peltier module facilitating visualization and image recording with the inverted camera of the platform. The Peltier module (white head with a black and a red wire) is positioned below the chip, on the pocket of the support specifically designed to accommodate this part of the

thermal assembly. The thermocouple (green wire) is placed in a way that its head junction is right above the central hole of the Peltier module and right below the protein reservoir of the chip ensuring that the temperature measurement is performed in the proximity of the protein reservoir. “Sandwiching” the thermocouple between the chip and the support was quite challenging. This is one of the reasons why the NTC thermistor, originally used as a temperature sensor with the TC-XX-PR-59 reversible controller, was replaced by a J type thermocouple that has a smaller head junction size. However, the NTC thermistor remains connected to the dedicated position on the controller, otherwise, the controller cannot be initialized, but it is not used for temperature reading. The J thermocouple is used for reading the temperature near the protein reservoir of the chip via the WAGO system (Section 3.3.3.1).

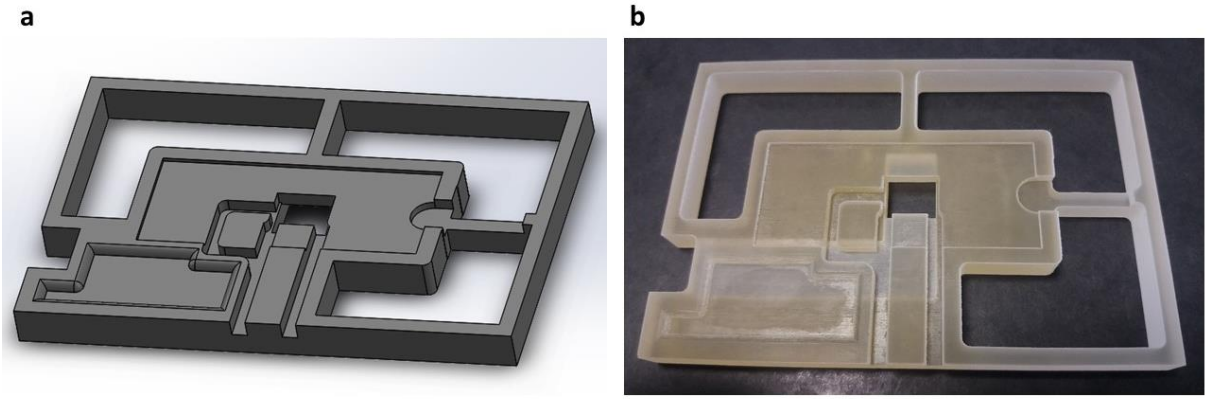

Figure 3.3.12: (a) The CAD design (Solidworks) of the first support developed for on chip thermal regulation and (b) the 3D printed support. The cavities for incorporating the thermocouple, the Peltier module, the microchip, the copper lamella and the heat dissipater are visible.

As mentioned in Section 3.3.2.4, we wanted to avoid voluminous equipment for dissipating the excess heat produced by the Peltier module in order to integrate the support for thermal regulation into the MicroCrys platform. An aluminium dissipater with cooling fins and an axial ventilator are used for dissipating the heat. The thermal contact between the dissipater and the Peltier module is achieved with an L-shaped copper lamella, as shown in Figure 3.3.13 (b). Copper and aluminium exhibit a good thermal conductivity with values of 385 W m^{-1} K^{-1} and 205 W m^{-1} K^{-1} at 293 K, respectively[33]. However, the copper lamella is not in direct contact with the Peltier module. In order to increase the thermal contact, a thin layer of silicone thermal grease (RS Components) is used with a thermal conductivity value of 5.2 W m^{-1} K^{-1}. Moreover, an 8 mm diameter hole has been drilled on the copper lamella (as illustrated in Figure 3.3.13 (b)) to visualize the protein reservoir of the microchip with the inverted camera. Despite the compact design, this first prototype for thermal regulation didn’t respond well to the experimental requirements. Preliminary tests were carried out to determine the response of the heat dissipater assembly to temperature variations. When setting the temperature at a certain point, as for example at 4° C or at 20 °C, commonly used for crystallization experiments, these values would be reached and remain constant for only a few

seconds. After this time, we observed a sudden increase in the temperature and an excessive local heating of the copper lamella, concluding that heat dissipation rate was not sufficient to keep the temperature of the Peltier element fixed at the set point value. The thickness of the copper lamella is approximately 2 mm and the width and the total length of the L-shaped piece is 1.5 cm and 15.5 cm, respectively. Using Fourier's law for heat conduction (Eq. (3.6)), the heat flux (Q in W) for the copper lamella is 2.61 W. The maximum power (power = I · V) produced by the Peltier module is approximately 8 W for I_{max} = 3.1 A and V_{max} = 2.6 V (third column, Table 3.3.1). Thus, the heat flux (2.61 W) of the copper lamella is not sufficient over time compared to the heat production rate (8 W) by the thermoelectric module. To address this issue, we designed a second prototype, which is fully metallic, the cooling fins are integrated within the main body of the support and a more powerful fan has replaced the axial one.

$$Q = \frac{k\,A\,\Delta T}{L} \quad (3.6)$$

Where k is the material's thermal conductivity (W m^{-1} K^{-1}), A is the cross section area (m^2), L is the length of the material (m) and ΔT (K) is the temperature difference between the two ends of the material. For the L-shaped copper lamella in contact with the Peltier module, a value of ΔT = 35 K was used for the calculation.

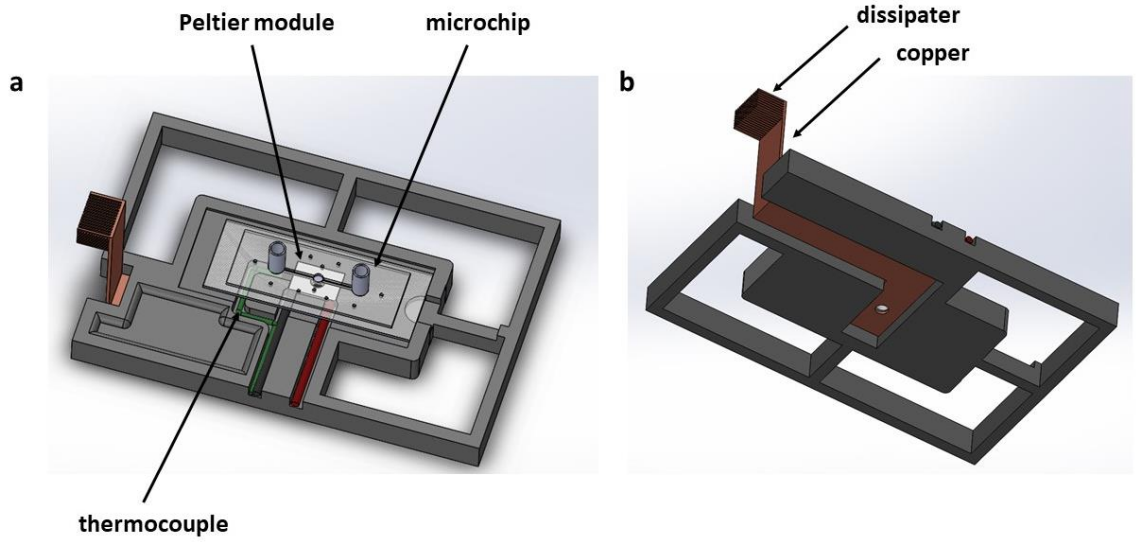

Figure 3.3.13: (a) A top view of the first support for thermal regulation (CAD design) illustrating the microchip, the Peltier module and the thermocouple mounted on the dedicated positions. (b) A bottom view of the same CAD design showing the mounted L-shaped copper lamella and heat dissipater. A hole has been drilled on the copper lamella for visualization of the chip's protein reservoir with the inverted camera of the MicroCrys platform.

The 3D printed resin support is shown in Figure 3.3.12 (b). Figure 3.3.14 shows the support on the metallic sample holder of the MicroCrys platform. The L-shaped copper lamella is held in place with screws, the heat dissipater is screwed on the copper lamella and the axial fan is fixed on the dissipater. The Peltier module and the J thermocouple (black and white wires) are positioned below the microchip. The protein reservoir of the chip is aligned with the central hole of the Peltier module and the hole on the copper lamella, right above the inverted UEye camera and below the back light of the platform.

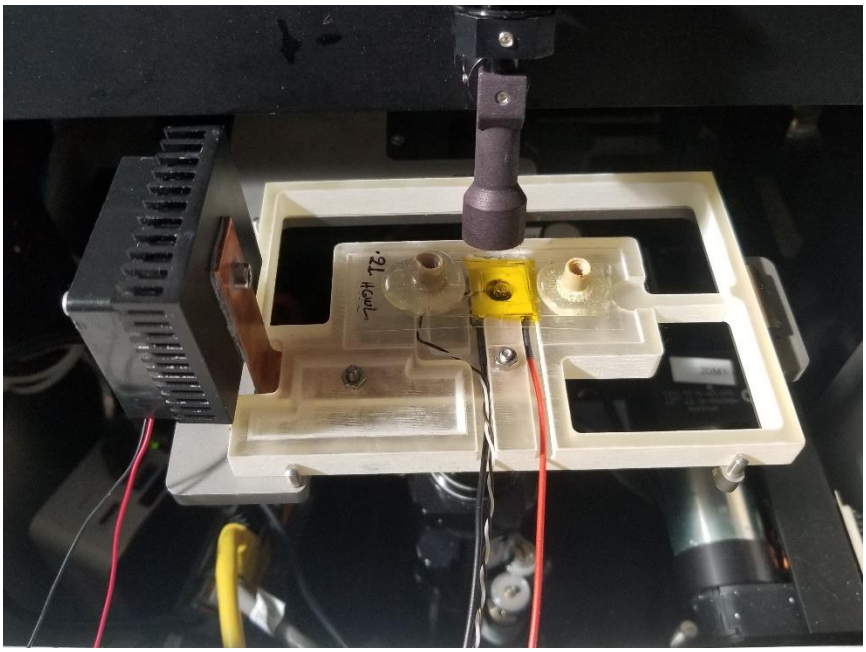

Figure 3.3.14: The 3D printed support for thermal regulation on the metallic sample holder of the MicroCrys platform. All the components (chip, Peltier module, J thermocouple, copper lamella, heat dissipater and axial ventilator) are mounted on the dedicated positions. The central hole of the Peltier module and the hole drilled on the copper lamella make it feasible to visualize the protein reservoir of the chip with the inverted camera.

3.3.4.2 Second prototype

For the second prototype, an AVC frameless cooling fan from an old NVIDIA Quadro 4000 graphics card was used. The diameter of the fan is 7 cm and it operates at 12 V DC power and 0.5 A current. The fan speed ranges between 3100 to 3900 rpm. The new fan operates as a turbine forcing the flow through all the cooling fins integrated in the main body of the metallic support. The support was designed with Solidworks and manufactured from aluminium at the SERAS platform. The main objective of fabricating the support entirely from a conductive metal was to enhance the heat dissipation. In this case, heat is dissipated by the cooling fins integrated in the main body of the support. The dimensions of the aluminium support are 12.7 cm (length) and 8.6 cm (width) and it fits precisely on the metallic sample holder of the OptiCrys platform. The top view of the CAD design indicating the cavity for the Peltier module

is shown in Figure 3.3.15 (a). A small part was designed as the lid for the Peltier module. The fabrication material of the lid was originally aluminium, as the main body of the support. However, during the preliminary tests, we noticed that the thermal transfer between the hot part of the Peltier module and the support was too large because the lid and the support, fabricated from the same conductive material, were in direct contact, as shown in transverse view in Figure 3.3.16 (a). In order to resolve this problem, we designed a lid for the thermoelectric module composed of two parts: a metallic part (aluminium or copper) for direct contact with the cold side of the Peltier module and a plastic (PVC or Derlin acetal resin) frame for insulating the main body of the support, as shown in Figure 3.3.15 (b) and in Figure 3.3.16 (b) in transverse view. The dimensions of the metallic piece and the plastic frame are 15 x 15 mm and 29 x 19 mm, respectively. The metallic piece has a hole of 5 mm diameter for enabling the visualization with the inverted camera of the MicroCrys platform. We made in-house the small piece from aluminium and the frame from a mixture of carbon fibers and epoxy adhesive (Figure 3.3.18 (a)) in order to use the support immediately, while the CAD designs have been forwarded to SERAS for manufacturing the final parts.

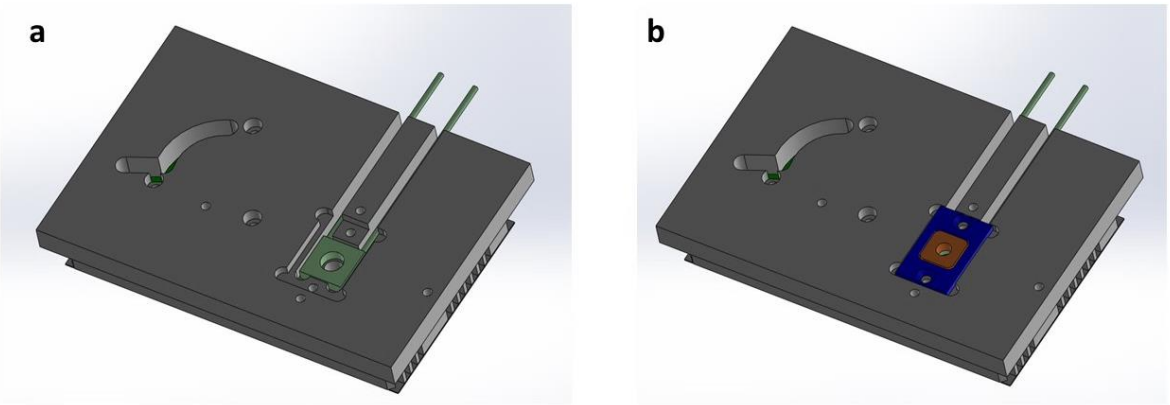

Figure 3.3.15: Top view of the CAD design (Solidworks) of the second support developed for on chip thermal regulation, illustrating the position for (a) the Peltier module (green color) and (b) the lid designed for the Peltier module. The metallic part of the lid is shown with brown color and the polymeric part with blue color.

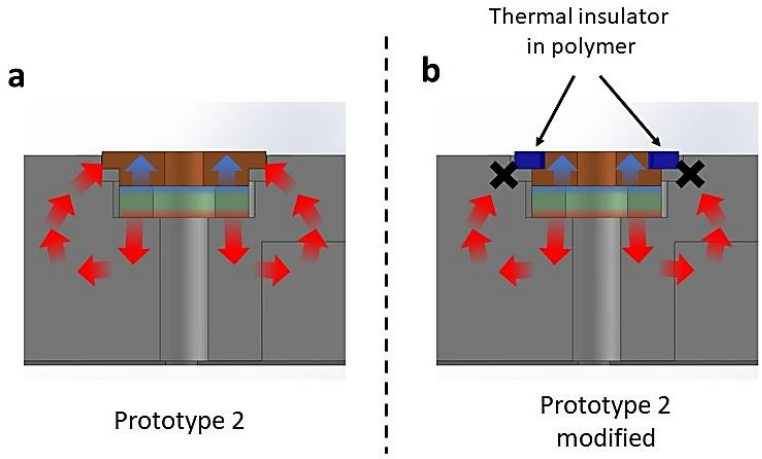

Figure 3.3.16: Transverse view of the CAD designs for the second support developed for on chip thermal regulation, illustrating (a) the metallic lid for the Peltier module (brown color) and the heat transfer from the hot side of the module (red arrows) and (b) the modified version of the lid containing a metallic part (brown color) and a polymeric part (blue color) that is used as a thermal insulator.

The bottom view of the CAD design for the second prototype is shown in Figure 3.3.17 (a), revealing the cooling fins and the cavity for the frameless cooling fan. The heat dissipater used with the first prototype has been replaced with nine cooling fins designed to be part of the support. The bottom part of the support is shielded with an aluminium lid as shown in Figure 3.3.17 (b). The support's lid dimensions are 120 x 72 mm and the diameter of the hole below the fan is 48 mm. Moreover, the support and the lid have a hole for visualizing the protein reservoir of the dialysis chip. The upper part of the aluminium support fits precisely on the holder of the MicroCrys platform, while the bottom part exceeds vertically by 15 mm below the holder allowing proper airflow through the cooling fins.

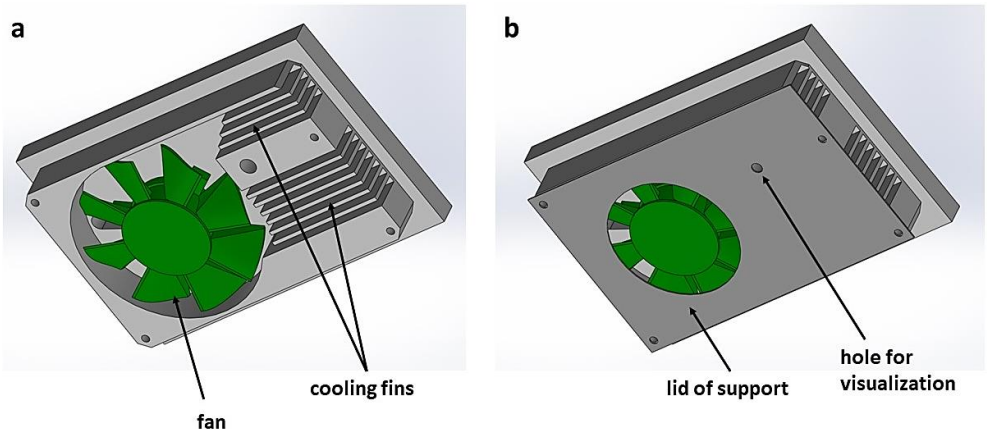

Figure 3.3.17: Bottom view of the CAD design of the second support developed for on chip thermal regulation, illustrating (a) the cooling fins integrated on the main body of the support and the position for the cooling fan and (b) the bottom lid of the support and its position on the metallic sample holder of the MicroCrys platform.

The second prototype for thermal regulation is shown in Figure 3.3.18 (a) on the sample holder of the MicroCrys platform. The protein reservoir of the microchip is positioned right above the Peltier module and it is aligned with the hole of the module and all the holes drilled on the aluminium support for light protrusion and visualization with the inverted camera. The lid of the Peltier module can be fixed with screws. The J type thermocouple is placed between the Peltier module and the chip in the proximity of the protein reservoir. Two holes on the support located near the inlet and outlet ports of the chip are designed for stabilizing the chip with two screws. Otherwise, the chip can be fixed on the support with insulating tape. The black and red wires of the fan (located at the bottom part of the support) protrude from a hemispherical cavity. The second prototype connected to the controller and the WAGO system developed for thermal regulation operated successfully, dissipating heat in a sufficient rate and regulating the temperature at values even below 0 °C. The whole system developed for thermal regulation, including the aluminium support, the reversible controller and the WAGO system, is shown in Figure 3.3.18 (b). The WAGO system, the controller and the resistance connected to the Peltier module are fixed on a metallic plate to optimize the spatial distribution of these elements. In the future, this plate can be integrated within the platform.

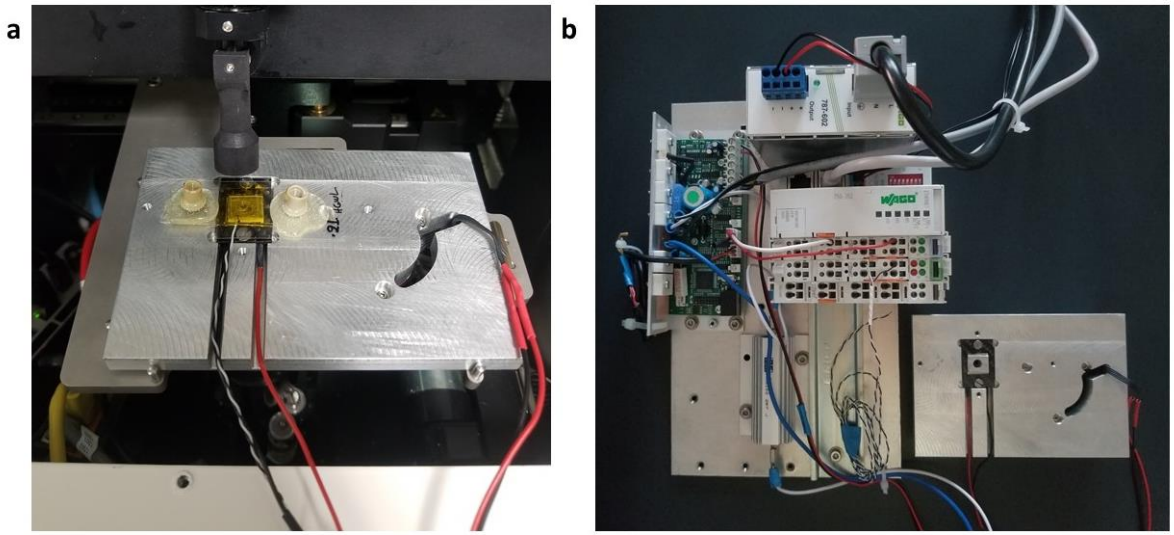

Figure 3.3.18: (a) The aluminium support for thermal regulation on the metallic sample holder of the MicroCrys platform. All the components (chip, Peltier module and its lid, J thermocouple, cooling fan) are mounted on the dedicated positions. The central hole of the Peltier module and the holes drilled on the lids of the Peltier module and the support allow visualization of the protein reservoir with the inverted camera. (b) The entire system developed for thermal regulation, including the aluminium support, the reversible controller and the WAGO cards.

3.4 Conclusions

A visualization platform (MicroCrys), integrating chemical composition and temperature control, has been developed for automating the on chip crystallization of proteins via microdialysis for investigating phase diagrams. MicroCrys is a miniaturization of two macro-scale pipelines previously developed in our laboratory for screening and optimizing protein crystallization, through the batch or the dialysis method, by mapping temperature and/or precipitant concentration phase diagrams[2,5]. The MicroCrys platform includes a step-wise motorized metallic support, an inverted digital camera with automated focus for real-time monitoring and image recording and three LED lights located near the camera and above the sample holder facilitating the visualization of the microchips. The metallic support, originally designed for commercial 96-well crystallization plates, can accommodate the 3D printed holder that we developed for the chips with external dimensions equal to the SBS standard crystallization plates. The 3D printed support can hold up to three chips simultaneously and it is also used for on chip and *in situ* X-ray diffraction experiments at synchrotron beamlines compatible with in plate protein crystallography. All the components of the platform are controlled by a custom-built LabVIEW software displaying a user-friendly graphical interface designed to manipulate the spatial movement of the support, the focus of the camera, the illumination level through the LED lights and to record images with a frequency (image per time unit) allocated by the user.

Moreover, a commercial fluidic system (Elveflow) for mixing and circulating the crystallization solution under constant flow or under constant differential pressure between the inlet and the outlet port of the fluidic channel has been incorporated in the MicroCrys platform. The system for fluid handling includes a pressure-driven controller with two pressure channels and two thermal-based digital flow sensors. The controller has two pressure channels used to drive the solutions from pressurized containers into the PTFE tubes connected to the inlet port of the microfluidic device. The two channels can be used independently to circulate a solution in two different chips, allowing two crystallization experiments to run simultaneously. Flow sensors can be connected at any point along the flow where the accurate measurement or regulation of the flow rate is important for the experiment. Pre-mixed crystallization solutions can be used with the pressure-driven controller or can be prepared in an automated way with a six-valve distributor. The distributor injects sequentially various salt or buffer solutions into a mixing reservoir in order to prepare the final mixture for crystallization. Interactive software (ESI) has been developed by the manufacturer for controlling all the instruments of the fluidic system. However, in the future we aim to integrate the functionalities of the ESI software in the main LabVIEW program developed for MicroCrys, in order to accommodate all the features of the platform for visualization and fluid handling in a single graphical user interface. So far, the pressure-driven controller has been integrated in the LabVIEW interface.

In order to investigate protein phase diagrams with the microchips, thermal regulation of the protein reservoir is a major parameter as temperature control combined with the dialysis crystallization method can be used to decouple nucleation and crystal growth. We developed two prototypes using the thermoelectric Peltier effect for heating and/or cooling the protein reservoir. The Peltier module has a 7.21 mm diameter hole facilitating visualization of the protein reservoir through the inverted camera of the MicroCrys platform. The diameter of the

protein reservoir for the 0.1 µL and the 0.3 µL chip is 1.5 mm and 2.8 mm, respectively. While in most applications, two Peltier modules are used to produce a temperature difference between the hot and the cold side, the TC-XX-PR-59 controller for thermoelectric assemblies is used for reversible control. Thus, a single Peltier module is sufficient for our application since the controller can reverse the side of the module that is in contact with the chip depending on whether we want to heat the protein reservoir or cool it down.

The same Peltier module and reversible controller were used for thermal regulation with the two prototypes. The difference lies on the system used for dissipating the excessive heat produced by the thermoelectric module. The first, 3D printed resin support used a copper lamella, a heat dissipater with integrated cooling fins and an axial fan. Even though copper has a good thermal conductivity (385 W m^{-1} K^{-1} at 293 K), the L-shaped lamella of the first prototype in combination with the dissipater and the fan could not dissipate heat at a rate sufficient to keep the temperature of the Peltier element fixed. Thus, the second support was manufactured entirely from aluminium. A frameless cooling fan used in computers' graphical cards replaced the axial fan and the cooling fins are part of the main aluminium body of the support. Various holes of appropriate diameter were drilled in different parts of the support for the visualization of the protein reservoir with the inverted camera. Both the 3D printed resin support and the aluminium support can be positioned on the sample holder of the MicroCrys platform.

Finally, a program written in LabVIEW accomplishes displaying and recording the temperature values read by the J type thermocouple at the computer. The thermocouple is positioned between the Peltier module and the chip and its junction head is placed close to the protein reservoir. The thermocouple and the Peltier module are both connected to the reversible controller. Laird Technologies has developed the LT interface for interactive manipulation of the TC-XX-PR-59 controller and its components by the user. However, the company provides a serial communication protocol for taking full command of the controller without the LT interface. In order to automate the use of the controller and to integrate the thermal system to the main LabVIEW interface of MicroCrys, an assembly of five electronic WAGO cards has been developed. The temperature of the J thermocouple is read with the WAGO cards and the MODBUS protocol via the LabVIEW program developed for thermal regulation. A graphical user interface allows to recover the numerical value of the thermocouple (°C) and to display the corresponding data as a function of time (s). The power supply of the Peltier module is realized directly with a PID algorithm that regulates the voltage in order to adjust the temperature on the side of the Peltier module that is in contact with the chip.

3.5 References

(1) Shim, J.; Cristobal, G.; Link, D. R.; Thorsen, T.; Fraden, S. Using Microfluidics to Decouple Nucleation and Growth of Protein Crystals. *Cryst. Growth Des.* **2007**, *7* (11), 2192–2194.

(2) Junius, N.; Oksanen, E.; Terrien, M.; Berzin, C.; Ferrer, J.-L.; Budayova-Spano, M. A Crystallization Apparatus for Temperature-Controlled Flow-Cell Dialysis with Real-Time Visualization. *J. Appl. Crystallogr.* **2016**, *49* (3), 806–813.

(3) Junius, N.; Jaho, S.; Sallaz-Damaz, Y.; Borel, F.; Salmon, J.-B.; Budayova-Spano, M. A Microfluidic Device for Both On-Chip Dialysis Protein Crystallization and in Situ X-Ray Diffraction. *Lab Chip* **2020**, *20* (2), 296–310.

(4) Jaho, S.; Junius, N.; Borel, F.; Sallaz-Damaz, Y.; Salmon, J.-B.; Budayova-Spano, M. Crystallization of Proteins on Chip by Microdialysis for In Situ X-Ray Diffraction Studies. *J. Visualized Exp.* **2021**, No. 170, e61660.

(5) Budayova-Spano, M.; Dauvergne, F.; Audiffren, M.; Bactivelane, T.; Cusack, S. A Methodology and an Instrument for the Temperature-Controlled Optimization of Crystal Growth. *Acta Crystallogr., Sect. D* **2007**, *63* (3), 339–347.

(6) Vahdatahar, E.; Junius, N.; Spano, M. B.-. Optimization of Crystal Growth for Neutron Macromolecular Crystallography. *J. Visualized Exp.* **2021**, No. 169, e61685.

(7) Junius, N.; Vahdatahar, E.; Oksanen, E.; Ferrer, J.-L.; Budayova-Spano, M. Optimization of Crystallization of Biological Macromolecules Using Dialysis Combined with Temperature Control. *J. Appl. Crystallogr.* **2020**, *53* (3), 686–698.

(8) Elwenspoek, M. Thermal Flow Micro Sensors. In *International Semiconductor Conference* **1999**, *2*, 423–435.

(9) Tabeling, P. Introduction to Microfluidics. OUP Oxford, **2005**.

(10) Miralles, V.; Huerre, A.; Malloggi, F.; Jullien, M.-C. A Review of Heating and Temperature Control in Microfluidic Systems: Techniques and Applications. *Diagnostics* **2013**, *3* (1), 33–67.

(11) Issadore, D.; J. Humphry, K.; A. Brown, K.; Sandberg, L.; A. Weitz, D.; M. Westervelt, R. Microwave Dielectric Heating of Drops in Microfluidic Devices. *Lab Chip* **2009**, *9* (12), 1701–1706.

(12) Maltezos, G.; Johnston, M.; Scherer, A. Thermal Management in Microfluidics Using Micro-Peltier Junctions. *Appl. Phys. Lett.* **2005**, *87* (15), 154105.

(13) Khandurina, J.; McKnight, T. E.; Jacobson, S. C.; Waters, L. C.; Foote, R. S.; Ramsey, J. M. Integrated System for Rapid PCR-Based DNA Analysis in Microfluidic Devices. *Anal. Chem.* **2000**, *72* (13), 2995–3000.

(14) Casquillas, G. V.; Fu, C.; Berre, M. L.; Cramer, J.; Meance, S.; Plecis, A.; Baigl, D.; Greffet, J.-J.; Chen, Y.; Piel, M.; T. Tran, P. Fast Microfluidic Temperature Control for High Resolution Live Cell Imaging. *Lab Chip* **2011**, *11* (3), 484–489.

(15) Yang, J.; Liu, Y.; B. Rauch, C.; L. Stevens, R.; H. Liu, R.; Lenigk, R.; Grodzinski, P. High Sensitivity PCR Assay in Plastic Micro Reactors. *Lab Chip* **2002**, *2* (4), 179–187.

(16) Mao, H.; Yang, T.; Cremer, P. S. A Microfluidic Device with a Linear Temperature Gradient for Parallel and Combinatorial Measurements. *J. Am. Chem. Soc.* **2002**, *124* (16), 4432–4435.

(17) Matsui, T.; Franzke, J.; Manz, A.; Janasek, D. Temperature Gradient Focusing in a PDMS/Glass Hybrid Microfluidic Chip. *ELECTROPHORESIS* **2007**, *28* (24), 4606–4611.

(18) Laval, P.; Lisai, N.; Salmon, J.-B.; Joanicot, M. A Microfluidic Device Based on Droplet Storage for Screening Solubility Diagrams. *Lab Chip* **2007**, *7* (7), 829–834.

(19) Shen, K.; Chen, X.; Guo, M.; Cheng, J. A Microchip-Based PCR Device Using Flexible Printed Circuit Technology. *Sens. Actuators, B* **2005**, *105* (2), 251–258.
(20) Vigolo, D.; Rusconi, R.; Piazza, R.; A. Stone, H. A Portable Device for Temperature Control along Microchannels. *Lab Chip* **2010**, *10* (6), 795–798.
(21) Wu, J.; Cao, W.; Wen, W.; Chang, D. C.; Sheng, P. Polydimethylsiloxane Microfluidic Chip with Integrated Microheater and Thermal Sensor. *Biomicrofluidics* **2009**, *3* (1), 012005.
(22) M. Guijt, R.; Dodge, A.; Dedem, G. W. K. van; Rooij, N. F. de; Verpoorte, E. Chemical and Physical Processes for Integrated Temperature Control in Microfluidic Devices. *Lab Chip* **2003**, *3* (1), 1–4.
(23) Astier, J.-P.; Veesler, S. Using Temperature To Crystallize Proteins: A Mini-Review. *Cryst. Growth Des.* **2008**, *8* (12), 4215–4219.
(24) Juárez-Martínez, G.; Steinmann, P.; Roszak, A. W.; Isaacs, N. W.; Cooper, J. M. High-Throughput Screens for Postgenomics: Studies of Protein Crystallization Using Microsystems Technology. *Anal. Chem.* **2002**, *74* (14), 3505–3510.
(25) Teychené, S.; Biscans, B. Microfluidic Device for the Crystallization of Organic Molecules in Organic Solvents. *Cryst. Growth Des.* **2011**, *11* (11), 4810–4818.
(26) Teychené, S.; Biscans, B. Crystal Nucleation in a Droplet Based Microfluidic Crystallizer. *Chem. Eng. Sci.* **2012**, *77*, 242–248.
(27) Holtz, J. Pulsewidth Modulation for Electronic Power Conversion. *Proceedings of the IEEE* **1994**, *82* (8), 1194–1214.
(28) Silva, E. R. C. da; Santos, E. C. dos; Jacobina, B. Pulsewidth Modulation Strategies. *IEEE Industrial Electronics Magazine* **2011**, *5* (2), 37–45.
(29) Barrett, S. F.; Pack, D. J. Microcontrollers Fundamentals for Engineers and Scientists. Morgan & Claypool Publishers, **2006**.
(30) Van Herwaarden, A. W.; Sarro, P. M. Thermal Sensors Based on the Seebeck Effect. *Sens. Actuators* **1986**, *10* (3), 321–346.
(31) Burns, G. W.; Scroger, M. G.; Strouse, G. F.; Croarkin, M. C.; Guthrie, W. F. Temperature-Electromotive Force Reference Functions and Tables for the Letter-Designated Thermocouple Types Based on the ITS-90. National Institute of Standards and Technology, **1993**.
(32) Gurevich, Y. G.; Logvinov, G. N. Physics of Thermoelectric Cooling. *Semicond. Sci. Technol.* **2005**, *20* (12), R57–R64.
(33) Young, H. D. University Physics. 8th ed.; Addison-Wesley Pub. Co.: Reading, Mass, **1992**.

Chapter 4

On chip protein crystallization and *in situ* X-ray diffraction experiments

Chapter 4

On chip protein crystallization and *in situ* X-ray diffraction experiments

4.1 On chip crystallization of soluble proteins

Two model soluble proteins were used for on chip crystallization with the microdialysis method and *in situ* X-ray diffraction studies. Lyophilized powder of Hen Egg White Lysozyme (HEWL) and Thaumatin from *Thaumatococcus danielli* were purchased from Sigma-Aldrich and dissolved in distilled water to obtain various final concentrations. All protein solutions were filtered through 0.22 μm Millipore filters prior to their use for the crystallization experiments. The crystallization solutions containing salts, buffers or PEGs, were all centrifuged and filtered to remove solid particles of precipitate or dust prior to their use. The MWCO of the RC dialysis membrane (Spectrum Labs) integrated within the dialysis chip, separating the protein reservoir and the fluidic channel, can be chosen according to the molecular weight of the protein sample. For the on chip crystallization experiments of HEWL and Thaumatin with 14.4 kDa and 22 kDa molecular weight, respectively, the MWCO of the RC membrane was 6 – 8 kDa. This value is sufficient to retain the protein sample within the protein reservoir of the chip and to allow the molecules of the crystallization solutions (mainly salts, buffers and low molecular weight PEG solutions[1]) to diffuse from the fluidic channel towards the protein reservoir.

4.1.1 Hen Egg White Lysozyme

Before setting up crystallization experiments on the microchips, conventional crystallization methods were used to perform a preliminary screening of crystallization conditions and evaluate the effect of protein concentration, precipitant concentration and the crystallization method itself on the crystal size and shape distribution and uniformity. In the case of HEWL, both hanging and sitting drop vapor diffusion methods were employed, as well as the dialysis method with standard dialysis buttons (Hampton Research). All experiments were performed at 293 K. Figure 4.1.1 illustrates some representative results of HEWL crystallization with sitting drop and dialysis. The protein concentration was approximately 30 mg mL^{-1} and in the case of the sitting drops, 10 μL of protein were mixed with 10 μL of the precipitant solution, while in the case of dialysis, buttons with 30 μL volume and RC dialysis membrane of 6 – 8 kDa were used. Figure 4.1.1 (a) shows HEWL crystals grown with the sitting drop vapor diffusion method in the presence of 0.8 M sodium chloride (NaCl) and 400 mM sodium acetate (CH_3COONa) pH 4.0 while the crystals shown in Figure 4.1.1 (b) were grown using the same method in the presence of 1 M NaCl and 400 mM CH_3COONa pH 4.0. A slight increase of the precipitant concentration from 0.8 M to 1 M, had a significant impact on the number and the size of the crystals. Figure 4.1.1 (c) and Figure 4.1.1 (d) show HEWL crystals

grown with dialysis in the presence of 0.8 M NaCl and 400 mM CH_3COONa pH 4.0 and in the presence of 1 M NaCl and 400 mM CH_3COONa pH 4.0, respectively. Numerous crystals were grown in both experiments, however higher precipitant concentration resulted in more and smaller crystals. An increase in the precipitant concentration increases the supersaturation value and the available nucleation sites. Considering the similar volumes of the initial mixture, the impact of the crystallization method on the crystal size and population can be seen by comparing Figure 4.1.1 (a) to Figure 4.1.1 (c) or Figure 4.1.1 (b) to Figure 4.1.1 (d), where crystals were grown under conditions of the same chemical composition but with different crystallization method. All photos were taken at the same time (1 day from the beginning of the experiments) and the scale bar represents 100 μm. More examples of HEWL crystals grown with conventional methods can be found in Appendix 4.1.1.

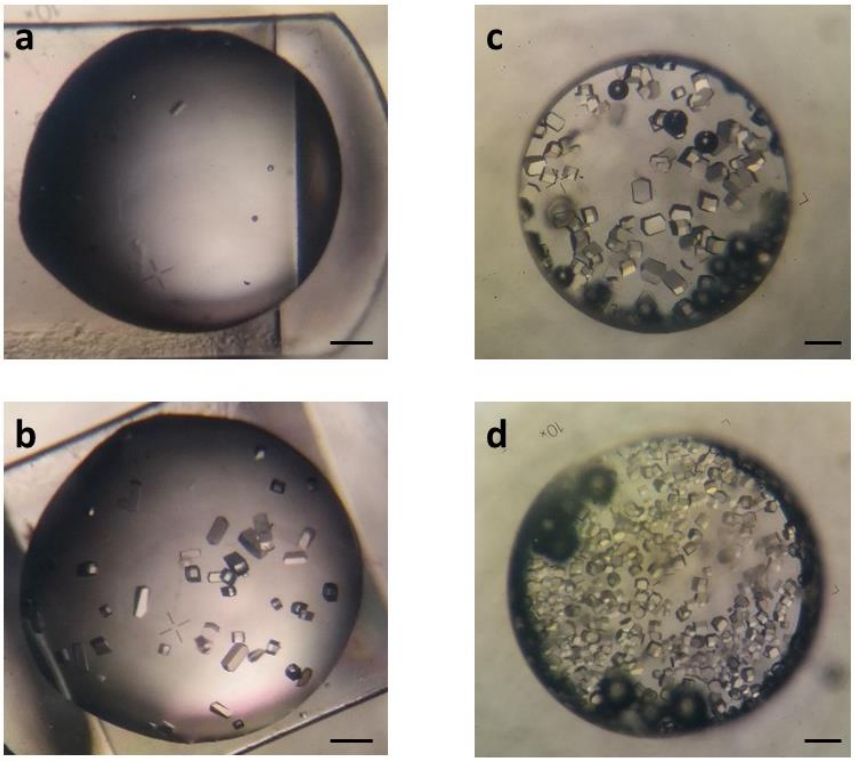

Figure 4.1.1: HEWL (30 mg mL^{-1}) crystals grown in the presence of 0.8 M (a, c) and 1 M (b, d) NaCl and 400 mM CH_3COONa pH 4.0 with sitting drop (a, b) and dialysis (c, d) at 293 K. The scale bar represents 100 μm.

HEWL was crystallized on chip using the microdialysis method (Section 4.1.1.1), the lipidic cubic phase method (Section 4.1.1.3), while large HEWL crystals were grown on chip for preliminary Neutron diffraction experiments (Appendix 4.1.2). Several experiments were conducted to evaluate the effect of protein and precipitant concentration on the crystallization of HEWL with the microdialysis method on the microfluidic chips. The experiments illustrated in Figure 4.1.2 were performed at 293 K. The volume of the protein reservoir was 0.3 μL and the MWCO of the RC membrane was 6 – 8 kDa. The crystals shown

in Figure 4.1.2 (a) and Figure 4.1.2 (b) were grown in the presence of 1 M NaCl and 100 mM CH_3COONa pH 4.0 and the protein concentration was approximately 30 mg mL^{-1} and 60 mg mL^{-1}, respectively. The HEWL crystals illustrated in Figure 4.1.2 (a) were captured 2 h after the onset of the experiment and the ones in Figure 4.1.2 (b) were captured 10 min after starting the experiment. Doubling the concentration of the protein sample increases significantly the supersaturation and the nucleation rate, resulting in the formation of multiple, smaller crystals. The crystals shown in Figure 4.1.2 (c) were grown in the presence of 1 M NaCl, 100 mM CH_3COONa pH 4.0 and 20 % v/v PEG 400, while the protein concentration was approximately 30 mg mL^{-1}. The photo was captured 30 min after the onset of the experiment. The effect of adding a second precipitant molecule (PEG 400) can be visualized by comparing Figure 4.1.2 (a) and Figure 4.1.2 (c). Smaller, numerous HEWL crystals were formed under the synergetic effect of NaCl and PEG 400, both acting as precipitants.

All the figures of the on chip protein crystallization experiments included in this section were captured with the inverted UEye color camera of the MicroCrys platform (see Chapter 3). As explained in Chapter 2 (Section 2.2.2), the on chip crystallization experiments can be performed either under static mode or continuous circulation mode. In the former case, the fluidic channel is filled with the crystallization solution manually with the aid of a disposable syringe or automatically with the aid of a syringe pump or a pressure-driven system and it is set aside under appropriate temperature and humidity conditions. For the continuous circulation mode, the precipitant solution is flowing within the fluidic channel continuously under constant flow or under constant differential pressure (ΔP) between the inlet and the outlet port of the fluidic channel using the Elveflow fluidic system presented in Chapter 3 (Section 3.2.2). The experiments illustrated in Figure 4.1.2 were carried out in a manual way by pipetting the protein sample within the 0.3 μL protein reservoir and filling the fluidic channel with the aid of a disposable syringe. Moreover, in Chapter 2 (Section 2.2.2), the details of bonding connectors on the inlet and outlet ports of the microchip were discussed, along with the protocol of encapsulating the protein sample within the protein reservoir with a piece of 175 μm thick PMMA foil and Kapton tape. The Kapton tape has a characteristic yellow color that adds up to the green color of the images captured by the UEye camera. An example of the images captured with MicroCrys is shown in Appendix 4.1.1 (Figure A4.2), where the Figure 4.1.2 is cited in its original version. The exposure and recording settings of the UEye camera can be adjusted by the LabVIEW program developed for the automated control of all parts of the MicroCrys platform. Applying white balance corrections on the part of the LabVIEW code controlling the camera settings can regulate the green hue in the images. However, the current version of the code uses the default settings for visualization. In order to facilitate the observation of the crystals grown on the chips in this chapter, all the figures are provided in black and white.

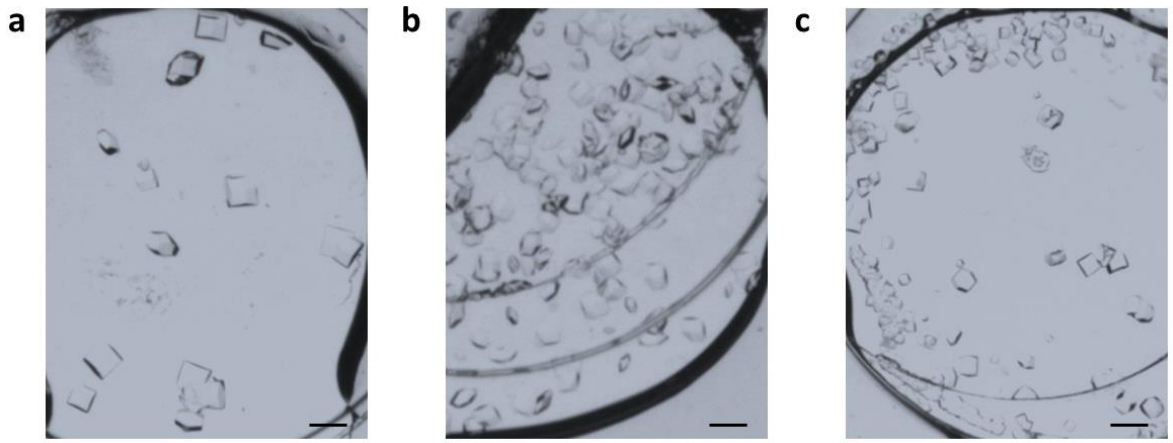

Figure 4.1.2: HEWL crystals grown on chip via microdialysis in the presence of 1 M NaCl and 100 mM CH_3COONa pH 4.0 and protein concentration 30 mg mL^{-1} (a) and 60 mg mL^{-1} (b). (c) HEWL (30 mg mL^{-1}) crystals on chip in 1 M NaCl, 100 mM CH_3COONa pH 4.0 and 20 % v/v PEG 400. All experiments were performed at 293 K. The scale bar represents 100 µm.

4.1.1.1 Using MicroCrys to study crystallization phase diagrams

The MicroCrys platform was used in combination with the continuous circulation mode for filling the fluidic channel in order to evaluate the reversibility of the dialysis method and the compatibility of the dialysis chip for studying crystallization phase diagrams. HEWL crystals were grown on chip at 293 K in the presence of 1 M NaCl and 100 mM CH_3COONa pH 4.0. The protein concentration was 30 mg mL^{-1} and the volume of the protein reservoir was 0.3 µL. The crystals are shown in Figure 4.1.3 (a) after 1 h from the beginning of the experiment. The crystallization solution was continuously flowing within the fluidic channel at a constant inlet pressure of 20 mbar using the pressure-driven fluidic system by Elveflow. In order to dissolve the crystals, the precipitant concentration was set to zero (0 M NaCl) and a solution containing only the buffer (100 mM CH_3COONa pH 4.0) was prepared and connected to the pressure-driven fluidic system. The dissolution of the HEWL crystals at 293 K started approximately 3 days after the beginning of the experiment. 400 µL of the new solution are sufficient to ensure a complete exchange between the precipitant solution used for crystallization and the buffer solution used for dissolution[2]. Figure 4.1.3 (b) and Figure 4.1.3 (c) show the progress of dissolution after 1 h and 1 day from the beginning of this step, respectively. Eventually, crystals were re-grown at 293 K in the presence of 0.8 M NaCl and 100 mM CH_3COONa pH 4.0, as shown in Figure 4.1.3 (d) after 1 h from the onset of the re-nucleation step. During all the steps the crystallization solution was injected automatically in the fluidic channel under constant inlet pressure of 20 mbar. However, the reservoir containing the crystallization solution (50 mL Falcon tube) connected to the pressure-driven fluidic system was filled manually with pre-mixed solutions every time that a new step (growth, dissolution or re-nucleation) started. This manipulation resulted in trapping air within the reservoir and the PTFE tubes connecting all the parts for fluid handling. These air bubbles were transferred towards the fluidic channel and are visible in all photos presented in Figure 4.1.3. In order to avoid the heterogeneities

added to the system by the air bubbles that could potentially affect crystallization, the inlet pressure was increased at 100 mbar, without exceeding the recommended limits[2], just for the time necessary to push the air bubbles towards the outlet of the fluidic channel. Then the pressure was set again at 20 mbar. The scale bar in all captures represents 100 µm.

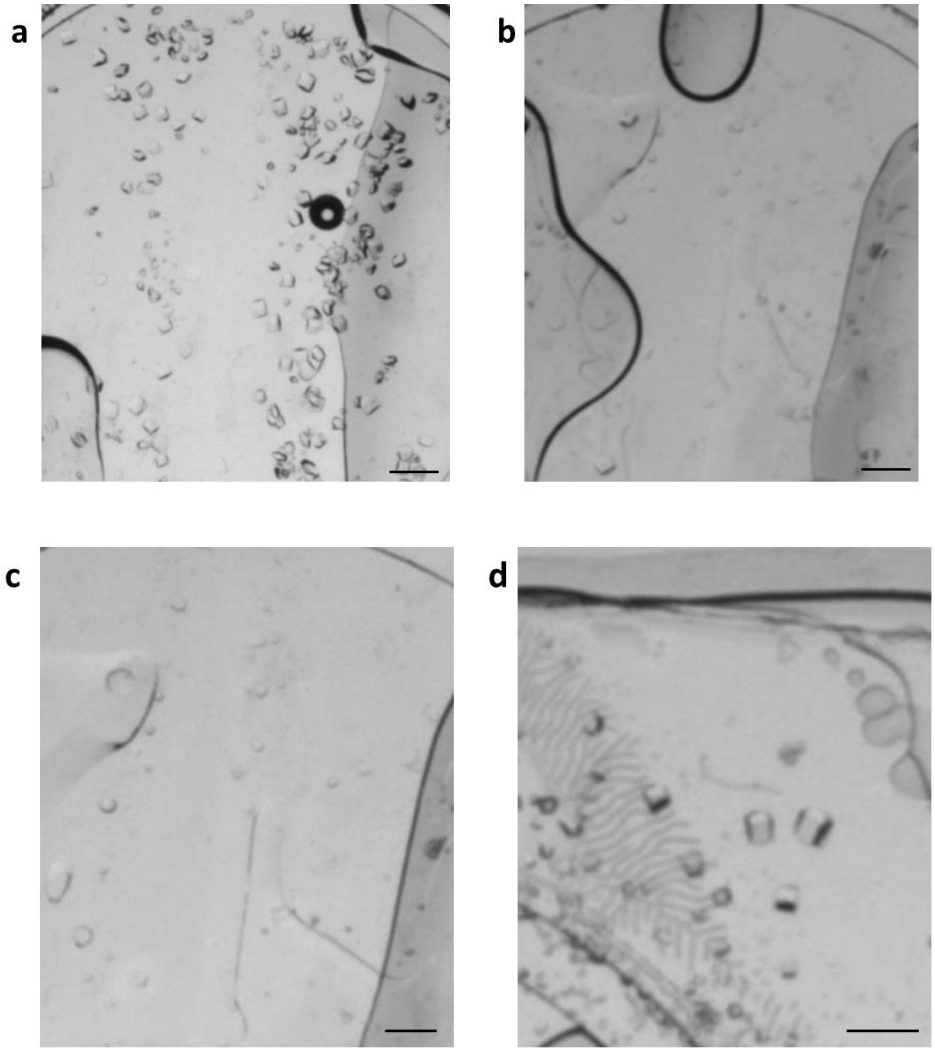

Figure 4.1.3: Dissolution and re-crystallization experiment performed on chip with the MicroCrys platform. (a) HEWL crystals grew in 1 M NaCl and (b) dissolved in 0 M NaCl. (c) The majority of the crystals were completely dissolved after 1 day and (d) were re-grown in the presence of 0.8 M NaCl. In all steps, the temperature was 293 K and the buffer concentration was 100 mM CH_3COONa pH 4.0. The scale bar represents 100 µm.

A schematic representation of the qualitative phase diagram illustrating the nucleation and dissolution steps of the experiment described in Figure 4.1.3, is shown in Figure 4.1.4 (a) and Figure 4.1.4 (b), respectively. The initial concentration of the protein solution is 30 mg mL^{-1} and the initial concentration of NaCl in the crystallization solution is 1 M. The gradual

transition from point I to point II (Figure 4.1.4 (a)) represents the increase of the precipitant concentration in the protein reservoir of the dialysis chip, as molecules of NaCl diffuse from the fluidic channel through the RC dialysis membrane towards the protein reservoir. At point II, nucleation starts as the protein solution is supersaturated and continues until reaching the final concentration of the precipitant. Then, the crystals already present in the solution continue to grow. This step is represented by the decrease in protein concentration until point III in the diagram (Figure 4.1.4 (a)). The dissolution begins (Figure 4.1.4 (b)) by a gradual decrease in the precipitant concentration by exchanging the crystallization solution with a solution containing only buffer (100 mM CH_3COONa pH 4.0). This step is represented by crossing the solubility curve (point IV), resulting in the dissolution of the HEWL crystals. At the same time, the protein concentration increases reaching the initial value (point V, Figure 4.1.4 (b)). After dissolution, re-nucleation is induced in a less supersaturated condition (0.8 M NaCl). This step follows a kinetic trajectory similar to the one illustrated in Figure 4.1.4 (a). Even though, the phase diagrams shown in Figure 4.1.4 are a qualitative representation, they demonstrate in a comprehensive way the kinetic pathway and the reversibility of the dialysis method and the possibility of studying protein phase diagrams through precipitant concentration variations on chip with the automation provided by the MicroCrys platform.

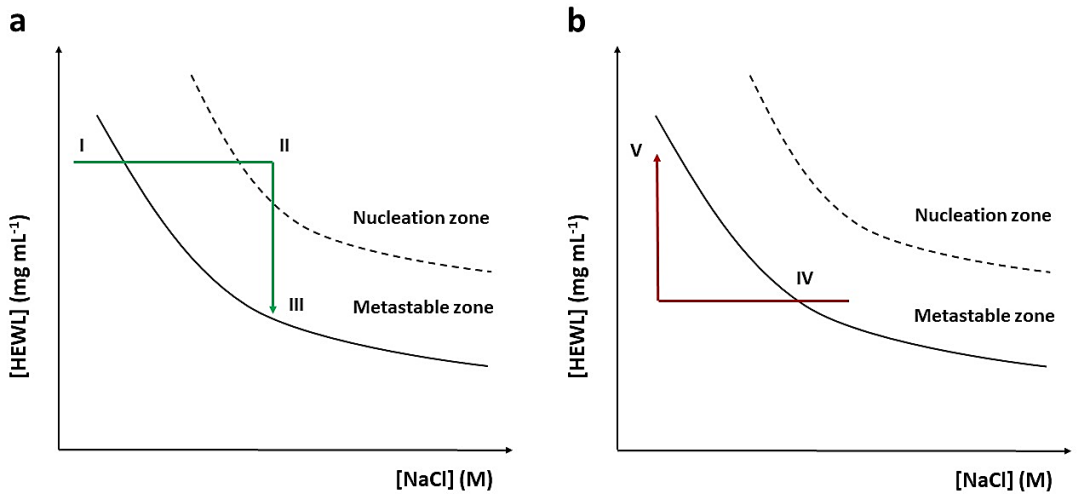

Figure 4.1.4: Schematic representation of the phase diagram for the growth and dissolution experiment performed on chip with the MicroCrys platform. (a) The kinetic pathway of the nucleation step is shown with green arrow, where the precipitant concentration (NaCl) increases (I to II) and crystal growth occurs while the protein concentration decreases (II to III). (b) The kinetic pathway of dissolution is shown with red arrow, where the NaCl concentration decreases gradually and HEWL crystals dissolve once the solubility curve is crossed (IV). HEWL concentration increases gradually until reaching the initial value (V).

4.1.1.2 *In situ* X-ray diffraction experiments

In situ X-ray diffraction data from HEWL crystals grown on chip with the microdialysis method were collected at BM30A-FIP beamline (ESRF). The microchips were mounted on the beamline with the aid of the 3D printed support shown in Figure 3.2.3 (Chapter 3), designed to carry up to three microchips simultaneously. BM30A-FIP beamline, compatible with in plate X-ray crystallography experiments, is equipped with a robotic arm and a plate gripper[3,4] to hold the chips' support in front of the X-ray beam. Moreover, the beamline is equipped with a web-based user interface (WIFIP) to control data collection parameters for standard goniometer-based protein cryo crystallography or *in situ* experiments[5]. The data collection on the microchips was carried out at room temperature. The X-ray wavelength during on chip data collection was 0.98 Å (12.656 keV), the flux was 3.32 x 10^{10} ph s^{-1} and the beam size was 250 µm x 250 µm. The diffraction images were recorded with an ADSC Quantum 315r detector with a matrix of 3 x 3 CCD for an active surface of 315 x 315 mm^2 and 9.4 mega pixels resolution. The data collection was performed under helium flux instead of atmospheric air, since the lower atomic number of helium decreases attenuation effects as discussed in Chapter 2 (Section 2.4).

Complete X-ray diffraction data sets were collected from two single HEWL crystals grown on chip in the presence of 1.5 M NaCl and 100 mM CH_3COONa pH 4.0 at 293 K. The protein concentration was 30 mg mL^{-1} in distilled water and the MWCO of the RC dialysis membrane was 6 – 8 kDa. The crystal morphology was cubic and the approximate size was 200 µm along each axis. The 3D printed support enabled data collection with an angular range of - 40° to + 40° around the crystal axis. The diffraction images were collected with 1° oscillation per exposure and 30 s exposure time. The observed reflections were processed, indexed and integrated using XDS[6], while the program Phaser[7] of the CCP4 suite was used for molecular replacement and determination of the phases for model building. The coordinates of the PDB entry 193L were used for the molecular replacement. Phenix[8] was used for refinement and the final protein model was inspected with COOT[9]. The analysis of the diffraction data sets was accomplished with the help of Dr. Franck Borel (Synchrotron Group, IBS, Grenoble). The crystallographic statistics for each HEWL crystal are provided in Table 4.1.1 reproduced from Jaho *et al*.[10].

Due to the high symmetry of HEWL crystals, complete data sets can be obtained from single crystals providing sufficient information for molecular replacement and refinement. For each crystal used for this experiment, 80 diffraction images were collected in total, with 1° oscillation per exposure at an angular range of - 40° to + 40° around the crystal axis. However, for the data analysis of the first crystal (column 2, Table 4.1.1) and the second crystal (column 2, Table 4.1.1) only 40 and 30 diffraction frames were used, respectively. The diffraction signal was slightly deteriorated during the collection of the last diffraction frames for each data set, presumably due to radiation damage provoked by the relatively long exposure time to X-ray radiation, which was 30 s per frame. The radiation damage on the HEWL crystals used for *in situ* X-ray diffraction at room temperature is discussed in Section 4.3 of this chapter and some interesting simulations and statistics are provided therein. The serial data collection strategy is a viable approach to overcome the issues rising from radiation damage and the degradation of the diffraction signal. In order to evaluate the possibility of the SSX approach from multiple crystals grown on the microchip, the two data sets from the single HEWL crystals were merged

providing better statistics and the results are included in the fourth column of Table 4.1.1. All the values in Table 4.1.1 provided in parentheses correspond to the highest resolution shell.

Table 4.1.1: *In situ* X-ray diffraction data collection parameters and refinement statistics of HEWL crystals grown on chip via microdialysis. The fourth column corresponds to values obtained after merging the data sets of the two single crystals. Values in parentheses correspond to the highest resolution shell. Reproduced from Jaho *et al*.[10]

Data collection			
Number of crystals	1	1	2
Number of diffraction frames	40	30	70
Oscillation (°) per exposure	1	1	
Exposure time (s)	30	30	
Space group	$P4_32_12$	$P4_32_12$	$P4_32_12$
Unit cell parameters	a=78.86 Å b=78.86 Å c=37.87 Å α=β=γ= 90.0°	a=79.17 Å b=79.17 Å c=37.95 Å α=β=γ= 90.0°	a=78.47 Å b=78.47 Å c=37.65 Å α=β=γ= 90.0°
Resolution range (Å)	27.31 – 1.95 (2.02 – 1.95)	27.39 – 1.96 (2.03 – 1.96)	27.17 – 1.85 (1.91 – 1.85)
Mosaicity (°)	0.319	0.121	
Total reflections (observed)	25127 (3552)	19991 (3001)	
Unique reflections (observed)	8641 (1357)	8295 (1321)	10404 (975)
Redundancy	2.90 (2.61)	2.41 (2.27)	
Completeness (%)	95.0 (94.8)	91.9 (93.3)	98.23 (93.15)
Mean I/σ	6.83 (1.16)	7.09 (1.66)	3.7
$CC_{1/2}$	99.1 (42.4)	97.9 (37.0)	97.0
R-merge			0.184
R-pim			0.116
R-meas	0.139	0.221	0.219
Refinement			
Reflections used in refinement	8645 (787)	8451 (857)	10391 (965)
Reflections used for R-free	864 (78)	846 (85)	1039 (96)
R-work	0.1988 (0.2968)	0.1853 (0.2872)	0.1839 (0.3102)
R-free	0.2430 (0.3437)	0.2297 (0.3622)	0.2207 (0.3703)
Number of non-hydrogen atoms	1069	1071	1096
macromolecules	1012	1012	1012
water	55	57	82
ligands	2	2	2
Protein residues	131	131	131
rms (bonds, Å)	0.008	0.009	0.005
rms (angles, °)	1.17	1.26	1.05
Ramachandran favored (%)	98.43	97.64	99.21
Ramachandran allowed (%)	1.57	2.36	0.79
Ramachandran outliers (%)	0.00	0.00	0.00
Average B-factor	34.26	28.54	24.34
protein	33.94	28.14	23.62
water	40.23	35.57	33.16
ligands	33.23	29.63	24.77

Electron density maps for a single HEWL crystal and the merged data set of the two crystals were obtained at 1.95 Å (Figure 4.1.5 (a)) and 1.84 Å (Figure 4.1.5 (b)) resolution, respectively. The maps were contoured at 1σ. Detailed structural information obtained by *in situ* X-ray diffraction experiments conducted at room temperature on the microchips are shown in both density maps. The structure refinement worked successfully as indicated by the R-work factor with values of 0.19 and 0.18 for the two single HEWL crystals and 0.18 for the merged data set respectively, and the R-free factors of 0.24 and 0.22 for the two single HEWL crystals and of 0.22 for the merged data set, respectively. High quality data can be obtained through *in situ* X-ray diffraction at room temperature using the dialysis chip and the serial data collection strategy is a feasible approach. The results of the *in situ* X-ray diffraction experiments discussed in this section were published recently[10].

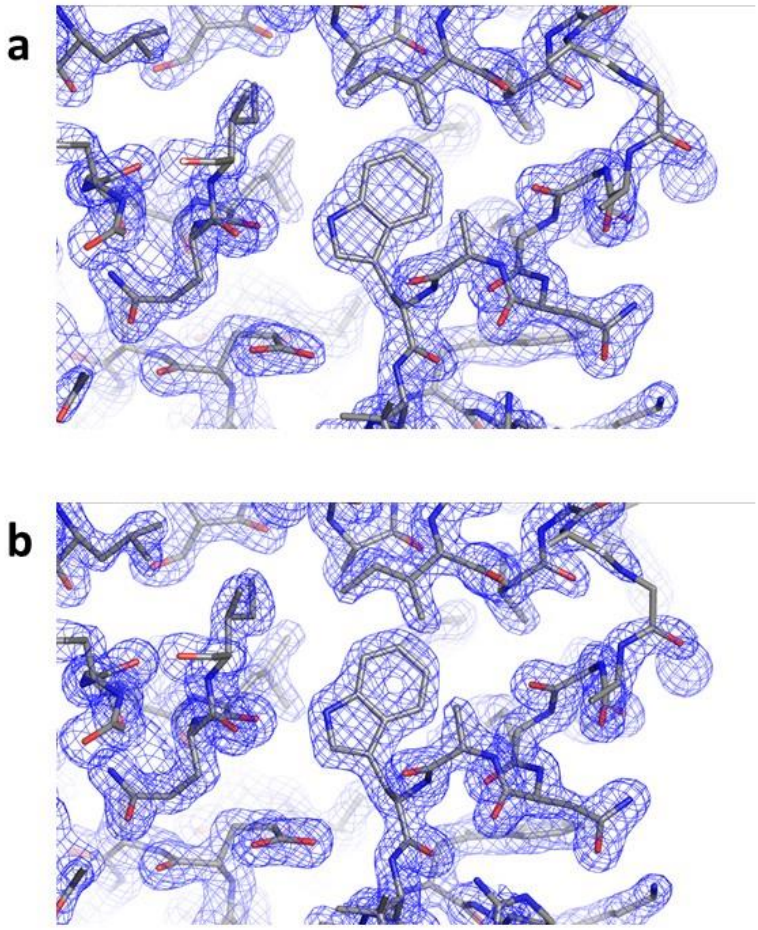

Figure 4.1.5: Electron density maps of the refined HEWL structure from (a) a single and (b) the merged data set of two crystals grown on chip via microdialysis at 293 K. The maps were calculated at 1.95 Å and 1.84 Å, respectively, and contoured at 1σ. Reproduced from Jaho *et al*.[10]

4.1.1.3 Crystallization with the LCP method

In Chapter 1, two approaches for membrane protein crystallization were discussed. The *in surfo* method (Section 1.1.4.1) relies on the use of amphiphilic detergents. Membrane proteins can be solubilized in the detergent micelles mimicking the natural lipid bilayer where membrane proteins reside. Then, the complex of membrane protein and detergent molecules can be crystallized in aqueous solutions using conventional crystallization techniques, such as vapor diffusion, dialysis, etc. The second approach of *in meso* crystallization (Sections 1.1.4.2 – 1.1.4.5) relies on the spontaneous self-assembly of lipids and detergents in vesicles, discoidal micelles or bicelles and liquid crystals or mesophases. The LCP method uses the bicontinuous cubic phase of monoacylglycerols when mixed with water in specific temperature and concentration conditions to reconstitute the protein in the lipidic bilayer. It should be mentioned that in the case of membrane proteins, the protein sample contains also detergent molecules used to solubilize the protein during production and purification. However, the LCP method has been successfully used for the crystallization of soluble proteins at 293 K, as for example chicken egg white lysozyme (CEWL)[11].

The most commonly used lipids with the LCP method are the *cis* monounsaturated monoacylglycerols (MAGs). The phase diagram of monoolein (9.9 MAG) has been extensively studied in the literature and the equilibrium temperature-composition phase diagram of the monoolein-water system is provided in Figure 1.1.7 (Section 1.1.4.4). The Pn3m cubic phase for LCP crystallization is formed at a composition of 40 % water and 60 % monoolein at 293 K. In the current chapter, monoolein was used to investigate the compatibility of the dialysis chip with the LCP crystallization method in combination with microdialysis. In the following sections, the procedure of setting up crystallization trials on the microchip using lipidic cubic phases is presented and it is based on the detailed protocol provided by Caffrey and Cherezov[12]. Moreover, the results of on chip HEWL crystallization in the lipidic cubic phase of monoolein using microdialysis at room temperature are provided along with the *in situ* X-ray diffraction studies performed at the PROXIMA-2A beamline at synchrotron Soleil.

4.1.1.3.1 The on chip LCP crystallization protocol

Before starting the experiment, monoolein (Molecular Dimensions) was removed from the freezer (193 K) and set to adjust to room temperature. Then the lipid was incubated in a heating block at 315 K in order to melt and facilitate its manipulation during the following steps of the protocol. The equipment necessary to prepare the lipidic cubic phase is shown in Figure 4.1.6 and includes two Hamilton glass syringes of 100 µL volume each for loading the molten lipid and the protein sample, one 10 µL Hamilton syringe for sample delivery, needles and ferrules for air tight connections (Figure 4.1.6 (a)), one dispenser (PB600-1 from Hamilton) for delivering the cubic phase on the chip and one coupler (Molecular Dimensions) for mixing the lipid with the protein solution to form the cubic phase (Figure 4.1.6 (b)).

First, the plunger was removed from one of the 100 µL Hamilton syringes and the molten lipid was loaded into the barrel from the plunger end with a pipette. For the experiments presented in this section, 40 µL of monoolein were used. The plunger was placed back into the barrel of the syringe without pushing the lipid and the syringe was held in a vertical

position. Then, the coupler, bearing ferrules at both ends, was carefully positioned and screwed to the open end of the syringe containing the lipid. Once the coupler was tightened, the lipid was pushed with the plunger inside the barrel of the syringe until the open end of the small needle of the coupler. The lipid-loaded syringe was ready and it was set aside while the second 100 µL Hamilton syringe was being prepared for the protein sample. It is recommended to heat all the pieces of equipment (Hamilton syringe, coupler, ferrules) used for the preparation of the lipid syringe in order to avoid potential solidification of the lipid due to a temperature difference between the lipid (approximately 315 K) and the equipment at room temperature (293 K).

The volume of the protein solution that should be used to form cubic phase with monoolein at full hydration was calculated. As already explained, the Pn3m cubic phase of monoolein is formed at a composition of 40 % water and 60 % monoolein at 293 K. These percentages refer to mass or volume ratios assuming that the density of water and monoolein at 293 K are close to 1 g mL^{-1} (0.998 g mL^{-1} and 0.942 g mL^{-1}, respectively)[12]. Thus, for 40 µL of monoolein, 26.7 µL of protein should be loaded in the second Hamilton syringe. The concentration of HEWL was 40 mg mL^{-1} in distilled water. Before loading the protein, it is important to centrifuge the sample for 2 – 5 min at 293 K to remove aggregates. The procedure of loading the protein solution is similar to the procedure described for loading the lipid. The plunger was removed from the second Hamilton syringe and 26.7 µL of HEWL were loaded into the barrel from the plunger end with a pipette. The plunger was placed back into the barrel of the syringe and the protein solution was pushed until the open end of the glass syringe where a meniscus formed by the solution should be visible. Then, the protein syringe was screwed to the open end of the coupler attached to the lipid syringe. By the way that both syringes were prepared, the lipid volume at the open end of the coupler is in direct contact with the protein volume at the open end of the protein syringe, ensuring that there is no dead volume before starting the mixing step. When loading the syringes, it is important to avoid entrapping air bubbles. If this happens, the syringe is held in vertical position and the plunger is moved up and down to remove the air bubbles. It is recommended to avoid over- or under-tightening the syringes and the coupler, otherwise the ferrules might be damaged or leakages might occur.

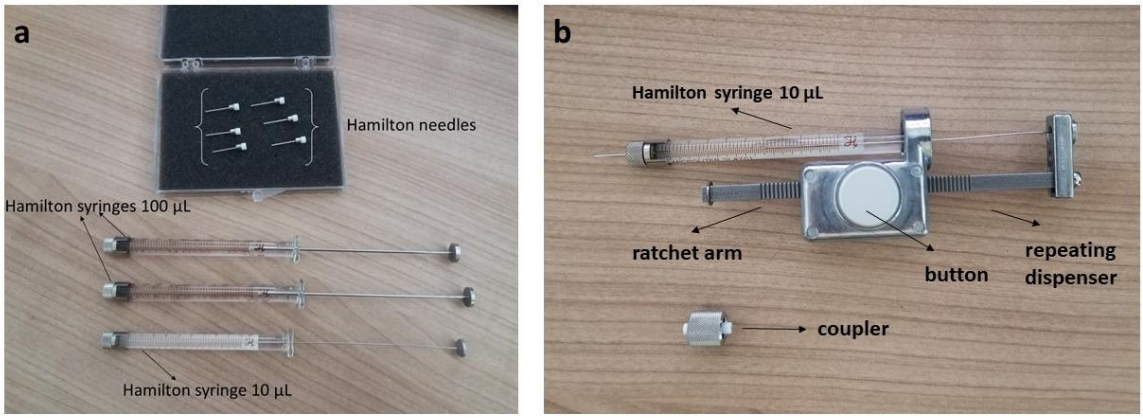

Figure 4.1.6: The equipment for preparing mesophases for crystallization experiments with the LCP method including (a) Hamilton glass syringes and needles and (b) a coupler and a repeating dispenser.

To initiate mixing, the plunger of the protein syringe was pushed to its limit driving the protein sample through the coupler towards the lipid syringe. An equal and opposite movement of the plunger in the lipid syringe occurred. Then, the plungers of the two syringes were moved back and forth alternately, using the thumb or index fingers, in order to properly mix and homogenize the protein-lipid mixture and form the cubic phase. When the mixing process starts, non-uniform and cloudy regions can be visible within the protein-lipid mixture, while moving the plungers of the glass syringes is difficult. However, at the end of the process, if mixing is performed properly, the mesophase should be homogeneous and optically transparent in the syringe barrel (Figure 4.1.7). In this case, moving the plungers requires less effort. The protein is reconstituted into the lipid bilayer and the cubic mesophase is formed and ready to be used for crystallization experiments.

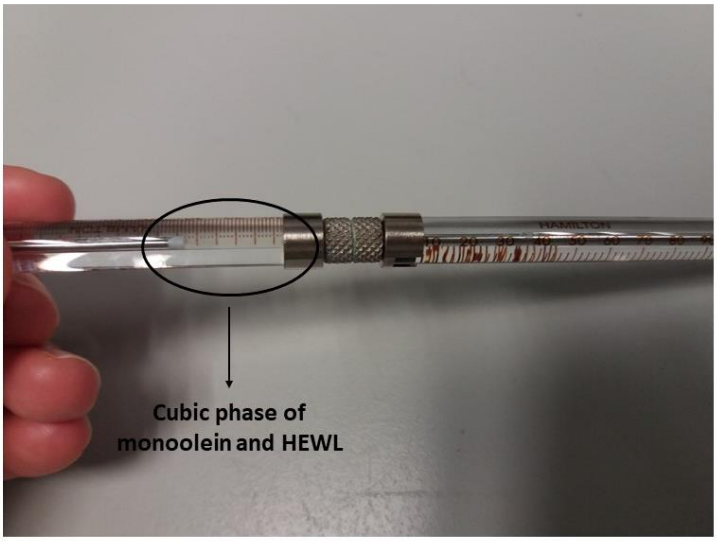

Figure 4.1.7: The optically transparent cubic mesophase prepared by mixing monoolein and HEWL solution (40 mg mL^{-1}) in a 3:2 volume ratio at 293 K.

For distributing the cubic mesophase within the protein reservoir of the dialysis chip, a repeating dispenser and the 10 µL Hamilton syringe (Figure 4.1.6 (b)) were used. First, the empty dispensing syringe (10 µL) was positioned on the holding ring of the repeating dispenser and the plunger of the syringe was positioned and slightly screwed in a small ring at the top end of the dispenser. The plunger was moved until the zero graduation mark of the barrel by moving the ratchet arm (Figure 4.1.6 (b)). The next step was to transfer the mesophase from the 100 µL syringe used during mixing to the dispensing syringe already accommodated on the dispenser. Therefore, the empty 100 µL syringe was disconnected from the coupler and the mesophase-loaded syringe with the coupler still attached to it was connected to the dispensing syringe. Then, simply by pushing the plunger of the 100 µL syringe, the mesophase was transferred through the coupler towards the dispensing syringe, moving the plunger of the dispensing syringe upwards. Once loading was accomplished, the assembly of the coupler and the mixing syringe were disconnected and a flat-tipped needle was tightened to the front end of the dispensing syringe, as shown in Figure 4.1.6 (b). In order to fill the void volume of

the needle, the button on the ratchet arm was pressed several times to advance the plunger in the barrel of the syringe until a string of the mesophase emerged at the tip of the needle. The dispensing assembly was then used to set up the crystallization experiments. It should be noted that the button on the ratchet arm is used for dispensing predefined volume of the mesophase every time that it is pressed. When used with a 10 µL syringe, the dispensing volume of the mesophase bolus is 0.2 µL at every repetition. This volume is compatible with the chip design where the protein reservoir volume is 0.3 µL. Automated, robotic systems developed for LCP crystallization screening on plates can dispense boluses down to 50 nL volume[13].

4.1.1.3.2 On chip HEWL crystallization with the LCP method

Several experiments were conducted to evaluate the compatibility of the dialysis chip with the LCP crystallization method. The experiments illustrated in Figure 4.1.8 were performed at 293 K. The volume of the protein reservoir was 0.3 µL and the volume of the mesophase bolus dispensed on the reservoir was 0.2 µL. The cubic mesophase was prepared by mixing monoolein and HEWL in a 3:2 volume ratio as described in Section 4.1.1.3.1. The protein concentration was 40 mg mL^{-1} in distilled water. The MWCO of the RC dialysis membrane in the chip was 6 – 8 kDa. The crystallization solution was continuously flowing within the fluidic channel of the chip at a constant inlet pressure of 50 mbar using the pressure-driven fluidic system with the MicroCrys platform. It should be mentioned that during conventional crystallization experiments with the LCP method set on glass plates designed for *in meso* crystallization, the crystallization solution is added on top of the mesophase bolus. For the experiments performed on the dialysis chip, the crystallization solution was circulating only within the fluidic channel and the precipitant molecules were diffusing through the RC membrane towards the protein reservoir where the mesophase bolus was dispensed. Thus, the combination of *in meso* and dialysis on chip crystallization were evaluated simultaneously.

The crystals shown in Figure 4.1.8 (a) were grown in the presence of 0.7 M NaCl, 100 mM CH_3COONa pH 4.0 and 4 % PEG 400 and the crystals in Figure 4.1.8 (b) were grown in 0.8 M NaCl, 100 mM CH_3COONa pH 4.0 and 8 % PEG 400. In both experiments, multiple micro-crystals with an average size of 10 – 20 µm were grown allowing a serial data collection strategy for the *in situ* X-ray diffraction experiments carried out at RPOXIMA-2A beamline (Soleil). However, doubling the PEG concentration from 4 % to 8 % has a dramatic effect on the crystal population. In the center of Figure 4.1.8 (b), the crystal population is so dense that it is practically difficult to visualize separate crystals. On the contrary, the crystals in Figure 4.1.8 (a) can be distinguished even if they are numerous. In order to eliminate the effect of PEG 400 on the supersaturation, a solution containing only 1 M NaCl and 100 mM CH_3COONa pH 4.0 was prepared and the formed HEWL crystals are shown in Figure 4.1.8 (c). In this case, the crystals are slightly larger, in the range of 20 – 50 µm, but still numerous and well distributed along the protein reservoir. The HEWL crystals shown in Figure 4.1.8 (a), 4.1.8 (b) and 4.1.8 (c) were captured 3 h, 1.5 h and 24 h, respectively, after starting the experiment. The scale bar represents 100 µm.

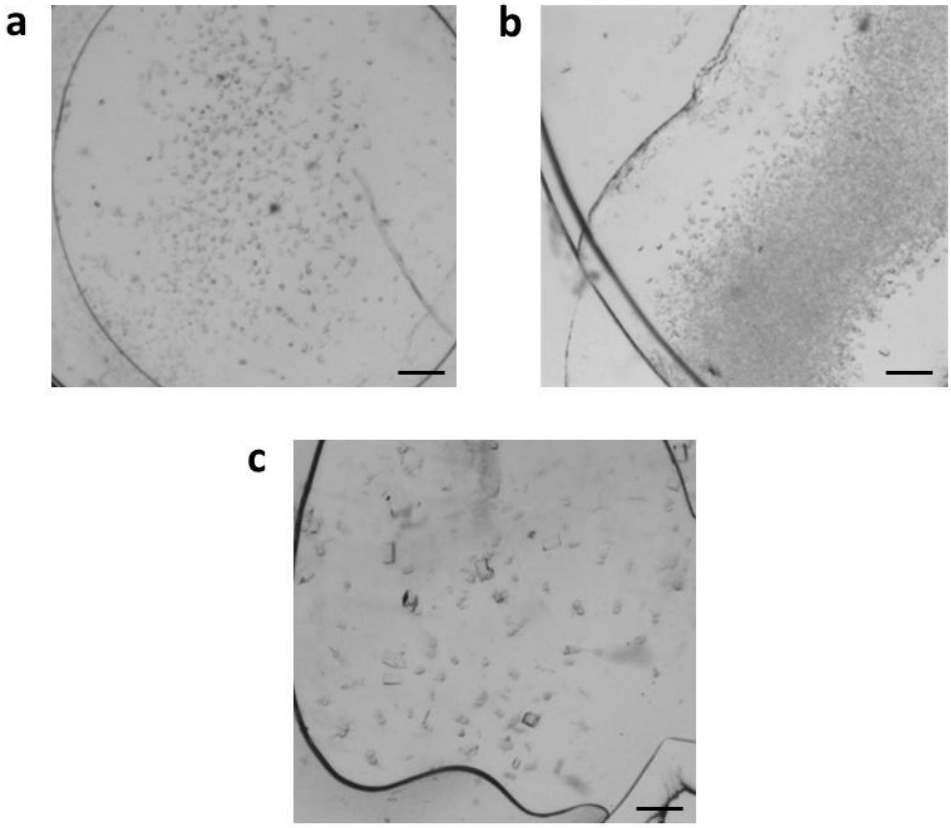

Figure 4.1.8: HEWL crystals grown on chip with the LCP method at 293 K in (a) 0.7 M NaCl, 100 mM CH_3COONa pH 4.0 and 4 % PEG 400, (b) 0.8 M NaCl, 100 mM CH_3COONa pH 4.0 and 8 % PEG 400 and (c) 1 M NaCl and 100 mM CH_3COONa pH 4.0. The scale bar represents 100 µm.

4.1.1.4 *In situ* serial X-ray crystallography experiments

In situ X-ray diffraction data from HEWL crystals grown on chip with the LCP method were collected at PROXIMA-2A beamline[14] at synchrotron Soleil. The microchips were mounted on the beamline with the aid of the 3D printed support (Figure 3.2.3, Chapter 3). The support for the chips is shown in Appendix 4.4 as mounted on POXIMA-2A and BM30A-FIP beamlines. PROXIMA-2A beamline, compatible with in plate X-ray crystallography experiments, is equipped with a robotic arm to hold the support in front of the X-ray beam[15]. The data collection on the microchips was carried out at room temperature. The X-ray energy during on chip data collection was 12.65 keV (0.98 Å), the flux was approximately 10^{12} ph s^{-1} and the beam size was 5 µm x 10 µm. The diffraction images were collected with the EIGER X 9M detector (Dectris) with an active surface of 233 x 245 mm^2 and a resolution of approximately 10 mega pixels.

Partial X-ray diffraction data sets were collected from 32 small, isomorphous HEWL crystals grown on chip with the LCP method in the presence of 0.7 M NaCl, 100 mM CH_3COONa pH 4.0 and 4 % PEG 400. The partial data sets were merged to a full data set confirming the compatibility of the dialysis chip with the *in situ* serial data collection approach. The protein

concentration was 40 mg mL^{-1}. The crystals are shown in Figure 4.1.9 (a) as captured with the beamline camera during the data collection. The cross is located on the crystal that has been selected for data collection and the scale bar corresponds to 100 µm. The micro-focus beam on PROXIMA-2A was a suitable selection for the micro-crystals grown on chip with the LCP method. Each crystal was rotated around its axis for 35° in total and each diffraction image was collected after 0.1° rotation and 0.01 s exposure time. The electron density map of the merged data set was obtained at 2.6 Å resolution (Figure 4.1.9 (b)) and the crystallographic statistics are provided in the second column of Table 4.1.2. The data analysis was carried out at Soleil synchrotron by Dr. Serena Sirigu (PROXIMA-2A beamline). Detailed structural information obtained by *in situ* serial X-ray diffraction experiments conducted at room temperature on the microchips are shown in the density map. The structure refinement worked successfully as indicated by the R-work factor of 0.18 and the R-free factor of 0.23. However, it should be mentioned that the refinement statistics in Table 4.1.2 do not correspond to final values and could be further improved by running the refinement process more times.

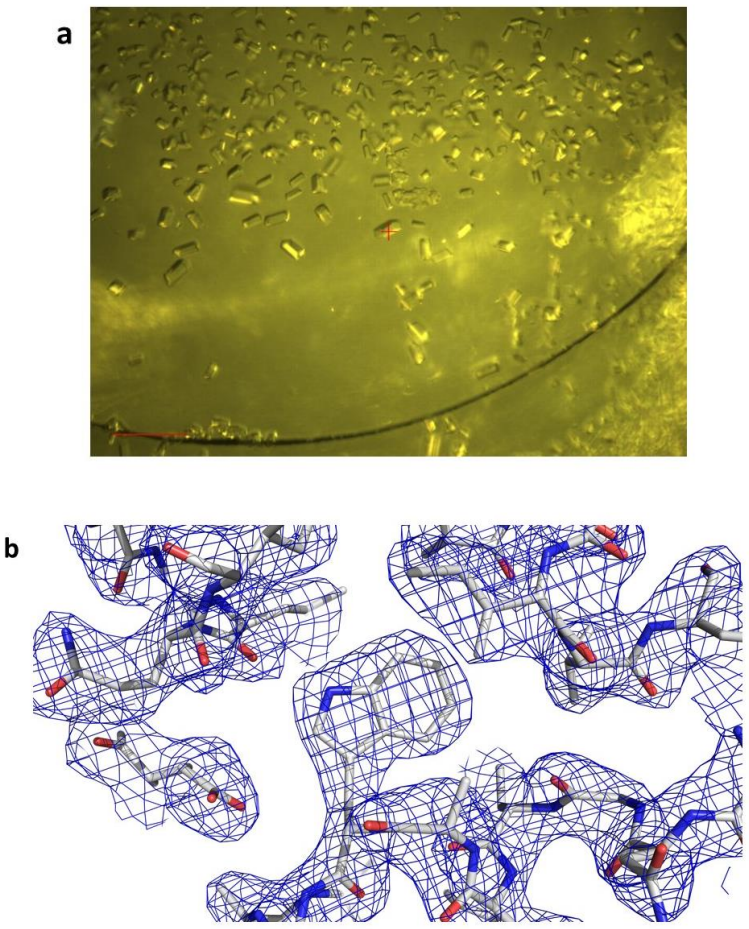

Figure 4.1.9: (a) Numerous, isomorphous HEWL crystals grown on chip with the LCP method during *in situ* serial X-ray diffraction data collection at room temperature at the PROXIMA-2A beamline. The scale bar represents 100 µm. (b) Electron density map of the refined HEWL structure from the merged data sets of multiple crystals grown on chip with the LCP method at 293 K. The map was calculated at 2.6 Å resolution and contoured at 1σ.

Table 4.1.2: *In situ* X-ray diffraction data collection parameters, processing and refinement statistics of the merged data sets from multiple HEWL crystals grown on chip with the LCP method (second column) and Thaumatin crystals (third column). Values in parentheses correspond to the highest resolution shell.

Protein	**HEWL_LCP**	**Thaumatin**
Data collection and processing		
Number of crystals	32	10
Total oscillation (°) range	35	35
Oscillation (°) per exposure	0.1	0.1
Exposure time (s)	0.01	0.01
Temperature (K)	293	293
Space group	$P4_32_12$ (96)	$P4_12_12$ (92)
Unit cell parameters	a=79.19 Å b=79.19 Å c=38.24 Å α=β=γ= 90.0°	a=58.58 Å b=58.58 Å c=151.54 Å α=β=γ= 90.0°
Resolution range (Å)	50.0 – 2.6 (2.67 – 2.60)	50.0 – 1.8 (1.85 – 1.80)
Completeness (%)	100 (100)	99.4 (92.8)
I/σ	12.17 (1.45)	31.11 (4.42)
$CC_{1/2}$	99.5 (47.6)	99.9 (98.1)
R_{sym}	33.1 (146.6)	21.9 (86.9)
Multiplicity	24.46 (8.07)	184.6 (61.6)
Number of reflections	3844	23941
Refinement		
Resolution range (Å)	39.60 – 2.60 (2.67 – 2.60)	46.34 – 1.8 (1.85 – 1.80)
R_{work} / R_{free} (%)	18.70 / 23.71 (34.4 / 44.4)	17.00 / 19.87 (31.2 / 32.8)
Mean B-factor ($Å^2$)	42.78	30.98
r.m.s deviations Bond lengths (Å) / Bond angles (°)	0.008 / 1.69	0.013 / 1.75

4.1.2 Thaumatin from *Thaumatococcus danielli*

As discussed in Section 4.1.1, conventional crystallization methods were applied for a preliminary screening of crystallization conditions before setting up experiments on the dialysis chips. In the case of Thaumatin, the hanging drop vapor diffusion method was used to evaluate the effect of protein and precipitant concentration on the crystal size and shape distribution. All experiments were performed at 293 K. Figure 4.1.10 illustrates some representative results of Thaumatin crystallization with vapor diffusion hanging drops. The protein volume was mixed with the crystallization solution in a 1:1 ratio. The characteristic bipyramidal Thaumatin crystals shown in Figure 4.1.10 (a) and Figure 4.1.10 (b) grew in the presence of 0.8 M sodium potassium tartrate ($C_4H_4KNaO_6$) and 50 mM ADA ($C_6H_{10}N_2O_5$) pH

6.5 and the protein concentration was approximately 19 mg mL^{-1} and 41 mg mL^{-1}, respectively. Increasing the concentration of the protein sample increases the supersaturation and the nucleation rate, resulting in the formation of numerous crystals. Both photos were taken at the same time (5 days from the beginning of the experiment) and the scale bar represents 100 µm. More examples of Thaumatin crystals grown with conventional methods can be found in Appendix 4.2.

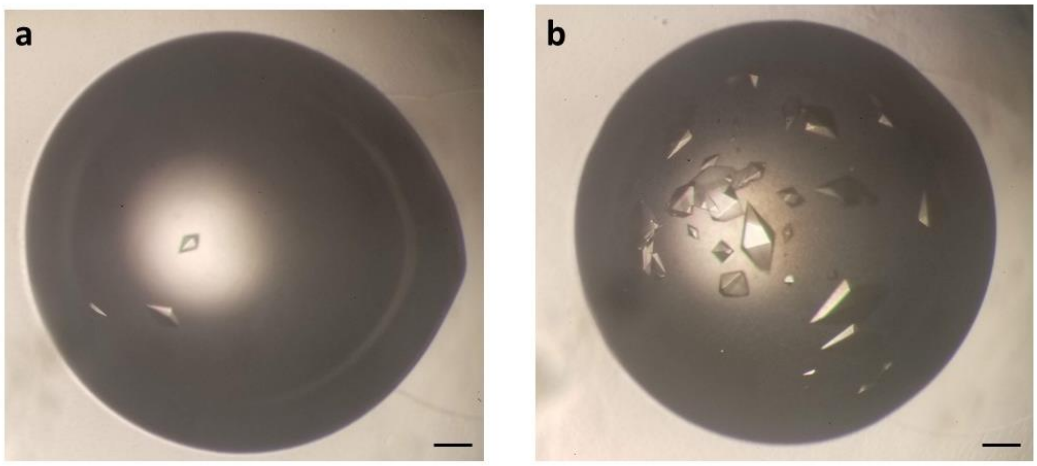

Figure 4.1.10: Thaumatin crystals grown with the hanging drop method at 293 K in 0.8 M sodium potassium tartrate and 50 mM ADA pH 6.5. The protein concentration was (a) 19 mg mL^{-1} and (b) 41 mg mL^{-1}. The scale bar represents 100 µm.

Several experiments were conducted to evaluate the effect of protein and precipitant concentration on the crystallization of Thaumatin with the microdialysis method on the microfluidic chips. The experiments illustrated in Figure 4.1.11 were performed at 293 K under the same protein and precipitant concentration conditions as the hanging drop experiments described in Figure 4.1.10. Specifically, the crystals shown in Figure 4.1.11 (a) and Figure 4.1.11 (b) were grown in the presence of 0.8 M sodium potassium tartrate and 50 mM ADA pH 6.5 and the protein concentration was approximately 19 mg mL^{-1} and 41 mg mL^{-1}, respectively. The volume of the protein reservoir was 0.3 µL and the MWCO of the RC membrane was 6 – 8 kDa. The crystallization solution was continuously circulating within the fluidic channel at a constant inlet pressure of 50 mbar using the pressure-driven fluidic system. The scale bar represents 100 µm. Both pictures were captured 1 day after the onset of the experiments using the MicroCrys platform. Doubling the concentration of the protein sample increases significantly the supersaturation and the nucleation rate, resulting in the formation of multiple crystals. In fact, the Thaumatin crystals illustrated in Figure 4.1.11 (b) have created a densely populated region within the protein reservoir where only the crystals at the edges of this region can be distinguished. Moreover, their shape is not clearly defined as opposed to the bipyramidal crystals shown in Figure 4.1.11 (a). Similar crystallization experiments were performed on chip at the same protein concentration values (19 mg mL^{-1} and 41 mg mL^{-1}) but higher precipitant concentration (1 M sodium potassium tartrate) and the results are included in Appendix 4.2.

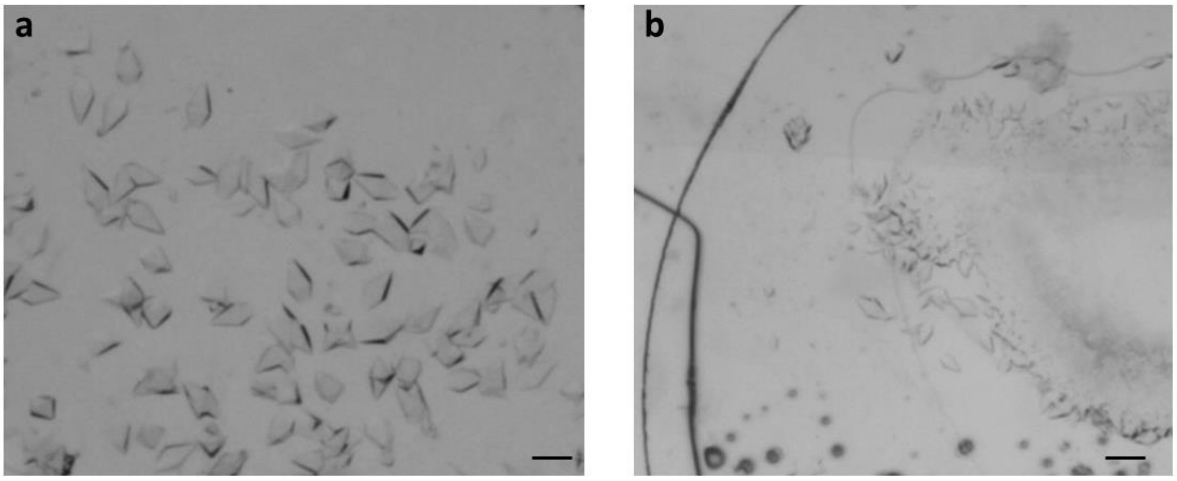

Figure 4.1.11: Thaumatin crystals grown on chip with the microdialysis method at 293 K in 0.8 M sodium potassium tartrate and 50 mM ADA pH 6.5. The protein concentration was (a) 19 mg mL^{-1} and (b) 41 mg mL^{-1}. The scale bar represents 100 µm.

4.1.2.1 *In situ* X-ray serial crystallography experiments

The *in situ* X-ray diffraction experiments with the Thaumatin crystals grown on chip were performed at PROXIMA-2A beamline under the same experimental parameters described in Section 4.1.1.4. The Thaumatin crystal shown in Figure 4.1.12, as captured during data collection with the beamline camera, was gown in the presence of 0.8 M sodium potassium tartrate and 50 mM ADA pH 6.5 at 293 K. Specifically, the cross in Figure 4.1.12 (a) shows the position of the crystal chosen for exposure to X-rays. The effect of radiation damage on the crystal is noticeable in Figure 4.1.12 (b) where a hole is left on the position chosen in Figure 4.1.12 (a) after irradiation. The scale bar represents 100 µm. Diffraction data were collected from 10 Thaumatin crystals and merged to a complete data set. Each crystal was rotated around its axis for 35° in total and each diffraction image was collected after 0.1° rotation and 0.01 s exposure time. The electron density map of the merged data sets was obtained at 1.8 Å resolution (Figure 4.1.13) and the crystallographic statistics are provided in the third column of Table 4.1.2. The data analysis was carried out at Soleil synchrotron by Dr. Serena Sirigu (POXIMA-2A beamline). The structure refinement worked successfully as indicated by the R-work factor of 0.17 and the R-free factor of 0.19. As for the case of HEWL grown with the LCP method (Section 4.1.1.4), it should be mentioned that the refinement statistics in Table 4.1.2 do not correspond to final values and could be further improved by running the refinement process more times.

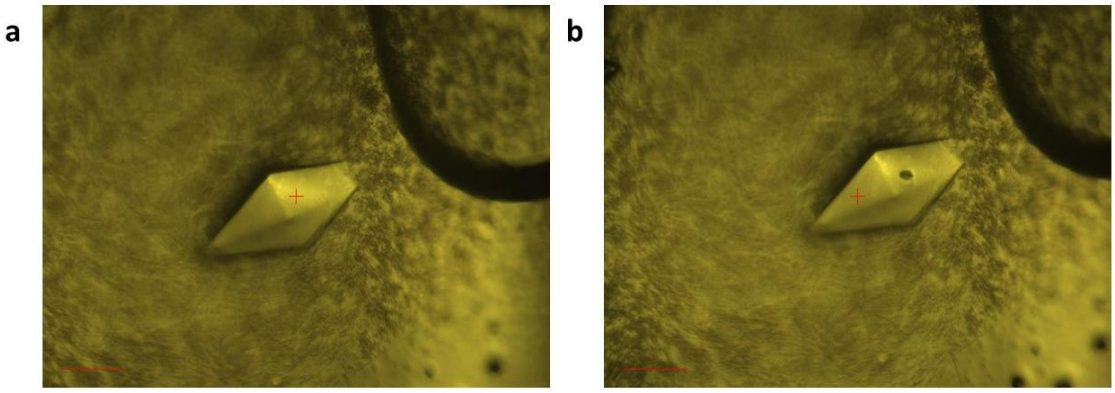

Figure 4.1.12: Thaumatin crystal on chip (a) before and (b) after exposure to X-rays during *in situ* serial data collection at room temperature at the PROXIMA-2A beamline. The effect of radiation damage is detectable by the hole left on the crystal site after irradiation. The scale bar represents 100 µm.

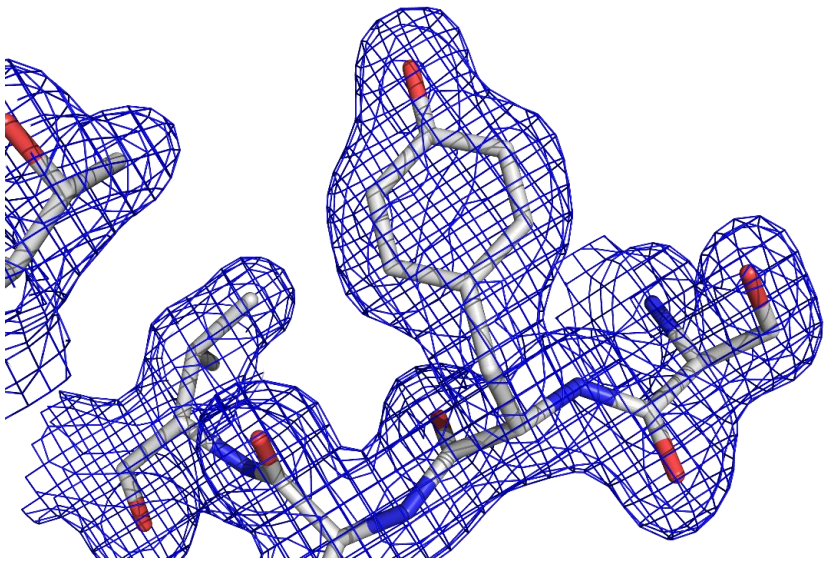

Figure 4.1.13: Electron density map of the refined Thaumatin structure from the merged data sets of multiple crystals grown on chip with the microdialysis method at 293 K. The map was calculated at 1.8 Å resolution and contoured at 1σ.

4.2 On chip crystallization of membrane proteins

Several membrane proteins were used for on chip crystallization with the microdialysis method and *in situ* X-ray diffraction studies. The multidrug efflux transporter AcrB from *Escherichia coli* and the TonB-dependent outer membrane transporter ShuA from *Shigella dysenteriae* are produced and purified in our laboratory at IBS (Institute de Biologie Structurale, Grenoble). The purification protocols were developed and optimized by Elham Vahdatahar (GSY group, IBS) as a major part of her PhD thesis entitled "Optimization of crystal growth of membrane proteins for advanced diffraction techniques" with the contribution of Dr. David Cobessi (GSY group, IBS). The calcium-transporting ATPase SERCA from *Oryctolagus cuniculus* was provided for on chip crystallization experiments by Dr. Samuel J. Hjorth-Jensen and Prof. Poul Nissen from the Department of Molecular Biology and Genetics – DANDRITE (Aarhus University, Denmark) and the sodium-pumping TmPPase from *Thermotoga maritima* was provided by Jannik Strauss and Prof. Adrian Goldman from the Astbury Centre for Structural Molecular Biology (University of Leeds, UK). For all the crystallization experiments carried out on chip with membrane proteins, the MWCO of the RC dialysis membrane integrated within the device was 12 – 14 kDa as high molecular weight PEG solutions were frequently used as precipitants. This MWCO is sufficient to retain the protein within the protein reservoir of the chip and allow the molecules of the crystallization solutions (salts, buffers, PEGs or glycerol) to diffuse from the fluidic channel towards the protein reservoir.

4.2.1 AcrB from *Escherichia coli*

Membrane protein crystallization on the dialysis chips was more challenging than the crystallization of model soluble proteins discussed in Section 4.1. Crystallization trials with conventional methods preceded the on chip experiments. The hanging drop vapor diffusion method was used for preliminary screening of crystallization conditions for AcrB to evaluate the effect of protein and precipitant concentration or the impact of additives on the crystal size, shape or population. Some results are shown in Figure 4.2.1 and Figure 4.2.2. For these experiments, I performed the production and purification of the protein sample and the respective protocols are provided in Appendix 4.5. AcrB was solubilized in 0.02 % v/v DDM (Anatrace) detergent and after purification 1 mL of protein with a concentration of 12.89 mg mL^{-1} was acquired. The hanging drops were prepared by mixing 2 µL of protein with 2 µL of the precipitant solution and the volume of the reservoir solution was 500 µL. All experiments were performed at 293 K. All photos were taken 1 week from the beginning of the experiment and the scale bar represents 100 µm. The native AcrB crystals shown in Figure 4.2.1 (a) grew in the presence of 8 % v/v PEG 3350 and 100 mM lithium sulphate ($LiSO_4$) and the crystals in Figure 4.2.1 (b) grew in the presence of 8 % v/v PEG 3350 and 100 mM magnesium sulphate ($MgSO_4$). In both experiments the concentration of the precipitant (PEG 3350) was the same but the impact of the buffer composition on the crystal size and morphology was evident. Numerous, relatively small, needle-like and pyramidal crystals grew in the presence of $LiSO_4$, while $MgSO_4$ led to the formation of few larger crystals. In the latter case, the morphology of the AcrB crystals was solely pyramidal.

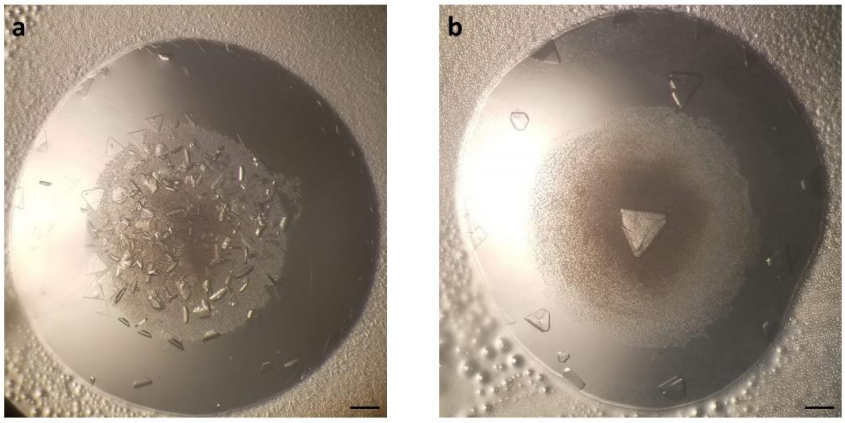

Figure 4.2.1: AcrB crystals grown with the hanging drop method at 293 K in 8 % v/v PEG 3350 and (a) 100 mM $LiSO_4$ and (b) 100 mM $MgSO_4$. The scale bar represents 100 µm.

The hanging drop method was also used to evaluate the effect of additives on the crystallization of AcrB. Rifampicin ($C_{43}H_{58}N_4O_{12}$) purchased from Sigma-Aldrich, an antibiotic used to treat bacterial infections, was added to the protein sample. The concentration of Rifampicin and AcrB was 1 mM and 12.89 mg mL^{-1}, respectively. The hanging drops were prepared by mixing 2 µL of protein with 2 µL of the precipitant solution and the volume of the reservoir solution was 500 µL. All experiments were performed at 293 K. All photos were taken 6 days from the beginning of the experiment and the scale bar represents 100 µm. The AcrB crystals shown in Figure 4.2.2 (a) and 4.2.2 (b) grew in the presence of 11 % v/v PEG 4000, 5 % v/v glycerol, 50 mM ADA pH 6.5 and 200 mM ammonium sulphate ($(NH_4)_2SO_4$). However, in Figure 4.2.2 (b) the protein sample was mixed with 1 mM Rifampicin that gives an orange color to the solution. In both experiments the morphology of the crystals is similar, including needle-like and plate-like crystals. The presence of Rifampicin led to the formation of numerous and uniformly sized crystals. More examples of AcrB crystals grown with the hanging drop are provided in Appendix 4.3.

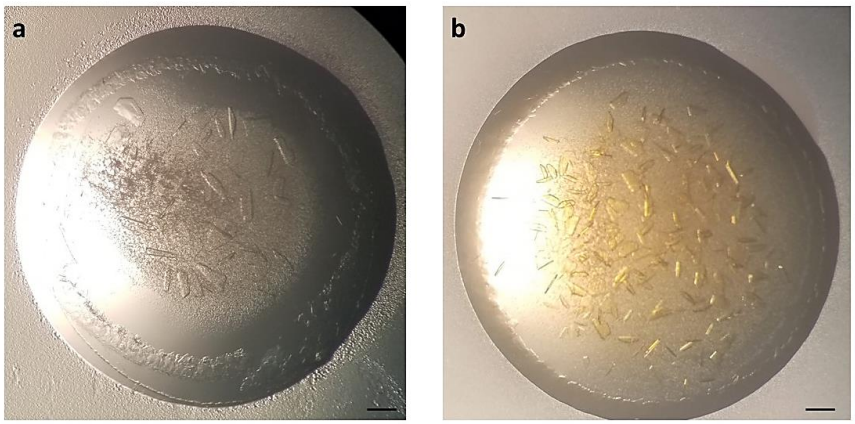

Figure 4.2.2: AcrB crystals grown with the hanging drop method at 293 K in 11 % v/v PEG 4000, 5 % v/v glycerol, 50 mM ADA pH 6.5 and 200 mM $(NH_4)_2SO_4$. (a) Native crystals and (b) crystals grown in the presence of 1 mM Rifampicin. The scale bar represents 100 µm.

4.2.1.1 On chip AcrB crystallization and *in situ* X-ray diffraction

Many experiments were performed to obtain AcrB crystals on chip with the microdialysis method and several conditions were screened. The protein concentration varied from 5 – 12 mg mL^{-1} and trials were done in the presence or absence of Rifampicin. One experiment yielding crystals is shown in Figure 4.2.3. The protein sample was provided by Elham Vahdatahar and the protein concentration was approximately 10 mg mL^{-1}. The volume of the protein reservoir was 0.3 µL and the MWCO of the RC membrane was 12 – 14 kDa. The photo was captured approximately 2 weeks from the beginning of the experiment and the scale bar is 100 µm. The AcrB crystals grew at 293 K in the presence of 10 % v/v PEG 4000, 5 % v/v glycerol, 50 mM ADA pH 6.5 and 150 mM $(NH_4)_2SO_4$. Moreover, the crystallization solution contained 0.02 % v/v DDM, the same concentration of detergent in which the protein sample was solubilized during purification. This addition of detergent in the crystallization solution was important to ensure equilibrium between the compartments and to avoid generating a concentration difference across the RC membrane resulting in dialysis of the detergent from the protein reservoir towards the fluidic channel where the crystallization solution circulates and therefore to affect the critical micelle concentration (CMC) of the detergent at which the DDM micelles form and guarantee the stability of the protein-detergent complex. To remind, the micelle size of DDM determined based on refractive index measurements is 72 ± 1.4 kDa[16]. It is noteworthy that when using the dialysis crystallization technique, it is crucial to include all the components of the protein buffer at the same concentration in the crystallization solution located in the reservoir compartment. Otherwise, these components can dialyze through the RC membrane out of the protein reservoir leading to protein precipitation or denaturation.

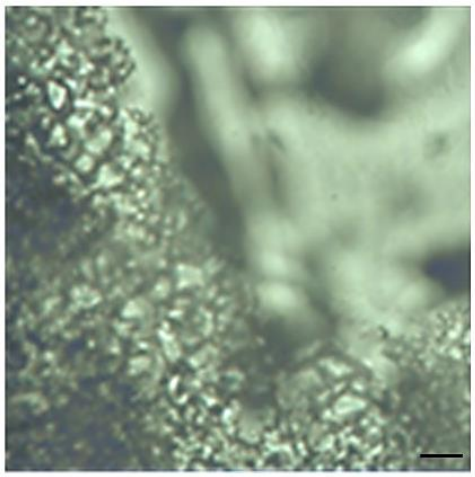

Figure 4.2.3: AcrB (10 mg mL^{-1}) crystals grown on chip via microdialysis at 293 K in 10 % v/v PEG 4000, 5 % v/v glycerol, 50 mM ADA pH 6.5 and 150 mM $(NH_4)_2SO_4$. The scale bar represents 100 µm.

Native AcrB crystals grown on chip were tested for their diffraction quality at the BL13 - XALOC beamline (ALBA synchrotron). The crystallization solution contained 10 % v/v PEG 4000, 5 % v/v glycerol, 50 mM ADA pH 6.5, 200 mM $(NH_4)_2SO_4$ and 0.02 % v/v DDM. The protein concentration was approximately 5 mg mL^{-1}, the volume of the protein reservoir was 0.1 µL and the MWCO of the RC membrane was 12 – 14 kDa. The crystallization and the *in situ* X-ray diffraction experiments were carried out at 293 K. The chip was mounted on the beamline with the aid of the 3D printed sample holder for magnetic goniometer base designed by the staff of the beamline. The X-ray wavelength during the on chip data collection was 0.98 Å (12.656 keV), the photon flux was 2 x 10^{12} ph s^{-1} and the beam size was 71 µm x 17 µm. The diffraction images were recorded with a PILATUS 6M (Dectris) detector with an active area of 424 x 435 mm^2 and 6 mega pixels resolution. The crystals diffracted weakly at a resolution lower than 14 Å, as can be seen from the diffraction pattern in Figure 4.2.4 (b). Figure 4.2.4 (a) is an image of the protein reservoir as captured with the beamline camera where the crystal used for X-ray diffraction is targeted.

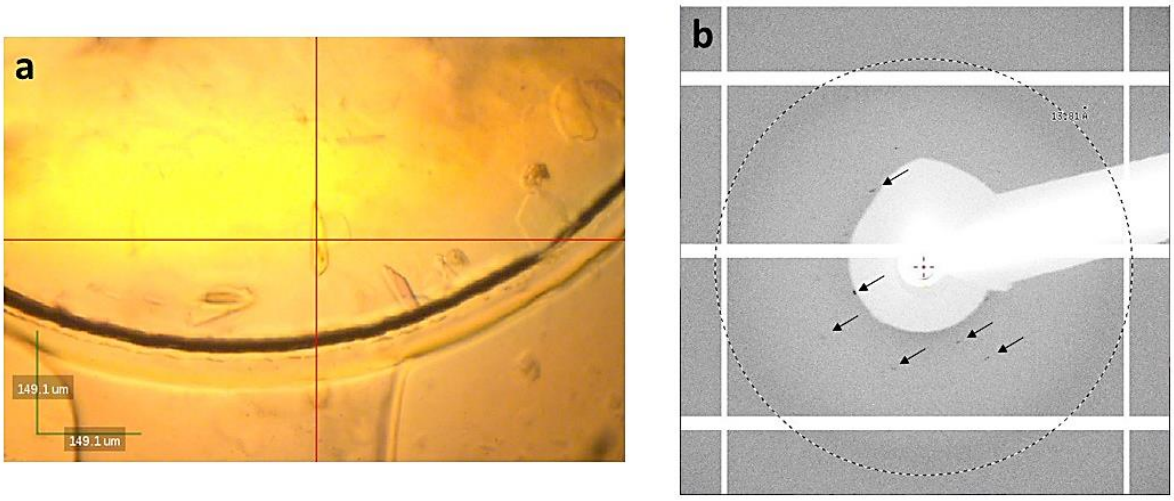

Figure 4.2.4: (a) AcrB crystals on the protein reservoir of the dialysis chip during *in situ* X-ray diffraction at BL13 - XALOC beamline (ALBA). (b) Diffraction image of AcrB crystals grown on chip. The diffraction spots are indicated with arrows at resolution lower than 14 Å.

4.2.2 ShuA from *Shigella dysenteriae*

ShuA was solubilized in octyl-POE (Bachem) during purification. The purification protocol is provided in Appendix 4.5.2. The octyl-POE detergent has a CMC value of approximately 7 mM[17]. For the crystallization experiments, octyl-POE was exchanged with β-OG (Anatrace) with a CMC value of 25 mM[18]. For detergent exchange, the protein sample obtained from the ion exchange chromatography was centrifuged in the presence of a buffer containing 10 mM Tris-HCl pH 8.0 and 1.4 % v/v OG. Figure 4.2.5 shows native ShuA crystals grown with the hanging drop method in the presence of 15 % PEG 1000, 100 mM NaCl and 100 mM MES pH 6.5. The protein concentration was 6.3 mg mL^{-1} and the drop was prepared by mixing protein

and crystallization solution in 1:1 volume ratio. The scale bar corresponds to 100 µm. Several conditions for ShuA crystallization were screened with the dialysis chip using different precipitants and buffers or varying the protein and precipitant concentration. Heavy atom salts (0.8 mM Europium (III) chloride hexahydrate from Sigma-Aldrich) were also tested as additives for co-crystallization. However, so far, the on chip trials via microdialysis have not yielded ShuA crystals. ShuA was also used for screening crystallization conditions with the LCP method. The respective protocols and results are provided in Appendix 4.5.3.

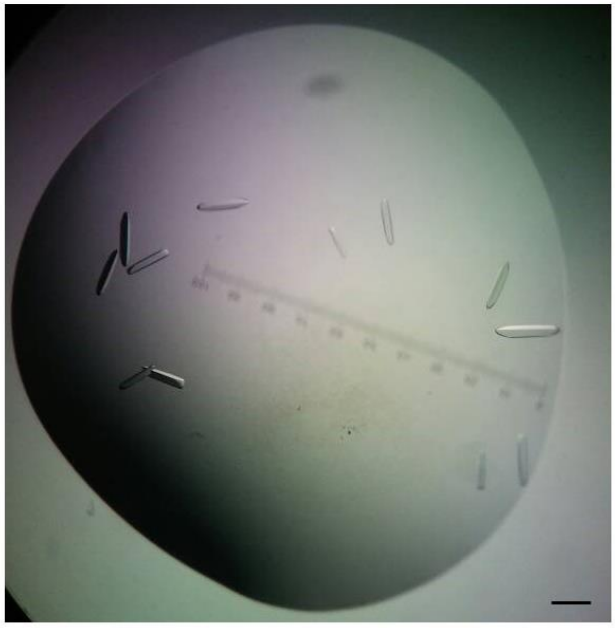

Figure 4.2.5: ShuA (6.3 mg mL^{-1}) crystals grown with the hanging drop method at 293 K in 15 % PEG 1000, 100 mM NaCl and 100 mM MES pH 6.5. The scale bar represents 100 µm.

4.2.3 SERCA from *Oryctolagus cuniculus*

SERCA was solubilized in octaethylene glycol monododecyl ether ($C_{12}E_8$) detergent with a CMC value of 0.09 mM[19]. The composition of the protein solution is given in the first column of Table 4.2.1. For crystallization experiments, the protein was mixed in a 1:1 volume ratio with the precipitant solution (column 2, Table 4.2.1). Native crystals of SERCA grown under the conditions given in Table 4.2.1 (column 3) with the hanging drop method at 293 K are shown in Figure 4.2.6. The protein concentration was approximately 14 mg mL^{-1} and the drop was prepared by mixing the protein solution (pre-mixed with the precipitant solution) and the crystallization solution in a 1:1 volume ratio. The crystals were formed 6 days after setting up the experiment and were used as seeds for a few on chip crystallization experiments, without however inducing nucleation.

Table 4.2.1: Composition of the protein, the precipitant and the crystallization solution for the crystallization experiments with SERCA.

Protein solution	Precipitant solution	Crystallization solution
20 % v/v glycerol	10 % v/v glycerol	12 % v/v PEG 6000
35 mM $C_{12}E_8$	200 mm CH_3COONa	8 % v/v glycerol
100 mM MOPS pH 6.8	(Sodium acetate)	100 mm CH_3COONa
80 mM KCl (potassium chloride)	6 % v/v tBu	3 % v/v tBu
3 mM $MgCl_2$ (magnesium chloride)	(tert-butyl hydroperoxide)	100 mM MOPS pH 6.8
10 mM $CaCl_2$ (calcium chloride)	100 mM MOPS pH 6.8	40 mM KCl
5 mM NaF (sodium fluoride)	10 mM BME	1.5 mM $MgCl_2$
0.33 mM $AlCl_3$ (aluminium chloride)		5 mM $CaCl_2$
5 mM BME (β-mercaptoethanol)		2.5 mM NaF
1 mM ADP (adenosine diphosphate)		0.165 mM $AlCl_3$
		7.5 mM BME
		0.5 mM ADP

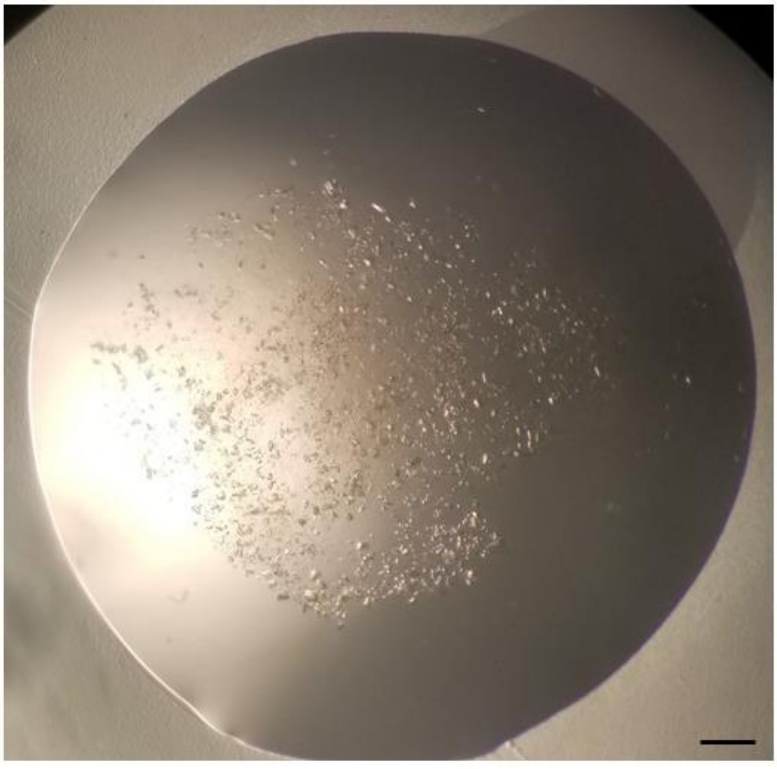

Figure 4.2.6: SERCA (14 mg mL^{-1}) crystals grown with the hanging drop method at 293 K in the conditions provided in Table 4.2.1 (third column). The scale bar represents 100 µm.

4.2.3.1 On chip SERCA crystallization and *in situ* X-ray diffraction

SERCA was also crystallized on chip with the microdialysis method and, so far, it has been the membrane protein target that has yielded the best diffraction with X-rays. Specifically, native SERCA crystals were tested for *in situ* X-ray diffraction at the BL13 - XALOC beamline (ALBA) using the same beamline configurations described for the diffraction experiment with AcrB crystals (Section 4.2.1.1). The protein solution had the same composition as described in Table 4.2.1, but the protein concentration was approximately 12 mg mL^{-1}. The crystallization solution contained 8 % v/v PEG 6000, 15 % v/v glycerol and 17.5 mM $C_{12}E_8$. The rest of the composition was identical to that provided in Table 4.2.1. The volume of the protein reservoir was 0.3 µL and the MWCO of the RC membrane embedded on the chip was 12 – 14 kDa. The crystallization and the *in situ* X-ray diffraction experiments were carried out at 293 K. The SERCA crystal shown in Figure 4.2.7 (a) spotted with the red cross diffracted close to 7 Å resolution (Figure 4.2.7 (b)).

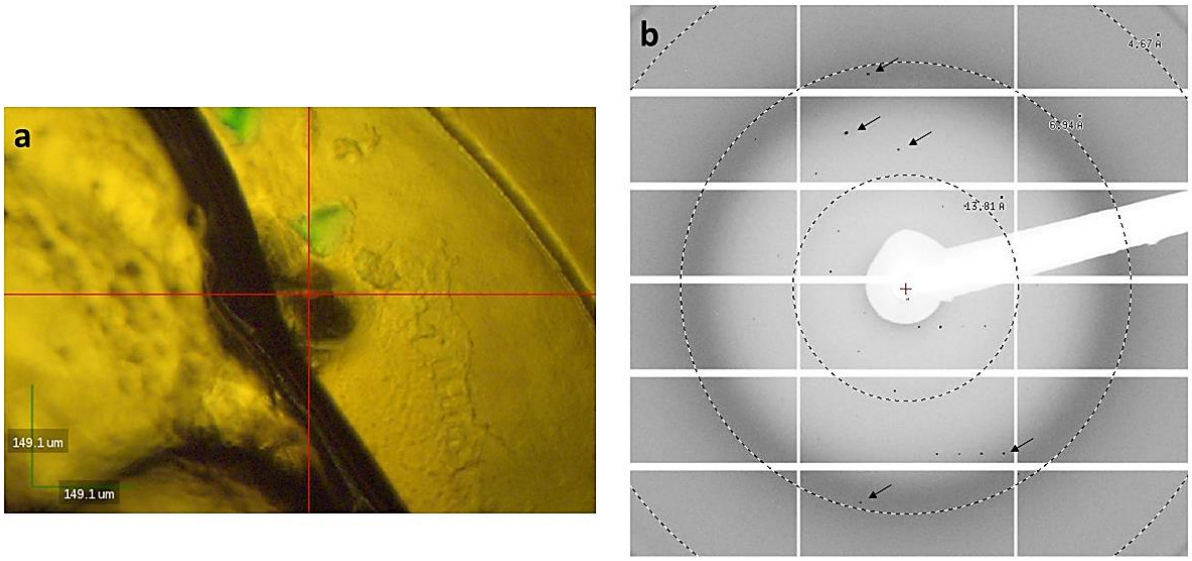

Figure 4.2.7: (a) SERCA crystal on the protein reservoir of the dialysis chip during *in situ* X-ray diffraction at BL13 - XALOC beamline (ALBA). (b) Diffraction image of SERCA crystals grown on chip. The diffraction spots close to the 7 Å resolution ring are indicated with arrows.

4.2.4 TmPPase from *Thermotoga maritima*

TmPPase was expressed in baker yeast cells and solubilized in 0.5 % v/v octyl glucose neopentyl glycol (OGNPG) detergent with a CMC value of 1.02 mM[20]. The composition of the protein and the crystallization solution is given in Table 4.2.2. The protein concentration was approximately 12.5 mg mL^{-1}. The volume of the protein reservoir was 0.1 µL and the MWCO of the RC membrane embedded on the chip was 12 – 14 kDa. TmPPase crystals that were

crystallized on chip with the microdialysis method are shown in Figure 4.2.8 (a). The on chip crystallization experiments were performed at the Center for Free Electron Lasers (CFEL) during my secondment in the laboratory of Prof. Arwen Pearson. TmPPase crystals grown on chip were tested for *in situ* X-ray diffraction at P14 beamline at PETRA III (DESY synchrotron). The chip was mounted on the beamline with the aid of the 3D printed support (Figure 3.2.3). The X-ray wavelength during on chip data collection was 0.98 Å, the photon flux was 2 x 10^{13} ph s^{-1} and the beam size was 2 µm x 6 µm. The diffraction images were recorded with an EIGER 16M (Dectris) detector with an active area of 311 x 327 mm^2 and 18 mega pixels resolution. Both crystallization and *in situ* X-ray diffraction experiments were carried out at 293 K. The TmPPase crystals diffracted weakly at a resolution around 15 Å, as shown in the diffraction pattern in Figure 4.2.8 (b).

Table 4.2.2: Composition of the protein and the crystallization solution for the on chip crystallization experiments with TmPPase.

Protein solution	Crystallization solution
50 mM MES-NaOH pH 6.5	28 % v/v PEG 400
50 mM KCl	50 mM Tris-HCl pH 8.0
5 mM $MgCl_2$	2 mM $MgCl_2$
3.5 % v/v glycerol	175 mM KCl
2 mM DTT (dithiothreitol)	2 mM DTT
4 mm Na_4IDP (imidodiphosphate sodium salt)	4 mm Na_4IDP
0.5 % v/v OGNPG	0.5 % v/v OGNPG

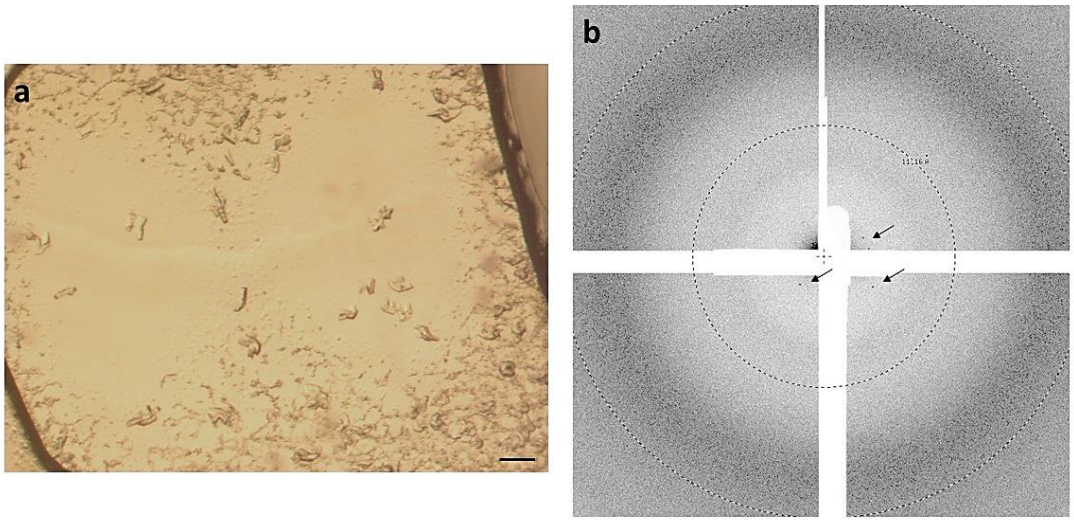

Figure 4.2.8: (a) TmPPase crystals grown on chip via microdialysis in the conditions provided in Table 4.2.2 (second column). (b) The *in situ* X-ray diffraction experiments with TmPPase were performed at P14 beamline (PETRA III). The diffraction spots are indicated with arrows at a resolution close to 15 Å. The scale bar represents 100 µm.

4.3 Radiation Damage

The term radiation damage refers to the limiting or detrimental effects that X-ray irradiation can introduce to macromolecular crystals. Radiation damage is inherent in ionizing radiation such as X-rays and macromolecular X-ray diffraction experiments can be highly compromised due to the impact of radiation damage on data acquisition, quality and interpretation. Understanding radiation damage and developing techniques to suppress or mitigate its deleterious impact on protein crystallography has been one of the major challenges in the field of structural biology for several decades. In simple terms, radiation damage is the energy lost by the X-ray beam while it passes through the crystal due to the interactions of the X-rays with the crystalline matter. There is a SI unit describing the amount of energy absorbed per unit mass and that is Gray (Gy = J kg^{-1}). So, radiation damage is described by dose and measured in Gy. The first step in understanding radiation damage and its impact on macromolecular crystallography is to comprehend how it is induced during diffraction experiments.

4.3.1 Interactions of X-rays with matter

At the X-ray energies typically used in MX experiments (5 – 17.7 keV or 2.5 to 0.7 Å)[21], the main interactions of the incident photons with the atoms of the crystals are Thomson (coherent or elastic) scattering, Compton (incoherent or inelastic) scattering and photoelectric absorption[21,22]. Some of these physical processes result in the deposition of energy in the crystalline material and the emergence of radiation damage. Thomson scattering arises from the elastic collision of the X-ray photon with the atoms of the crystal. In this case, the energy is not deposited in the crystal but remains in the photon that scatters coherently and gives rise to the diffraction pattern (Figure 4.3.1 (a)). Compton scattering takes place when the incident photon scatters electrons incoherently. The energy from the incident photon is transferred to electrons of the atoms and another lower energy photon is emitted incoherently (Figure 4.3.1 (b)). The background noise often observed in diffraction images is attributed mainly to Compton scattering. The energy loss during Compton scattering varies with the incident energy level and the scattering angle, nevertheless, the amounts of energy deposited on the crystal are negligible compared to the energy deposited due to photoelectric absorption. During the photoelectric absorption, the third interaction type, the incoming photon is completely absorbed and a lower level core electron is ejected from the atom carrying the excess energy as kinetic energy (Figure 4.3.1 (c)). Photoabsorption is the main interaction between the X-rays and the crystal in the photon energy regime used in MX. The atom at which photoabsorption occurs loses an electron and the energy deposited in the crystal contributes to mechanical disruption of the crystal lattice, thermal heating, ionization events and breakage of chemical bonds which are all aspects of radiation damage. Apart from these events, the excited atom might lose part of the excess potential energy via fluorescence or Auger process. In the former process, a higher shell electron fills the vacancy created by the emission of the photoelectron and characteristic X-rays of the atom are produced. Fluorescence becomes significant mainly for higher atomic number atoms. The Auger effect is observed when the outer electrons are ejected from the atom following the photoelectric absorption. Even though the ionization events produced by photoelectric absorption have a

probabilistic nature, it has been estimated in the literature that a single absorbed photon can produce approximately 500 subsequent ionization events[23]. Many studies have been conducted for the correlation of photoabsorption and radiation damage, as it generates free radicals, which are directly correlated to secondary and specific structural radiation damage (Section 4.3.2.1).

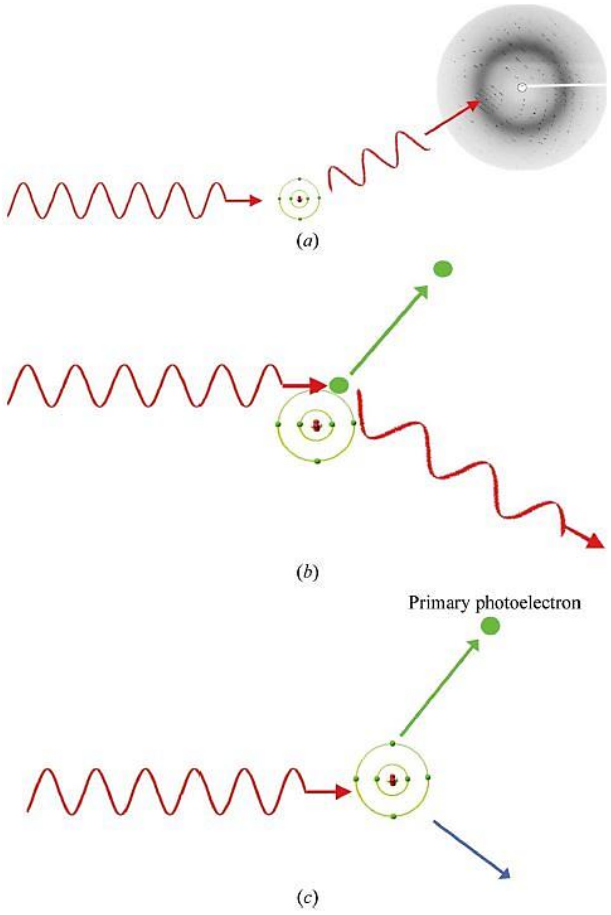

Figure 4.3.1: The main interactions of the incident photons with the atoms of the crystals are (a) Thomson (coherent or elastic) scattering, (b) Compton (incoherent or inelastic) scattering and (c) photoelectric absorption. Reproduced from [24].

The relative contribution of the Thompson scattering, the Compton scattering and the photoelectric absorption can be estimated by the cross section of each process. For the incident energy levels or wavelengths used for MX experiments, photoelectric absorption has the higher cross section contributing over 90 % of the total energy deposited by the beam[24]. Graphs of the cross section (in barns/atom) of each interaction process as a function of the photon energy (eV) for each element were published by Hubbell *et al*.[25–27] and shown in Figure 4.3.2. Figure 4.3.2 (a) illustrates the respective graph for carbon (atomic number Z = 6). The cross section for Thompson scattering (σ_{coh}) and Compton scattering (σ_{incoh}) are approximately equal at 10^4 eV, but above this energy level Compton scattering dominates and peaks at

around 10^5 eV. The cross section for Thompson scattering at 10^4 eV is an order of magnitude less than the respective one for photoelectric absorption and at 4 x 10^4 eV is an order of magnitude less than Compton scattering. So, X-ray energies between 10 – 40 keV are suggested, if the goal is to maximize the ratio of elastic scattering to the sum of inelastic scattering and photoabsorption[22]. For higher energy levels (> 10^6 eV) processes like nuclear field pair production (k_n), electron field pair production (k_e) and nuclear photoabsorption (σ_{ph}) become dominant. Similar remarks can be concluded from Figure 4.3.2 (b) illustrating the cross section of lead (Z = 82) as a function of photon energy. A simple comparison shows that the cross section increases with atomic number, Z, and at the same energy the cross section for elastic scattering for lead is nearly an order of magnitude larger than carbon's.

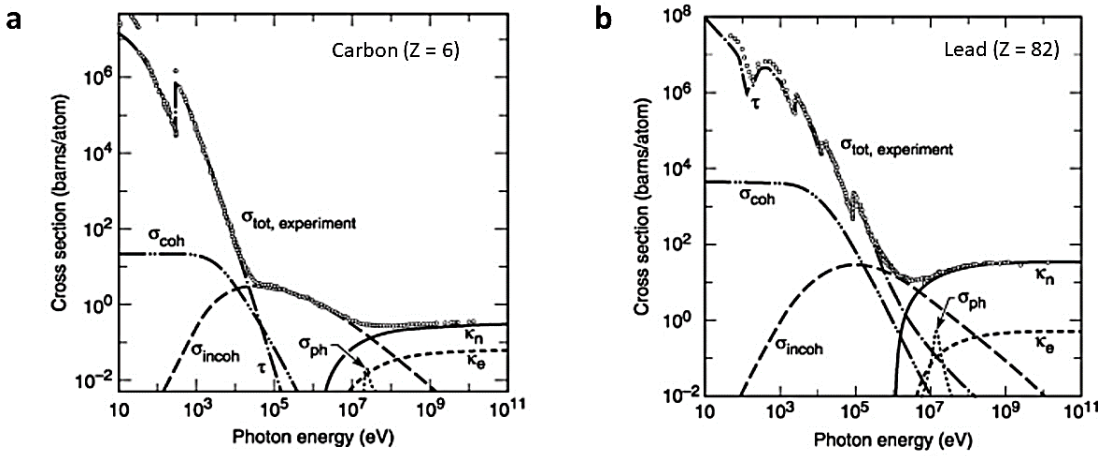

Figure 4.3.2: Graphs of the cross section (barns/atom) of each interaction process of X-rays with matter as a function of the photon energy (eV) for (a) carbon and (b) lead. The contributions are Thompson scattering (σ_{coh}), Compton scattering (σ_{incoh}), atomic photo-effect (τ), nuclear field pair production (k_n), electron field pair production (k_e) and photonuclear absorption (σ_{ph}). The total photon cross section is shown as σ_{tot}. Reproduced from [27].

4.3.2 Classification of radiation damage

Based on the interactions of X-rays with the crystal, radiation damage can be classified in primary, secondary and tertiary[24]. Primary damage is the ionization of an atom caused by photoelectric absorption and Compton scattering and occurs in a femtosecond timescale[28] while the absorbed energy is not uniformly deposited in the crystal but it is deposited in amounts of 20 – 100 eV in regions named spurs[28,29]. Primary damage cannot be avoided. If the primary event occurs in the protein molecule, then the damage can be further classified as direct, while it is indirect if the solvent surrounding the macromolecule absorbs the radiation. In the latter case, reactive species such as solvated electrons, hydroxyl and hydrogen radicals are formed and interact with the protein[24]. This kind of indirect ionization of the protein molecule can be minimized by using scavenger molecules[23,30]. Low-energy secondary

electrons are formed[24,31] and can diffuse into the crystal causing further ionization and excitation events. The damage arising from the interaction of these secondary and thermalized electrons with the crystal component, that can lead even to the breakage of chemical bonds, is called secondary damage. O'Neil *et al*.[23] predicted that if ionization events are produced by a 12 keV incoming photon, then the emitted electron with approximately the same energy can produce up to 500 ionization events, considering that 25 eV energy is required per ionization event. The tertiary radiation damage is mainly related to mechanical disturbances such as damage on the crystal lattice invoked by the excess of energy that the crystal absorbs. The above-mentioned classifications are not quite consistent in the literature. However, they are briefly mentioned in order to comprehend the extent of physical and chemical processes that are linked to radiation damage of macromolecules and the substantial efforts made to deeply understand its nature and implications.

4.3.2.1 Global and specific radiation damage

There is indeed a universal classification of radiation damage that is interesting for macromolecular crystallography and structural biology. Radiation damage can be separated in global and specific. Global or non-specific radiation damage is related to changes observed in the reciprocal space and the metrics used by crystallographers to describe it. These are the diffraction limit, the sample mosaicity and the Wilson B factor[28,32]. A loss of diffraction spots intensity is considered the first indication of global damage and it can be attributed to the production of hydrogen gas in the crystal[24]. Moreover, Ravelli and McSweeney[28] studied numerous data sets from 3 different proteins (HEWL, Winged bean Chymotrypsin Inhibitor (WCI), *Torpedo californica* acetylcholinesterase (TcAChE)) and observed a clear increase in the unit cell volume. They suggested that the unit cell volume could be an additional, new metric of global damage. Gonzalez and Nave[32] studied the effect of global damage on the diffraction quality of tetragonal HEWL crystals at 100 K by analyzing Laue diffraction patterns after each exposure and comparing them with a reference pattern generated at the onset of the experiment. Their pioneering work concluded that radiation damage is feasible and observable even at cryogenic conditions and there is a size limit to the protein crystal for obtaining a full data set depending on the experimental parameters (photon flux and exposure time). Even though radiation damage manifests itself as decay in the overall quality of the diffraction data, many studies have shown that synchrotron radiation can cause specific damage on the protein sample.

Specific radiation damage is related to real space changes observed in the electron density map like breakage of disulfide bonds and decarboxylation of acidic residues[33–36] and can be up to approximately 60 times faster than global damage[37]. Weik *et al*.[33] studied the effect of specific chemical and structural damage in cryogenic temperatures for the enzymes TcAChE and HEWL and they observed cleavage of the disulfide bridges in cysteine residues for both proteins, with the Cys254 –Cys265 and the Cys6 – Cys127 bond being the most susceptible to damage in TcAChE and HEWL, respectively. Moreover, an increase in B factors for both protein samples revealed that acidic residues, like glutamate and aspartate, are also susceptible to damage provoked by synchrotron radiation. They argue that this increase in B factors can be attributed to increased mobility or decarboxylation induced by ionizing radiation. Similarly, Ravelli and McSweeney[28] noticed by inspecting electron density maps of

three different proteins that the increase in B factor per residue was greater for cysteine, glutamic acid and aspartic acid, assigning these changes to disulfide bond breakage. Burmeister[35] used cry-cooled crystals of myrosinase to study structural changes induced by synchrotron radiation. Characteristic global changes, like a decrease in the total diffracted intensity and a subtle expanse of the unit cell, were prominent. However, using Fourier difference maps and occupancy refinement, he observed specific damage concerning the breakage of disulfide bonds, decarboxylation of aspartate and glutamate residues, a loss of hydroxyl groups from tyrosine and loss of the methylthio group from methionine, while in the same manuscript possible mechanisms for the explanation of these structural alterations were thoroughly discussed.

4.3.2.2 Radiation damage at cryogenic and room temperature

Systematic radiation damage studies have been carried out for more than two decades and there is a vast extent of published work available for comprehending the implications of radiation damage in structural biology, its manifestations and mechanisms of action as well as estimating the parameters that affect, progress or mitigate radiation damage and the questions arising from the ongoing research. Critical reviews on radiation damage can be found in the literature[24,38,39], as for example some reviews citing the work presented from various groups in Radiation Damage Workshops[40–43] or review/guides focusing mainly on the prevention of the phenomenon[37]. The majority of the studies on radiation damage have been implemented at cryogenic temperatures (around 100 K) because of a decrease in radiation sensitivity of protein crystals and a prolongation of the crystal lifetime of approximately a factor of 70 compared to diffraction experiments conducted at room temperature[24,39]. Cryogenic methods, like flash cooling of protein crystals in liquid nitrogen, were implemented to improve the crystal lifetime when using X-ray diffraction techniques because they cause immobilization of the reactive radicals produced either directly from the protein molecule or indirectly by the surrounding solvent, ceasing or slowing down the diffusion of these species and the generation of secondary damage effects[44,45] or stabilizing the crystal lattice[22]. However, even if this time-dependent secondary damage is less significant at cryo-temperatures, primary dose-dependent damage still occurs. Henderson[46] estimated that an incident X-ray dose of 20 MGy can destroy a protein crystal at cryogenic conditions. This value is known as the Henderson limit and refers to the dose limit which is the maximum dose that a crystal can tolerate before the diffraction fades to half of its original value ($D_{1/2}$). Owen *et al*.[47] examined experimentally the dose limit and found that a dose of 30 MGy, which is the maximum dose that the crystal can tolerate at cryogenic conditions before the diffraction fades to 70 % of its initial value ($D_{0.7}$), can be suitable before crucial biological information are compromised due to radiation damage. Nonetheless, many studies have shown that secondary damage can still happen at cryogenic conditions as hydroxyl radicals or free electrons are mobile at liquid nitrogen temperature (77 K)[28]. Radiation damage inducing structural alterations on the membrane protein bacteriorhodopsin (bR) at 100 K has also been reported by Borshchevskiy *et al*.[34] for X-ray dose lower than 0.06 MGy, a value 500 times lower than the recommended experimental dose limit at cryo-temperatures. Moreover, cryocooling protein crystals can result in increased mosaicity, may induce mechanical damage when fragile crystals have to be mounted on loops and time must be spent in finding the optimal conditions for crystal preservation in cryogenic conditions. For these reasons and despite the proven

prolonged crystal lifetime in cryogenic temperatures, there has been an increased interest in protein crystallography carried out at room temperature and an increasing research on radiation damage at these experimental conditions. Room temperature crystallography offers the benefit of avoiding the use of cryoprotectants and the mechanical stress applied to the protein crystal due to manual handling and mounting on loops. Moreover, time-resolved kinetic experiments can be performed and biologically relevant structural details can be revealed since the flexibility and the conformational configurations of the targeted protein are not biased due to cryocooling which may distort the protein's backbone fold[41,48].

Warkentin *et al*.[49] provide a review on global radiation damage and its temperature dependence demonstrating that there is a transition in radiation sensitivity at around 200 K[50]. Above this limit diffusive motions in the protein and the solvent are dominant and the progression of global damage continues even when the incident X-ray beam is turned off. Specific radiation damage at room temperature has been also investigated with some controversial reports in the literature. Southworth-Davies *et al*.[31] investigated the dose limit for room temperature (292 K) X-ray diffraction experiments on HEWL crystals and they found that the decay of the total diffraction intensity as a function of dose was first order. This observation is in agreement with the pioneering work of Blake and Philips[51] who studied the radiation damage at room temperature for myoglobin crystals. Moreover, they showed that the use of higher dose rates during the X-ray irradiation could prolong the crystal lifetime at room temperature. Specifically, according to the authors, a 60 % increase in the dose rate at room temperature can lead to a 4-fold increase in the dose required for the total diffraction intensity to reduce to half of its initial value. Their findings indicate that radiation damage in room temperature depends on the dose rate and not only on the absorbed dose, as it is the case for radiation damage in cryogenic conditions. Moreover, by analyzing Fourier difference electron density maps, they saw evidence of disulfide bond cleavage at room temperature, confirmed by another study by Coquelle *et al*.[52] who performed serial synchrotron data collection at room temperature on lysozyme crystals using micro- and nano- focused beam.

The discovery by Owen *et al*.[53] that free radicals formation can be outrun in room temperature adds up to the increasing interest in room temperature macromolecular crystallography. The authors used crystals of three different samples and showed that the mean lifetime of the crystals increases as a function of dose rate, suggesting that at high dose rates (roughly 1 MGy s^{-1}) radical recombination, quenching and diffusion occurs (in timescales < 60 ms) and the remaining free radicals that can lead to crystal damage are far less in number. More recently, de la Mora *et al*.[54] used the advent of SSX in order to investigate radiation damage on HEWL crystals both at cryo- and room temperature. The diffraction intensity of the collected data sets reached half of its initial value at average dose ($D_{1/2}$) of 0.57 and 15.3 MGy at room temperature and 100 K, respectively. Moreover, they observed specific radiation damage at disulfide bonds at room temperature, but not at the acidic residues usually observed at cryogenic conditions[28,33,35]. A dose limit of 0.38 MGy per dataset is recommended in static and time-resolved synchrotron crystallography conducted at room temperature, which can vary depending on the protein sample and the resolution limit.

4.3.3 Estimating radiation damage and RADDOSE

In order to estimate and monitor radiation damage in MX, several metrics based on global or specific effects have been used in the literature. The disadvantage of using different metrics is that data obtained under various experimental conditions cannot be compared. There is one metric that can be estimated even though it is not directly experimentally measurable and that is the dose. As has been already mentioned, the dose is the energy absorbed per unit mass of sample and it is expressed in Gray units (Gy = J kg^{-1}). This amount of absorbed energy is the energy lost by the incident X-ray beam. Assuming that the intensity of the incident beam is J_0, then the intensity decay (J) for a crystal with thickness χ and linear absorption coefficient μ_{abs} is given as[38]:

$$J = J_0 e^{-\mu_{abs}\chi} \quad (4.1)$$

The energy lost by the X-ray beam in the sample or the absorbed dose is $J_0 - J$ multiplied by the energy of the incident beam. Estimating the dose requires information concerning the atomic composition of the crystal and the precipitant solution, as well as information on the beam energy, size and profile and the exposure time. A computer program named RADDOSE-3D has been developed in order to model dose estimations spatially and temporally for macromolecular X-ray diffraction experiments[55].

The first version of the program was introduced by Murray *et al*.[21]. It was written in FORTRAN 77 and used CCP4 library routines. The absorption coefficients were calculated by the program for different X-ray energies and then used to estimate the absorbed dose for a specific crystal and beam. The crystal size was usually smaller than the beam size, rendering the calculated dose almost independent of the crystal size, since the whole crystal was irradiated nearly uniformly by the incident X-ray beam. The input information is the crystal size, the volume and contents of the unit cell and the solvent content. RADDOSE uses the total cross section (σ) to calculate the attenuation coefficient (μ_{att}) and only the photoelectric cross section for the calculation of the absorption coefficient (μ_{abs}). The total linear attenuation coefficient of the crystal can be calculated by equation[56]:

$$\mu_{att} = \frac{1}{V}\sum_{j=1}^{n} \sigma_j \quad (4.2)$$

Where V is the unit cell volume and σ is the atomic cross section for all the atoms of the crystal (j = 1,…,n) and is given as:

$$\sigma = \sigma_{Thompson} + \sigma_{Compton} + \sigma_{photoelectric} \quad (4.3)$$

This calculation assumes that the atomic cross section is independent of the surrounding environment of the crystal which is valid for light atoms but not for heavy atoms close to absorption edge energies. These two coefficients (μ_{att} and μ_{abs}) are different since Thompson and Compton scattering contribute little to absorption but more to the attenuation of the beam. Moreover, inputs to the program are the photon flux and energy, the beam size, the

exposure time per image and the image number. Nevertheless, the rotation of the crystal is not considered in the first version of RADDOSE, as well as in versions 2 and 3[56,57].

The first version of RADDOSE also assumes that all the energy of the X-rays that may lead to the production of a photoelectron is absorbed within the crystal. As has been already mentioned, when a photoelectron is ejected, the atom is left in an excitation state followed by the emission of an Auger electron or fluorescent X-ray. In the latter case, the fluorescent X-ray may escape from the crystal. Therefore, the absorbed dose calculated by RADDOSE is overestimated since not all the incident energy is deposited in the crystal. The second version of RADDOSE[56] takes into account this energy loss due to the escape of fluorescent photons produced when the energy of the incident beam is greater than the absorption edge energies (K, L or M) of the atoms present. X-ray fluorescence is negligible for light atoms but increases with the atomic number (Z). Paithankar *et al*.[56] modified RADDOSE to account this fluorescence escape and some example calculations on the absorbed dose are presented for several proteins.

The third version of RADDOSE[57] includes the effect of Compton scattering in calculating the absorbed dose. In the previous versions[21,56], the absorption coefficient (μ_{abs}) was calculated only by the photoelectric cross section contribution which is a fair approximation for the incident energies used in a typical MX experiment (5 – 20 keV). However, for higher X-ray energies (> 20 keV) the contribution of the Compton scattering cross section becomes significant. An example given by Paithankar and Garman[57], indicates that for a 100 μm thick CEWL crystal irradiated at 12.4 and 40 keV, Compton scattering accounts for 5.4 % and 67 % of the total interaction, respectively. The new version of RADDOSE proposed by the authors includes the effect of inelastic scattering to the calculations of the total absorption coefficient, indicating that at high incident X-ray energies radiation damage rate may be reduced for the same diffraction intensities. Finally, it should be mentioned that none of the above-mentioned versions of RADDOSE considers crystal rotation during the diffraction experiment.

All three versions of RADDOSE yield a one-dimensional profile of the absorbed dose for a stationary macromolecular crystal and allow for prediction of the crystal lifetime in comparison to the experimental dose limit of 30 MGy[47]. The assumptions and simplifications used for the development of these software versions were sufficient enough in cases where the crystal was smaller than the beam and the beam profile was uniform. Zeldin *et al*.[55] developed a new version, RADDOSE-3D, for the full 3D mapping of the absorbed dose distribution in MX experiments. The new version, written in Java, is designed to overcome the limitations posed by the previous versions of the software such as the photoelectron escape which could lead to reduced absorbed dose, the dose distribution within the irradiated crystal volume which was not accounted for rotating crystals and non-uniform beam profiles, the non-realistic crystal shapes and beam profiles and the fact that more regions of a crystal can be exposed to the incident radiation for crystals lager than the X-ray beam. RADDOSE-3D simulates the spatial and temporal distribution of the dose within the crystal volume for a number of iterations in small angular steps across several data wedges. It should also be noted that RADDOSE-3D calculates the two absorption coefficients (μ_{att} and μ_{abs}) separately at each depth point of the crystal, correcting the approximations made by the previous versions.

The input file requires information on the crystal size and morphology, the beam and the wedge[55] and always describes a single crystal and one or more beams and wedges of contiguous data. The output file contains several dose metrics (Table 4.3.1) and it is updated

after calculating each wedge providing the dose state at every voxel and every temporal step. The voxel represents a value of a regular grid in a 3D space being the 3D equivalent of the pixel. The term itself is a fusion of the terms volume and pixel. In the case of crystals, the voxel represents a partial volume of the total crystal volume. Zeldin *et al*.[58] showed that the profile of the beam has a crucial effect on the dose distribution within the crystal, with the top-hat beam profile resulting in more uniform distribution compared to the Gaussian one. When using a Gaussian beam, the best data collection strategy for even dose distribution is to match the beam size to the crystal, which can be achieved by applying a helical scan.

Table 4.3.1: Dose metrics as provided by the RADDOSE-3D output file.

Dose metric	**Explanation/units**
Average dose – whole crystal (AD-WC)	Total absorbed energy divided by the mass of the whole crystal/ MGy [40]
Average dose – exposed region (AD-ER)	Total absorbed energy divided by the mass of a region defined as any voxel having nonzero dose/ MGy [55]
Threshold average dose (TAD)	The average dose inside a volume bounded by the isosurface calculated to enclose a fraction of the total absorbed energy (default 95 %)/MGy [55]
Maximum dose (max dose)	The dose in the voxel with the highest dose value anywhere in the crystal/ MGy [55]
Dose contrast	Maximum dose divided by threshold average dose: a measure of the contrast in the dose distribution [55]
Used volume	The fraction of the crystal voxels with a nonzero dose/ % [55]
Absorbed energy	The sum of the absorbed energy for all the voxels in the crystal/ J [55]
Final dose histogram	A histogram showing the fraction of voxels in each dose range [55]
Dose Inefficiency	The maximum dose over the total absorbed energy/ kg^{-1} [58]
Diffraction weighted dose (DWD)	Combines information from dose aggregation within each volume element of the crystal up to a given time, with the way the crystal is being exposed at that moment/ MGy [59]
Elastic yield	Elastically scattered photons/photons [59]
Diffracted dose efficiency (DDE) or Diffraction efficiency	The ratio of elastically scattered photons to the diffraction weighted dose/ photons MGy^{-1} [59]

The aggregate metrics, like average dose or maximum dose, refer to the final state of the whole crystal once the data collection is completed. For example, the AD-WC metric weights equally each volume element of the crystal no matter how each volume element was

irradiated during the exposure. In order to evaluate the fluence (photons per unit area) that each volume element of the crystal receives during the exposure and the extent of damage in time, Zeldin *et al*.[59] introduced the diffraction-weighted dose (DWD) metric. As opposed to aggregate metrics, DWD is calculated per each diffraction image and the dose at each volume element is weighted by how much the specific volume element has contributed to the current image. A more recent publication reports on the extension of RADDOSE-3D for dose estimation in SAXS experiments, as well as, modifications in order to include the effects of Compton scattering and photoelectron escape in dose calculations[60]. For the experimental results and simulations presented in Section 4.3.4 and Appendix 4.6, DWD and maximum dose are used as metrics.

4.3.4 Experimental results and simulations

RADDOSE-3D was used to simulate dose estimations for an *in situ* X-ray diffraction experiment of HEWL crystals grown on the microfluidic chips with the microdialysis method at 293 K. The lyophilized HEWL powder was dissolved in water to a final concentration of approximately 30 mg $mL^{-1}$and crystals were grown in the presence of 1.5 M NaCl and 100 mM CH_3COONa pH 4.0. The volume of the protein sample was 0.3 µL. HEWL crystals grew 1 h after the onset of the on chip crystallization experiment and the *in situ* data collection was performed after 7 days at BM30A-FIP beamline (ESRF) at room temperature. The crystal morphology was cubic and the approximate size was 200 µm along each axis. For the data collection, the microchip was mounted in front of the X-ray beam with the aid of a 3D-printed support (Figure 3.2.3, Chapter 3) and diffraction data were collected from - 40° to + 40° angular resolution. For the full data set, 80 diffraction images were collected with 1° oscillation per exposure and 30 s exposure time. The beam profile at BM30A-FIP was top hat, the beam size was 250 µm x 250 µm, the beam energy of 12.6578 keV (Se K edge) and the flux of 3.32 x 10^{10} ph s^{-1} were employed. Under these experimental conditions, the maximum dose estimated by RADDOSE-3D is 0.6267 MGy, a value far below the Henderson limit (20 MGy) or the experimental dose limit of 30 MGy, estimated by Owen *et al*.[47]. The DWD value is 0.3028 MGy. A color-map dose profile for the 200 µm x 200 µm x 200 µm cuboid crystal at 2 $µm^3$ voxel resolution exposed over an angular range of 80 ° (- 40° to + 40°) for a total exposure time of 2400 s (30 s per 1° oscillation) is shown in Figure 4.3.3. The map illustrates the dose attributed to each voxel of the cuboid crystal and the color map shows the variation of the dose state in the crystal volume. The blue color indicates the less exposed regions to the beam, therefore the voxels with the lowest dose, and the red color indicates the voxels with the highest absorbed dose. The beam is set along the z-axis and the rotation of the crystal is right-handed about the y-axis. The visualization has been produced with the open source software Paraview (https://www.paraview.org). Figure 4.3.3 shows a uniform distribution of the dose in the crystal volume, as expected for data collection strategies where the beam size is equal or larger than the crystal size. The majority of the voxels are in the high-dose regime (red) for this experiment, but the highest dose value is 0.63 MGy (< 30 MGy). Only the edges of the crystal lie within the low-dose regime (between 0.42 to 0.5 MGy as illustrated with blue color).

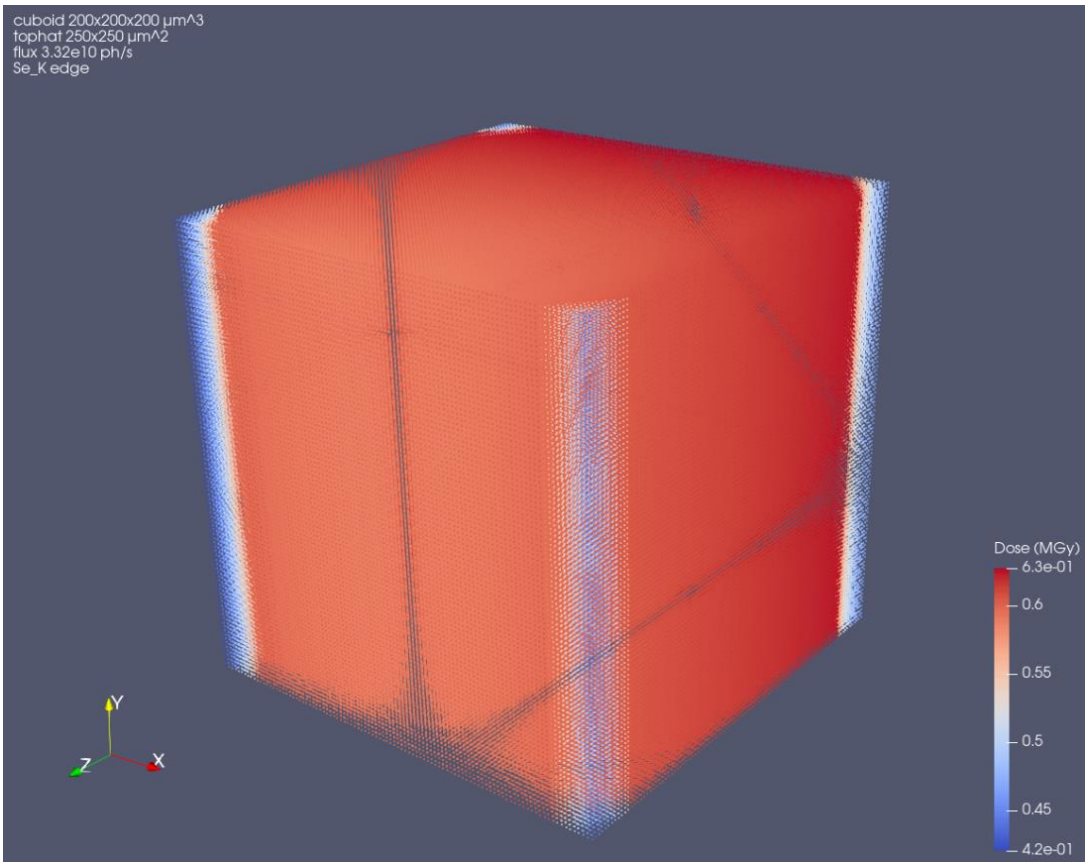

Figure 4.3.3: Dose map for the 200 µm x 200 µm x 200 µm cuboid HEWL crystal irradiated at BM30A-FIP beamline (ESRF) at room temperature, with a photon energy of 12.6578 keV and flux 3.32 x 10^{10} ph s^{-1}. The dose is given in MGy and the map was produced with Paraview.

BM30A-FIP (ESRF) had operational energy limits from 6.9769 keV (Eu L3 edge) to 17.1663 keV (U L3 edge). The same beamline has been reconstructed and is currently called BM07-FIP2 with energy limits from 4.9392 keV (Te L1 edge) to 25.5140 keV (Ag K edge). Simulations were performed using RADDOSE-3D for the same experimental conditions (crystal size, beam profile, beam size and flux) by varying the beam energy. The dose maps generated with Paraview are shown in Figure 4.3.4 for BM30A-FIP and in Figure 4.3.5 for BM07-FIP2. The DWD and the maximum dose metrics for each energy level are provided in Table 4.3.2. A uniform dose distribution can be seen for the energy values of 17.1663 keV (Figure 4.3.4 (b)) and 25.5140 keV (Figure 4.3.5 (b)), similar to the dose distribution of the real experiment (as shown in Figure 4.3.3), but with different dose limits (0.22 – 0.32 MGy for Figure 4.3.4 (b) and 0.098 – 0.14 MGy for Figure 4.3.5 (b)). However, a different dose distribution can be distinguished for data collection strategies at lower energies. Figures 4.3.4 (a) (6.9769 keV) and Figure 4.3.5 (a) (4.9392 keV) show that only half of the crystal volume in both cases has been exposed in the high-dose regime (red).

Table 4.3.2: DWD (MGy) and maximum dose (MGy) metrics as calculated by RADDOSE-3D for the energy limits of BM30A-FIP and BM07-FIP2 (ESRF).

Energy (keV)	DWD (MGy)	Max Dose (MGy)
6.9769	0.9231	2.1853
17.1663	0.1597	0.3249
4.9392	1.4749	4.3433
25.5140	0.0690	0.1393

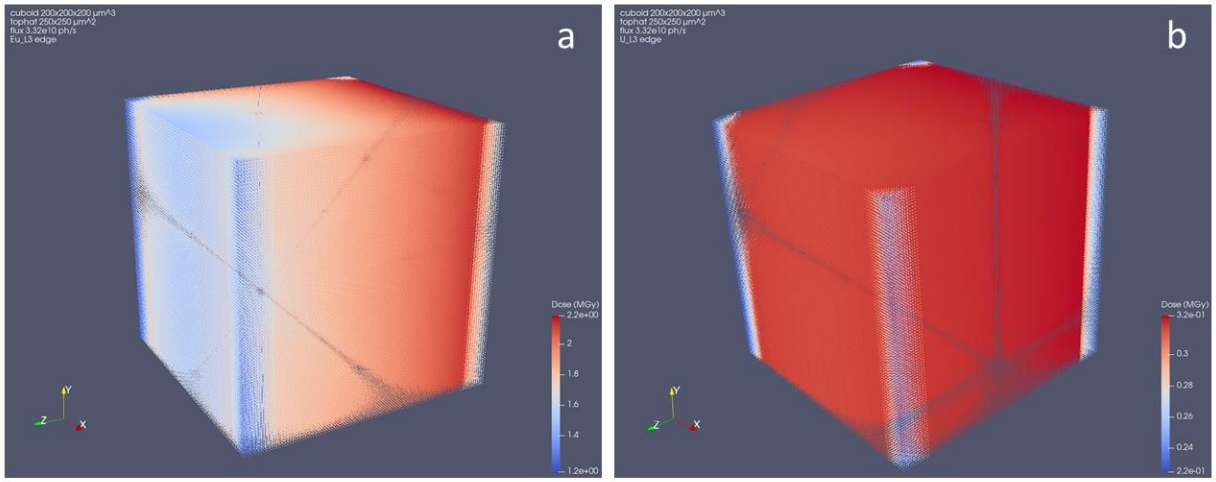

Figure 4.3.4: Simulations of the dose map for the 200 µm x 200 µm x 200 µm cuboid HEWL crystal for (a) 6.9769 keV and (b) 17.1663 keV, the energy limits of BM30A-FIP (ESRF). The photon flux is 3.32 x 10^{10} ph s^{-1}. The dose is given in MGy and the maps were produced with Paraview.

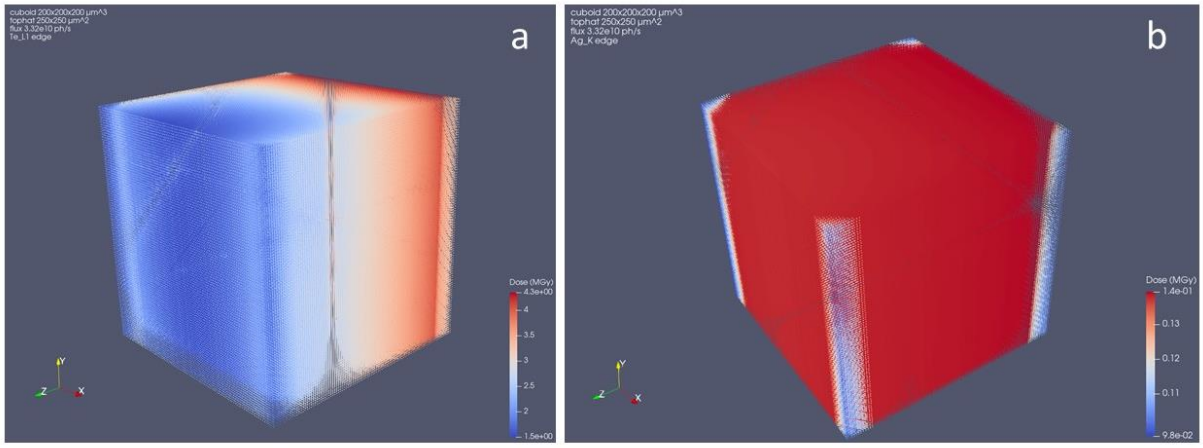

Figure 4.3.5: Simulations of the dose map for the 200 µm x 200 µm x 200 µm cuboid HEWL crystal for (a) 4.9392 keV and (b) 25.5140 keV, the energy limits of BM07-FIP2 (ESRF). The photon flux is 3.32 x 10^{10} ph s^{-1}. The dose is given in MGy and the maps were produced with Paraview.

Apart from the photon energy, other parameters than can affect the dose distribution and the dose metrics are the crystal size, the beam size and profile and the photon flux. All these parameters are input parameters for RADDOSE-3D and can be altered in order to estimate the dose state of the irradiated crystal and design the optimum diffraction data collection strategy, especially when the absorbed dose is close to the experimental limit (30 MGy) or when the protein crystals are difficult to reproduce or the protein sample is limited. Even in the case of HEWL, a widely studied, model soluble protein that produces robust and well-diffracting crystals, the simulations show that the choice of the experimental parameters during data collection has a significant impact on dose distribution. So far (Figures 4.3.3 – 4.3.5), the only parameter altered has been the photon energy. Some example simulations with different crystal morphology and size, beam size and photon flux are provided in Appendix 4.6 (Figure A4.14) to comprehend how these parameters can affect the dose distribution.

Another way of inspecting the dose distribution is to divide the crystal's voxels into dose bins. This is automatically performed by RADDOSE-3D, which separates the voxels of the crystal in 11 bins. Each bin contains the percentage of the voxels that lie within a dose range, with the first bin attributed to the 0.0 – 0.1 MGy range, the second bin to 0.1 – 3.4 MGy, etc. The 11^{th} bin contains the voxels with an estimated dose value > 30 MGy. Table 4.3.3 summarizes the bins and the percentage of voxels in each bin for a 200 µm x 200 µm x 200 µm cuboid crystal exposed to a 50 µm x 50 µm top hat beam with a 3.32 x 10^{10} ph s^{-1} flux at 12.6578 keV. For this example, nearly 70 % of the voxels were exposed to a dose range between 0.1 – 6.7 MGy, while no volume voxel was exposed to more than 16.7 MGy. Similar conclusions can be drawn for cases with different input parameters (crystal size, beam size and profile, photon flux), as the output file of RADDOSE-3D generates the division of voxels into dose bins. Accumulative histograms are provided in Figures 4.3.6 and Figure A4.15 in Appendix 4.6, where the percentage of voxels (% voxels) is plotted against 11 dose bins (MGy) for various beam size values for a 200 µm x 200 µm x 200 µm crystal (Figure 4.3.6 (a)) and a 50 µm x 50 µm x 50 µm crystal (Figure 4.3.6 (b)). In both histograms, the crystal is considered as cuboid, the beam profile is top hat and the photon flux is 3.32 x 10^{10} ph s^{-1} at 12.6578 keV. The beam size values investigated are: 300 µm x 300 µm, 250 µm x 250 µm, 200 µm x 200 µm, 150 µm x 150 µm, 100 µm x 100 µm, 50 µm x 50 µm, 10 µm x 10 µm and 5 µm x 5 µm. Regardless of the crystal size, the majority of the voxels are exposed to the low-dose regime (up to 3.4 MGy) when the beam size is between 300 µm x 300 µm and 150 µm x 150 µm. The choice of these values would constitute a suitable data collection strategy as the larger volume of the crystal is exposed to relatively low dose and can withstand until a full data set is collected without compromising the biological relevance of the recorded data. For both crystals, a wider dose distribution among the bins can be observed for smaller beam size values, while the dose exceeds the limit of 30 MGy when the beam size is 10 µm x 10 µm or 5 µm x 5 µm. Dose histograms for a Gaussian beam profile are provided in Appendix 4.6.

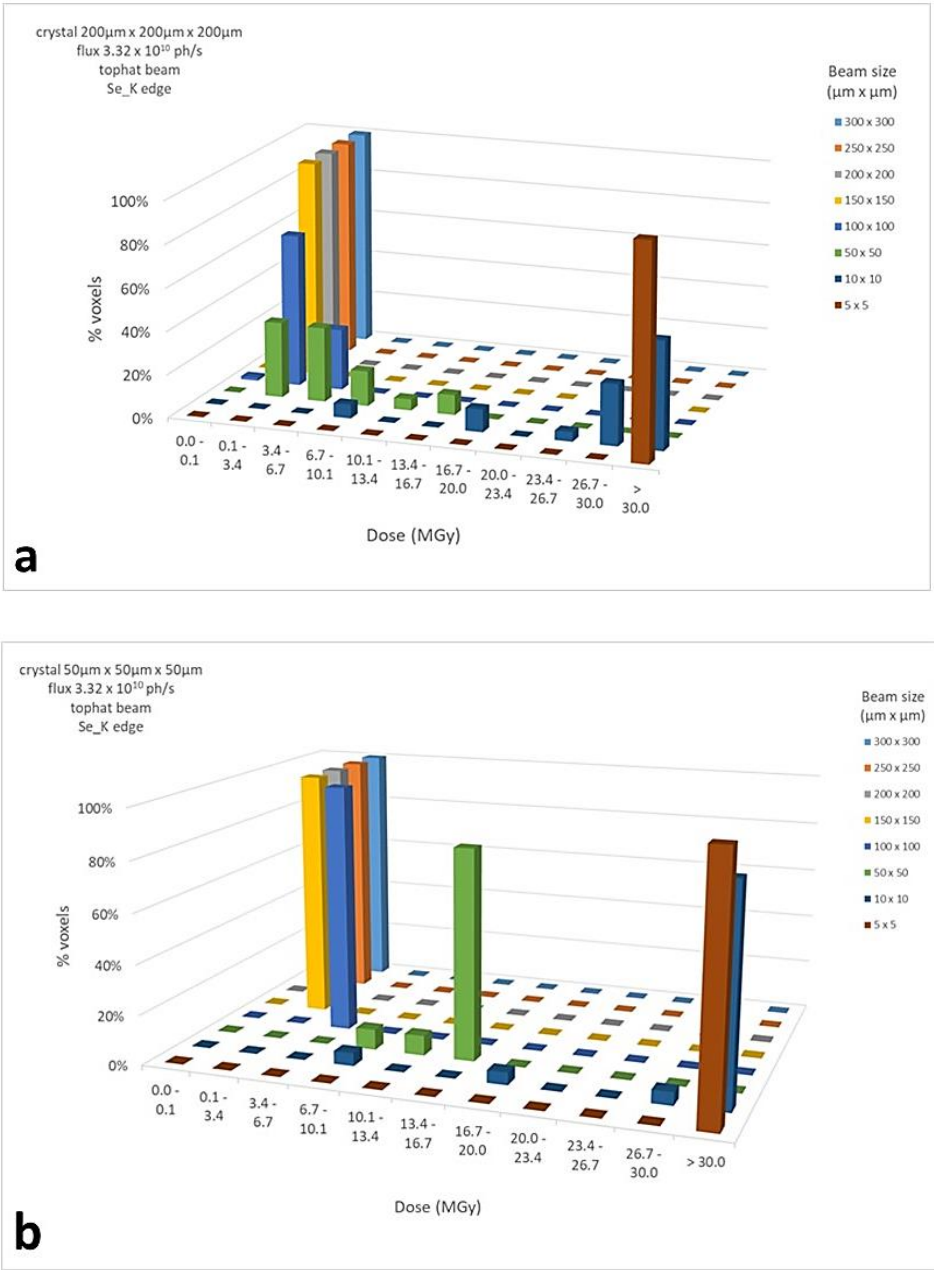

Figure 4.3.6: Dose histograms of the percentage of voxels (%) against 11 dose range bins (MGy) for various beam size values for (a) a 200 µm x 200 µm x 200 µm crystal and (b) a 50 µm x 50 µm x 50 µm crystal. The crystal is cuboid, the beam profile is top hat and the photon flux is 3.32 x 10^{10} ph s^{-1} at 12.6578 keV.

Table 4.3.3: The bins and the percentage of voxels in each bin, as calculated by RADDOSE-3D, for a 200 µm x 200 µm x 200 µm cuboid HEWL crystal exposed to a 50 µm x 50 µm top hat beam with a 3.32 x 10^{10} ph s^{-1} flux at 12.6578 keV.

Dose range (MGy)	% of voxels
0.0 – 0.1	0
0.1 – 3.4	34.9
3.4 – 6.7	34.4
6.7 – 10.1	16.2
10.1 -13.4	5.2
13.4 – 16.7	9.3
16.7 – 20.0	0
20.0 – 23.4	0
23.4 – 26.7	0
26.7 – 30.0	0
> 30.0	0

The impact of the photon flux, the crystal size and the beam size for a top hat beam on the DWD (MGy) metric calculated by RADDOSE-3D as a function of the beam energy (keV) is shown in Figure 4.3.7 and Figure A4.16 in Appendix 4.6, respectively. The energy values used in these graphs are the limit values for the beamline BM30A-FIP (6.9769 keV, 17.1663 keV and 20.9476 keV), the limit values for the beamline BM07-FIP2 (4.9392 keV, 25.5140 keV) and the energy value of 12.6578 keV (Se K edge) where the HEWL diffraction data set was collected on chip at room temperature. The crystal size is 200 µm x 200 µm x 200 µm, the beam is top hat with a size of 250 µm x 250 µm and the flux values are 3.32 x 10^{10} ph s^{-1} (experimental value used during data collection), 3.32 x 10^{11} ph s^{-1} and 3.32 x 10^{12} ph s^{-1} (theoretical values used for the simulations). From the plot in Figure 4.3.7, it can be concluded that the value of DWD is lower for higher beam energies and higher for lower energies in all three photon flux values. Moreover, for the highest flux value (3.32 x 10^{12} ph s^{-1}), DWD value increases significantly for photon energies < 10 keV. The DWD has been estimated to be 1.4749 MGy (flux 3.32 x 10^{10} ph s^{-1}), 14.7499 MGy (3.32 x 10^{11} ph s^{-1}) and 147.4992 MGy (3.32 x 10^{12} ph s^{-1}) at 4.9392 keV, while the respective estimations at 25.5140 keV are 0.0690 MGy (3.32 x 10^{10} ph s^{-1}), 0.6902 MGy (3.32 x 10^{11} ph s^{-1}) and 6.9027 MGy (3.32 x 10^{12} ph s^{-1}).

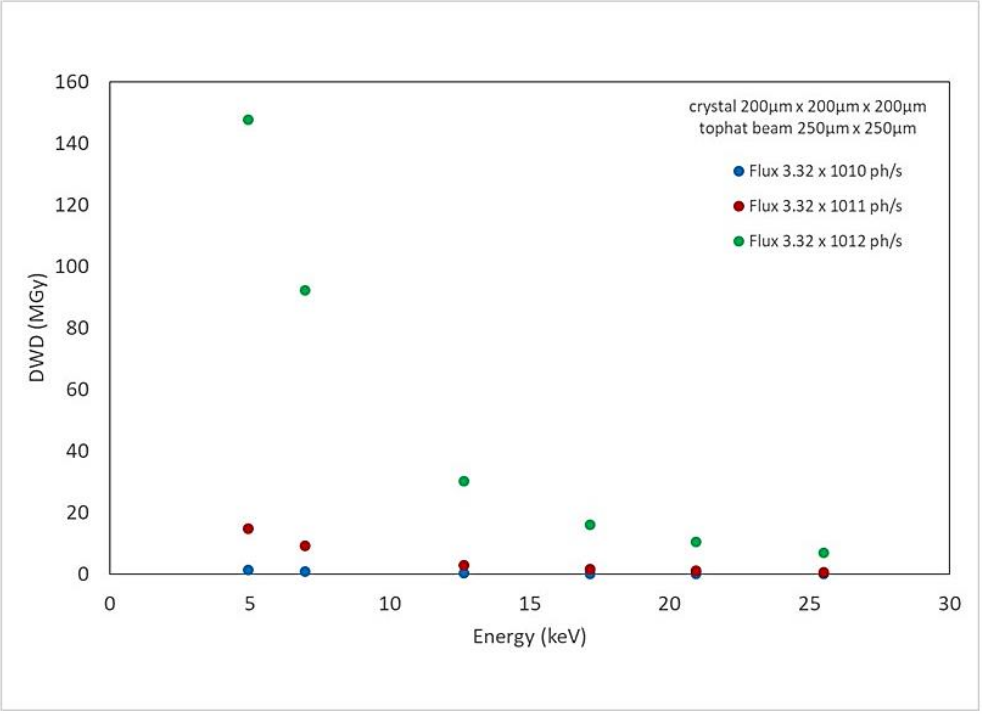

Figure 4.3.7: DWD (MGy) calculated by RADDOSE-3D as a function of the beam energy (keV) and the flux value (ph s^{-1}) for a cuboid HEWL crystal of 200 µm x 200 µm x 200 µm and a top hat beam of 250 µm x 250 µm.

4.4 Conclusions

Two model soluble proteins, HEWL and Thaumatin, were used for on chip crystallization with the microdialysis method and *in situ* X-ray diffraction studies. Crystallization conditions for both proteins were first screened with conventional methods, such as vapor diffusion and dialysis, and the effect of protein or precipitant concentration on the nucleation time, the crystal size and shape and the uniformity of the crystal population was investigated. On chip crystallization experiments were performed with the pre-screened conditions via microdialysis or other conditions that were not used with conventional methods were explored. In the case of on chip crystallization of soluble proteins, the MWCO of the RC dialysis membrane embedded within two layers of the device was 6 – 8 kDa and the volume of the protein reservoir was either 0.1 µL or 0.3 µL. The crystallization solution was pre-mixed manually and was injected within the fluidic channel manually with a disposable syringe or in an automated mode with the pressure-driven fluidic system incorporated in the MicroCrys platform (Chapter 3). All the experiments were performed at 293 K. Multiple crystallization conditions were screened with the dialysis chip for HEWL and Thaumatin by varying the protein or the precipitant concentration or the nature of the precipitant itself.

HEWL was used as a model protein to investigate the compatibility of the dialysis chip for growing large crystals for neutron crystallography in the presence of deuterated solutions.

Moreover, HEWL was used to perform a qualitative study of the phase diagram of the protein as a function of the precipitant (NaCl) concentration. HEWL crystals were grown at 293 K in the presence of 1 M NaCl, dissolved in 0 M NaCl and then, nucleation was induced again at a lower precipitant concentration (0.8 M NaCl). The MicroCrys platform was used in combination with the continuous circulation mode for filling the fluidic channel and exchanging the crystallization solutions in order to confirm the reversibility of the on chip dialysis method and the compatibility of the chip for studying phase diagrams. Finally, HEWL was used to prepare cubic mesophase of monoolein at 293 K in 3:2 (monoolein: protein) ratio in order to set up on chip crystallization experiments with the LCP method. Multiple, isomorphous, small crystals of HEWL were grown on chip with the LCP method at 293 K in various crystallization conditions.

In situ X-ray diffraction experiments were carried out at different beamlines (BM30A-FIP/ESRF, PROXIMA-2A/Soleil, BL13 – XALOC/ALBA and P14/PETRA III) confirming the compatibility of the dialysis chip with *in situ* data collection at room temperature. Detailed electron density maps were produced for HEWL crystals at a resolution higher than 2 Å. Partial diffraction data sets of numerous, isomorphous, small crystals of HEWL grown on chip with the LCP method and Thaumatin crystals were recently collected at PROXIMA-2A beamline at room temperature, verifying the compatibility of on chip cubic phase crystallization with the requirements of synchrotron serial X-ray crystallography (SSX). The HEWL crystals grown with the LCP method and the Thaumatin crystals diffracted close to 3 Å and 2 Å, respectively.

Four membrane proteins were used for on chip crystallization experiments. The MWCO of the RC dialysis membrane was 12 – 14 kDa and the volume of the protein reservoir was either 0.1 µL or 0.3 µL. Experiments were performed at 293 K. The crystallization solution was injected within the fluidic channel manually with a disposable syringe or in an automated mode with the pressure-driven fluidic system. Crystallization conditions were screened in advance with conventional methods. Several conditions varying the protein concentration, the precipitant concentration or the composition of the crystallization solution were tested on chip. Moreover, in the case of AcrB and ShuA additive molecules were also used for co-crystallization. Rifampicin was used with AcrB and Europium salt with ShuA. However, the on chip crystallization of membrane proteins was more challenging than the case of soluble proteins. AcrB, SERCA and TmPPase crystals grew on chip via microdialysis and their diffraction quality was tested. AcrB crystals diffracted at a resolution lower than 14 Å, TmPPase diffracted close to 15 Å, while SERCA diffracted close to 7 Å, yielding the best resolution acquired with membrane protein crystals on chip so far.

Finally, RADDOSE-3D was used to simulate dose estimations for the *in situ* X-ray diffraction experiment of HEWL crystals grown on chip via microdialysis at 293 K. A dose map for the 200 µm x 200 µm x 200 µm cuboid HEWL crystal irradiated at BM30A-FIP at room temperature, with a photon energy of 12.6578 keV and flux 3.32 x 10^{10} ph s^{-1} was produced showing a uniform distribution of the dose in the crystal volume, as expected for data collection strategies where the beam size is equal or larger than the crystal size. The majority of the crystal volume was in the high-dose regime for this experiment but the highest dose value of 0.63 MGy was still much lower than the experimental dose limit of 30 MGy. More simulations were conducted based on this case study by varying the crystal size or shape, the beam profile or size, the photon flux or the photon energy value to investigate the effects of these parameters on dose metrics related to radiation damage.

4.5 References

(1) Apostolopoulou, V.; Junius, N.; Sear, R. P.; Budayova-Spano, M. Mixing Salts and Poly(Ethylene Glycol) into Protein Solutions: The Effects of Diffusion across Semipermeable Membranes and of Convection. *Cryst. Growth Des.* **2020**, *20* (6), 3927–3936.

(2) Junius, N.; Jaho, S.; Sallaz-Damaz, Y.; Borel, F.; Salmon, J.-B.; Budayova-Spano, M. A Microfluidic Device for Both On-Chip Dialysis Protein Crystallization and in Situ X-Ray Diffraction. *Lab Chip* **2020**, *20* (2), 296–310.

(3) Jacquamet, L.; Ohana, J.; Joly, J.; Borel, F.; Pirocchi, M.; Charrault, P.; Bertoni, A.; Israel-Gouy, P.; Carpentier, P.; Kozielski, F.; Blot, D.; Ferrer, J.-L. Automated Analysis of Vapor Diffusion Crystallization Drops with an X-Ray Beam. *Structure* **2004**, *12* (7), 1219–1225.

(4) Jacquamet, L.; Joly, J.; Bertoni, A.; Charrault, P.; Pirocchi, M.; Vernede, X.; Bouis, F.; Borel, F.; Périn, J.-P.; Denis, T.; Rechatin, J.-L.; Ferrer, J.-L. Upgrade of the CATS Sample Changer on FIP-BM30A at the ESRF: Towards a Commercialized Standard. *J. Synchrotron Radiat.* **2009**, *16* (1), 14–21.

(5) Sallaz-Damaz, Y.; Ferrer, J.-L. WIFIP: A Web-Based User Interface for Automated Synchrotron Beamlines. *J. Synchrotron Radiat.* **2017**, *24* (5), 1105–1111.

(6) Kabsch, W. XDS. *Acta Crystallogr., Sect. D: Biol. Crystallogr.* **2010**, *66* (2), 125–132.

(7) Winn, M. D.; Ballard, C. C.; Cowtan, K. D.; Dodson, E. J.; Emsley, P.; Evans, P. R.; Keegan, R. M.; Krissinel, E. B.; Leslie, A. G. W.; McCoy, A.; McNicholas, S. J.; Murshudov, G. N.; Pannu, N. S.; Potterton, E. A.; Powell, H. R.; Read, R. J.; Vagin, A.; Wilson, K. S. Overview of the CCP4 Suite and Current Developments. *Acta Crystallogr., Sect. D: Biol. Crystallogr.* **2011**, *67* (4), 235–242.

(8) Liebschner, D.; Afonine, P. V.; Baker, M. L.; Bunkóczi, G.; Chen, V. B.; Croll, T. I.; Hintze, B.; Hung, L.-W.; Jain, S.; McCoy, A. J.; Moriarty, N. W.; Oeffner, R. D.; Poon, B. K.; Prisant, M. G.; Read, R. J.; Richardson, J. S.; Richardson, D. C.; Sammito, M. D.; Sobolev, O. V.; Stockwell, D. H.; Terwilliger, T. C.; Urzhumtsev, A. G.; Videau, L. L.; Williams, C. J.; Adams, P. D. Macromolecular Structure Determination Using X-Rays, Neutrons and Electrons: Recent Developments in Phenix. *Acta Crystallogr., Sect. D: Struct. Biol.* **2019**, *75* (10), 861–877.

(9) Emsley, P.; Lohkamp, B.; Scott, W. G.; Cowtan, K. Features and Development of Coot. *Acta Crystallogr, Sect. D: Biol. Crystallogr.* **2010**, *66* (4), 486–501.

(10) Jaho, S.; Junius, N.; Borel, F.; Sallaz-Damaz, Y.; Salmon, J.-B.; Budayova-Spano, M. Crystallization of Proteins on Chip by Microdialysis for In Situ X-Ray Diffraction Studies. *J. Visualized Exp.* **2021**, No. 170, e61660.

(11) Aherne, M.; Lyons, J. A.; Caffrey, M. A Fast, Simple and Robust Protocol for Growing Crystals in the Lipidic Cubic Phase. *J. Appl. Crystallogr.* **2012**, *45* (6), 1330–1333.

(12) Caffrey, M.; Cherezov, V. Crystallizing Membrane Proteins Using Lipidic Mesophases. *Nature Protoc.* **2009**, *4* (5), 706–731.

(13) Cherezov, V.; Peddi, A.; Muthusubramaniam, L.; Zheng, Y. F.; Caffrey, M. A Robotic System for Crystallizing Membrane and Soluble Proteins in Lipidic Mesophases. *Acta Crystallogr., Sect. D: Biol. Crystallogr.* **2004**, *60* (10), 1795–1807.

(14) Duran, D.; Couster, S. L.; Desjardins, K.; Delmotte, A.; Fox, G.; Meijers, R.; Moreno, T.; Savko, M.; Shepard, W. PROXIMA 2A – A New Fully Tunable Micro-Focus Beamline for Macromolecular Crystallography. *J. Phys.: Conf. Ser.* **2013**, *425* (1), 012005.

(15) Jeangerard, D.; Ciccone, L.; Desjardins, K.; Haouz, A.; Le Jollec, A.; Savko, M.; Shepard, W. From Plate Screening to Artificial Intelligence: Innovative Developments on PROXIMA 2A at Synchrotron SOLEIL. *Proceedings of the Mechanical Eng. Design of Synchrotron Radiation Equipment and Instrumentation* **2018**.
(16) Strop, P.; Brunger, A. T. Refractive Index-Based Determination of Detergent Concentration and Its Application to the Study of Membrane Proteins. *Protein Sci.* **2005**, *14* (8), 2207–2211.
(17) Tribet, C.; Audebert, R.; Popot, J.-L. Amphipols: Polymers That Keep Membrane Proteins Soluble in Aqueous Solutions. *PNAS* **1996**, *93* (26), 15047–15050.
(18) Shinoda, K.; Yamaguchi, T.; Hori, R. The Surface Tension and the Critical Micelle Concentration in Aqueous Solution of β-D-Alkyl Glucosides and Their Mixtures. *Bull. Chem. Soc. Jpn.* **1961**, *34* (2), 237–241.
(19) le Maire, M.; Champeil, P.; Møller, J. V. Interaction of Membrane Proteins and Lipids with Solubilizing Detergents. *Biochim. Biophys. Acta - Biomembranes* **2000**, *1508* (1), 86–111.
(20) Chae, P. S.; Rasmussen, S. G. F.; Rana, R. R.; Gotfryd, K.; Chandra, R.; Goren, M. A.; Kruse, A. C.; Nurva, S.; Loland, C. J.; Pierre, Y.; Drew, D.; Popot, J.-L.; Picot, D.; Fox, B. G.; Guan, L.; Gether, U.; Byrne, B.; Kobilka, B.; Gellman, S. H. Maltose–Neopentyl Glycol (MNG) Amphiphiles for Solubilization, Stabilization and Crystallization of Membrane Proteins. *Nature Methods* **2010**, *7* (12), 1003–1008.
(21) Murray, J. W.; Garman, E. F.; Ravelli, R. B. G. X-Ray Absorption by Macromolecular Crystals: The Effects of Wavelength and Crystal Composition on Absorbed Dose. *J. Appl. Crystallogr.* **2004**, *37* (4), 513–522.
(22) Nave, C. Radiation Damage in Protein Crystallography. *Radiat. Phys. Chem.* **1995**, *45* (3), 483–490.
(23) O'Neill, P.; Stevens, D. L.; Garman, E. Physical and Chemical Considerations of Damage Induced in Protein Crystals by Synchrotron Radiation: A Radiation Chemical Perspective. *J. Synchrotron Radiat.* **2002**, *9* (6), 329–332.
(24) Garman, E. F. Radiation Damage in Macromolecular Crystallography: What Is It and Why Should We Care? *Acta Crystallogr., Sect. D: Biol. Crystallogr.* **2010**, *66* (4), 339–351.
(25) Hubbell, J. H.; Gimm, H. A.; O/verbo/, I. Pair, Triplet, and Total Atomic Cross Sections (and Mass Attenuation Coefficients) for 1 MeV-100 GeV Photons in Elements Z=1 to 100. *J. Phys. Chem. Ref. Data* **1980**, *9* (4), 1023–1148.
(26) R. Henderson. The Potential and Limitations of Neutrons, Electrons and X-Rays for Atomic Resolution Microscopy of Unstained Biological Molecules. *Q. Rev. Biophys.* **1995**, *28* (2), 171–193.
(27) Albert C. Thompson; David T. Attwood; Eric M. Gullikson; Malcolm R. Howells; Jeffrey B. Kortright; Arthur L. Robinson; James H. Underwood; Kwang-Je Kim; Janos Kirz; Ingolf Lindau; Piero Pianetta; Herman Winick; Gwyn P. Williams; James H. Scofield; Douglas Vaughan. *X-RAY DATA BOOKLET*, Lawrence Berkeley National Laboratory, University of California, Berkeley, **2001**.
(28) Ravelli, R. B.; McSweeney, S. M. The 'Fingerprint' That X-Rays Can Leave on Structures. *Structure* **2000**, *8* (3), 315–328.
(29) Singh, A.; Singh, H. Time-Scale and Nature of Radiation-Biological Damage: Approaches to Radiation Protection and Post-Irradiation Therapy. *Prog. Biophys. Mol. Biol.* **1982**, *39*, 69–107.
(30) Allan, E. G.; Kander, M. C.; Carmichael, I.; Garman, E. F. To Scavenge or Not to Scavenge, That Is STILL the Question. *J. Synchrotron Radiat.* **2013**, *20* (1), 23–36.

(31) Southworth-Davies, R. J.; Medina, M. A.; Carmichael, I.; Garman, E. F. Observation of Decreased Radiation Damage at Higher Dose Rates in Room Temperature Protein Crystallography. *Structure* **2007**, *15* (12), 1531–1541.
(32) Gonzalez, A.; Nave, C. Radiation Damage in Protein Crystals at Low Temperature. *Acta Crystallogr., Sect. D: Biol. Crystallogr.* **1994**, *50* (6), 874–877.
(33) Weik, M.; Ravelli, R. B. G.; Kryger, G.; McSweeney, S.; Raves, M. L.; Harel, M.; Gros, P.; Silman, I.; Kroon, J.; Sussman, J. L. Specific Chemical and Structural Damage to Proteins Produced by Synchrotron Radiation. *PNAS* **2000**, *97* (2), 623–628.
(34) Borshchevskiy, V.; Round, E.; Erofeev, I.; Weik, M.; Ishchenko, A.; Gushchin, I.; Mishin, A.; Willbold, D.; Büldt, G.; Gordeliy, V. Low-Dose X-Ray Radiation Induces Structural Alterations in Proteins. *Acta Crystallogr., Sect. D: Biol. Crystallogr.* **2014**, *70* (10), 2675–2685.
(35) Burmeister, W. P. Structural Changes in a Cryo-Cooled Protein Crystal Owing to Radiation Damage. *Acta Crystallogr., Sect. D: Biol. Crystallogr.* **2000**, *56* (3), 328–341.
(36) Sutton, K. A.; Black, P. J.; Mercer, K. R.; Garman, E. F.; Owen, R. L.; Snell, E. H.; Bernhard, W. A. Insights into the Mechanism of X-Ray-Induced Disulfide-Bond Cleavage in Lysozyme Crystals Based on EPR, Optical Absorption and X-Ray Diffraction Studies. *Acta Crystallogr., Sect. D: Biol. Crystallogr.* **2013**, *69* (12), 2381–2394.
(37) Holton, J. M. A Beginner's Guide to Radiation Damage. *J. Synchrotron Radiat.* **2009**, *16* (2), 133–142.
(38) Elspeth F. Garman; Martin wEIK. Radiation Damage in Macromolecular Crystallography. Methods in Molecular Biology, Springer, **2017**, *1607*.
(39) Nave, C.; Garman, E. F. Towards an Understanding of Radiation Damage in Cryocooled Macromolecular Crystals. *J. Synchrotron Radiat.* **2005**, *12* (3), 257–260.
(40) Garman, E. F.; Weik, M. Radiation Damage to Biological Macromolecules: Some Answers and More Questions. *J. Synchrotron Radiat.* **2013**, *20* (1), 1–6.
(41) Garman, E. F.; Weik, M. Radiation Damage to Macromolecules: Kill or Cure? *J. Synchrotron Radiat.* **2015**, *22* (2), 195–200.
(42) Garman, E. F.; Weik, M. X-Ray Radiation Damage to Biological Samples: Recent Progress. *J. Synchrotron Radiat.* **2019**, *26* (4), 907–911.
(43) Garman, E. F.; Weik, M. X-Ray Radiation Damage to Biological Macromolecules: Further Insights. *J. Synchrotron Radiat.* **2017**, *24* (1), 1–6.
(44) Garman, E. F.; Schneider, T. R. Macromolecular Cryocrystallography. *J. Appl. Crystallogr.* **1997**, *30* (3), 211–237.
(45) Garman, E. Cool Data: Quantity AND Quality. *Acta Crystallogr., Sect. D: Biol. Crystallogr.* **1999**, *55* (10), 1641–1653.
(46) Henderson, R.; Clarke, B. C. Cryo-Protection of Protein Crystals against Radiation Damage in Electron and X-Ray Diffraction. *Proceedings of the Royal Society of London. Series B: Biological Sciences* **1990**, *241* (1300), 6–8.
(47) Owen, R. L.; Rudiño-Piñera, E.; Garman, E. F. Experimental Determination of the Radiation Dose Limit for Cryocooled Protein Crystals. *PNAS* **2006**, *103* (13), 4912–4917.
(48) Fraser, J. S.; Bedem, H. van den; Samelson, A. J.; Lang, P. T.; Holton, J. M.; Echols, N.; Alber, T. Accessing Protein Conformational Ensembles Using Room-Temperature X-Ray Crystallography. *PNAS* **2011**, *108* (39), 16247–16252.
(49) Warkentin, M.; Hopkins, J. B.; Badeau, R.; Mulichak, A. M.; Keefe, L. J.; Thorne, R. E. Global Radiation Damage: Temperature Dependence, Time Dependence and How to Outrun It. *J. Synchrotron Radiat.* **2013**, *20* (1), 7–13.

(50) Warkentin, M.; Thorne, R. E. Glass Transition in Thaumatin Crystals Revealed through Temperature-Dependent Radiation-Sensitivity Measurements. *Acta Crystallogr., Sect. D: Biol. Crystallogr.* **2010**, *66* (10), 1092–1100.
(51) Blake C. C. F.; Phillips D. C. Biological Effects of Ionizing Radiations at the Molecular Level. *International Atomic Energy Agency, Vienna* **1962**, 183–191.
(52) Coquelle, N.; Brewster, A. S.; Kapp, U.; Shilova, A.; Weinhausen, B.; Burghammer, M.; Colletier, J.-P. Raster-Scanning Serial Protein Crystallography Using Micro- and Nano-Focused Synchrotron Beams. *Acta Crystallogr., Sect. D: Biol. Crystallogr.* **2015**, *71* (5), 1184–1196.
(53) Owen, R. L.; Axford, D.; Nettleship, J. E.; Owens, R. J.; Robinson, J. I.; Morgan, A. W.; Doré, A. S.; Lebon, G.; Tate, C. G.; Fry, E. E.; Ren, J.; Stuart, D. I.; Evans, G. Outrunning Free Radicals in Room-Temperature Macromolecular Crystallography. *Acta Crystallogr., Sect. D: Biol. Crystallogr.* **2012**, *68* (7), 810–818.
(54) Mora, E. de la; Coquelle, N.; Bury, C. S.; Rosenthal, M.; Holton, J. M.; Carmichael, I.; Garman, E. F.; Burghammer, M.; Colletier, J.-P.; Weik, M. Radiation Damage and Dose Limits in Serial Synchrotron Crystallography at Cryo- and Room Temperatures. *PNAS* **2020**, *117* (8), 4142–4151.
(55) Zeldin, O. B.; Gerstel, M.; Garman, E. F. RADDOSE-3D: Time- and Space-Resolved Modelling of Dose in Macromolecular Crystallography. *J. Appl. Crystallogr.* **2013**, *46* (4), 1225–1230.
(56) Paithankar, K. S.; Owen, R. L.; Garman, E. F. Absorbed Dose Calculations for Macromolecular Crystals: Improvements to RADDOSE. *J. Synchrotron Radiat.* **2009**, *16* (2), 152–162.
(57) Paithankar, K. S.; Garman, E. F. Know Your Dose: RADDOSE. *Acta Crystallogr., Sect. D: Struct. Biol.* **2010**, *66* (4), 381–388.
(58) Zeldin, O. B.; Gerstel, M.; Garman, E. F. Optimizing the Spatial Distribution of Dose in X-Ray Macromolecular Crystallography. *J. Synchrotron Radiat.* **2013**, *20* (1), 49–57.
(59) Zeldin, O. B.; Brockhauser, S.; Bremridge, J.; Holton, J. M.; Garman, E. F. Predicting the X-Ray Lifetime of Protein Crystals. *PNAS* **2013**, *110* (51), 20551–20556.
(60) Bury, C. S.; Brooks-Bartlett, J. C.; Walsh, S. P.; Garman, E. F. Estimate Your Dose: RADDOSE-3D. *Protein Science* **2018**, *27* (1), 217–228.

Chapter 5

Conclusions and perspectives

Chapter 5

Conclusions and perspectives

My thesis project was to automate and optimize the on chip crystallization of model soluble and membrane proteins for investigating the three-dimensional structure of these biological macromolecules with the *in situ* X-ray diffraction method. It has been part of the ITN MSCA RAMP program **(**https://ramp-itn.eu/sofia-jaho/**)**. My project can be divided in three main objectives including the design of microfluidic devices for on chip protein crystallization via the microdialysis method, the development of instrumentation and computer software for the control and automation of the on chip crystallization process and the study of various protein targets exhibiting biological significance with on chip crystallization and *in situ* X-ray diffraction experiments. In this final chapter, I will elaborate on the outcomes and the concluding remarks of this work, the successful outcomes, the encountered difficulties and the promising perspectives for future implementations.

On the microfluidic chips

A microfluidic chip has been developed for the on chip protein crystallization with the microdialysis method compatible with *in situ* X-ray diffraction experiments. The main body of the chip consists of the NOA 81 photocurable resin supported on a PMMA substrate. The dialysis chip combines the advantages of the microfluidic technology, such as minute sample consumption and fine control over transport phenomena, and the dialysis protein crystallization method allowing an accurate control and tuning of the experimental parameters. Specifically, two devices have been designed with 0.1 µL or 0.3 µL maximum volume capacity of the protein reservoir. Dialysis operates based on the diffusion and equilibration of precipitant molecules through a semi-permeable membrane and offers a kinetic pathway allowing an extensive exploration of the protein phase diagram. Moreover, dialysis combined with temperature control facilitates decoupling nucleation from crystal growth and multiple crystallization conditions can be screened with the same protein sample. In order to integrate the dialysis method into our microchips, a small piece of RC membrane is incorporated directly within two layers of the chip during the fabrication process without requiring chemical bonding or mechanical manipulation. The MWCO of the membrane can be chosen according to the molecular weight of the protein sample and the precipitant solution. RC dialysis membranes are commercially available and the fabrication protocol of the chips can be adjusted to incorporate any kind of polymeric membrane for dialysis, as for example poly(ether sulfone) (PES) or polycarbonate membranes.

The rapid prototyping of the chips, the flexibility of choosing commercially available membranes with appropriate MWCO for the application and the relatively inexpensive materials enable the fabrication of numerous chips. Approximately 20 – 30 chips can be fabricated in a single working day in a clean room. Moreover, the chips can be washed and reused as long as the dialysis membrane or the adhesion of the NOA 81 sticker on the PMMA substrate are not compromised.

The design of the dialysis chip includes a linear channel for the circulation of the crystallization solution, a central cavity for the manual loading of the protein sample and two cavities (pillars) at the edges of the channel dedicated to act as the inlet and outlet ports for fluid handling. The fluidic channel and the protein reservoir are separated by a small piece of RC dialysis membrane. A major modification of the original protocol for the fabrication of the chips was the reduction of the volume of the protein reservoir from 0.2 µL or 0.7 µL to 0.1 µL and 0.3 µL (Chapter 2, Section 2.2.1). This volume could be further reduced if pipetting such small quantities of the protein sample can be achieved either manually or with the aid of automated platforms developed for setting up nL-droplets with conventional crystallization methods in 96-well plates. Another potential modification on the chip's design is related to the length of the fluidic channel. For both designs (0.1 µL and 0.3 µL) the length of the channel is approximately 3.5 cm and the volume of the precipitant solution required to fill the channel is approximately 0.9 µL. Shorter channels would require smaller volumes of crystallization solutions, an important advantage in cases where the crystallization mixture includes expensive additives for pharmaceutical drug design experiments.

Nevertheless, reducing the channel length poses some restrictions concerning the connectors for fluid handling. As explained in Chapter 2, commercially available PEEK connectors or disposable pipette tips are glued on the inlet and outlet ports of the channel for injecting and circulating the crystallization solution. These connectors have a relatively large diameter compared to the diameter of the inlet/outlet pillars of the chip, while the fast epoxy glue used for this application spreads around the connectors before it solidifies (Figure 2.2.5, Chapter 2). Both these factors contribute to the coverage of the chip's surface and sometimes, the epoxy glue can reach close to the protein reservoir rendering the encapsulation of the protein sample with the PMMA piece and the Kapton tape challenging. The length of the channel and subsequently the length of the chip have been designed to avoid this problem. However, reducing the length is not prohibitive if connectors with smaller diameter comparable to the diameter of the inlet/outlet pillars (1 mm) can be used. Another way to address this issue would be to envision the integration of lateral needle-like connectors. A simplified design is shown in Figure 5.1. These connectors would be integrated in the chip during the fabrication process. The idea is to "sandwich" the connectors between the two layers of the chips during the fabrication step where the RC membrane is "sandwiched" between the protein reservoir and the fluidic channel. The inner or outer diameter of the connectors should be appropriate for connecting PTFE tubes for fluid circulation.

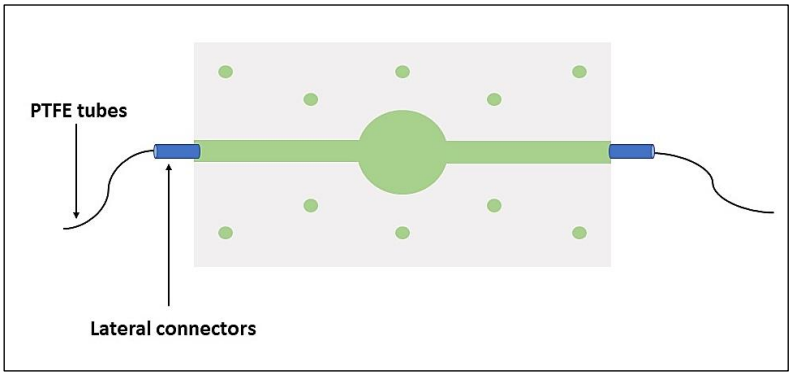

Figure 5.1: Schematic illustration of a dialysis chip with lateral inlet and outlet connectors.

In order to address issues raised by the integration of the RC membrane and potential deformation or leaks during the circulation of the crystallization solution under constant pressure, the potential of fabricating hydrogel membranes directly in the chips by *in situ* photo-patterning was explored. Two chips were developed using different fabrication (PEGDA 250, NOA 81) and substrate (glass, COC) materials. The two designs constitute a potential alternative to the dialysis chip; however, more experiments should be conducted to establish a well-functioning protocol for their use with on chip protein crystallization via microdialysis. The MWCO of the hydrogel membranes can be adjusted by altering the composition of the formulation mixture. Moreover, the potential of parallelizing crystallization experiments is feasible by designing a device with multiple protein compartments where the membrane can be fabricated *in situ* in exact positions. A simplified design for a chip with hydrogel membranes for screening crystallization conditions is shown in Figure 5.2. Two protein samples with different concentration can be injected in 8 wells and 8 channels can be used for injecting crystallization solutions of various compositions. In total, 8 different conditions can be screened with a single device. This is merely a simple example of how multiple parallel experiments can be set up with a chip and the number of channels or the protein reservoirs or the complexity of the device can only be limited by our designing imagination.

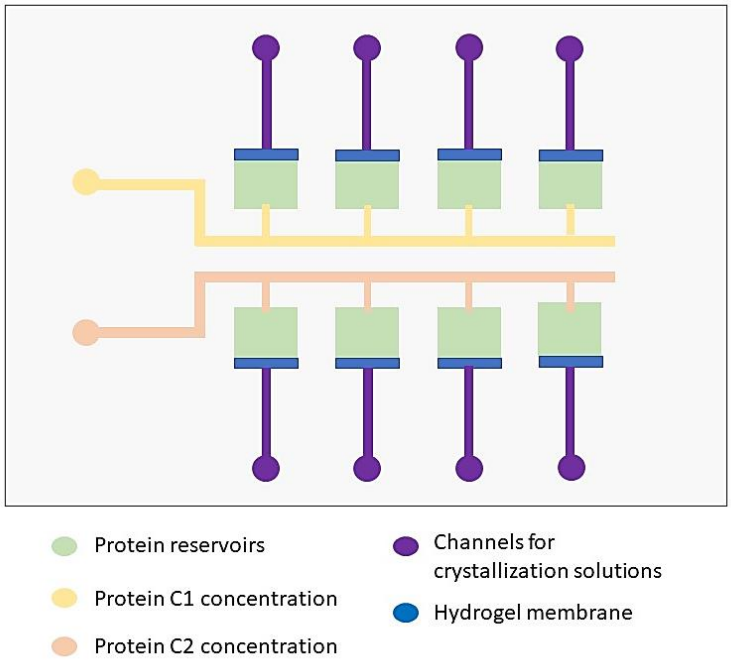

Figure 5.2: Schematic illustration of a multi-well microchip for *in situ* fabrication of hydrogel membranes for screening protein crystallization conditions.

Finally, the dialysis chips are compatible with *in situ* X-ray diffraction studies at room temperature. The *in situ* data collection approach at room temperature addresses issues associated with cryogenic cooling, manual harvesting and radiation damage of the protein crystals. Once protein crystals are grown on the dialysis chip, the chip can be mounted directly in front of the X-ray beam on synchrotron beamlines, with the aid of a 3D printed support

(Figure 3.2.3, Chapter 3). However, the 3D printed support limits the range of accessible beamlines as it is mainly designed for beamlines compatible with in plate X-ray diffraction experiments equipped with a gripper for 96-well crystallization plates (SBS standard). To address this problem, another support should be designed allowing the position of the chips in any MX beamline. The support could resemble a standard magnetic base for goniometer heads, as the example shown in Figure 5.3 (a).

The dialysis chip has been successfully used for *in situ* synchrotron serial crystallography (SSX) experiments and the perspective of *in situ* serial femtosecond X-ray crystallography (SFX) using XFEL sources is promising. Moreover, performing on chip and *in situ* time-resolved experiments is a possibility that would be interesting for the crystallographic community. Reagents that could trigger time-resolved studies could be introduced within the microfluidic channel either manually with a syringe or with an automated fluidic system. A chip including an additional inlet port for injecting reagents can be fabricated (Figure 5.3 (b)) ensuring the feasibility of the experiments. However, the diffusion of the reagents through the dialysis membrane has to be ensured in advance by selecting a membrane with the appropriate MWCO and preliminary experiments should be conducted to study diffusion and mixing times. The timescale in time-resolved experiments and the response time of the protein target to external triggers are crucial parameters. Therefore, it is also important to ensure that the diffusion time of the reagents through the dialysis membrane lies within the timescale of the experiment.

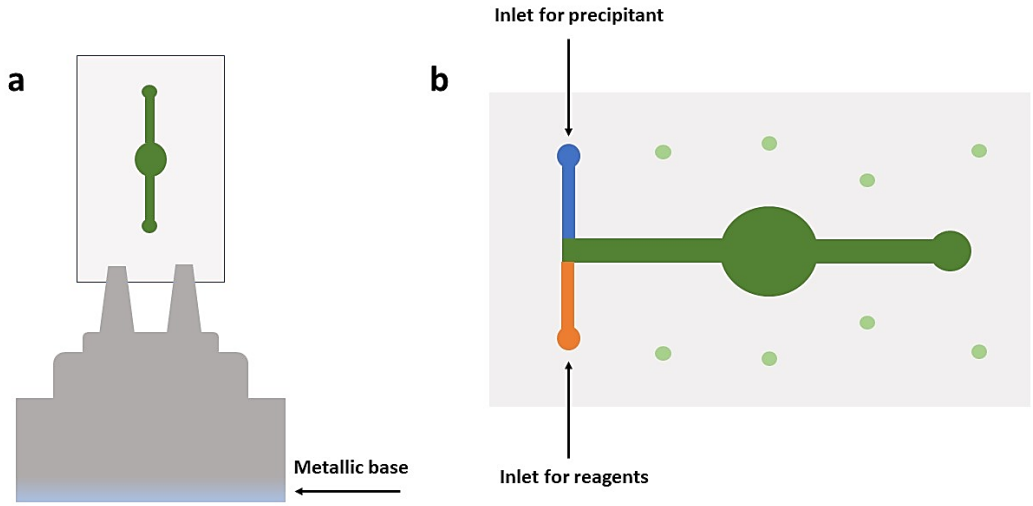

Figure 5.3: (a) Schematic illustration of a magnetic base supporting the dialysis chip compatible with standard goniometer base for *in situ* X-ray diffraction studies. (b) A dialysis chip with two inlet channels for the precipitant solution and reagents triggering *in situ* time-resolved experiments.

The background noise generated by the interaction of X-rays with the materials comprising the dialysis chip (PMMA, Kapton, RC membrane) has been evaluated, rendering the chips compatible with *in situ* X-ray diffraction experiments. Even though, other materials like COC were also tested for supporting the NOA 81 resin instead of the 175 µm thick PMMA

substrate, we continued to mainly fabricate the dialysis chip with PMMA substrate due to the mechanical stability that it offers during the on chip crystallization experiments or when mounting the chips in MX beamlines. The same PMMA foil is used to encapsulate the protein sample within the protein reservoir as described in Chapter 2 (Section 2.2.2). However, the thickness of this PMMA piece used for protein encapsulation can be reduced since it is not crucial to be as thick (175 μm) as the substrate. The reduction of this layer of the microfluidic assembly can reduce further the background noise generated by the interaction of X-ray radiation with the chip's materials.

On the MicroCrys platform

The MicroCrys platform has been developed for automating the on chip crystallization of proteins via microdialysis. Chemical composition and temperature control has been integrated for investigating protein phase diagrams. MicroCrys includes a stepwise motorized metallic support, an inverted digital camera with automated focus and LED lights facilitating real-time monitoring and image recording of the microchips. The metallic support can accommodate the 3D printed holder developed for positioning 3 chips simultaneously for crystallization or for *in situ* X-ray diffraction experiments. The components of the platform are controlled by custom-built LabVIEW software displaying a user-friendly graphical interface designed to manipulate the spatial movement of the support, the focus of the camera, the illumination level and to record images with a frequency allocated by the user.

Even though the platform is robust from a manufacturing point of view, additional features relevant to microfluidic protein crystallization could be added. For example, a humidity box surrounding the microchips can be fixed on the metallic support of the platform (Figure 5.4). One of the major challenges encountered with the on chip crystallization experiments was related to evaporation, especially when experiments lasted for prolonged time (weeks). This humidity box can open from one side allowing the manipulation of the chips and it can be manufactured from optically transparent material, as for example Plexiglas, ensuring the visualization of the experiments.

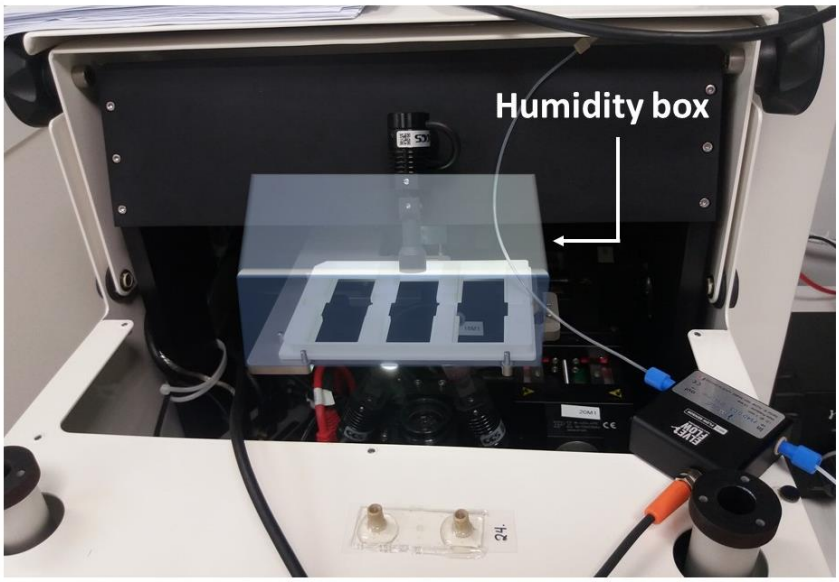

Figure 5.4: Schematic illustration of a transparent humidity box positioned on the sample holder of the MicroCrys platform.

In order to automate fluid transfer and circulation within the linear channel of the chips, a commercial fluidic system (Elveflow) has been integrated in the MicroCrys platform. The system for fluid handling includes a pressure-driven controller with two pressure channels for mixing and circulating the crystallization solution under constant flow or under constant pressure difference between the inlet and the outlet port of the fluidic channel and two thermal-based digital flow sensors. The controller has two pressure channels used to drive the solutions from pressurized containers into the PTFE tubes connected to the inlet port of the microfluidic device. The two channels can be used independently to circulate a solution in two different chips, allowing two crystallization experiments to run simultaneously. However, the manufacturer offers the possibility to add up to four pressure channels in one controller. This feature can be an important asset when setting up crystallization experiments on several chips simultaneously or when chips with multiple inlets (Figure 5.2) are used for parallel experiments.

Moreover, the Elveflow system includes flow sensors that can be connected at any point along the flow were the accurate measurement or regulation of the flow rate is important for the experiment. Pre-mixed crystallization solutions can be used with the pressure-driven controller or can be prepared in an automated way with a six-valve distributor. The distributor injects sequentially various salt, buffer or PEG solutions into a mixing reservoir for preparing the final mixture for crystallization. Indeed, there are several components for fluid handling that can be added for an easy and precise control of fluid transfer in microfluidics. Our goal was to verify the compatibility of these components with our application of on chip protein crystallization, integrate the separate parts in MicroCrys and automate their control with our LabVIEW program. So far, the pressure-driven controller has been integrated in the LabVIEW interface. In the future, the flow sensors and the six-valve sequential distributor can be added. Adding features and functionalities for mixing solutions can upgrade the existing user

interface. The user can set input parameters such as the concentration of the reagents (salt, buffer or PEG solutions) and the final volume of the crystallization solution and the program can calculate automatically the mixing ratio and prepare the mixture with the sequential distributor.

Thermal regulation of the protein reservoir is crucial for investigating crystallization phase diagrams. We developed a prototype using the thermoelectric Peltier effect for heating and/or cooling the protein reservoir. Frequently, two Peltier modules are used to produce a temperature difference between the hot and the cold side. However, a single Peltier module is sufficient for our application since a reversible controller for thermoelectric assemblies can reverse the side of the module that is in contact with the chip depending on whether we want to heat the protein reservoir or cool it down. The Peltier module has a 7.21 mm diameter hole facilitating visualization of the protein reservoir through the inverted camera of the MicroCrys platform. Nevertheless, reducing the diameter of the Peltier element to a size comparable to the diameter of the protein chamber would guarantee a more precise thermal control. The diameter of the protein reservoir for the 0.1 µL and the 0.3 µL chip is 1.5 mm and 2.8 mm, respectively. Ordering a custom-build Peltier module from the manufacturing company is a viable solution for future applications. Finally, simulations on the heat transfer must be conducted to acknowledge the thermal distribution across the protein reservoir. Undesirable temperature gradients within the protein reservoir can compromise the crystallization process and the accuracy of phase diagrams.

The final support developed for on chip thermal regulation was manufactured entirely from aluminium. The cooling fins used for heat dissipation are part of the main aluminium body of the support. The support can be used with the MicroCrys platform. Several holes of appropriate diameter were drilled in different parts of the support for the visualization of the protein reservoir with the inverted camera.

A J type thermocouple is used to read the temperature value near the protein reservoir. The thermocouple is stabilized externally in the dedicated position of the support for thermal regulation. Incorporating the thermocouple within the microchip during the fabrication process could guarantee better precision on thermal regulation. A thermocouple with thin wires can be “sandwiched” between the two layers of the chip and positioned at the exact edge of the protein reservoir. At a first glance, this suggestion of using a thermocouple per chip doesn’t seem financially viable. However, the thermocouple can be removed when the chip is disposed and re-used.

The thermocouple and the Peltier module are connected to the reversible controller. Laird Technologies (the manufacturer of the controller) provides a serial communication protocol for taking full command of the controller and its components. In order to automate the use of the controller, we developed a custom-built program written in LabVIEW for displaying and recording the temperature value read by the J type thermocouple at the computer. A graphical user interface allows to recover the numerical value of the thermocouple (°C) and to display the corresponding data as a function of time (s). An assembly of five electronic WAGO cards has been developed to read the temperature of the J thermocouple via the LabVIEW program. The LabVIEW code for thermal regulation can be added in the main LabVIEW program of the MicroCrys platform for an overall control over the instrumental developments associated to the on chip crystallization. The user will be able to

control and configure the experimental parameters concerning the platform, the fluidic system and the thermal regulation through a single graphical interface.

On protein crystallization and *in situ* X-ray diffraction

Two model soluble proteins (HEWL and Thaumatin from *Thaumatococcus danielli*) and four membrane proteins (ShuA from *Shigella dysenteriae*, AcrB from *Escherichia coli*, SERCA from *Oryctolagus cuniculus* and TmPPase from *Thermotoga maritima*) were used for on chip crystallization with the microdialysis method and *in situ* X-ray diffraction studies. Prior to the on chip crystallization trials, crystallization conditions for all proteins were screened with conventional methods, such as vapor diffusion hanging drop and dialysis. The effect of protein or precipitant concentration on the nucleation time, the crystal size and shape and the uniformity of the crystal population were investigated. On chip crystallization experiments were performed with the pre-screened conditions via microdialysis. When the pre-screened conditions did not yield crystals, other crystallization conditions were explored on chip by varying the protein or the precipitant concentration or the nature of the precipitant itself. Moreover, for AcrB and ShuA proteins, additive molecules were also used for co-crystallization. Rifampicin was used with AcrB and Europium salt with ShuA. In the case of on chip crystallization of soluble proteins, the MWCO of the RC dialysis membrane was 6 – 8 kDa, while for membrane protein crystallization the MWCO was 12 – 14 kDa. All the on chip crystallization experiments were carried out at 293 K. The crystallization solution was pre-mixed and was injected within the fluidic channel manually with a disposable syringe or in an automated mode with the pressure-driven fluidic system of the MicroCrys platform.

HEWL was used as a model protein for verifying the compatibility of our dialysis chip with different crystallization methods or X-ray diffraction data collection strategies. Specifically, HEWL was used to perform a preliminary, qualitative study of the crystallization phase diagram of the protein as a function of the precipitant (NaCl) concentration. HEWL crystals grew on chip at 293 K in the presence of 1 M NaCl, dissolved in 0 M NaCl and re-nucleated at a lower precipitant concentration (0.8 M NaCl). The MicroCrys platform was used in combination with the continuous circulation mode for exchanging the crystallization solutions demonstrating the reversibility of the on chip microdialysis method and the feasibility of studying phase diagrams with MicroCrys. Future experiments should also exploit the prototype developed for thermal regulation for investigating temperature-concentration protein phase diagrams.

HEWL was also used to prepare cubic mesophase of monoolein at 293 K in 3:2 (monoolein: protein) ratio in order to set up on chip crystallization experiments with the LCP method. Multiple, isomorphous, small crystals of HEWL were grown on chip with the LCP method in various crystallization conditions. The advantages of the LCP method were thoroughly discussed in the manuscript but the main advantage with a practical aspect was the stabilization of the protein sample within the protein reservoir. Occasionally, the protein sample would move around within the reservoir of the chip when air was trapped during the encapsulation of the protein or when pressure was applied during the injection of the crystallization solution in the channel. The viscous nature of the cubic mesophase completely eliminated this problem. A characteristic example is shown in Figure 5.5 (a) where HEWL (20

mg mL^{-1}) crystals grew on chip in the presence of 1 M NaCl, 100 mM CH_3COONa pH 4.5, and 30 % PEG 400. The HEWL (40 mg mL^{-1}) crystals in Figure 5.5 (b) grew with the LCP method in the presence of 1 M NaCl, 100 mM CH_3COONa pH 4.0 and 30 % PEG 400.

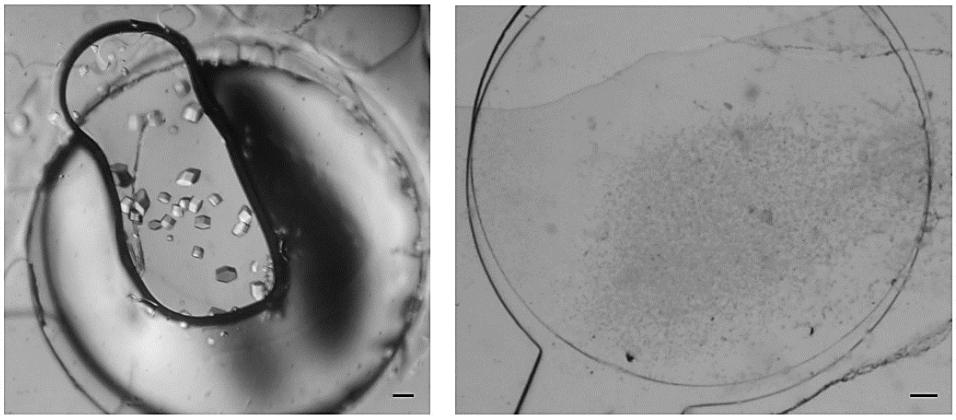

Figure 5.5: HEWL crystals grown on chip in the presence of (a) 1 M NaCl, 100 mM CH_3COONa pH 4.5, and 30 % PEG 400 and (b) 1 M NaCl, 100 mM CH_3COONa pH 4.0 and 30 % PEG 400 with the LCP method. The scale bar represents 100 µm.

Finally, HEWL was used to investigate the compatibility of the dialysis chip for growing large crystals for neutron crystallography in the presence of deuterated solutions. Even though relatively large crystals grew on chip, the thickness of the crystals can be restricted by the height of the dialysis reservoir that is approximately 45 µm. In the future, it would be interesting to examine the diffraction of such crystals *in situ* using our chips with an adapted depth in the neutron diffraction tests, while at the same time, the interaction of neutrons with the materials of the device (PMMA, Kapton, RC membrane) should be studied to evaluate the background noise.

In situ X-ray diffraction experiments were carried out at different beamlines (BM30A-FIP/ESRF, PROXIMA-2A/Soleil, BL13 – XALOC/ALBA and P14/PETRA III) confirming the compatibility of the dialysis chip with *in situ* data collection at room temperature. Detailed electron density maps were produced for HEWL crystals at a resolution higher than 2 Å. Partial diffraction data sets of numerous, isomorphous, small crystals of HEWL grown on chip with the LCP method and Thaumatin crystals were recently collected at PROXIMA-2A beamline at room temperature, validating the compatibility of on chip LCP crystallization with SSX experiments. The HEWL crystals grown with the LCP method and the Thaumatin crystals diffracted close to 2.6 Å and 1.8 Å, respectively. Despite the advantages of the on chip LCP method related to sample stabilization and diffraction quality of the crystals, studies must be conducted on the contribution of the cubic mesophase of monoolein on the background noise during *in situ* data collection. Figure 5.6 shows a diffraction image of HEWL crystals grown with the LCP method collected *in situ* at PROXIMA-2A beamline. Diffusive rings attributed to the lipidic mesophase can be distinguished close to the beam center. SAXS is the most suitable technique to investigate this contribution and characterize the lipidic mesophases on chip. We had been allocated beamtime to perform the experiments at the P12 beamline (PETRA III) and

investigate the phase diagram of monoolein on chip at 293 K in the presence of various solutions (salts, buffers, PEGs, detergents) commonly used for protein crystallization. However, due to the worldwide sanitary crisis and the restrictions on travelling, the experiments were cancelled. In the future, this investigation should be carried out to reveal essential information for applying the LCP method with the dialysis chip.

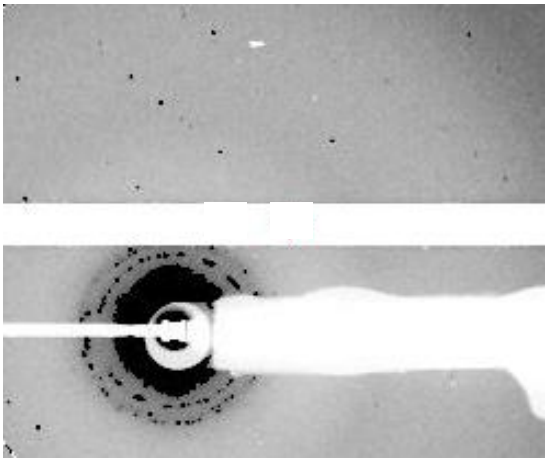

Figure 5.6: Diffraction image of HEWL crystals grown on chip with the LCP method during *in situ* X-ray diffraction at PROXIMA-2A beamline. Diffusive rings attributed to the lipidic mesophase of monoolein are visible close to the beam center.

The on chip crystallization of membrane proteins was more challenging than the case of soluble proteins. AcrB, SERCA and TmPPase crystals grew on chip via microdialysis and their diffraction quality was tested. AcrB crystals diffracted at a resolution lower than 14 Å, TmPPase diffracted close to 15 Å, while SERCA diffracted close to 7 Å, yielding the best resolution acquired with membrane protein crystals on chip so far. Several crystallization conditions that were tested in advance with conventional methods by the collaborators, who provided the protein samples, were also tested with the dialysis chip. However, the on chip crystallization trials were not always successful. Assuming that induction times for nucleation are prolonged at the microscale, the chips carrying the membrane protein samples were left to incubate for longer time intervals from several days up to several weeks. Evaporation issues were encountered. The humidity box proposed for the MicroCrys platform (Figure 5.4) could potentially address this problem. Moreover, multiple crystallization conditions must be screened on chip in order to find the optimal conditions that can increase the supersaturation and induce nucleation of the membrane protein crystals.

Finally, RADDOSE-3D was used to simulate dose estimations for the *in situ* X-ray diffraction experiment of HEWL crystals grown on chip via microdialysis at 293 K. A dose map for a cuboid HEWL crystal irradiated at BM30A-FIP at room temperature was produced, showing a uniform distribution of the dose in the crystal volume, as expected for data collection strategies where the beam size is equal or larger than the crystal size. Most of the crystal volume was in the high-dose regime for this experiment but the highest dose value of 0.63 MGy was still much lower than the experimental dose limit of 30 MGy. Simulations were conducted based on this case study by varying the crystal size or shape, the beam profile or

size, the photon flux or the photon energy value to investigate the effects of these parameters on dose metrics related to radiation damage. Using a beam size equal or larger than the protein crystal is indeed a good choice. But this is not always feasible, especially when using micro-focused beams. A characteristic example of radiation damage on a Thaumatin crystal during *in situ* serial data collection at room temperature at the PROXIMA-2A beamline was given in Figure 4.1.12 (Chapter 4). Thus, it is important to estimate the expected dose prior to *in situ* X-ray diffraction experiments in order to establish the optimal data collection strategy. Despite this fact, as for the quality of the crystallographic statistics for Thaumatin, it does not appear to have been compromised. A detailed electron density map was generated at a resolution of 1.8 Å by merging partial data sets collected from several crystals and only future careful structural analysis could possibly reveal traces of radiation damage.

Appendices

Appendices

Appendix for Chapter 2

2.1 Profilometer measurements for the dialysis chip

A profilometer was used to measure the thickness of the deposited SU-8 film on the silicon wafers after photolithography. The profilometer used at LOF (Laboratory of the Future) was the non-contact, 3D surface profiler Sensofar S neox and the measurements were taken by using the program SensoSCAN 6.3 which was set on the function of Vertical Scanning Interferometry (VSI) providing nanometer vertical resolution. The bright field objective used was a Nikon DI 10X.

The black patterns on the photomasks of Figure 2.1.2 (a) and Figure 2.1.2 (b) remain soluble in the PGMEA developer after the UV exposure during photolithography and the channels and pillars are engraved on the masters, as illustrated in Figure 2.1.3. Therefore, the thickness of the SU-8 resist after photolithography can be measured as the depth of the channels and pillars on the masters. This depth (ΔZ) is the vertical distance from the surface of the master where the SU-8 photoresist was polymerized after the UV exposure (transparent features of the photomasks in Figure 2.1.2 (a) and Figure 2.1.2 (b)). Figure A2.1 shows the profilometer measurements for the two SU-8 masters produced for the chip design with a protein reservoir volume of 0.1 µL. Specifically, Figure A2.1 (a) shows the depth of the protein reservoir (central pillar) and Figure A2.1 (b) the depth of the fluidic channel. The respective measured values are approximately 48 µm for both the protein reservoir and the channel, indicating a uniform deposition of the photoresist on the masters. The SU-8 3050 resist was spin coated on the silicon wafers in order to acquire a nominal thickness of 50 µm. The actual experimental value of 48 µm confirms a satisfactory deposition during photolithography, deviating only 4 % from the nominal thickness. Figure A2.2 shows the profilometer measurements for the two SU-8 masters produced for the chip design with a protein reservoir volume of 0.3 µL. The depth value measured for the central protein reservoir (Figure A2.2 (a)) and the linear fluidic channel (Figure A2.2 (b)) is approximately 44 µm, deviating by 12 % from the nominal value.

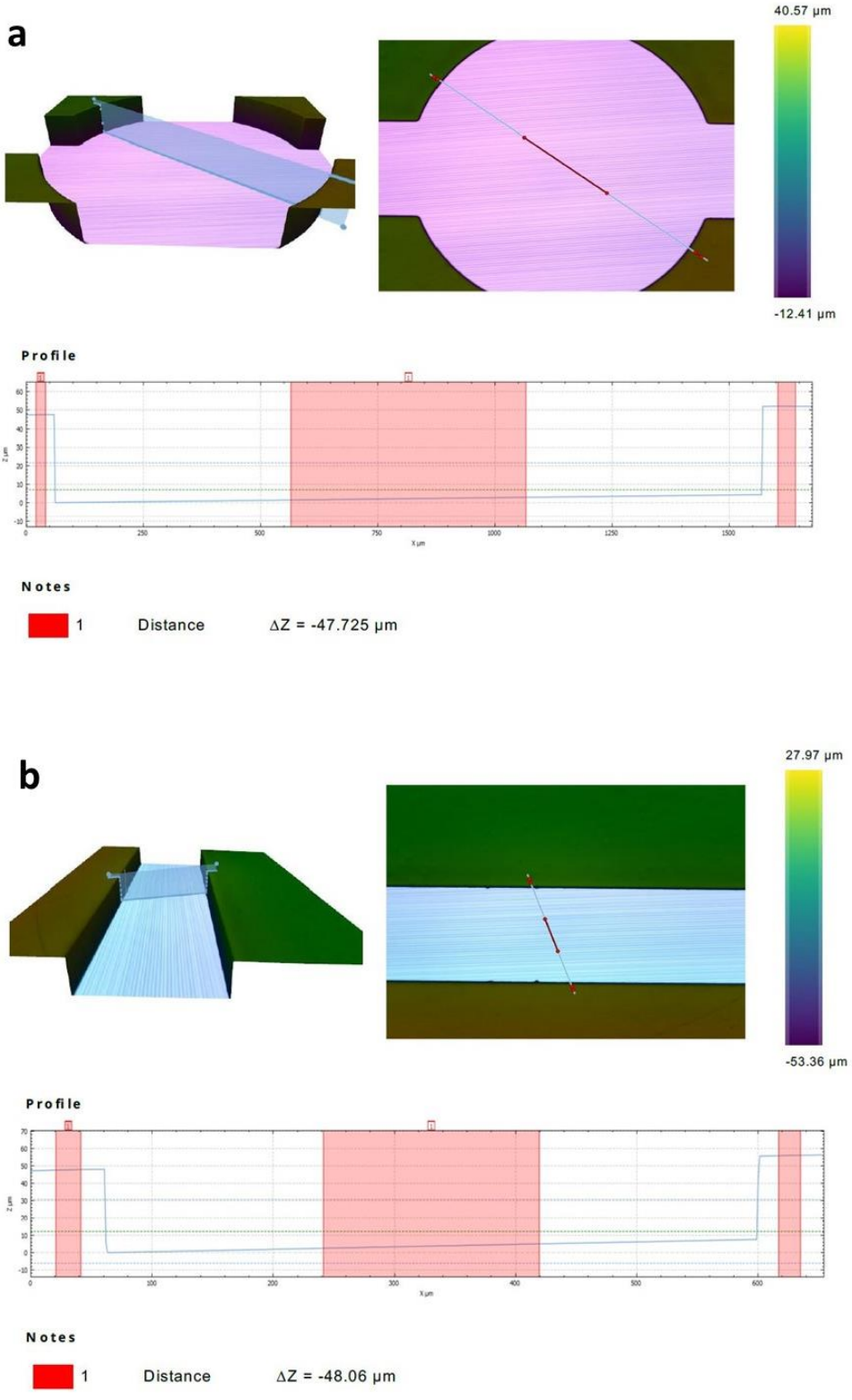

Figure A2.1: Profilometer measurements of (a) the central pillar and (b) the fluidic channel for the SU-8 master produced for the chip design with protein reservoir volume of 0.1 µL.

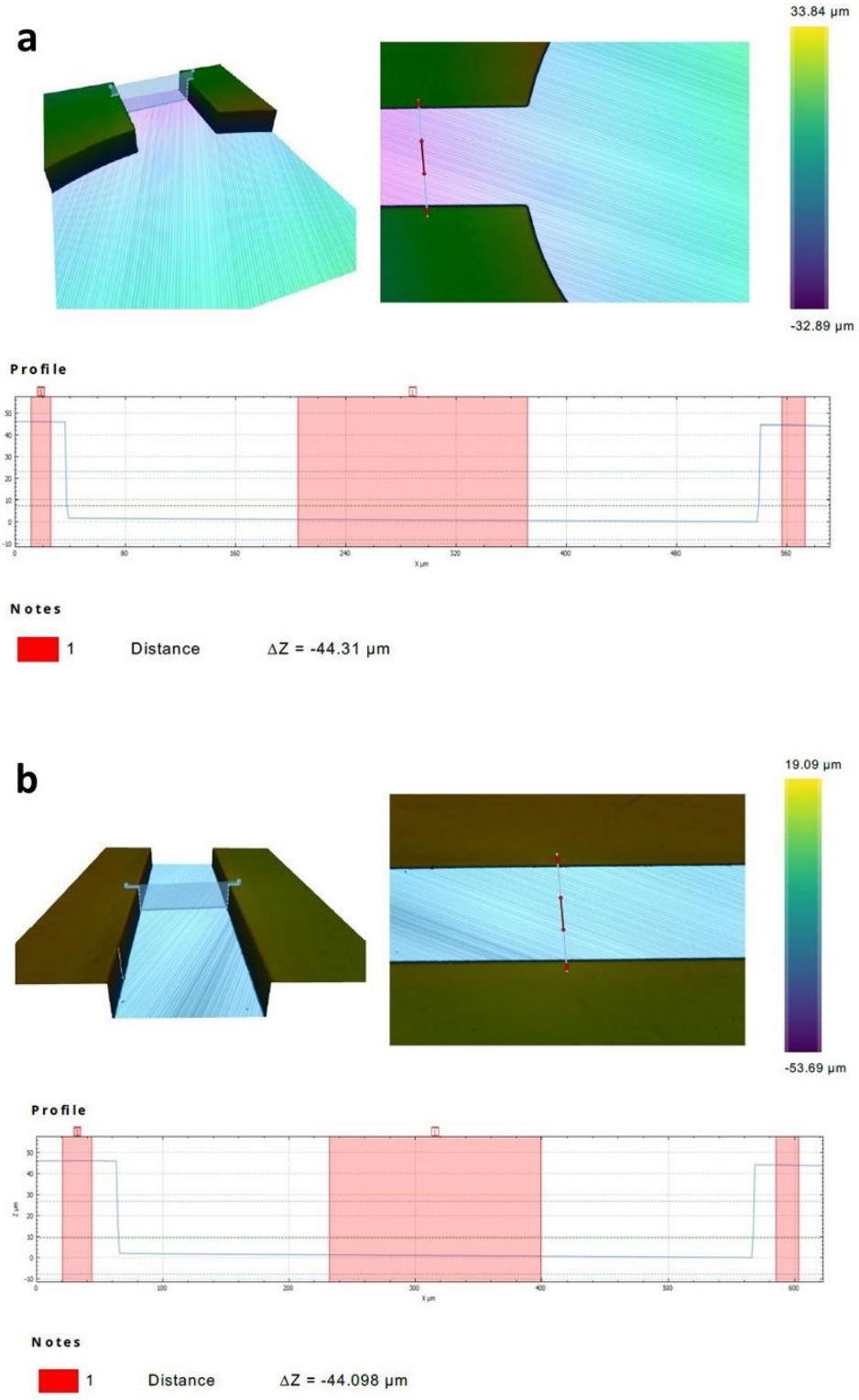

Figure A2.2: Profilometer measurements of (a) the central pillar and (b) the fluidic channel for the SU-8 master produced for the chip design with protein reservoir volume of 0.3 µL.

2.2 *In situ* fabrication of hydrogel membranes

2.2.1 Designs and masks

The design illustrated in Figure 2.3.1 (a) is the final design that was used to develop the microfluidic chips for *in situ* photo-patterning of hydrogel membranes. Two more masks were tested before the final one ("SJ_mask 4"). These masks had the same design but some features were different. Specifically, in the first mask ("SJ_pattern 1") the channels had larger dimensions and the pillars had a larger diameter and were more numerous (Figure A2.3 (a)). In Figure A2.3 (b), the second mask ("SJ_mask 3") is shown, where the dimensions of the patterns are the same with the first mask ("SJ_pattern 1") but less pillars are included. Both these designs did not work very well for the chip fabrication and the final design ("SJ_mask 4", Figure 2.3.1 (a)) was developed.

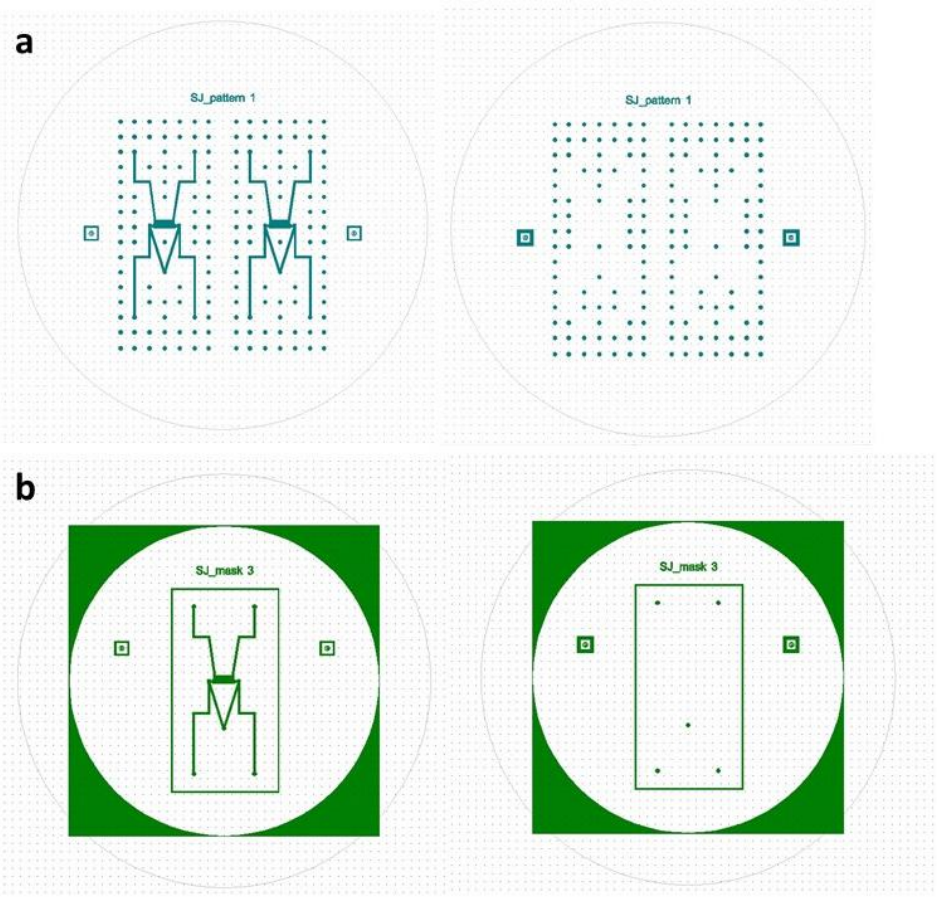

Figure A2.3: (a) The patterns of the first design ("SJ_pattern1") and (b) the second design ("SJ_mask3") for *in situ* photo-patterning of hydrogel membranes as designed with CleWin.

During my second secondment at LOF (2019), I designed another device ("SJ_1 µL") for *in situ* fabrication of hydrogel membranes. Figure A2.4 (a) shows the design of the first layer containing the channels and pillars on the left and the second layer patterning only the pillars on the right. The respective masks used for photolithography are illustrated in Figure A2.4 (b). The volume of the protein reservoir, which is the hemisphere in the design, is 1 µL. The interface between the protein reservoir (hemisphere) and the precipitant reservoir (rectangular) is the location where the hydrogel membranes are fabricated.

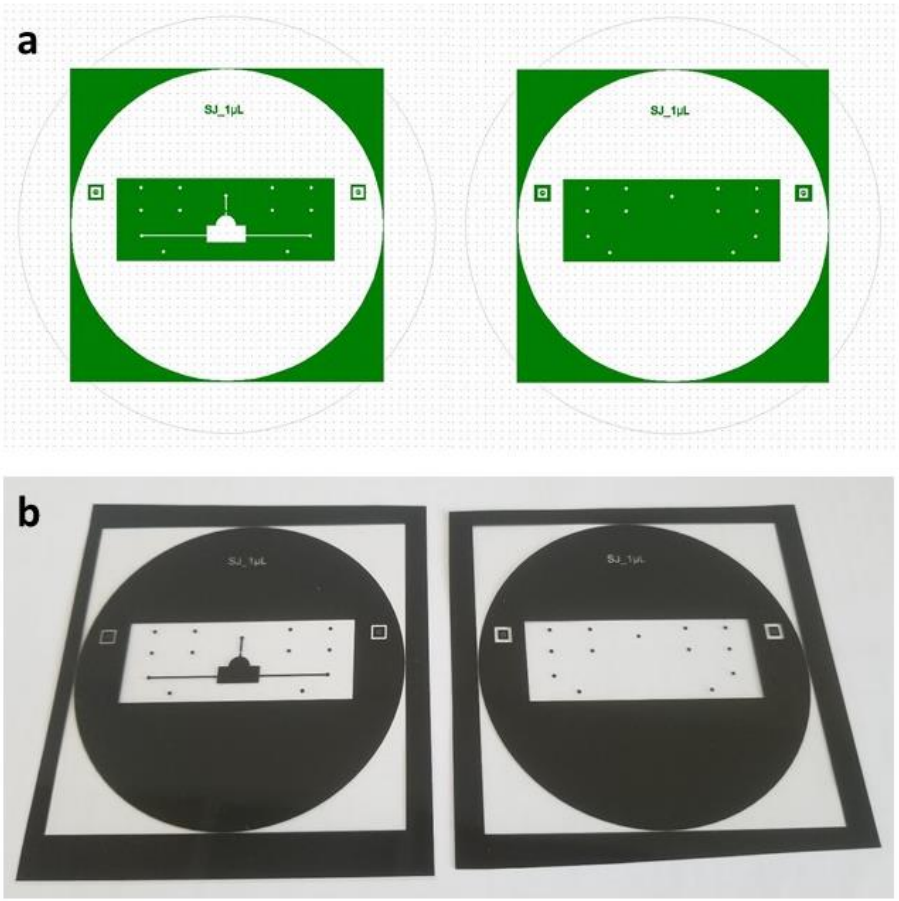

Figure A2.4: (a) The patterns of the microfluidic chip ("SJ_1 µL") for *in situ* photo-patterning of hydrogel membranes as designed with CleWin and (b) the respective masks for photolithography.

Photolithography was implemented to acquire the master for the design "SJ_1 µL" (Figure A2.4). The protocol is described in the following section. The SU-8 3000 series negative photoresist was used on silicon wafers (76.2 mm diameter and 500 ± 20 µm thickness). The equipment used for plasma treatment, spin coating, soft baking and the mask aligner are the same as described in Section 2.1 (Chapter 2). Moreover, the surface measurements of the SU-8 masters of all the designs tested for *in situ* photo-patterning of hydrogel membranes are included in Appendix 2.2.3.

2.2.2 Protocol for "SJ_1 μL" design

For the fabrication of the PEGDA or NOA 81 chips based on the "SJ_1 μL" design, one master was developed for each one of the photomasks shown in Figure A2.4 (b). The first master patterns the channels and the pillars and the second master patterns only the pillars. Both masters were developed by one-layer photolithography. First, the silicon wafer was rinsed with isopropanol and acetone, dried with nitrogen gas and its surface was treated with air plasma for 3 min. For a thickness of approximately 50 μm, the SU-8 3050 resist was applied as follows:

- Spin coating: 10 s spin at 500 rpm with acceleration of 100 rpm/s followed by 30 s spin at 3500 rpm with acceleration at 300 rpm/s
- Soft bake: 15 min at 368 K on a hot plate followed by 2 min at room temperature
- UV exposure: 8 s with a power of 41 mW cm^{-2}
- PEB: 5 min at 368 K on a hot plate followed by 2 min at room temperature
- Development: 15 min in PGMEA bath

The masters with the photoresist structures on them were rinsed with isopropanol, dried with nitrogen gas and stored in Petri dishes. Finally, the masters were placed in a tapped hot plate for 10 min at 368 K under the vapor atmosphere of HMDS.

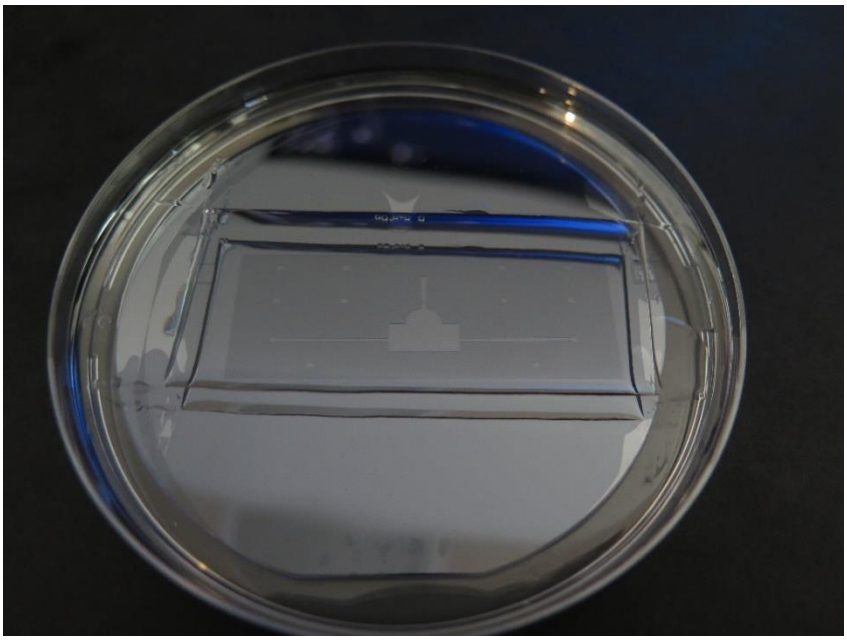

Figure A2.5: The SU-8 master patterning the channels and the pillars of the "SJ_1 μL" design developed for *in situ* photo-patterning of hydrogel membranes.

2.2.3 Surface measurements of the SU-8 masters

Many measurements were taken across the channels of each wafer and at the inlet/outlet ports (pillars) with the Sensofar S neox profilometer. Table A2.1 summarizes the average values of the thickness for the different designs. Specifically, in the second column is given the average thickness (μm) of the channels and in the third column the average thickness (μm) of the pillars for five different masters. The masters named "SJ_pattern 1" and "SJ_mask 3" were the two designs that did not give satisfactory results. The master named "SJ_mask 4" is the one that gave good results and was used to fabricate a plethora of PEGDA chips. Trapped air bubbles during the fabrication of the PEGDA chips is the reason why the first two designs ("SJ_pattern 1" and "SJ_mask 3") were not very efficient during microfabrication. The "SJ_mask 4" design would also lead sometimes to the trapping of undesired air bubbles within the very thin PEGDA chips.

Table A2.1: Profilometer measurements for all SU-8 masters and designs developed for *in situ* photo-patterning of hydrogel membrane.

Master	Height of channels (μm)	Height of holes (μm)
"SJ_pattern 1"	8.3	94.7
"SJ_mask 3"	7.9	97.8
"SJ_mask 4"	7.9	92.8
"SJ_1 μL"	47.9	42.3

In the following figures some results from the SensoSCAN program are shown. Figure A2.6 illustrates a scan of the whole surface of the "SJ_mask 4" master. Some patterns on the SU-8 master are missing like for example, the pillar at the V-shaped motif on the right or part of a channel near the V-shaped motif on the left. This damage was caused after the master was used several times to fabricate PEGDA chips directly on the wafer's surface. During the cleaning step of the master following the chips' fabrication, more subtle manipulation should be made in order to avoid the accidental damage of the motifs.

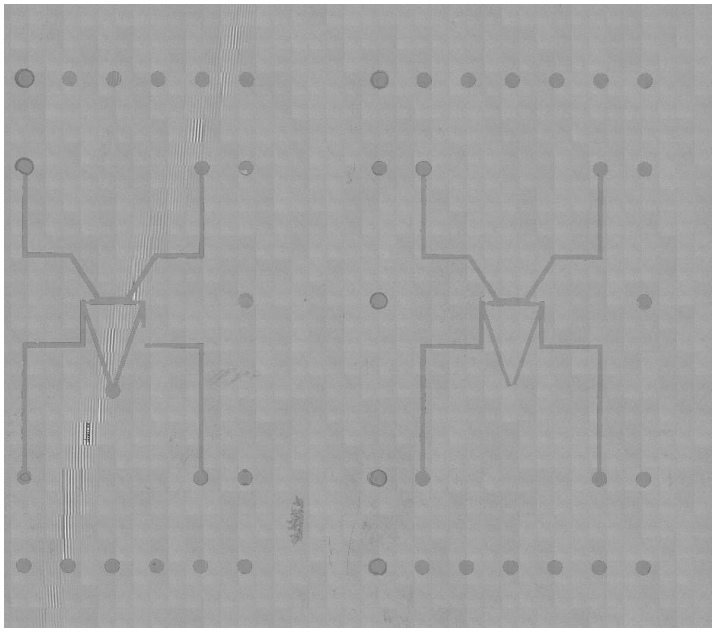

Figure A2.6: Scan of the surface of the "SJ_mask 4" master with the Sensofar S neox profilometer. The damaged structures can be located on the channel (left) and the pillar (right) near the V-shaped motif.

The transparent patterns on the photomasks of Figure 2.3.1 (b) get crosslinked after the UV exposure of the SU-8 photoresist during photolithography, while the opaque features of the masks remain soluble in the PGMEA developer. Thus, the height of the channels and the pillars of the "SJ_mask 4" exceeding vertically the surface of the silicon wafer define the thickness of the deposited SU-8 photoresist. On the contrary, the channels and pillars of the "SJ_1 µL" master appear opaque (black) on the photomasks (Figure A2.4 (b)), remaining soluble during the development of the SU-8 resin, and are engraved on the masters, as illustrated in Figure A2.5. Therefore, the thickness of the SU-8 resist after photolithography can be measured as the depth of the channels and pillars on the "SJ_1 µL" master. This depth (ΔZ) is the vertical distance from the surface of the master where the SU-8 photoresist was polymerized after the UV exposure (transparent features of the photomasks in Figure A2.4 (b)). Figure A2.7 (a) shows the height of the pillar of the V-shaped patter of the "SJ_mask 4" master and Figure A2.7 (b) the depth of a channel of the "SJ_1 µL" master. The respective values are approximately 98 µm for the height of the pillar and 48 µm for the depth of the channel. The SU-8 photoresist was spin coated on the silicon wafers in order to acquire a nominal thickness of 100 µm for the "SJ_mask 4" master and 50 µm for the "SJ_1 µL" master. The measured values indicate a satisfactory deposition during photolithography deviating only by 2 % and 4 % from the theoretical values, respectively.

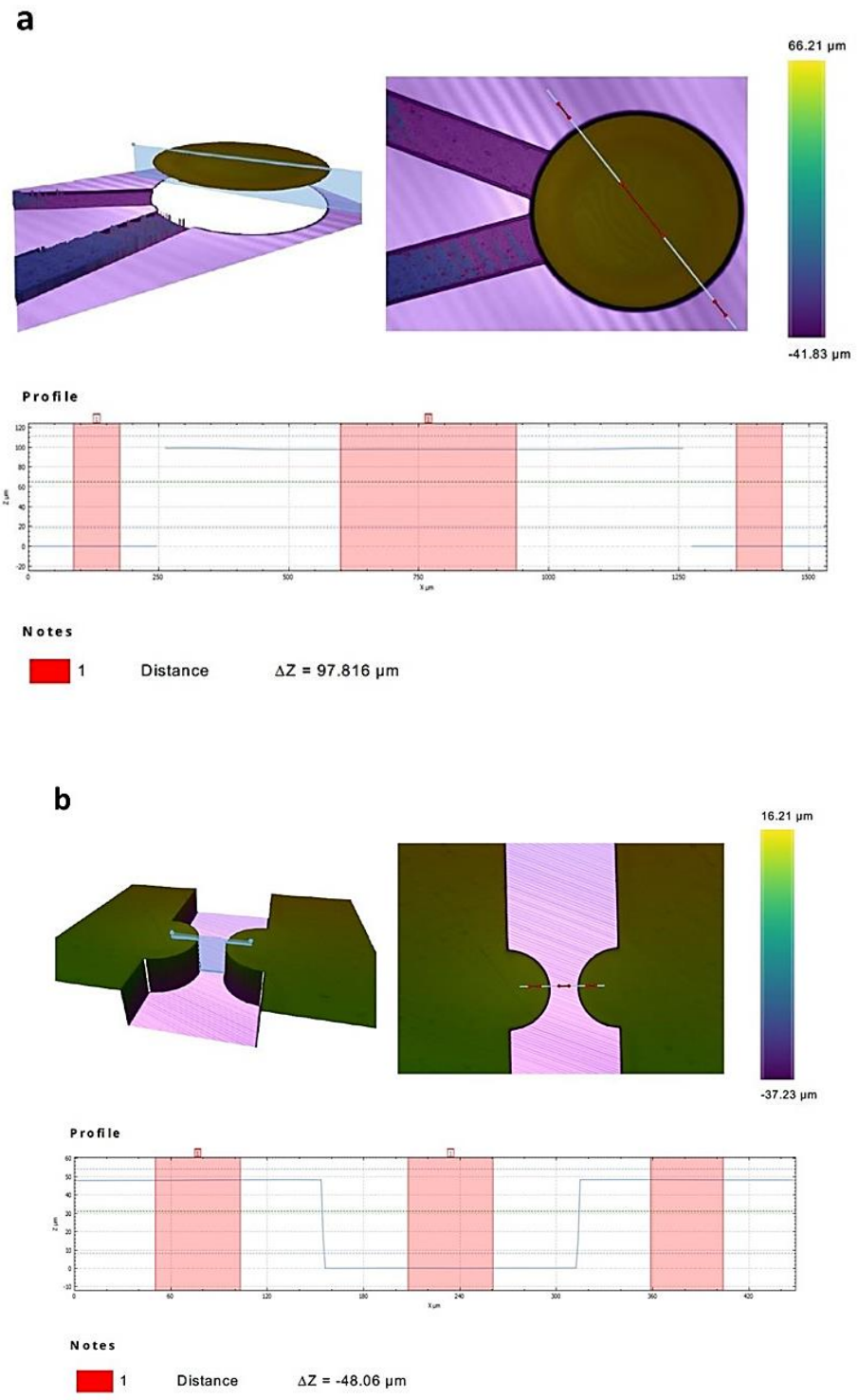

Figure A2.7: Profilometer measurements of (a) the pillar of the V-shaped pattern of the "SJ_mask 4" master and (b) the channel of the "SJ_1 µL" master.

2.3 Fabrication of PEGDA chips

2.3.1 1st method: Fabrication of PDMS molds

The protocol is shown schematically in a transverse view in Figure A2.8 and Figure A2.9. First, a PDMS stamp was made, as illustrated in Figure A2.8 (a) (from top to bottom). For this purpose, a mixture of 10:1 of silicone base: curing agent was prepared. A thick layer of the PDMS mixture was purred on the patterned master and crosslinked at 338 K for 1 h. Then, the PDMS block was peeled off the SU-8 master and the surface of the patterned PDMS stamp was treated with HMDS vapor at 368 K for 10 min. The PDMS stamp contains the reverse patterns of the SU-8 master.

Once the PDMS stamp was ready, a PDMS anti-stamp was prepared, as shown in Figure A2.8 (b) (from top to bottom). First, a thick layer of a 10:1 PDMS mixture was purred on a flat Petri plate. The polymer was heated at 338 K for 15 min. This time period was sufficient for the PDMS block to be partially crosslinked and not entirely rigid. Then, the PDMS stamp was placed above the PDMS block and “sank” within the PDMS block which remained partially liquid. The assembly was heated for 1 h at 338 K and afterwards, the PDMS stamp was peeled off. Finally, the PDMS anti-stamp, which contained the same pattern as the original SU-8 master, was ready. A similar procedure was used to prepare a flat PDMS stamp. A thick layer of 10:1 PDMS mixture was purred on a flat silicon wafer previously treated with HMDS at 368 K for 10 min. The assembly was heated at 338 K for approximately 1 hour. Finally, the flat PDMS stamp was peeled off the silicon wafer. Both the PDMS anti-stamp and the PDMS flat stamp were treated with HMDS at 368 K for 10 min. After this final step, they could be used for the fabrication of PEGDA chips.

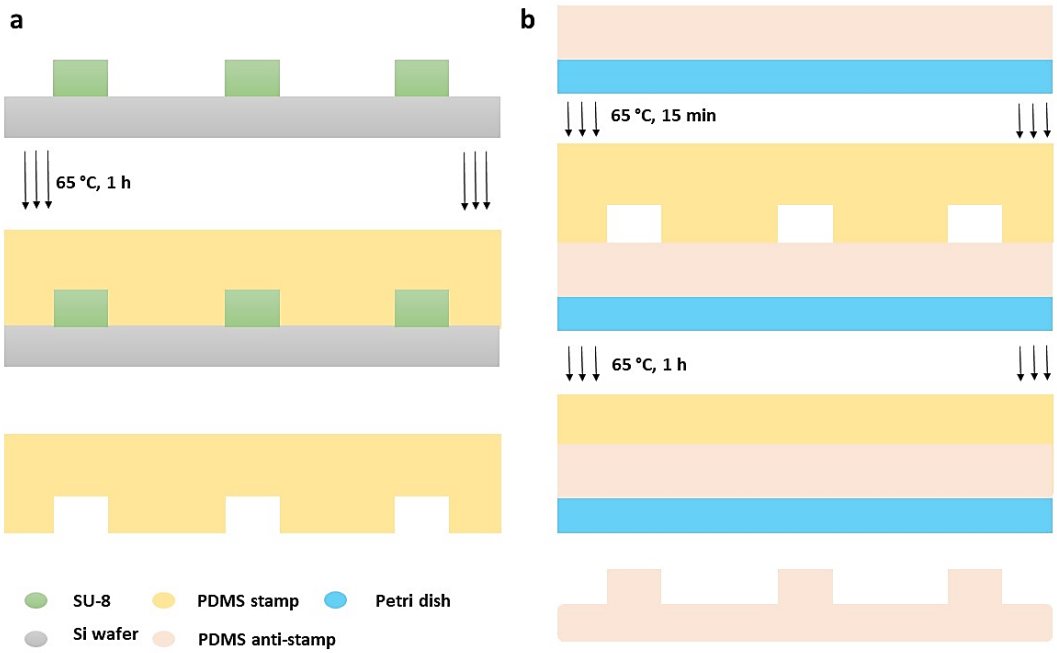

Figure A2.8: Fabrication of (a) the PDMS stamp containing the reverse patterns of the SU-8 master and (b) the PDMS anti-stamp featuring the original patterns of the SU-8 master by replica molding.

Figure A2.9 illustrates schematically the procedure of the PEGDA chips fabrication (top to bottom). The PDMS anti-stamp was placed on a microscope glass slide and the flat PDMS stamp was placed above the anti-stamp. The empty space between the two PDMS stamps was filled by capillarity with the PEGDA 250 solution. The assembly was exposed to UV light for 6 – 8 s and the thin PEGDA layer was crosslinked but it also had some uncured superficial layers because of the oxygen permeability of the PDMS stamps. Then, the PEGDA sticker was pressed gently on a silanized glass slide. The glass slide was previously treated by vapor deposition of an acrylate-based silane (3-(trimethoxysilyl)propyl acrylate, Sigma-Aldrich) in a closed environment at 338 K for 24 h. The sticker was exposed again to UV light for 20 s and it was, finally, covalently bonded on the glass slide.

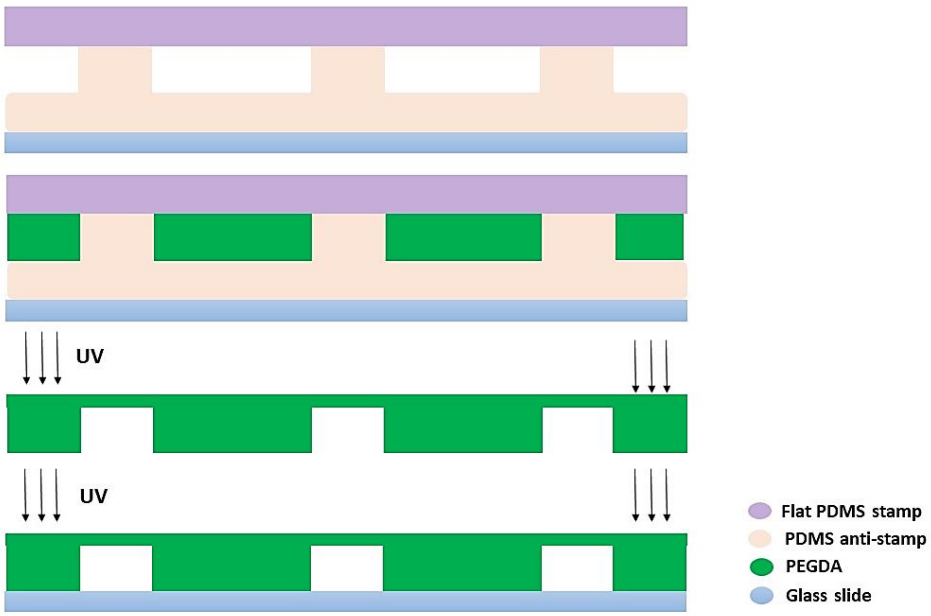

Figure A2.9: Schematic representation of the first method for fabricating PEGDA chips. From top to bottom: the PDMS stamp and anti-stamp are supported on a glass slide. The PEDGA 250 solution fills in the space between the two PDMS stamps by capillarity and UV light (8 s) is used to partially polymerize the hydrogel solution. The partially crosslinked PEGDA layer is pressed on a silanized glass slide and the polymerization is completed by a second UV exposure (20 s).

2.3.2 Fabrication of chips with the "SJ_1 µL" design

The "SJ_1 µL" master (Figure A2.5) was developed to address and improve the issues raised from the droplet tests performed with the PEGDA chips fabricated from the "SJ_mask 4" master (Chapter 2). The chips were fabricated with the NOA 81 resin on COC substrate following the protocol described in Section 2.2.1 and the modifications on the exposure time provided in Section 2.2.2. The chip is shown in Figure A2.10 where fluidic connectors are glued on the inlet and outlet ports of the channel designed for the injection of the precipitant solution. The chip is supported on a microscope glass slide in order to be placed on the maskless UV projection setup, as the COC foil is quite flexible. The *in situ* photo-patterning of hydrogel membrane failed as the channels were blocked possibly by leaks of the NOA 81 resin within the channels and the injection of the hydrogel solution was not feasible. However, PEGDA hydrogel membrane microwindows (HMM) have been fabricated *in situ* by microscope projection photolithography in NOA 81 stickers by Paustian *et al.*, (https://journals.aps.org/prx/abstract/10.1103/PhysRevX.3.041010) suggesting that the failure of our tests is not owned to the feasibility of the procedure but mainly attributed to the chip's fabrication protocol and the blockage of the channels.

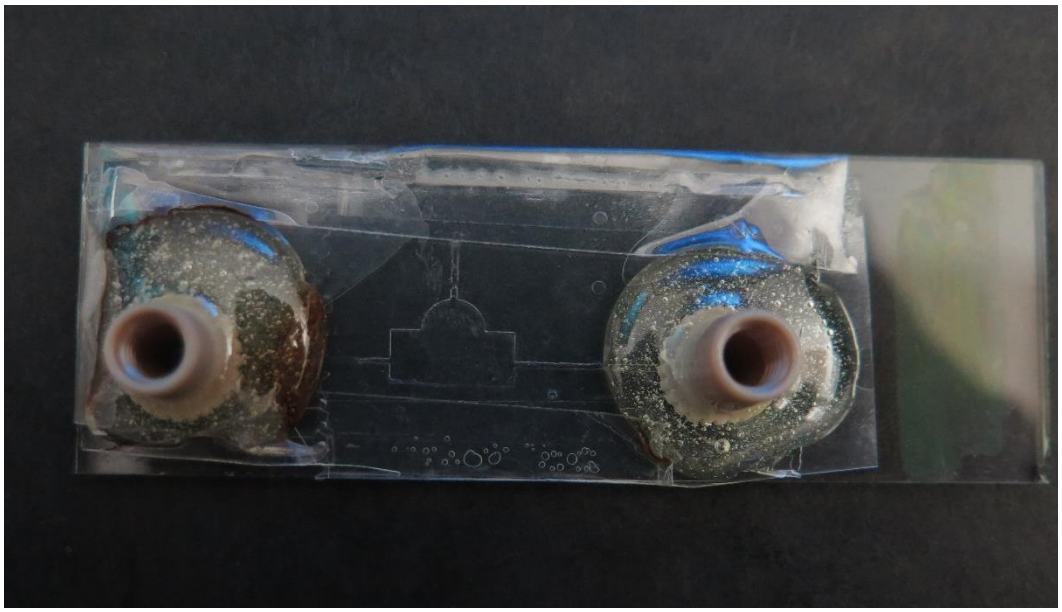

Figure A2.10: NOA 81 chip on a 50 µm thick COC substrate fabricated from the "SJ_1 µL" design for *in situ* photo-patterning of hydrogel membranes.

2.4 Material characterization for *in situ* X-ray diffraction studies

2.4.1 Impact of the sample-detector distance on the background noise

Two parameters considered during the measurements for the material characterization were the distance between the sample and beamline detector and the exposure time. Several tests were performed to examine the impact of the detector to sample distance and the exposure time on the intensity of the background noise and two examples are shown in Figure A2.11 and Figure A2.12 for a 50 µm thick COC foil and a polymerized PEGDA 250 layer, respectively. The detector to sample distance values tested were 200, 300 or 400 mm and the exposure time was 10, 20 or 50 s. The samples were perpendicular to the X-ray beam and the intensity values correspond to the values recorded by the detector subtracting the measurements without any sample in He atmosphere. The characteristic diffusing peaks of COC (Figure A2.11) and PEGDA 250 (Figure A2.12) can be distinguished in a resolution range from 4 – 6 Å, independently of the experimental parameters. From the respective scattering images (Figure 2.4.2, Chapter 2), it can be seen that PEGDA 250 has a wide diffusive ring, while the COC foil has three, well-defined rings in the same resolution range (4 – 6 Å) implying that its internal structure is less amorphous. In the intensity versus resolution plot, these three rings correspond to the three peaks included in the wider peak within 4 – 6 Å resolution (Figure A2.11). By inspecting Figure A2.11 and Figure A2.12, it is clear that highest intensity value is reached when the sample is set 200 mm from the detector and exposed for 20 s. These (200 mm, 20 s) are the values used for the experiments. A 200 mm distance allows for recording diffraction patterns to a resolution up to 1.5 Å. Hence, these values were chosen in compliance with the diffraction experiments on HEWL crystals that were performed in the same beamline (BM30A-FIP, ESRF) discussed in Chapter 4.

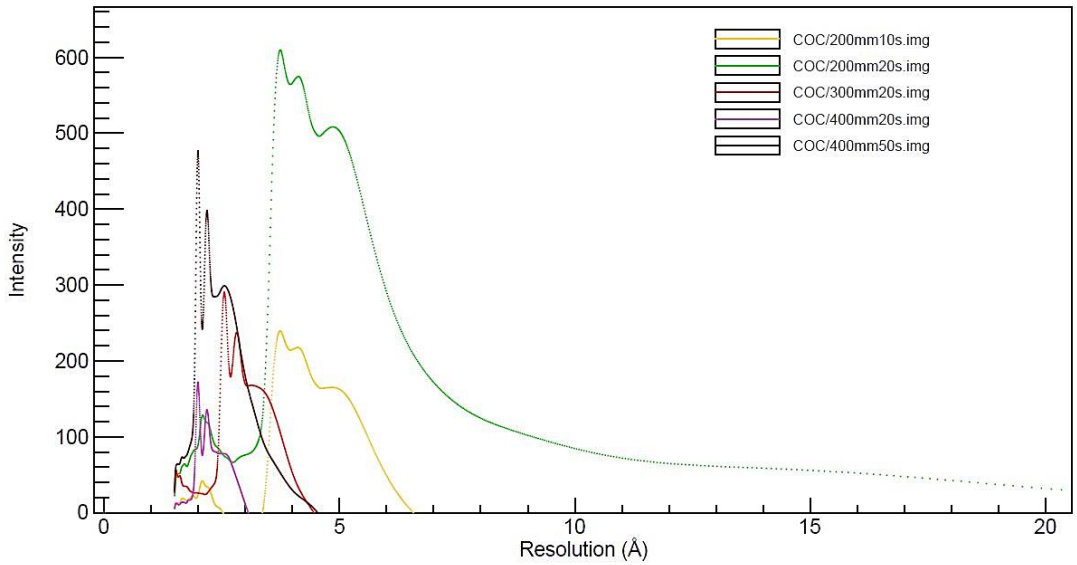

Figure A2.11: Background scattering intensity of the COC foil as a function of resolution (Å) for various values of exposure time and sample-to-detector distance.

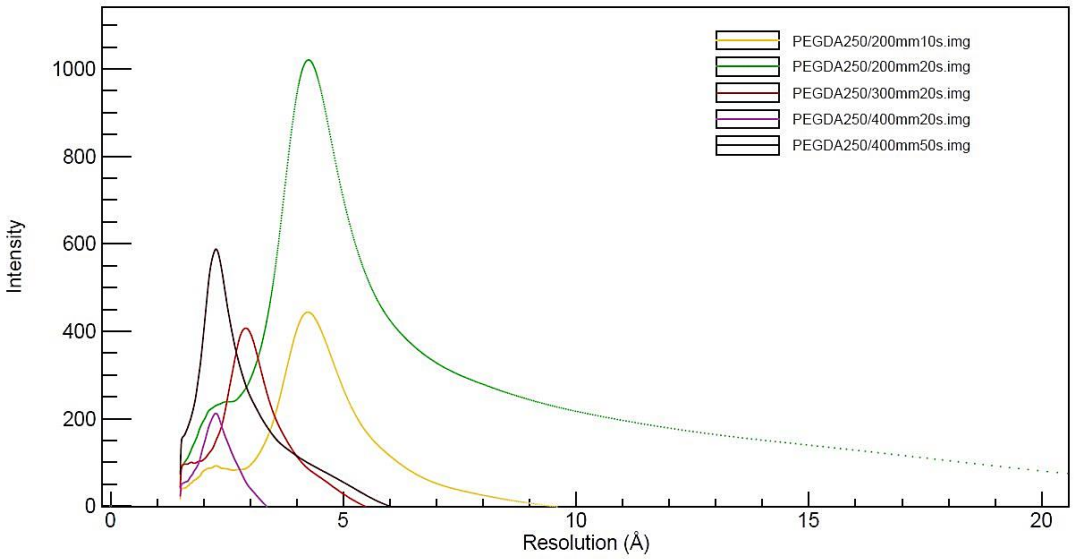

Figure A2.12: Background scattering intensity of the UV polymerized PEGDA 250 layer as a function of resolution (Å) for various values of exposure time and sample-to-detector distance.

2.4.2 Impact of the exposure time on the background noise

In order to evaluate the impact of a long exposure on the background noise, a supplementary study was performed at BM30A-FIP. Scattering data were collected for each of the materials comprising the chip's protein reservoir and their assembly, i.e. the microchip, for an angular range of - 2° to + 3°. An image was recorded every 0.1° and the exposure time for each step was 20 s. Therefore, the first image was recorded after 20 s and the last one after 1000 s. The sample-to-detector distance was 200 mm. Figure A2.13 illustrates the intensity plots for the Kapton tape, the 175 µm thick PMMA sheet, the RC dialysis membrane and the microchip calculated from the scattering data collected at the onset (20 s exposure time) and the end of the experiment (1000 s exposure time). The plots show a similar tendency for all the materials: the intensity of the material's characteristic peak is lower after the long exposure to the X-ray radiation, i.e. after 1000 s. This observation could be linked to radiation damage invoked on the materials' structure after a long exposure time. However, the two images recorded at 20 and 1000 s for each material, were also recorded in different rotation angles. The first image was recorded at - 1.9° and the last one at 3° rotation around the sample axis. An intensity plot for the chip is given in Figure A2.14, where the rotation of the sample is taken into consideration. The plot represents the scattering data collected for the microchip at 20 s where the chip was rotated - 1.9° from the beam axis, at 400 s where the chip was perpendicular to the beam, at 800 s where the chip was rotated + 1.9° and at 1000 s where the chip was rotated + 3° from the beam axis. The tendency related to the exposure time and the rotation angle is clear, indicating that the highest the exposure time and the sample rotation, the lower is the background intensity value. In order to decouple the effect of the rotation angle and the exposure time, the data recorded at the same rotation angle of the sample (-1.9° and + 1.9°) but at different time (20 and 800 s, respectively), show clearly that the tendency on the loss of the peak's intensity by 4 % is mainly related to the duration of the exposure. A close-up illustration of the chip's intensity peaks at various rotation angles and exposure time has been added in Figure A2.14 to facilitate the visualization of the plots.

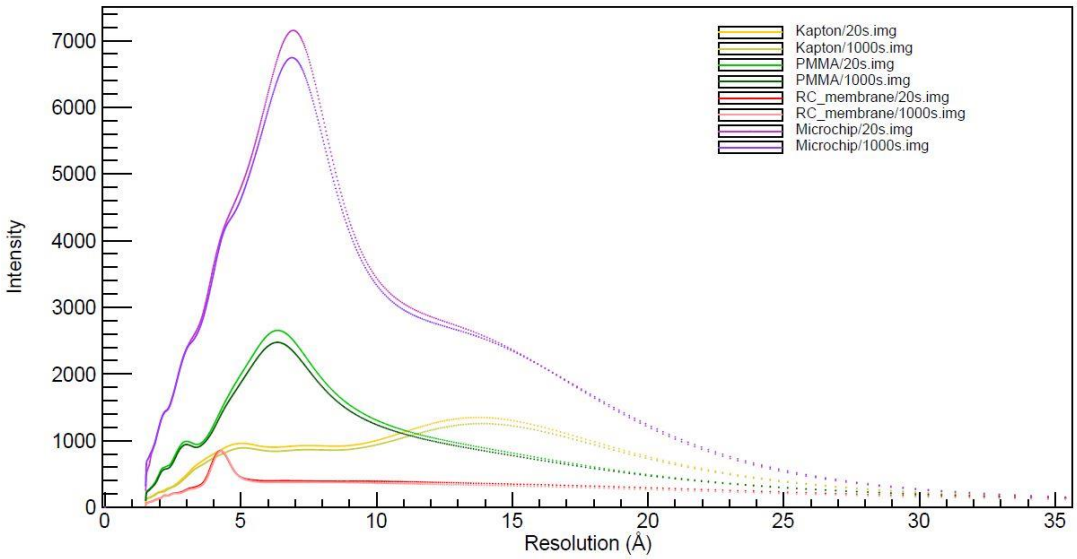

Figure A2.13: Background scattering intensity plots of various materials (Kapton, PMMA, RC dialysis membrane, microchip) as a function of resolution (Å) for short (20 s) and long (1000 s) exposure time.

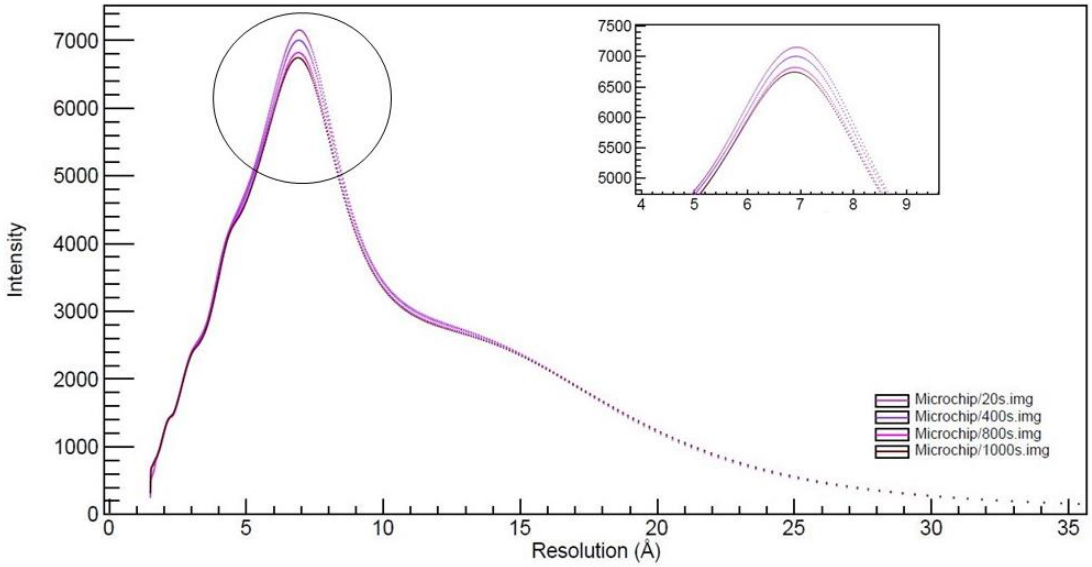

Figure A2.14: Background scattering intensity plots of the dialysis microchip as a function of resolution (Å) for various values of exposure time.

Appendix for Chapter 3

3.1 Data acquisition with the reversible controller

The TC-XX-PR-59 reversible controller can be manipulated by user-friendly PC software, the LT-Interface, developed by Laird Technologies (Figure A3.1). The interface allows the user to input parameters and visualize output parameters in real time. Once the communication port between the controller and the computer is chosen and the controller is set to one of the available regulation modes, online information from the controller is displayed on the LT interface. The controller can operate as a PID regulator or through on/off, power or algorithm mode. There are six tabs on the interface allowing the user to modify the parameters, as for example, to choose the temperature sensor type that is connected to the regulator and set a temperature point, to visualize the operation parameters in real time through a scaled graph, to set alarm settings for the voltage and the current of the controller and its connected components (fan, temperature sensor) or to set functional parameters for the controller, the fan and the sensor.

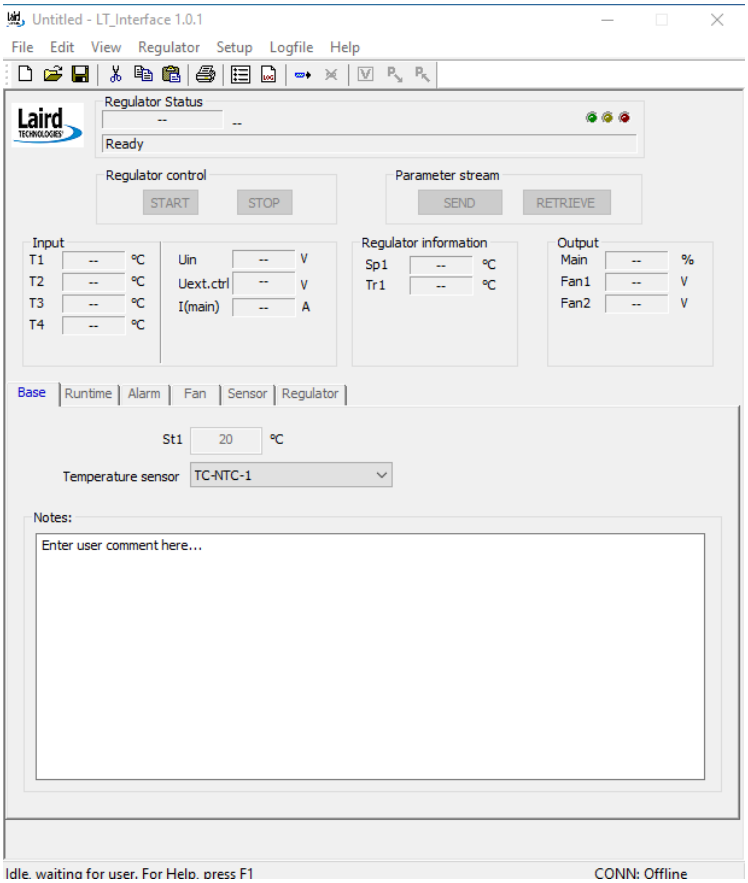

Figure A3.1: The LT-Interface (Laird Technologies) for manipulating in real time the input and output parameters of the TC-XX-PR-59 reversible controller.

3.2 LabVIEW for thermal regulation

The block diagram of the LabVIEW program developed for thermal regulation of the dialysis chip (Figure A3.2) includes an event structure for reading the J thermocouple through the MODBUS protocol and putting the values in the waveform chart and for the regulation of the controller. The values of the PID regulation algorithm of the LabVIEW program are set to - 0.05 for the proportional parameter (P), to 0.07 for the integral parameter (I) and to 0 for the derivative term. However, these parameters can be optimized if the response of the regulation deteriorates.

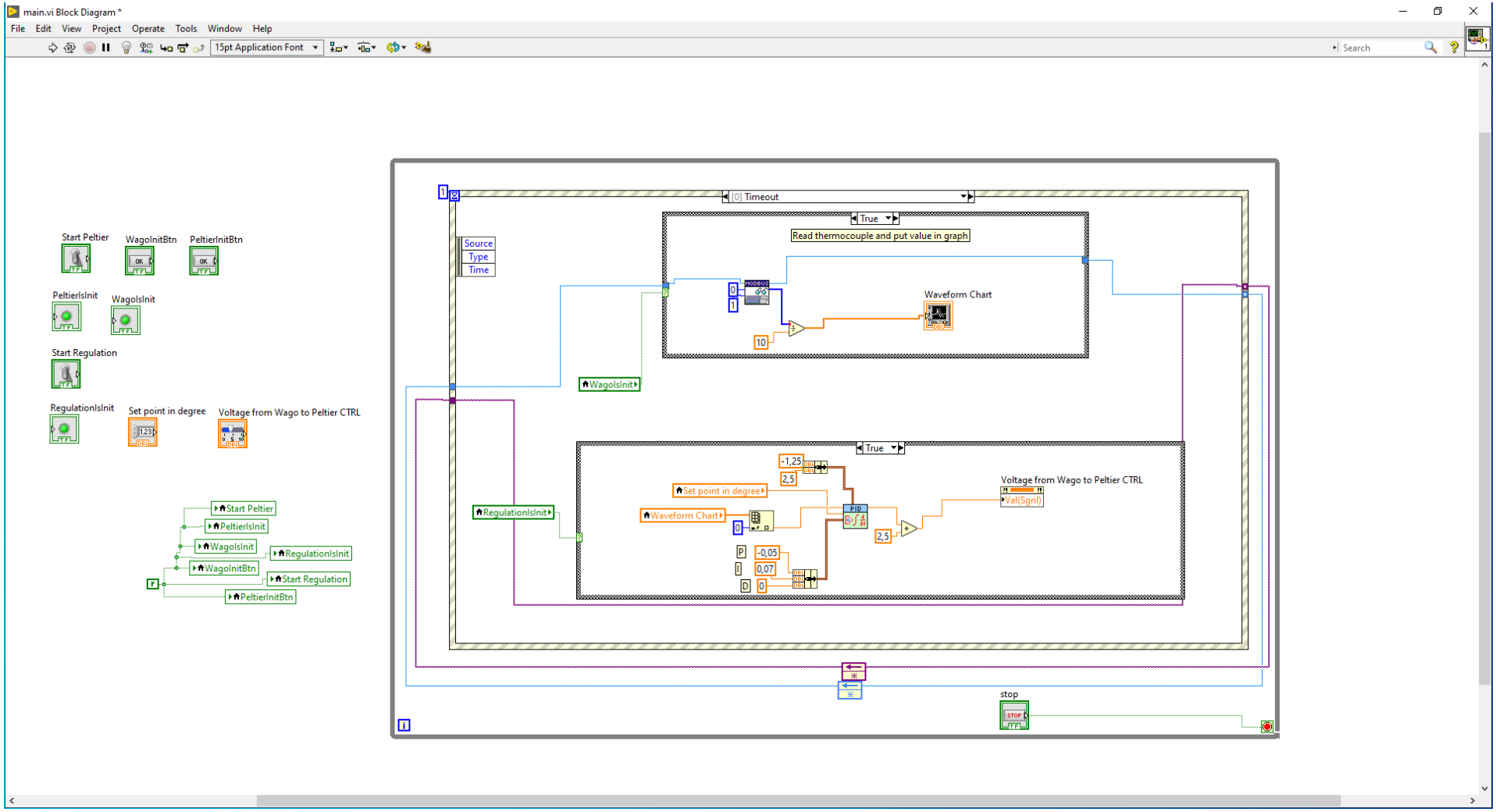

Figure A3.2: The block diagram of the LabVIEW main VI developed for thermal regulation.

Appendix for Chapter 4

4.1 Hen Egg White Lysozyme

4.1.1 Crystallization experiments

HEWL crystals grown with the vapor diffusion hanging drop or sitting drop method at 293 K are shown in Figure A4.1. The crystallization conditions are provided in Table A4.1. The effect of protein concentration, the precipitant concentration and the crystallization method itself on the crystal size and shape or the uniformity of the crystal population can be seen by comparing the various conditions. For example, by increasing the precipitant concentration from 0.8 M NaCl (Figure A4.1 (a)) to 1.2 M NaCl (Figure A4.1 (b)), a significant impact can be seen on the number of crystals grown with the hanging drop.

Table A4.1: Crystallization conditions for the HEWL crystals shown in Figure A4.1.

	Crystallization method	**Crystallization conditions**
Figure A4.1 (a)	Hanging drop	HEWL 30 mg mL^{-1} 0.8 M NaCl 100 mM CH_3COONa pH 4.0
Figure A4.1 (b)	Hanging drop	HEWL 30 mg mL^{-1} 1.2 M NaCl 100 mM CH_3COONa pH 4.0
Figure A4.1 (c)	Hanging drop	HEWL 60 mg mL^{-1} 1 M NaCl 100 mM CH_3COONa pH 4.0
Figure A4.1 (d)	Sitting drop	HEWL 60 mg mL^{-1} 1 M NaCl 100 mM CH_3COONa pH 4.0
Figure A4.1 (e)	Sitting drop	HEWL 30 mg mL^{-1} 0.8 M NaCl 100 mM CH_3COONa pH 4.0
Figure A4.1 (f)	Sitting drop	HEWL 30 mg mL^{-1} 1.2 M NaCl 100 mM CH_3COONa pH 4.0

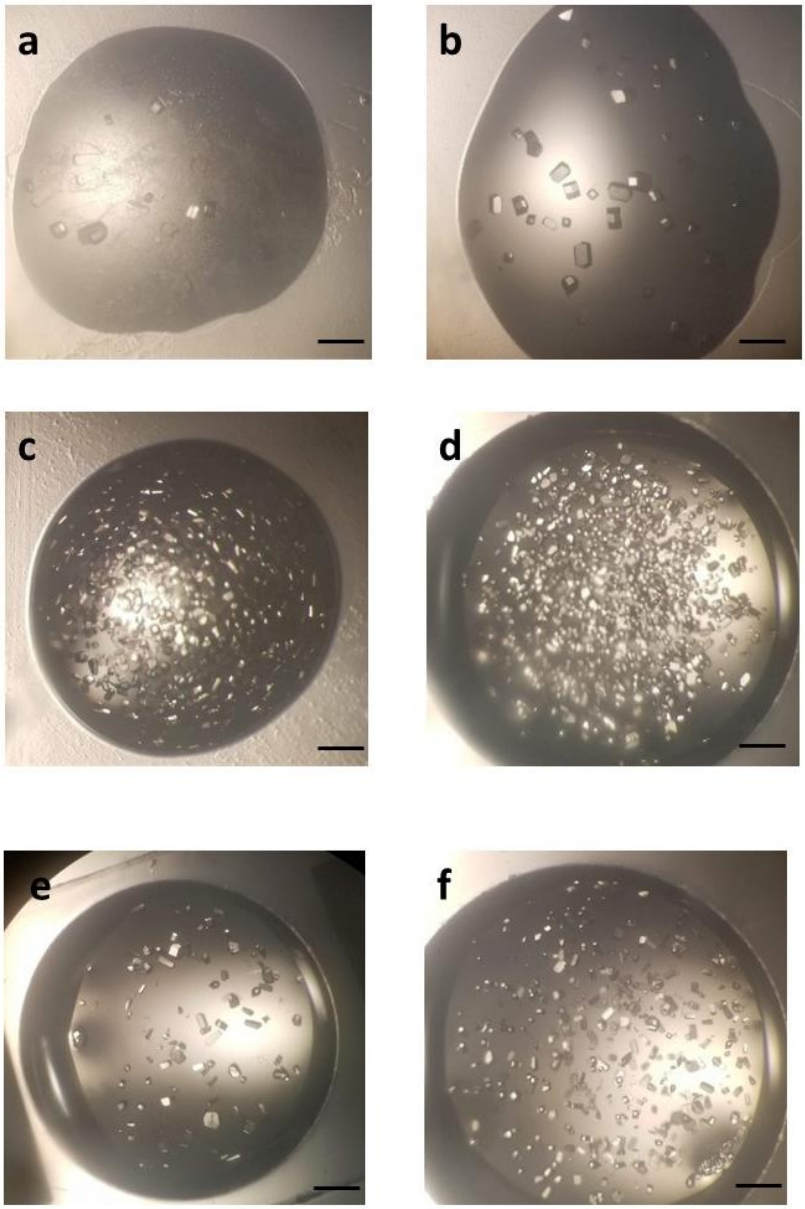

Figure A4.1: HEWL crystals grown with the hanging drop or the sitting drop method at 293 K. The crystallization conditions are provided in Table A4.1. The scale bar represents 100 μm.

Figure A4.2 is the original version of Figure 4.1.2 provided in Chapter 4. The images were captured with the inverted UEye color camera of the MicroCrys platform (Chapter 3). As explained in Chapter 4, applying white balance corrections on the part of the LabVIEW code controlling the camera settings can regulate the green hue in the images. However, the current version of the code uses the default settings for visualization. In order to facilitate the observation of the crystals grown on the chips in Chapter 4, all the figures captured with MicroCrys are provided in black and white. The crystallization conditions for the experiments

shown in Figure A4.2 are provided in Table A4.2. The HEWL crystals grew on chip at 293 K. The volume of the protein reservoir was 0.3 µL and the MWCO of the RC membrane was 6 – 8 kDa.

Table A4.2: Crystallization conditions for the HEWL crystals shown in Figure A4.2.

	Crystallization conditions
Figure A4.2 (a)	HEWL 30 mg mL^{-1} 1 M NaCl 100 mM CH_3COONa pH 4.0
Figure A4.2 (b)	HEWL 60 mg mL^{-1} 1 M NaCl 100 mM CH_3COONa pH 4.0
Figure A4.2 (c)	HEWL 30 mg mL^{-1} 1 M NaCl 100 mM CH_3COONa pH 4.0 20 % v/v PEG 400

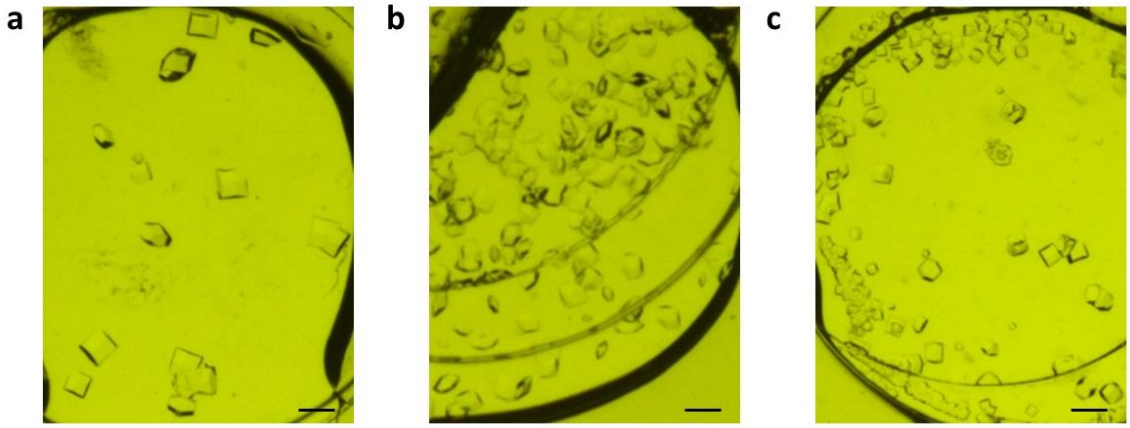

Figure A4.2: HEWL crystals grown on chip via microdialysis at 293 K. The crystallization conditions are provided in Table A4.2. The scale bar represents 100 µm. The images were captured with the inverted UEye color camera of the MicroCrys platform.

4.1.2 Growing large HEWL crystals for preliminary Neutron diffraction experiments

A solution of HEWL in deuterated water (D_2O) was prepared to a final concentration of 30 mg mL^{-1} for growing large crystals on chip with the dialysis method in order to demonstrate the compatibility with *in situ* neutron diffraction experiments. The experiments, originally planned to take place at the second quasi-Laue neutron diffractometer DALI developed at Institut Laue-Langevin (ILL) in Grenoble, France, have not been conducted yet, however, the

idea is to demonstrate that large crystals can be grown within the dialysis chip. Large crystals are usually required for diffraction experiments using neutron sources, as the neutron flux is much lower than the photon flux produced in synchrotron facilities. The smallest crystals used for neutron diffraction were grown to a volume range of approximately 0.1 – 0.2 mm^3 which interprets to growing isometric crystals with a size of approximately 500 µm in all three dimensions[3]. Figure A4.3 shows HEWL crystals grown on chip in two different precipitant concentrations. For these experiments, deuterated stock solutions of NaCl and CH_3COONa pD 4.5 were prepared. The relationship between pH and pD is: pD ≈ pH + 0.3 according to Lumry *et al*. (https://doi.org/10.1021/ja01153a090). The crystals shown in Figure A4.3 (a) were grown in the presence of 0.5 M NaCl and 100 mM CH_3COONa pD 4.5 and the crystals shown in Figure A4.3 (b) were grown in 0.4 M NaCl and 100 mM CH_3COONa pD 4.5. In the latter case, reducing the precipitant concentration resulted in fewer but larger crystals with a final size of approximately 300 µm in the largest dimension. Both photos were captured with MicroCrys 62 h from the beginning of the experiments. The experiments were conducted in a continuous circulation mode of the crystallization solution under 50 mbar constant inlet pressure in the fluidic channel and the volume of the protein reservoir was 0.3 µL. The scale bar represents 100 µm.

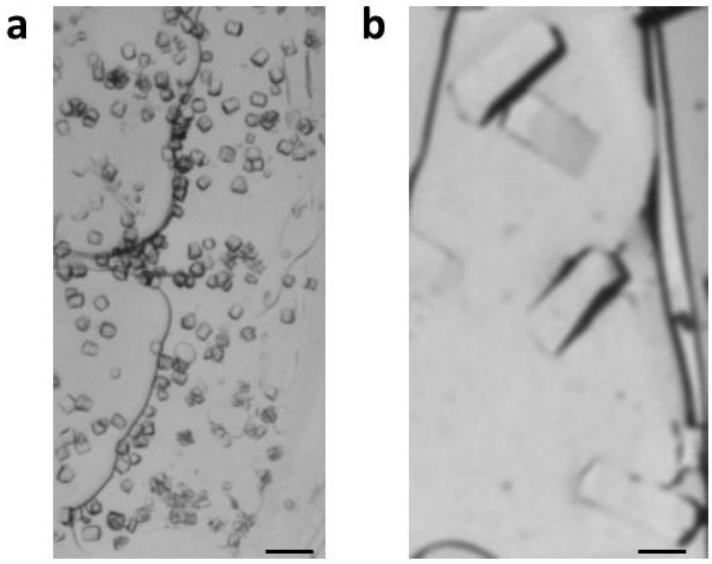

Figure A4.3: HEWL (30 mg mL^{-1}) crystals grown on chip via microdialysis in the presence of deuterated 0.5 M (a) and 0.4 M (b) NaCl and 100 mM CH_3COONa pD 4.5 at 293 K. The scale bar represents 100 µm.

4.2 Thaumatin from *Thaumatococcus danielli*

Thaumatin crystals grown with the vapor diffusion hanging drop method at 293 K are shown in Figure A4.4. The crystallization conditions are provided in Table A4.3. Comparing the two different conditions can illustrate the effect of precipitant concentration on the crystal size and the crystal population.

Table A4.3: Crystallization conditions for the Thaumatin crystals shown in Figure A4.4.

	Crystallization method	**Crystallization conditions**
Figure A4.4 (a)	Hanging drop	Thaumatin 15 mg mL^{-1} 0.6 M sodium potassium tartrate 50 mM ADA pH 6.5
Figure A4.4 (b)	Hanging drop	Thaumatin 15 mg mL^{-1} 0.8 M sodium potassium tartrate 50 mM ADA pH 6.5

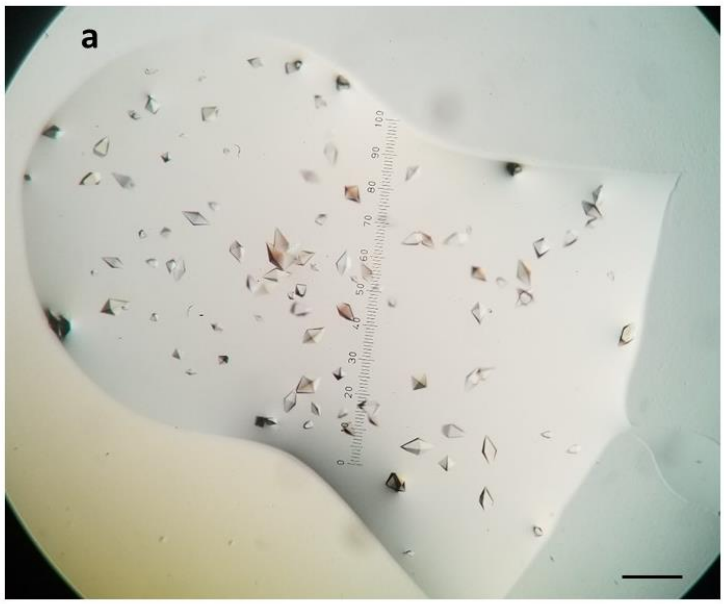

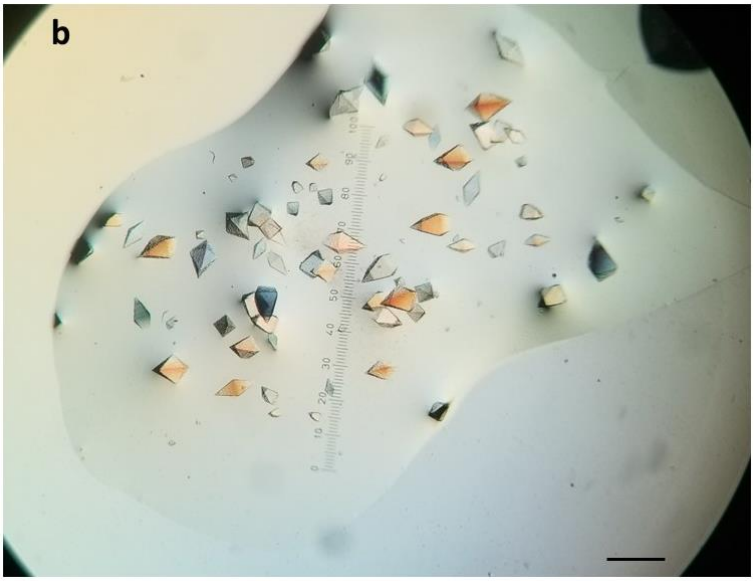

Figure A4.4: Thaumatin crystals grown with the hanging drop method at 293 K. The crystallization conditions are provided in Table A4.3. The scale bar represents 100 µm.

Thaumatin crystals grew on chip with the microdialysis method at 293 K in various conditions. Figure A4.5 shows Thaumatin crystals on chip grown in the same concentration of the precipitant but in different protein concentrations. The volume of the protein reservoir was 0.3 µL and the MWCO of the RC membrane was 6 – 8 kDa. The experimental conditions are given in Table A4.4.

Table A4.4: Crystallization conditions for the Thaumatin crystals shown in Figure A4.5.

	Crystallization conditions
Figure A4.5 (a)	Thaumatin 19 mg mL^{-1} 1 M sodium potassium tartrate 50 mM ADA pH 6.5
Figure A4.5 (b)	Thaumatin 41 mg mL^{-1} 1 M sodium potassium tartrate 50 mM ADA pH 6.5

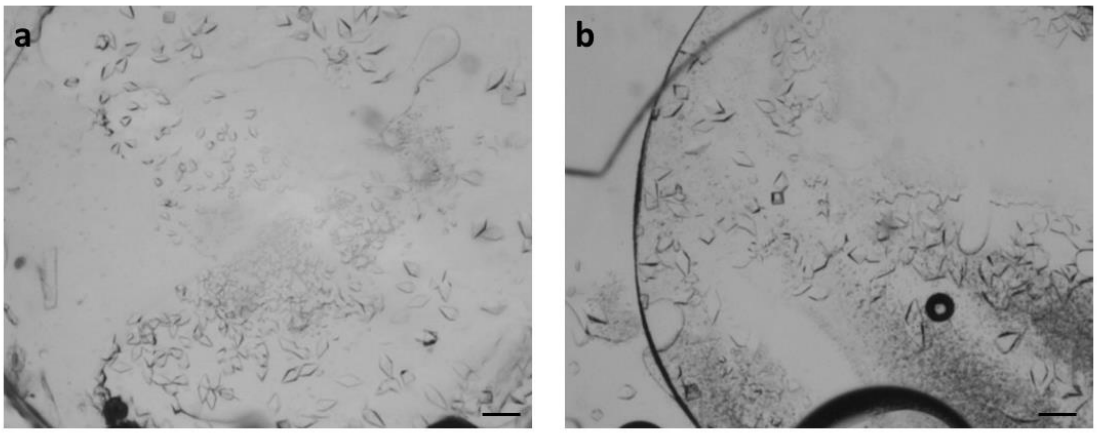

Figure A4.5: Thaumatin crystals grown on chip via microdialysis at 293 K. The crystallization conditions are provided in Table A4.4. The scale bar represents 100 µm.

4.3 AcrB from *Escherichia coli*

AcrB crystals grown with the hanging drop vapor diffusion method are shown in Figure A4.6. AcrB was solubilized in 0.02 % v/v DDM and crystallized at 293 K. The effect of the protein concentration on the crystal size and population can be seen by comparing Figure A4.6 (a) to Figure A4.6 (b), while the effect of the additive (1 mM Rifampicin) can be seen by comparing Figure A4.6 (a) to Figure A4.6 (c).

Table A4.5: Crystallization conditions for the AcrB crystals shown in Figure A4.6.

	Crystallization conditions
Figure A4.6 (a)	AcrB 12 mg mL^{-1} 12 % PEG 4000 5 % glycerol 50 mM ADA pH 6.5 200 mM $(NH_4)_2SO_4$
Figure A4.6 (b)	AcrB 6 mg mL^{-1} 12 % PEG 4000 5 % glycerol 50 mM ADA pH 6.5 200 mM $(NH_4)_2SO_4$
Figure A4.6 (c)	AcrB 12 mg mL^{-1} and 1 mm Rifampicin 12 % PEG 4000 5 % glycerol 50 mM ADA pH 6.5 200 mM $(NH_4)_2SO_4$

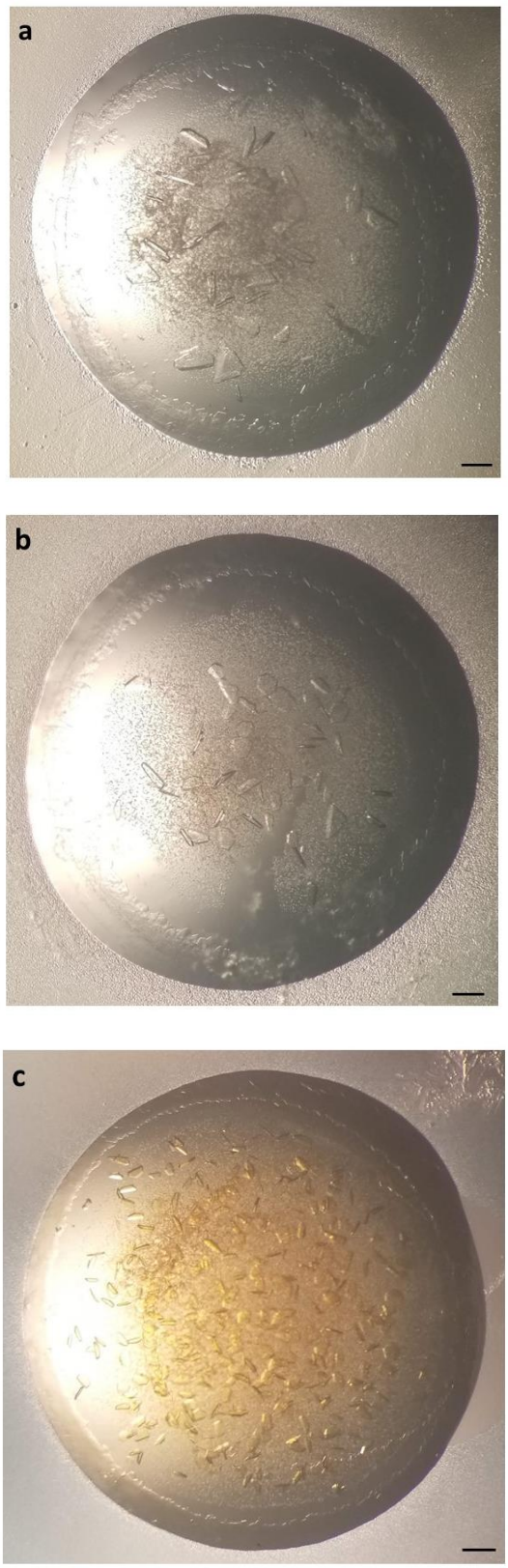

Figure A4.6: AcrB crystals grown with the hanging drop method at 293 K. The crystallization conditions are provided in Table A4.5. The scale bar represents 100 µm.

4.4 *In situ* X-ray diffraction experiments

As explained in Chapter 4, the microchips are mounted in protein crystallography beamlines compatible for in plate X-ray diffraction data collection with the aid of a 3D printed support that can carry up 3 chips simultaneously. Figure A4.7 shows the chips as mounted on the BM30A-FIP beamline at ESRF (Figure A4.7 (a)) and on the PROXIMA-2A beamline at synchrotron Soleil (Figure A4.7 (b)).

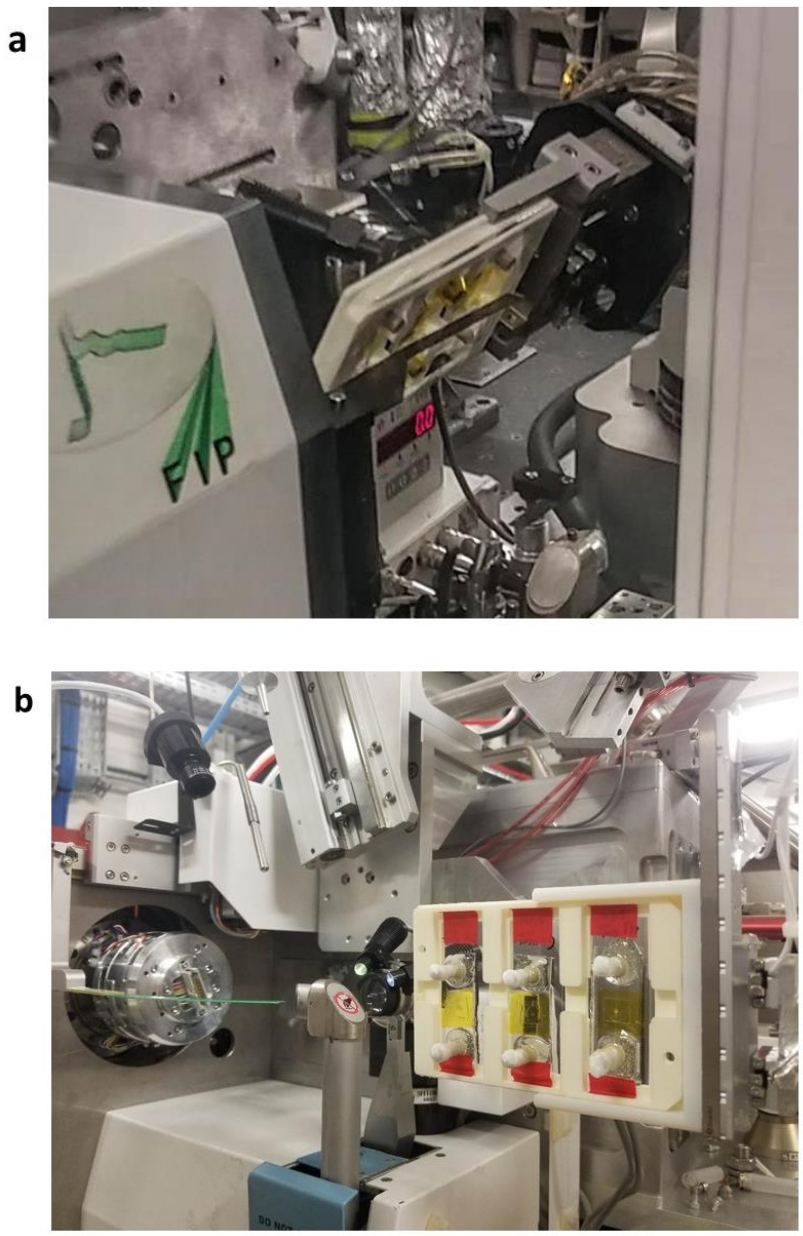

Figure A4.7: The microchips mounted on (a) BM30A-FIP (ESRF) and (b) PROXIMA-2A (Soleil) beamline with the 3D printed support designed for *in situ* X-ray diffraction experiments.

4.5 Purification protocols

4.5.1 AcrB from *Escherichia coli*

The protocol for the production and purification of the multidrug efflux pump AcrB from *Escherichia coli* was optimized by Elham Vahdatahar and Dr. David Cobessi (group GSY, IBS, Grenoble). AcrB was overexpressed in *E. coli* and the cell pellets were kept at -20 °C. The protocols for cell pellets production and purification are given below.

AcrB production in *E. coli*

1. Preparation of solutions and pre-culture of *E. coli* cells

- Prepare 4 L of LB Broth with a concentration of 20 g L^{-1} and autoclave the solution
- Prepare 3 sterilized tubes of 13 mL each containing:
    - 5 mL of LB Broth
    - 5 µL Kanamycin (50 mg mL^{-1} in distilled water)
    - 1 single colony of *E. coli* bacteria containing the gene that expresses AcrB
- Incubate for 6 h (310 K, 200 rpm)
- Transfer the pre-culture to 6 sterilized Erlenmeyer flasks of 250 mL. Each flask contains:
    - 50 mL LB Broth (20 g L^{-1})
    - 50 µL Kanamycin (50 mg mL^{-1})
    - 50 µL of the pre-culture
- Incubate overnight (310 K, 180 rpm)

2. Increase the volume of the cell cultures and induce the expression of AcrB

- Check the optical density (OD) of the pre-culture solutions by absorption at visible light at 600 nm. The OD value should be approximately 0.3 – 0.4. If the absorbance value is not within the acceptable limits, the pre-culture solutions should be left more time at the incubator.
- Use 8 sterilized Erlenmeyer flasks of 3 L for the culture solutions. Each flask contains:
    - 1 L LB Broth (20 g L^{-1})
    - 1 mL Kanamycin (50 mg mL^{-1})
    - 16 mL pre-culture solution
- Incubate approximately for 3 h (310 K, 180 rpm) until the value of OD_{600} is 0.6 – 0.8
- Once the OD_{600} value is within the limits, transfer the 8 flasks at 303 K and incubate for 30 min (180 rpm)
- Add 1 mL of isopropyl β-d-1-thiogalactopyranoside (IPTG) 0.5 mM in each one of the culture solutions. IPTG is used to overexpress the genes encoding AcrB within the *E. coli* cells
- Incubate for 4 h (303 K, 180 rpm)
- Preparation of the *E. coli* cell pellets
    - Centrifuge all the culture solutions (30 min, 5500 rpm, 293 K) and keep the cell pellets

- Solubilize the pellets with 150 mL of buffer A (20 mM Tris-HCl pH 8.0, 500 mM NaCl)
- Centrifuge again (30 min, 4000 g, 277 K) and keep the cell pellets
- Store the cell pellets in 50 mL Falcon tubes at 253 K or at 193 K for long-term storage

AcrB purification

Table A4.6 contains the composition of all buffer solutions used during purification. The chemicals were purchased from Sigma-Aldrich or Roth. All the stock solutions and the buffer solutions were filtered through 0.22 μm Millipore filters. The components of the solubilization buffer must be added in the exact order as given in Table A4.6.

Table A4.6: The composition of all the buffers used for AcrB purification.

Buffer A	20 mM Tris-HCl pH 8.0 500 mM NaCl
Buffer B	20 mM Tris-HCl pH 8.0 500 mM NaCl 2 mM $MgCl_2$
Solubilization buffer	10 % v/v glycerol 50 mM Tris-HCl pH 7.0 10 mM Imidazole pH 7.0 2 % v/v DDM ½ tablet of protease inhibitor (EDTA free)
Buffer C	20 mM Tris-HCl pH 7.0 0.2 % v/v DDM 10 % v/v glycerol 10 mM Imidazole pH 7.0
Buffer D	20 mM Tris-HCl pH 7.0 0.02 % v/v DDM 10 % v/v glycerol 50 mM Imidazole pH 7.0
Buffer E	20 mM Tris-HCl pH 7.0 0.02 % v/v DDM 10 % v/v glycerol 200 mM Imidazole pH 7.0
Buffer F	10 mM Hepes pH 7.0 0.02 % v/v DDM

1. Thaw the cell pellets and resuspend each with 25 mL of buffer B
2. Use a Microfluidizer (15000 psi) for the cell lysis
3. Centrifuge (10000 g, 15 min, 293 K) and keep the supernatant
4. Ultracentrifuge (Ti70 rotor, 46000 rpm, 1 h, 277 K) and keep the pellets
5. Resuspend the pellets using 6 mL of buffer A

6. Add the resuspended pellets in 40 mL of the solubilization buffer
7. Incubate the membrane suspension at 277 K for 1 h while slowly rotating the sample to solubilize the membranes
8. Ultracentrifuge (Ti70 rotor, 40000 rpm, 45 min, 277 K) and keep the supernatant
9. Prepare Ni-NTA (Nickel-nitrilotriacetic acid) column
    - Add 6 mL of Ni-NTA solution in a falcon tube. The solution contains 50 % resin and 50 % ethanol (EtOH). Once centrifuged, only 3 mL of resin are left.
    - Add 3 mL of distilled water
    - Wash the resin by pipetting up and down
    - Centrifuge for 1 min at the highest speed to eliminate the solvent (EtOH)
    - Wash the column with 15 mL of buffer C
10. Mix the supernatant with the Ni-NTA resin and incubate overnight at 277 K on a rotating wheel
11. Use of Ni-NTA column for affinity chromatography
    - Pack the column containing the resin and the supernatant and collect the flow through
    - Wash the column with 15 mL of buffer C (washing buffer)
    - Wash with 15 mL of buffer D (Buffer D is used to remove other proteins possible present)
    - Elute the protein with buffer E (elution buffer) in 8 fractions of 1.5 mL each. For fractions 2 – 4 incubate the column with 1.5 mL of buffer E for 5 min before elution.
    - Wash the column with distilled water and store in 20 % EtOH
12. Measure the absorbance at 280 nm (A_{280}) of the fractions collected after the Ni-NTA column with Nanodrop spectrophotometer. Use buffer E as blank for the measurements.
13. Run SDS-PAGE gel for the protein fractions of step 11. Also run any other sample during the purification steps (for example the flow through of the Ni-NTA column or the wash of the Ni-NTA column, etc.)
14. Pull together the fractions with the highest concentration and start concentrating the protein by centrifuging at 4000 g and 277 K
    - Use Amicon concentrator with a MWCO 100 kDa
    - Concentrate to approximately 200 µL final volume
15. Exchange buffer E to buffer F
    - Add 5 mL of buffer F and centrifuge (2000 g, 5 min, 277 K)
    - Add 5 mL of buffer F and centrifuge again (2000 g, 5 min, 277 K)
    - Add 3 mL of buffer F and centrifuge again (2000 g, 5 min, 277 K)
    - Measure the A_{280} value
16. Store the concentrated protein at 277 K before using it for crystallization experiments

For the purified AcrB sample used with the crystallization experiments described in Chapter 4 (Section 4.2.1) the final volume of the protein was 1 mL and the concentration 12.892 mg mL^{-1}. The absorbance measurements (A_{280}) of the fractions from the Ni-NTA column are given in Table A4.7 and the SDS-PAGE gel in Figure A4.8. The fractions on the gel are named F1 to F8 corresponding to the 8 fractions from the Ni-NTA column, while the marking bands are illustrated at the left of the image. AcrB can be distinguished close to the

100 kDa band as the molecular weight of the protein is 114 kDa. In the third line of Table A4.7, the concentration of the fractions is given in mg mL^{-1}, after applying the Beer-Lambert law: $A = \varepsilon \cdot l \cdot c$, where A is the absorption value, l (cm) is the path length, c (mg mL^{-1}) is the concentration of the solution and ε is the extinction coefficient. For AcrB, the extinction coefficient is 89855 in units of M^{-1} cm^{-1}, at 280 nm measured in water (https://web.expasy.org/cgi-bin/protparam/protparam1?P31224@noft@ for entry P31224) meaning that for absorption value of 0.791 the concentration of AcrB in aqueous solution is 1 mg mL^{-1}.

Table A4.7: The absorbance measurements (A_{280}) and concentration (mg mL^{-1}) of the AcrB fractions from the Ni-NTA column.

Ni-NTA fraction	1	2	3	4	5	6	7	8
A_{280}	0.220	3.492	3.020	2.569	0.759	0.212	0.140	0.025
C (mg mL^{-1})	0.278	4.414	3.817	3.247	0.959	0.268	0.176	0.031

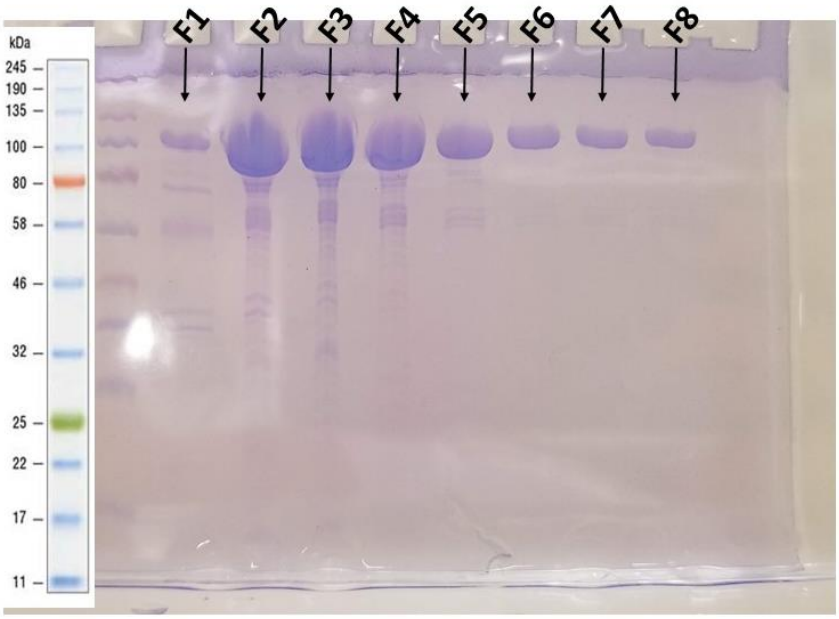

Figure A4.8: The SDS-PAGE gel of the fractions from the Ni-NTA column during the purification of AcrB. The fractions on the gel are named F1 to F8.

4.5.2 ShuA from *Shigella dysenteriae*

The protocol for the production and purification of the TonB-dependent outer membrane transporter ShuA from *Shigella dysenteriae* was optimized and implemented in the laboratory by Elham Vahdatahar and Dr. David Cobessi (group GSY, IBS, Grenoble). ShuA was overexpressed in *E. coli*. The protocols for producing the cell pellets and purifying the protein are given briefly below.

ShuA production in *E. coli*

1. Preparation of solutions and pre-culture of *E. coli* cells
   - Prepare 4 L of LB Broth with a concentration of 20 g L^{-1} and autoclave the solution
   - Use 8 sterilized Erlenmeyer flasks of 250 mL for the pre-culture solutions. Each flask contains:
     - 70 mL LB Broth
     - 35 µL Ampicillin (1 g per 10 mL of distilled water)
     - 1 single colony of *E. coli* bacteria cells containing the gene that expresses ShuA
   - Incubate overnight (180 rpm, 310 K)

2. Culture of *E. coli* cells
   - Check the optical density (OD) of the pre-culture solutions by absorption at visible light at 600 nm. The OD_{600} value should be approximately 0.5 – 0.6. If the absorbance value is not within the acceptable limits, the pre-culture solutions should be left more time at the incubator.
   - Use 8 sterilized Erlenmeyer flasks of 3 L each for the culture solutions. Each flask contains:
     - 1 L LB Broth
     - 25 mL of pre-culture solution
     - 1 mL Ampicillin
   - Incubate for 2 h (180 rpm, 310 K)
   - Measure the OD_{600} value
- Add 1 mL of IPTG 0.5 mM in each one of the culture solutions. IPTG is used to overexpress the genes encoding ShuA within the *E. coli* cells.
- Incubate overnight (303 K, 180 rpm)
- Preparation of the *E. coli* cell pellets
  - Centrifuge all the culture solutions (25 min, 5500 rpm, 293 K) and keep the cell pellets
  - Solubilize the pellets with 200 mL of 50 mM Tris-HCl pH 8.0
  - Centrifuge again (1 h, 3600 rpm, 277 K) and keep the cell pellets
  - Store the cell pellets in 50 mL Falcon tubes at 253 K or at 193 K for long-term storage

ShuA purification

Table A4.8 contains the composition of all buffer solutions used during purification. The chemicals were purchased from Sigma-Aldrich. All the stock solutions and the buffer solutions were filtered through 0.22 µm Millipore filters. The buffers used for chromatography (A2 and B2) should be degassed before being injected in the ion exchange column.

Table A4.8: The composition of the purification, the chromatography and the dialysis buffer used for ShuA purification.

Purification buffers	
A1	50 mM Tris-HCl pH 8.0 250 mM NaCl 10 mM Imidazole pH 8.0
B1	50 mM Tris-HCl pH 8.0 100 mM NaCl 500 mM Imidazole pH 8.0
Chromatography buffers	
A2	50 mM Tris-HCl pH 8.0 1 % v/v octyl-POE
B2	50 mM Tris-HCl pH 8.0 1 M NaCl 1 % v/v octyl-POE
Dialysis buffer	50 mM Tris-HCl pH 8.0 50 mM NaCl 1 % v/v octyl-POE

1. Thaw the cell pellets and solubilize each pellet with 25 mL of buffer A1
2. Use a Microfluidizer (15000 psi) for the cell lysis
3. Centrifuge (10000 g, 10 min, 293 K) and keep the supernatant
4. Ultracentrifuge (Ti45 rotor, 40000 rpm, 30 min, 277 K) and keep the pellets
5. Resuspend the pellets using 25 mL of buffer A1 and 10 % v/v octyl-POE
6. Incubate the membrane suspension at 277 K for 1 h while slowly rotating the sample to solubilize the membranes
7. Ultracentrifuge (Ti70 rotor, 40000 rpm, 30 min, 277 K) and keep the supernatant
8. Prepare the Ni-NTA column (affinity chromatography)
    - Add 6 mL of Ni-NTA solution
    - Wash the resin with distilled water
    - Centrifuge for 1 min at the highest speed to eliminate the solvent (Ni-NTA resin is stored in 20 % v/v EtOH)
    - Wash the column with 40 mL of buffer A1 containing 1 % v/v octyl-POE
    - Mix the supernatant from step 7 with the resin and incubate for 1 h at 277 K on a rotating wheel. This step promotes the binding of the His-tagged ShuA on the resin.

9. Use of Ni-NTA column for affinity chromatography
    - Pack the column containing the resin and the supernatant and collect the flow through
    - Wash the column with 20 mL of buffer A1 containing 1 % v/v octyl-POE (washing buffer)
    - Wash with 20 mL of buffer B1 containing 1 % v/v octyl-POE (elution buffer) and collect 10 fractions of 2 mL each
    - Wash the column with distilled water and store in 20 % v/v EtOH
10. Measure the absorbance at 280 nm (A_{280}) of the fractions collected after the Ni-NTA column with Nanodrop spectrophotometer. Use buffer B1 as blank for the measurements.
11. Select the fractions with the highest concentration and use dialysis tube to remove the excess of Imidazole in the fractions collected from the Ni-NTA column.
    - Prepare 2 L of dialysis buffer
    - Centrifuge the fractions from the Ni-NTA column (4000 g, 30 min, 277 K) and load all the samples in the dialysis tube
    - Add the dialysis buffer in a beaker, place the dialysis tube loaded with the protein fractions within the beaker and stir overnight at low speed
12. Transfer the protein sample from the dialysis tube into a 50 mL Falcon tube or Eppendorf tube (depending on the volume) and centrifuge (4000 g, 30 min, 277 K)
13. Prepare the column for ion exchange chromatography (Mono Q® 5/50 GL manufactured by Sigma-Aldrich) and the buffer A2 and B2
14. Use an AKTA purifier FPLC system (GE) to perform the ion exchange chromatography
    - Wash the column with buffer A2, B2 and A2 again
    - Inject the protein sample from step 12
    - Collect fractions of 0.5 mL
    - Wash the column with buffer A2, buffer B2 and distilled water
    - Store the column in 20 % v/v EtOH
15. Measure the absorbance at the wavelength of 280 nm (A_{280} value) of the fractions collected from the ion exchange column. Use buffer A2 as blank for the measurements.
16. Run SDS-PAGE gel for the protein fractions of step 14
17. Pull together the fractions with the highest concentration and start concentrating the protein by centrifuging at 1500 g and 277 K for the time necessary to reach the desired final concentration. Use a 50 kDa Amicon concentrator.
18. Store the concentrated protein at 277 K before using it for crystallization experiments

During my secondment in Trinity College Dublin (TCD) in the lab of Prof. Martin Caffrey (Membrane Structural and Functional Biology/MSFB lab), I purified ShuA to use it for crystallization screening with the LCP method. The results of the purification are summarized below. The final volume of the protein was 50 µL and the concentration 9.27 mg mL^{-1}. The absorbance measurements (A_{280}) of the fractions from the Mono Q column are given in Table A4.9 and the SDS-PAGE gel in Figure A4.9. The fractions on the gel are named A5 to A11, while the marking bands are illustrated at the left of the image. ShuA can be distinguished close to the 70 kDa band. In the third column of Table A4.9, the concentration of the fractions is given in mg mL^{-1}, after applying the Beer-Lambert law. For ShuA, the extinction coefficient is 117690 in units of M^{-1} cm^{-1} at 280 nm measured in water (https://web.expasy.org/cgi-

bin/protparam/protparam1?P72412@noft@ for entry P72412) meaning that for absorption value of 1.692 the concentration of ShuA in aqueous solution is 1 mg mL^{-1}.

Table A4.9: The absorbance measurements (A_{280}) and concentration (mg mL^{-1}) of the ShuA fractions from the Mono Q column.

Mono Q fraction	A_{280}	C (mg mL^{-1})
A5	0.59	0.35
A6	0.65	0.38
A7	0.42	0.25
A8	0.43	0.25
A9	0.31	0.18
A10	0.19	0.11
A11	0.12	0.07

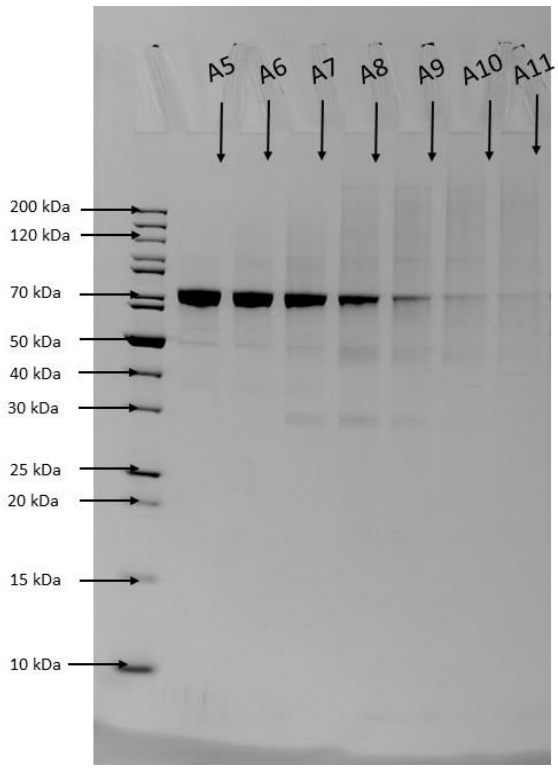

Figure A4.9: The SDS-PAGE gel of the fractions from the Mono Q column during the purification of ShuA. The fractions on the gel are named A5 to A11.

The results of the FPLC (Fast Protein Liquid Chromatography) acquired by using a Mono Q® 5/50 GL column are shown in Figure A4.10. The absorption value (mAU) is plotted against the volume (mL) of the elution buffer (buffer B2) that was running in the column. The

characteristic double peak of ShuA can be seen in the graph corresponding to fractions A5 and A6, which are the fractions with the highest concentration of protein (also confirmed by the SDS-PAGE gel).

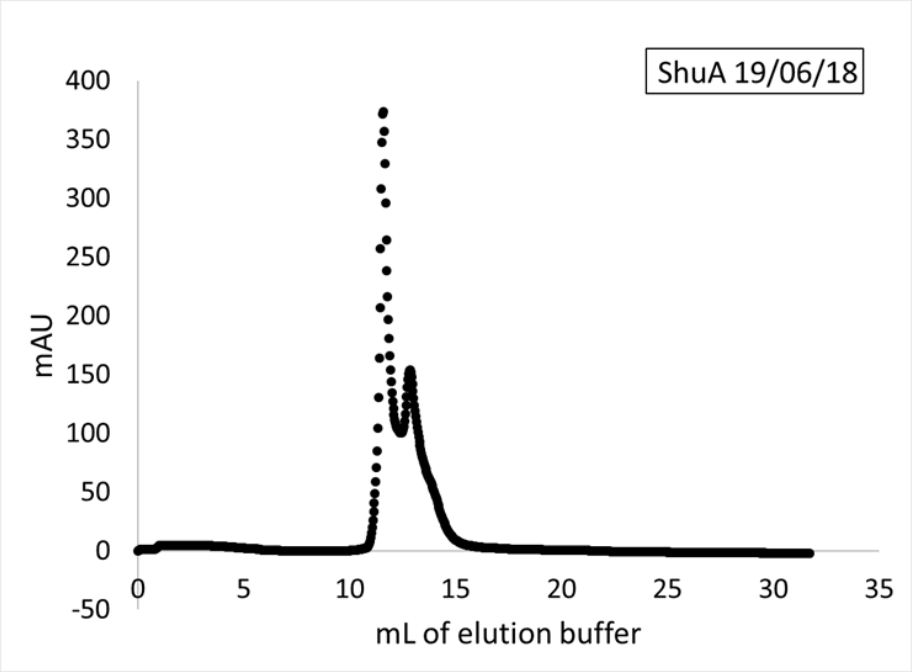

Figure A4.10: The absorption value (mAU) against the volume (mL) of the elution buffer (B2) running in the Mono Q column during ShuA purification. The characteristic double peak of ShuA can be seen.

4.5.3 ShuA crystallization with the LCP method

The ShuA sample that I purified at TCD was used for crystallization experiments with the LCP method. The protein concentration was 9.27 mg mL^{-1} and the lipidic mesophase was prepared with monoolein in a 3:2 (lipid: protein) ratio at 293 K according to the protocol described thoroughly in Chapter 4 (Section 4.1.1.3). 96-well glass plates (Jena Bioscience) compatible with LCP crystallization were first silanized and then used with the SIAS robot (Xantus) for setting up the crystallization trials in an automated way. In each well, 50 nL of mesophase bolus was used and 800 nL of precipitant solution was dispensed above the mesophase bolus. Figure A4.11 (a) and A4.11 (b) show the dispensing process of the bolus and the precipitant solution, respectively, with the SIAS robot. Once all the wells of a glass plate were filled, a cover slip was positioned above the wells. Figure A4.12 illustrates the mesophase bolus and the precipitant solution drop within the wells of the glass plates. The plates were appropriately labelled and incubated in a temperature-controlled chamber (FORMULATRIX Storage and Imaging System) for crystallization at 293 K. Images were regularly recorded with bright field light and polarized filters. 16 plates were prepared with the ShuA-monoolein

mesophase using several commercially available crystallization kits for screening (Table A4.10).

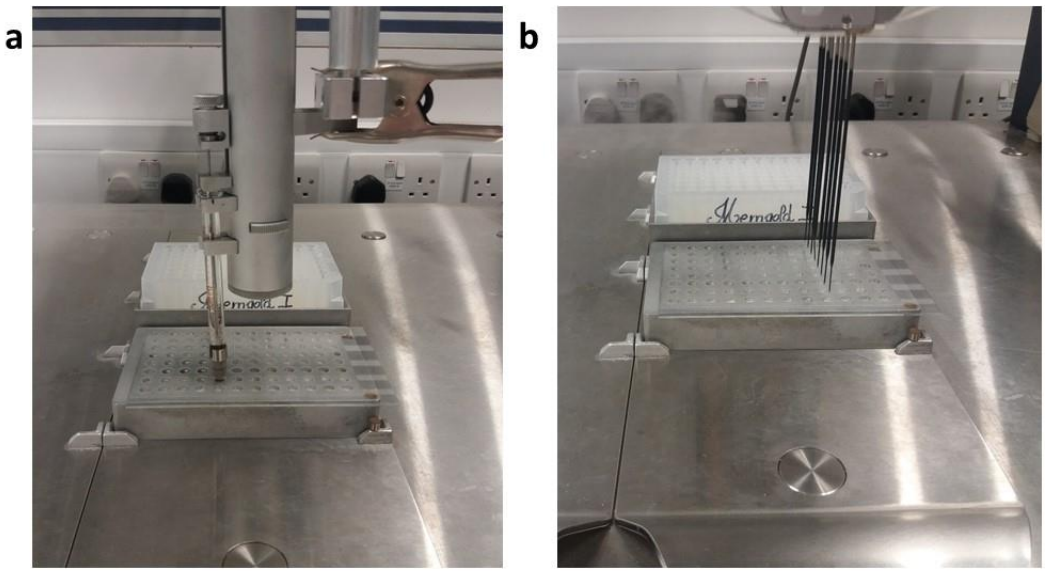

Figure A4.11: Dispensing of the (a) ShuA-monoolein mesophase bolus and (b) the precipitant solution on the 96-well glass plates with the SIAS robot (Xantus).

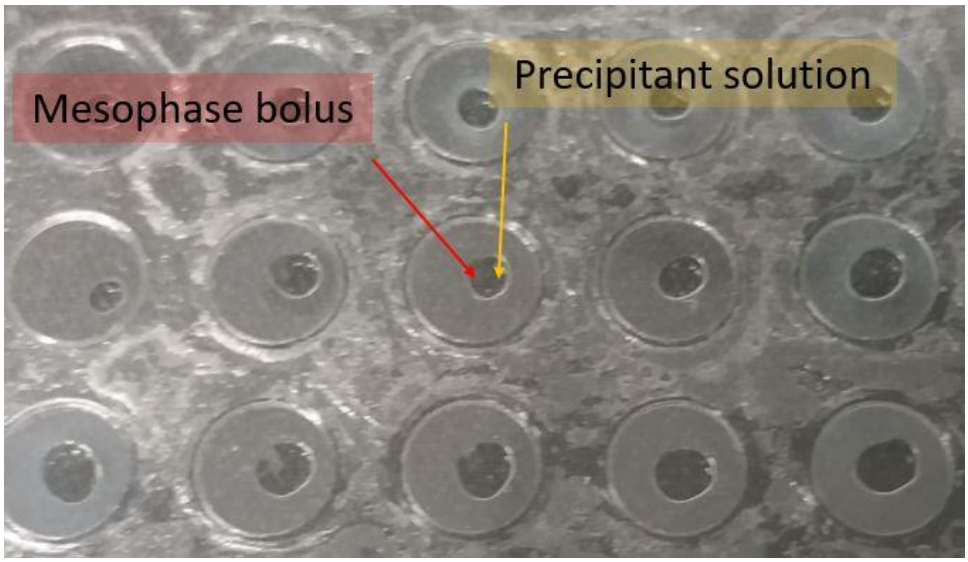

Figure A4.12: The ShuA-monoolein mesophase bolus and the precipitant solution drop within the wells of the 96-well glass plates compatible with the LCP crystallization method.

Table A4.10: The commercial kits for screening crystallization conditions with the LCP method.

Screen	Company
MemGold™	Molecular Dimensions
MembFac	Hampton Research
MemPlus™	Molecular Dimensions
MemMeso™ HT-96	Molecular Dimensions
MemTrans™ ECO MD1-113	Molecular Dimensions
MemGoldMeso™ MD1-115	Molecular Dimensions
Wizard Cubic Screen™ HT96	Molecular Dimensions
Crystal Screen Lite™	Hampton Research
PEG/Ion Screen™	Hampton Research
JB Screen LCP	Jena Bioscience

The crystallization plates were inspected regularly with the Rock Maker Website developed for remote access of the FORMULATRIX Storage and Imaging System. Figure A4.13 shows bright field pictures of a well as recorded 1 day (Figure A4.13 (a)) and 1 month (Figure A4.13 (b)) from the beginning of the experiment and polarized pictures (Figure A4.13 (c) and A4.13 (d)) recorded at the same time intervals. The scale bar corresponds to 100 µm. The crystals grew with the LCP method in the presence of 100 mM magnesium chloride hexahydrate ($MgCl_2(H_2O)_6$), 100 mM sodium citrate tribasic dihydrate ($C_6H_5Na_3O_7(H_2O)_2$) pH 5.0 and 40 % v/v PEG 200 (MemMeso™ HT-96 screen). The crystals were mounted on loops and cry-cooled by the staff of the MSFB lab and tested at Diamond Light Source for X-ray diffraction, but they were salt crystals of magnesium chloride.

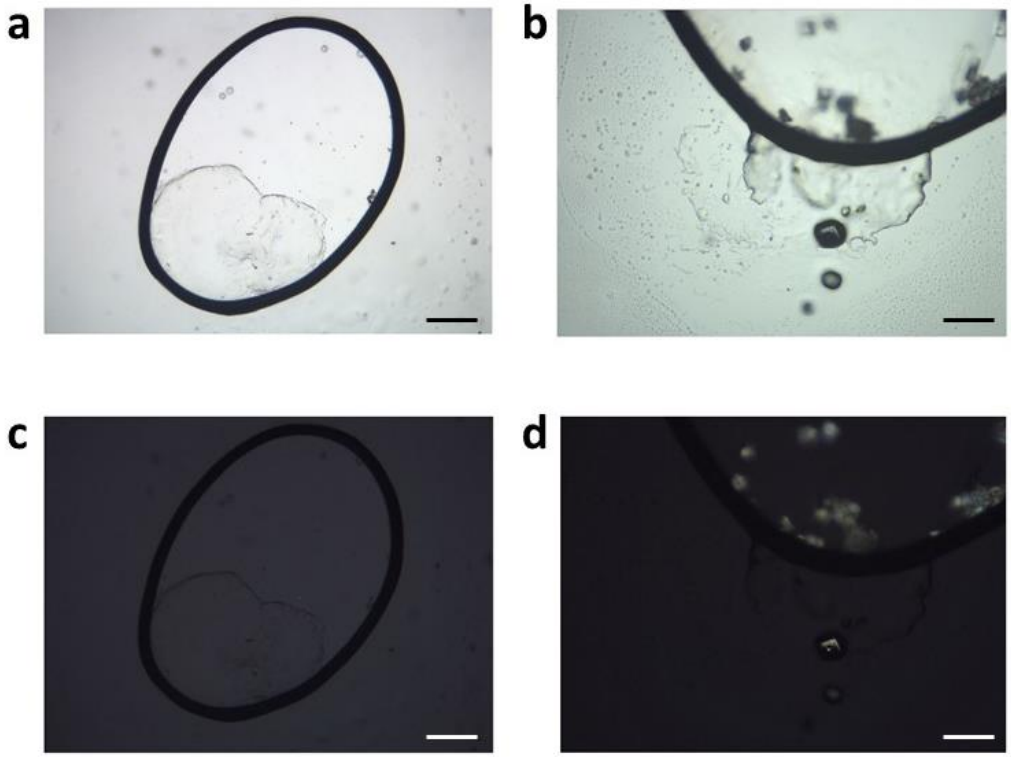

Figure A4.13: Images of the ShuA experiments performed with the LCP method as recorded by the FORMULATRIX Storage and Imaging System. Bright field images (a) 1 day and (b) 1 month and polarized images (c) 1 day and (d) 1 month from the beginning of the experiment. The scale bar represents 100 µm.

4.6 Radiation Damage

Some example simulations are shown in Figure A4.14 for a HEWL crystal exposed to X-rays of 12.6578 keV (Se K edge), over an angular range of 80 ° (- 40° to + 40°) for a total exposure time of 2400 s. Figure A4.14 (a) represents a cuboid crystal of 200 µm x 100 µm x 50 µm, exposed to a top hat beam of 250 µm x 250 µm with a photon flux of 3.32 x 10^{10} ph s^{-1}. Figure A4.14 (b) represents a cuboid crystal of 200 µm x 200 µm x 200 µm, exposed to a top hat beam of 150 µm x 150 µm with a photon flux of 3.32 x 10^{10} ph s^{-1}, while Figure A4.14 (c) represents a cuboid crystal of 200 µm x 200 µm x 200 µm, exposed to a top hat beam of 250 µm x 250 µm with a photon flux of 3.32 x 10^{12} ph s^{-1}. Figures A4.14 (a), A4.14 (b) and A4.14 (c) can be compared to Figure 4.3.3 (Chapter 4) and draw conclusions on the effect of the crystal size, the beam size and the photon flux, respectively, for an X-ray diffraction experiment at 12.6578 keV. Changing the crystal size (from 200 µm x 200 µm x 200 µm in Figure 4.3.3 to 200 µm x 100 µm x 50 µm in Figure A4.14 (a)) doesn't change considerably the dose metrics, as shown in Table A4.11, however, it has a significant impact on the distribution of the dose in the crystal volume since only half of the crystal volume in Figure A4.14 (a) is exposed in the high-dose regime (0.622 – 0.63 MGy). Altering the beam size (from a top hat beam of 250 µm x 250 µm in Figure 4.3.3 to a top hat beam of 150 µm x 150 µm in Figure A4.14 (b)) affects

both the dose metrics (Table A4.11) and the dose distribution as illustrated by the dose map. As may be seen in Figure A4.14 (b), mainly the central region of the cubic crystal along the z-axis is exposed in the high-dose regime (1 – 1.7 MGy). Finally, changing merely the photon flux (from 3.32 x 10^{10} ph s^{-1} in Figure 4.3.3 to 3.32 x 10^{12} ph s^{-1} in Figure A4.14 (c)) doesn't impact the dose distribution on the crystal's voxels but what actually changes are the dose metrics (DWD and maximum dose), as shown in Table A4.11. Both dose metrics exceed the limit value of 30 MGy when using a higher flux value and the fidelity of the biological information when interpreting the electron density map generated in this case is compromised.

Table A4.11: DWD (MGy) and maximum dose (MGy) metrics as calculated by RADDOSE-3D for a HEWL crystal irradiated at 12.6578 keV in various conditions.

	DWD (MGy)	**Max Dose (MGy)**
Figure 4.3.3	0.3028	0.6267
Figure A4.14 (a)	0.3108	0.6270
Figure A4.14 (b)	0.7371	1.7410
Figure A4.14 (c)	30.2821	62.6791

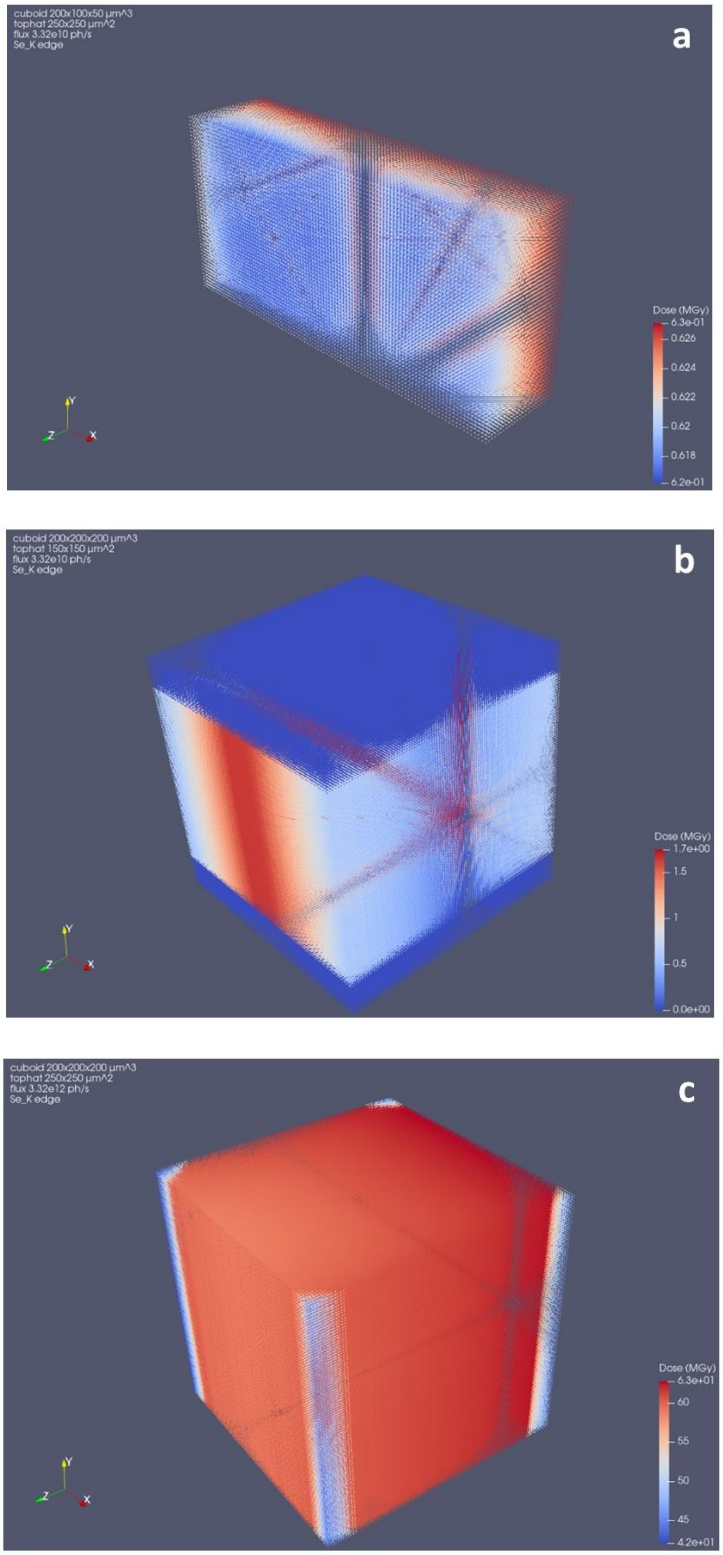

Figure A4.14: Dose map simulations for a HEWL crystal irradiated at 12.6578 keV. (a) Cuboid crystal of 200 µm x 100 µm x 50 µm, exposed to a top hat beam of 250 µm x 250 µm with a photon flux of 3.32 x 10^{10} ph s^{-1}, (b) cuboid crystal of 200 µm x 200 µm x 200 µm, exposed to a top hat beam of 150 µm x 150 µm with a photon flux of 3.32 x 10^{10} ph s^{-1} and (c) cuboid crystal of 200 µm x 200 µm x 200 µm, exposed to a top hat beam of 250 µm x 250 µm with a photon flux of 3.32 x 10^{12} ph s^{-1}. The dose is given in MGy and the maps were produced with Paraview.

Dose histograms are shown in Figure A4.15 for a Gaussian beam profile with a FWHM (full width at half maximum) of 50 µm vertical x 200 µm horizontal. The photon flux is 3.32 x 10^{10} ph s^{-1} at 25.5140 keV (Figure A4.15 (a)) and at 4.9392 keV (Figure A4.15 (b)), the limit energy values at BM07-FIP2. The percentage of voxels (% voxels) is plotted against 11 dose range bins (MGy) for various cuboid crystal size values: 200 µm x 200 µm x 200 µm, 100 µm x 100 µm x 100 µm, 50 µm x 50 µm x 50 µm and 10 µm x 10 µm x 10 µm. Figure A4.15 (a) shows that all the volume voxels are exposed to the low-dose regime (up to 3.4 MGy), regardless of the crystal size. However, Figure A4.15 (b) shows a wider dose range distribution among the voxel bins at 4.9392 keV for all crystal size values, except for the smallest size (10 µm x 10 µm x 10 µm) where the crystal is completely exposed to a dose > 30 MGy.

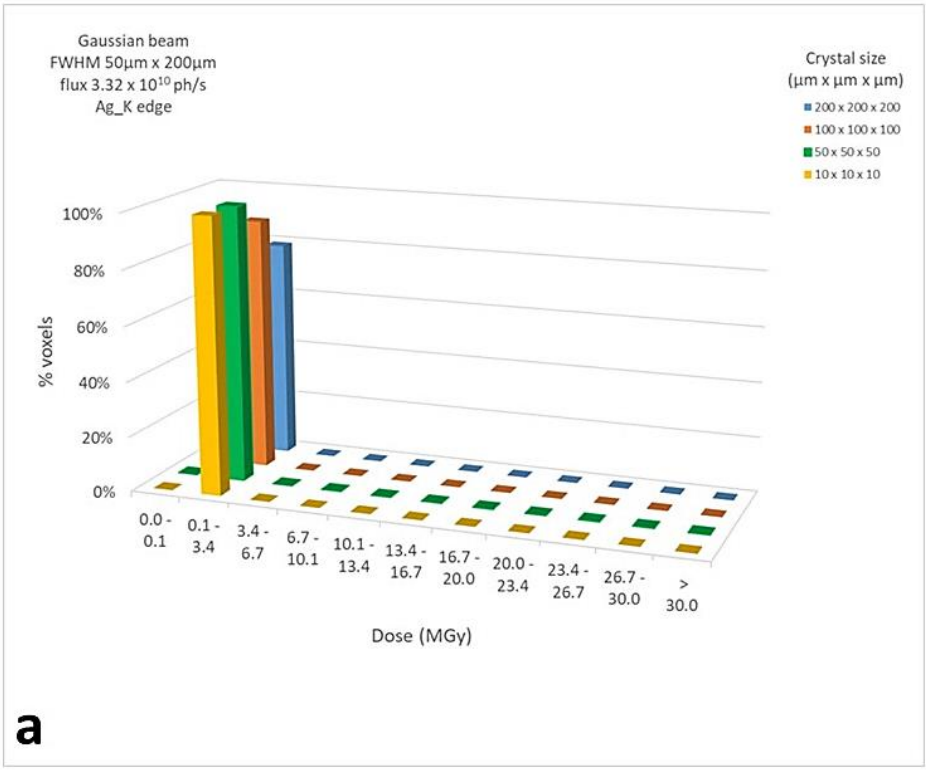

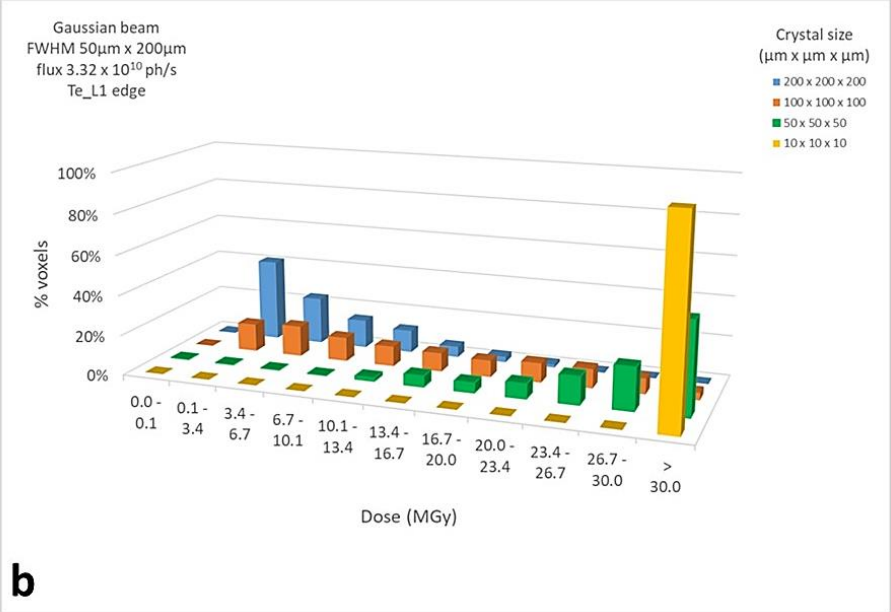

Figure A4.15: Dose histograms of the percentage of voxels (%) against 11 dose range bins (MGy) for a Gaussian beam of 50 µm x 200 µm and various crystal size values. The photon flux is 3.32 x 10^{10} ph s^{-1} and the photon energy is (a) 25.5140 keV and (b) 4.9392 keV.

Figure A4.16 (a) illustrates a plot of the DWD (MGy) against the photon energy (keV) for various size values of a cuboid crystal. The beam is a top hat with a size of 250 µm x 250 µm and the photon flux 3.32 x 10^{10} ph s^{-1} (experimental value). The crystal shape is cuboid and the size is 200 µm x 200 µm x 200 µm, 100 µm x 100 µm x 100 µm or 50 µm x 50 µm x 50 µm or 200 µm x 100 µm x 50 µm. In all cases represented in this plot, DWD increases as the photon energy decreases. Specifically, DWD lies within the range of 1.4749 MGy (200 µm x 200 µm x 200 µm crystal) to 1.9457 MGy (50 µm x 50 µm x 50 µm crystal) at 4.9392 keV, while at 25.5140 keV the respective DWD values are within the range 0.0690 MGy (200 µm x 200 µm x 200 µm crystal) to 0.0695 (50 µm x 50 µm x 50 µm crystal).

The impact of the beam size for a top hat beam is shown in Figure A4.16 (b), where DWD (MGy) is plotted against the photon energy (keV) for 8 different beam size values: 300 µm x 300 µm, 250 µm x 250 µm, 200 µm x 200 µm, 150 µm x 150 µm, 100 µm x 100 µm, 50 µm x 50 µm, 10 µm x 10 µm and 5 µm x 5 µm. The photon flux is 3.32 x 10^{10} ph s^{-1} (experimental value) and the cuboid crystal is 200 µm x 200 µm x 200 µm. Two major conclusions can be drawn from the interpretation of this plot: the DWD value is lower for higher beam energies regardless of the beam size, while the beam size has a significant impact on DWD for photon energies < 10 keV. Specifically, a ten-fold increase on DWD can be seen for beams with a size much smaller than the crystal size. The DWD has been estimated to be within 1.0303 MGy (300 µm x 300 µm beam) and 414.3988 MGy (5 µm x 5 µm beam) at 4.9392 keV and within 0.0480 MGy (300 µm x 300 µm beam) and 22.8472 MGy (5 µm x 5 µm beam) at 25.5140 keV.

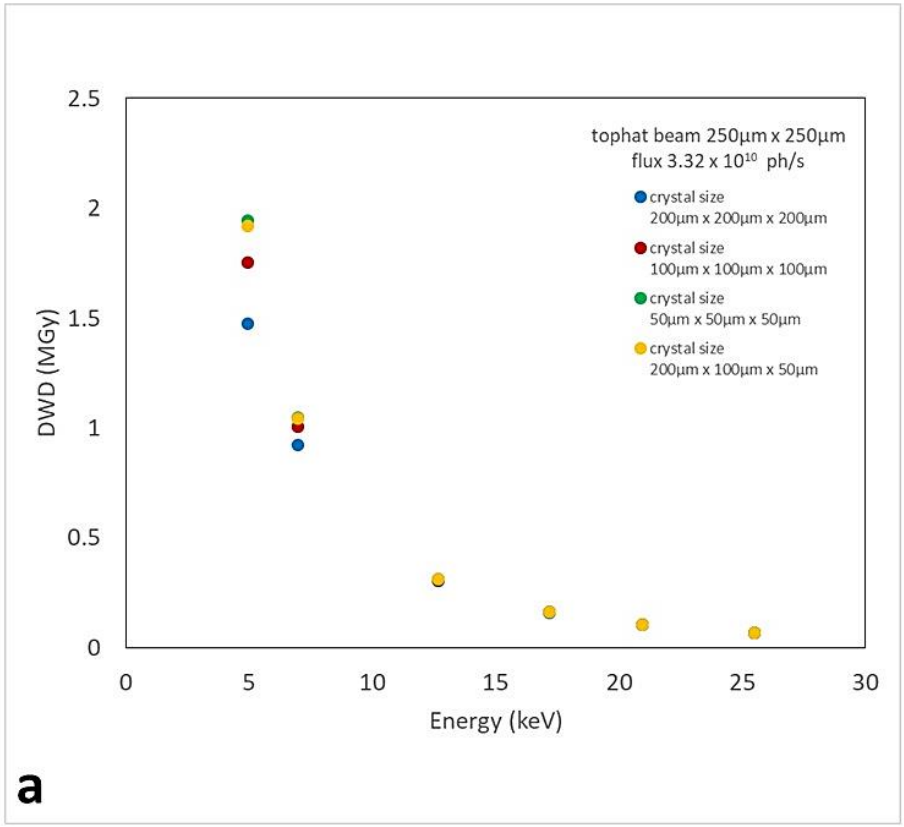

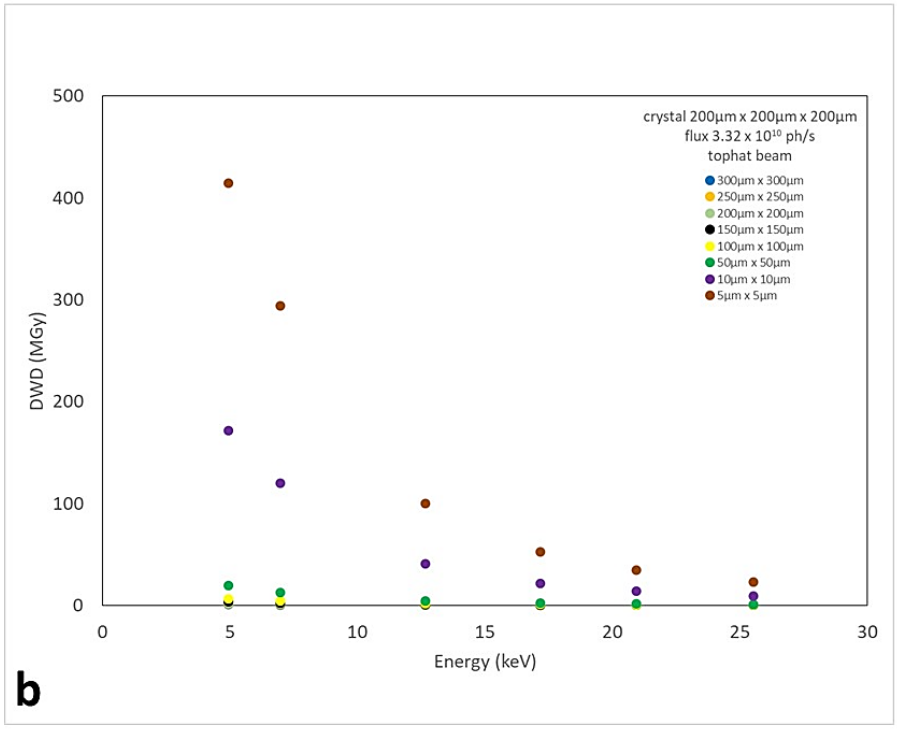

Figure A4.16: DWD (MGy) calculated by RADDOSE-3D as a function of the beam energy (keV) and (a) the crystal size for a top hat beam of 250 µm x 250 µm and photon flux of 3.32 x 10^{10} ph s^{-1}, and (b) the beam size of a top hat beam for a cuboid crystal of 200 µm x 200 µm x 200 µm and photon flux of 3.32 x 10^{10} ph s^{-1}.

Publications

1. Crystallization of proteins on chip by microdialysis for in situ X-ray diffraction studies
   Sofia Jaho, Niels Junius, Franck Borel, Yoann Sallaz-Damaz, Jean-Baptiste Salmon and Monika Budayova-Spano
   Journal of Visualized Experiments, 2021 (doi: 10.3791/61660)

2. A microfluidic device for both on-chip dialysis protein crystallization and in situ X-ray diffraction
   Niels Junius, **Sofia Jaho**, Yoann Sallaz-Damaz, Franck Borel, Jean-Baptiste Salmon and Monika Budayova-Spano
   Lab on a Chip, 2020, 20, 296 (https://doi.org/10.1039/C9LC00651F)

Lab on a Chip

PAPER

View Article Online
View Journal | View Issue

Cite this: *Lab Chip*, 2020, **20**, 296

A microfluidic device for both on-chip dialysis protein crystallization and *in situ* X-ray diffraction†

Niels Junius, ‡[a] Sofia Jaho, [a] Yoann Sallaz-Damaz,[a] Franck Borel, [a] Jean-Baptiste Salmon [b] and Monika Budayova-Spano *[a]

This paper reports a versatile microfluidic chip developed for on-chip crystallization of proteins through the dialysis method and *in situ* X-ray diffraction experiments. A microfabrication process enabling the integration of regenerated cellulose dialysis membranes between two layers of the microchip is thoroughly described. We also describe a rational approach for optimizing on-chip protein crystallization *via* chemical composition and temperature control, allowing the crystal size, number and quality to be tailored. Combining optically transparent microfluidics and dialysis provides both precise control over the experiment and reversible exploration of the crystallization conditions. In addition, the materials composing the microfluidic chip were tested for their transparency to X-rays in order to assess their compatibility for *in situ* diffraction data collection. Background scattering was evaluated using a synchrotron X-ray source and the background noise generated by our microfluidic device was compared to that produced by commercial crystallization plates used for diffraction experiments at room temperature. Once crystals of 3 model proteins (lysozyme, IspE, and insulin) were grown on-chip, the microchip was mounted onto the beamline and partial diffraction data sets were collected *in situ* from several isomorphous crystals and were merged to a complete data set for structure determination. We therefore propose a robust and inexpensive way to fabricate microchips that cover the whole pipeline from crystal growth to the beam and does not require any handling of the protein crystals prior to the diffraction experiment, allowing the collection of crystallographic data at room temperature for solving the three-dimensional structure of the proteins under study. The results presented here allow serial crystallography experiments on synchrotrons and X-ray lasers under dynamically controllable sample conditions to be observed using the developed microchips.

Received 5th July 2019,
Accepted 25th September 2019

DOI: 10.1039/c9lc00651f

rsc.li/loc

Introduction

X-ray crystallography has been for many years the principal experimental technique for studying the structure of complex macromolecules such as soluble and membrane proteins. The most powerful sources for generating X-rays are synchrotrons, which have become numerous over the last few years and have increased photon flux and smaller beam size. However, the use of X-ray crystallography for the determination of the atomic structure of proteins is restricted, firstly, by the size and quality of the protein crystals. Obtaining well diffracting protein crystals with an adequate size, usually bigger than 10 μm,[1] can be challenging and time-consuming. Another restrictive parameter is the radiation damage caused by the long exposure times of the protein crystals in front of the X-ray beam. To overcome this barrier, cryogenic cooling of the crystals prior to their exposure to X-ray radiation is used in order to improve the signal-to-noise ratio during the collection of the diffraction data sets. Nevertheless, the optimal cryocooling conditions need to be determined in advance for each protein since cryocooling can conceal conformational changes of the three-dimensional structure of the protein molecules.[2,3] Another challenge that must be addressed during conventional X-ray crystallography experiments is sample delivery. The most widely used methods for growing protein crystals are batch crystallization and vapor diffusion. Once the protein crystals are grown to a sufficient size, they need to be harvested from the bulk and delivered in front of the X-ray beam, a process that can damage fragile samples.

The direct observation and acquisition of functional conformations of proteins or other biological macromolecules remains the major goal in structural biology. Current studies focus on the use of small crystals and more challenging protein targets due to the ongoing development of increasingly bright and micro-focused synchrotron X-ray beams, as well as

[a] *Université Grenoble Alpes, CEA, CNRS, IBS, F-38000 Grenoble, France*
[b] *CNRS, Solvay, LOF, UMR 5258, Univ. Bordeaux, F-33600 Pessac, France.*
E-mail: monika.spano@ibs.fr

† Electronic supplementary information (ESI) available. See DOI: 10.1039/c9lc00651f

‡ Current address: ELVESYS – Innovation Center, 1 rue Robert et Sonia Delaunay, 75 011 Paris, France.

the emergence of X-ray free-electron lasers (XFELs). Crystals considered too small for conventional X-ray crystallography can be used for structure determination at new generation synchrotron beamlines and XFEL sources.[4] Limitations related to radiation damage, long exposure times and sample manipulation can be eliminated by using serial data collection strategies.[5] The use of serial synchrotron X-ray crystallography (SSX) at synchrotrons or serial femtosecond X-ray crystallography at XFELs is based on the merging of data sets collected from multiple small, isomorphous crystals.

Microfluidics may exhibit many advantages related to both the protein crystallization process and the structural X-ray analysis. First of all, setting up crystallization experiments in microfluidic devices requires minute amounts of protein samples,[5] therefore reducing the production and purification costs of these high-valued biomolecules. Moreover, microscale geometries yield large surface area-to-volume ratios and small dimensions, enabling fine control over transport phenomena within the microfluidic structures.[6,7] Microfluidic scales also limit inertial and convective phenomena,[5,8] and diffusion-limited heat and mass transfer in microfluidic environments facilitates the control over temperature and concentration gradients, necessary for the growth of uniformly sized crystal populations. For all these reasons, microfluidic devices are suitable for investigating phase diagrams[9–11] and performing high-throughput screening of diverse crystallization conditions by using only a few nL–μL of samples.[6,11–14] Various and innovative solutions have been reported pointing out the challenges encountered while using microfluidics for investigating and screening the crystallization conditions of soluble proteins[15–17] and membrane proteins.[18,19]

While microfluidic tools display several benefits for controlling the size uniformity and the morphology of crystals grown on microchips, the need to handle and harvest crystals prior to their use with crystallography methods has not yet been fully surpassed. The novel approach of *in situ* and on-chip X-ray diffraction data collection has been proposed by many groups working on the field of structural biology.[5,20] Designing and fabricating microfluidic devices compatible for *in situ* X-ray measurements shows restrictions related to the interactions of X-rays with matter, mainly absorption and scattering. Attenuation, induced by the absorption of the material itself, must be considered since the presence of the microfluidic device adds more material in the path of the X-ray beam.[8] The nature of the materials used for fabricating a microfluidic device and its thickness are highly relevant parameters since attenuation can reduce the intensity of both the incident and diffracted X-rays.[5,6,8] Moreover, the thickness of the devices can severely reduce the impact of quasi-elastic scattering. Scattering effects from the materials of the device add up to X-ray scattering induced by the presence of air surrounding the experiment and/or the presence of fluids within the crystal structure and lead to increased background noise.[5,6,8] Thus, decreasing the total thickness of the chip or using low density materials can moderate the impact of attenuation and scattering on the diffraction measurements. Nonetheless, decreasing the thickness of such devices also gives rise to some limitations concerning their mechanical stability and the fabrication process could be complicated.[5]

Microfluidic technologies have been proven crucial to couple and facilitate protein crystallization and structural studies in a single device. Many designs and materials have been proposed for *in situ* X-ray experiments and the following examples constitute only a small portion of available proposed solutions. PDMS-based devices using vapor diffusion[21] or free interface diffusion (FID)[22] have been developed for the crystallization and *in situ* X-ray diffraction measurements of soluble proteins. Hybrid microfluidic devices made of PDMS, COC (cyclic olefin copolymer) or PMMA (poly(methyl methacrylate))[14] or PDMS and COC[6] were also used to collect *in situ* structural data of soluble proteins and evaluate the fabrication materials for their transparency to X-rays and their contribution to the background noise. *In situ* data collection has been also applied in more challenging protein targets. Kisselman *et al.*[23] developed the X-CHIP for microbatch crystallization, and Perry *et al.*[13] fabricated a device made of thin layers of PDMS, COC and Duralar® for on-chip anomalous diffraction measurements, while Schieferstein *et al.*[24] studied the crystallization of membrane proteins with microseeds using microchips[6] made of PDMS and COC. Microfluidic chips composed of multiple levels of various fabrication materials (PDMS, COC, PMMA, graphene films or epoxy glue) can also be used for *in situ* X-ray data collection for serial crystallography.[3,8,25]

As listed above, various methods (vapor diffusion, microbatch, and free interface diffusion) have been used for the crystallization of soluble and membrane proteins on microfluidic devices and *in situ* X-ray diffraction experiments. High throughput screening and optimization of crystallization conditions on the microscale is another major issue that needs to be addressed. Li and Ismagilov[31] published a critical and complete review on the major developments in the field of microfluidic technology for protein crystallization and high-throughput screening. They have included the milestones in microfluidic protein crystallization that have been developed and successfully tested to implement traditional crystallization methods (microbatch, vapor diffusion and free interface diffusion) in valve-, droplet- and well-based devices. Well-based microfluidic platforms are one of the most recently adapted technologies for on-chip screening of multiple crystallization conditions. Recently, Li *et al.*[32] published their results for using a triple-gradient generator device in order to screen the conditions for crystallizing three different proteins. Droplet-based microfluidics combined with either the micro-batch crystallization method, pseudo-vapor diffusion or counter diffusion is more automated and used for setting up high-throughput screening of crystallization conditions.[5,10,12,14,28] Abdallah *et al.*[33] developed a PDMS microfluidic device in order to address the challenging problem of optimization in microfluidics. The device was used in high-throughput batch-type crystallization experiments for multi-

dimensional screening and the investigation of phase diagrams of two different proteins.

Another method used in protein crystallization is dialysis. Dialysis enables precise and reversible control over the crystallization conditions[9] and can be used, combined with temperature control, to decouple nucleation and crystal growth during the investigation of phase diagrams.[9,28] Semipermeable membranes are used with a molecular weight cut-off (MWCO) smaller than the dimensions of the macromolecule under study, allowing small molecules, like salts or solvents, to diffuse through the membrane. Many approaches have been reported in order to integrate membranes into microfluidic chips. A review by de Jong *et al.*[29] summarizes the integration of membranes into microfluidics in four main categories. The first method involves the direct incorporation of membranes into microfluidic devices by gluing or clamping.[30] Commercially available membranes can be employed like regenerated cellulose (RC) dialysis membranes which are widely used in the crystallization of biological macromolecules. A microfluidic setup including two separate modules, a "dialysis chip" and an "exposure chip" for *in situ* SAXS data collection, was reported by Skou *et al.*[40] In their dialysis chip, an RC membrane is sandwiched in-between two PDMS sheets, clamped together using two pieces of 5 mm-thick PMMA plates. Such a dialysis chip was used to concentrate a flowing protein solution using an imposed osmotic pressure difference that drives a solvent flow through the semi-permeable membrane. This dialysis chip is connected to the "exposure chip" for acquiring SAXS spectra from the osmotically-concentrated dilute protein solution.

In a previous work, we developed the prototype of an integrated apparatus for the rational optimization of crystal growth by manipulating and mapping temperature–precipitant concentration phase diagrams.[9,26] The so-called crystallization bench comprises a flow cell dialysis set-up (typical volume >20 μL) to exchange conditions and control temperature during the experiments. Based on this macro scale instrument, the present work focuses on a miniaturized device that allows precise control of the experimental parameters[27] exploiting the advantages of microfluidics such as the control of transport phenomena and the reduced sample volume needed per experiment (typical volume <1 μL). The new system that we developed couples microfluidics with the micro-dialysis method for on-chip crystallization of proteins and investigation of phase diagrams. The principle of the dialysis method applied to a macro scale flowing system has been discussed in our previous work.[9] The novelty of our work is the use of the dialysis method on a unique versatile microfluidic device, designed to meet the requirements of both on-chip protein crystallization and *in situ* X-ray crystallography. Microfluidic dialysis is used here for monitoring the crystallization process in response to precipitant concentration exchange, but our microfluidic device also allows future possibilities of studying experimentally induced structural changes by serial X-ray crystallography under dynamically controlled sample conditions. We have designed a microchip for on-chip crystallization of proteins *via* microdialysis that can be set directly in front of an X-ray beam for data collection without the need for harvesting the protein crystals. Collecting data *in situ* prevents the modification of the environment surrounding the crystals, as it takes place in a sealed controlled volume, avoiding the degradation of the crystal quality induced by evaporation or the risk of damaging the crystals due to manual handling. We describe a microfabrication protocol to insert RC membranes in the microfluidic chip, as well as crystallization assays carried out on-chip in order to optimize the crystallization process, *in situ* X-ray diffraction studies and a prototype to control the temperature. Precipitant concentration is controlled *via* a platform for fluid handling and an interactive software interface that we designed for the preparation of the crystallization solution.[9] Salts, solvents, buffers and other solutions can be pre-mixed and subsequently pumped into the microfluidic channel in a fully automated way. Uncontrolled concentration variations observed in traditional crystallization techniques due to random mixing can be eliminated. Temperature can be controlled within the microfluidic devices *via* a prototype using external heating through Peltier modules and copper elements (see the ESI†). Homogeneous temperature distribution or temperature gradients can be achieved across the chip. We propose a robust and inexpensive way for manufacturing numerous chips in a few hours.

Materials and methods

Microfluidic device fabrication

The fabrication of our microfluidic device is directly inspired by the protocol developed by Bartolo *et al.*[34] for "stencil"-like micro-patterned stickers made of the thiolene-based resin NOA 81 (Norland Optical Adhesive) with soft imprint lithography. The same team (Morel *et al.*[35]) modified the original protocol in order to make photocurable resin-based microchips embedding commercial membranes to study the diffusion of various components across the membrane without applying any stress on the biological samples (cell cultures). Our microfluidic chips were made based on this pioneering work, in order to couple microfluidics with the crystallization of proteins through the dialysis method in a single device.

The fabrication protocol is shown schematically in Fig. 1. The first step of the fabrication process (Fig. 1A) is photolithography where the patterns of the device are obtained on masters fabricated on silicon wafers (3 inch Si-wafers) using negative photoresist (SU-8 3000 series, Microchem). After the photolithography, the surface of both silicon wafers containing the micro patterns were treated with a vapor of HMDS (hexamethyldisilazane, Sigma Aldrich) at 95 °C for 10 min to facilitate the detachment of the PDMS stamps. The second step of the fabrication protocol consists of obtaining two PDMS (silicone elastomer base, Sylgard 184 Dow Corning or RTV-615 Momentive) stamps by replica molding of the two silicon masters. The first PDMS stamp consists of two successive layers: one layer where the microfluidic channels are

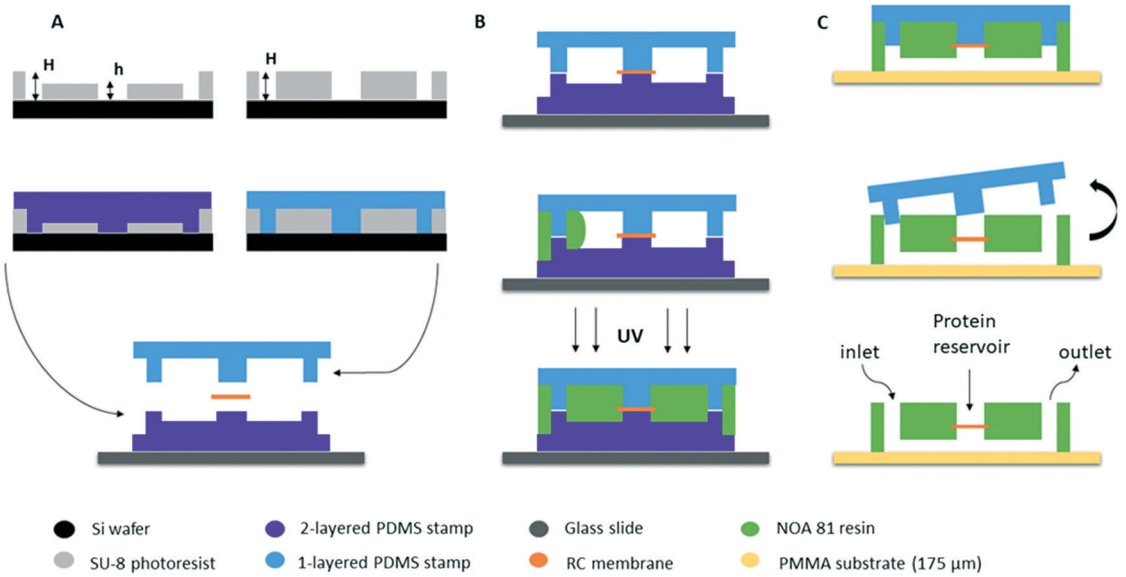

Fig. 1 Schematic illustration of the fabrication process of the microfluidic chips embedding an RC dialysis membrane (transverse view). (A) Two silicon wafers containing the microfluidic channels and pillars are produced using negative photoresist *via* photolithography (top) and two PDMS stamps are made by replica molding (middle). The stamps are then supported on a glass slide, incorporating the RC dialysis membrane (bottom). The heights of the micro-patterns are H = 100 μm and h = 50 μm. (B) The space between the two PDMS stamps is filled with the photocurable resin (NOA) by capillarity (middle) and the resin is cured by UV exposure (bottom). (C) The bottom PDMS stamp is removed and the rest of the assembly (upper PDMS stamp and the partially cured NOA layer containing the RC membrane) is gently pressed on a glass slide or a 175 μm thick PMMA substrate (top). The new assembly is exposed again to UV to fully reticulate the NOA resin and the upper PDMS stamp can be finally detached (middle), revealing the micro-patterns, as the central well designed to be the protein reservoir and the inlet and outlet for the microfluidic connectors (bottom).

located with an approximate height of 50 μm and one layer containing the pillars for the solution flow and the protein reservoir of about h = 50 μm as well. The total height of the two-layered stamp is H = 100 μm (Fig. 1A left). The second PDMS stamp consists of a single layer containing only the pillars with a total height of approximately H = 100 μm (Fig. 1A right). The total height of the patterns in each PDMS stamp is defined by the height of the respective pattern on the silicon wafers.

The two-layered PDMS stamp is placed on a rigid microscope glass slide (3 in × 1 in, Dutscher) in order to enhance the support of the assembly, with the patterned channels and pillars facing upwards (Fig. 1A bottom). This way, the central pillar of the two-layered PDMS stamp which is the protein reservoir exceeds vertically by 50 μm from the horizontal surface of the stamp. A dry piece of the regenerated cellulose (RC) dialysis membrane is cut and deposited on the PDMS stamp at the exact location of the exceeding pillar (center of the stamp) which is the protein reservoir. The dialysis membranes are commercially available (Spectra/Por®) and the MWCO is defined by the molecular weight of the proteins under study. Then, the one-layered PDMS stamp has to be placed and aligned with its microstructures facing downwards. The one-layered stamp also consists of a central pillar that exceeds the surface by 100 μm and can be visually seen without any extra equipment. Therefore, the alignment can be achieved by moving the upper PDMS stamp until the central pillar of the one-layered stamp is at the exact same position as the central pillar of the two-layered stamp. This way, the dialysis membrane is "sandwiched" in between the two PDMS stamps (Fig. 1B top). The assembly is desiccated (30 min) in order to remove trapped air bubbles, to degas PDMS, and to accelerate further the insertion of the resin.

Once the alignment of the two PDMS stamps is achieved, the two pieces are kept in place simply by the good PDMS–PDMS adhesion and no external pressure or other way of bonding is applied. The empty space between the two PDMS stamps is then filled with photocurable resin NOA by capillarity (Fig. 1B). The adhesion between the two PDMS stamps prevents the liquid resin from seeping in between the pillars of the stamps. This resin has high viscosity and it takes a few minutes for NOA 81 (300 mPa s at 298 K) and NOA 61 (300 mPa s at 298 K) or approximately 30 minutes for NOA 68 (4500–5500 mPa s at 298 K) to fill the gap by capillary imbibition. No pre-treatment of the NOA resin was implemented prior to its use for the fabrication process. The commercial product was kept in a fridge at approximately 4 °C and was removed 1 or 2 hours prior to the experiment in order to reach room temperature. The resin is then cured by UV exposure through the transparent PDMS stamps (Fig. 1B bottom). We observed that the exposure settings depend on the nature of PDMS we used. In the case of Sylgard 184, the assembly was uniformly illuminated with a total deposited energy of 100 mJ cm^{-2} and in the case of RTV-615 the total deposited energy should be 200 mJ cm^{-2}. These values were obtained

using a UVITEC Cambridge Crosslinker at a wavelength of 365 nm. Exposure of the PDMS material to UV light can change its surface chemistry. Bhagat *et al.*[44] used both Sylgard 184 (Dow Corning) and RTV-615 (GE Silicones) in order to directly pattern micro structures in PDMS. They prepared the PDMS mixtures by mixing the base and the curing agent in a 10 : 1 (m/m) ratio and they added benzophenone, a photoinitiator used to initiate free-radical polymerization by UV light. The PDMS was directly patterned by exposure to UV light (<365 nm) at 12 mW cm^{-2} for 10 min and both PDMS formulas yielded the same results concerning the patterned micro structures. Our main hypothesis on this divergence in the behavior of the two PDMS types is the formula provided by the two different companies, as according to Bhagat *et al.*[44] there should be no difference in patterning microstructures with the two types of PDMS.

The first exposure allows NOA to be partially crosslinked. The gas permeability of PDMS and the inhibition of polymerization by oxygen ensure that a very thin layer of NOA in contact with the PDMS stamps on both sides remains uncured.[34] The excess of NOA was cut gently from the external sides of the stamps. The top PDMS stamp with the partially cured NOA stuck on it, was removed from the bottom PDMS stamp. The upper assembly (one-layer PDMS stamp + NOA) was then gently pressed on a conventional 1 mm thick microscope glass slide or a 175 μm thick PMMA sheet (poly(methyl methacrylate), Goodfellow), as shown in Fig. 1C (top). The new assembly (glass slide or PMMA + NOA + one-layer PDMS stamp) was reticulated again at a higher energy, approximately ten times higher than the first exposure (1000 mJ cm^{-2} for Sylgard 184 stamps for example), leading to the adhesion of the NOA layer on the glass or PMMA substrate without any further treatment. Finally, the remaining PDMS stamp was removed (Fig. 1C). Both PDMS stamps can be re-used 4–5 times after washing with isopropanol and acetone. After using the PDMS stamps multiple times, they can be a little bit bended. This is mainly due to manipulation of the stamps. When this happens, NOA can leak between the pillars of the PDMS stamps and the stamps have to be replaced.

Following the fabrication protocol, the dialysis membrane is directly incorporated into the NOA sticker; thus no mechanical clamping or further manipulation was needed to fix the membrane on the microchip's material. Kornreich *et al.*[30] developed a microfluidic device composed of two PDMS layers (a material widely used in microfabrication) separated by a cellulose ester dialysis membrane but the device was used only for cross polarization microscopy. Morel *et al.*[35] also confronted the problem of multi-level clamping in PDMS, resulting in the development of a protocol using the NOA resin, for which the dialysis membrane is directly embedded into the microchip. Moreover, the permeability of PDMS to both water and air was a prohibitory factor while choosing fabrication materials, since crystallization experiments may last up to several days, as shown in Fig. 5.

Studies have been conducted to estimate the effect of UV radiation on structural and transport parameters of polymeric membranes. In the case of RC membranes, Vaquez *et al.*[41] treated a sample with UV light at 40 W and 317 nm for 48 h in an air-circulated artificial ageing chamber. They measured a 5% increase in salt permeability (NaCl) for a UV treated sample *versus* an untreated sample. As suggested by Vaquez *et al.*,[41] this result could be related to a change in the packing of the polymer chains (expansion of the polymer chains), which results in an increase of the fractional void volume in the case of UV-treated RC membranes. According to the above-mentioned studies, there is an increase of permeability of polymeric membranes after treatment with UV radiation. During the fabrication of our microchips, the RC membrane is exposed two times to UV radiation at 365 nm and the deposited energy is 100 mJ cm^{-2} and 1000 mJ cm^{-2} in the case of Sylgard 184. These exposures can be considered negligible in terms of deposited energy as compared to what has been reported in the work of Vaquez *et al.*[41]

Pictures of the microchips, micro-compartments and connectors are shown in Fig. 2. The design of the microfluidic chip proposed in this work is based on the idea of introducing the crystallization solution into a fluidic, linear channel with an automated pressure driven system and the protein solution being manually introduced by pipetting it into the protein reservoir. Both the protein reservoir and the linear channels can be distinguished from the photographs in Fig. 2A and B. During the fabrication process, the microfluidic channel is imprinted on the two-layer PDMS stamp, as shown in Fig. 1. Once the empty space between the two PDMS stamps is filled by NOA and the stamps are removed after the resin is crosslinked, the linear channel is located at the second, bottom layer of the chip (height of 50 μm) and consists of one inlet for the introduction of the crystallization solution and one outlet for the disposal of the solution (Fig. 2B). Their total height is 200 μm and they resemble holes on the photographs of the various chips (Fig. 2A and B). The reservoir designed for the deposition of the protein solution is also featured in Fig. 2A–C. The protein reservoir is the chamber located above the dialysis membrane and is imprinted on the one-layer PDMS stamp during the fabrication process (Fig. 1C bottom). The height of the protein reservoir is 100 μm and its volume differs based on the different prototypes that were designed. In Fig. 2A and B (top), a microchip containing only one reservoir for the protein solution with a maximum volume of 0.7 μL is shown. The same protein reservoir is shown in Fig. 2C. The reservoir was investigated through an optical microscope (Leica) for the alignment of the 2 layers. The piece of the RC dialysis membrane which is embedded within the microfluidic chip can be clearly distinguished in the same figure, as well as the microfluidic channels (scale 400 μm). Another chip, similar to the one illustrated in Fig. 2A and B, was designed with a maximum volume of 0.2 μL (not shown here). The microchip depicted in Fig. 2B (bottom) contains six reservoirs of 0.7 μL each for the protein solution. The objective for developing a device with six protein reservoirs is to facilitate the investigation of phase diagrams. A protein

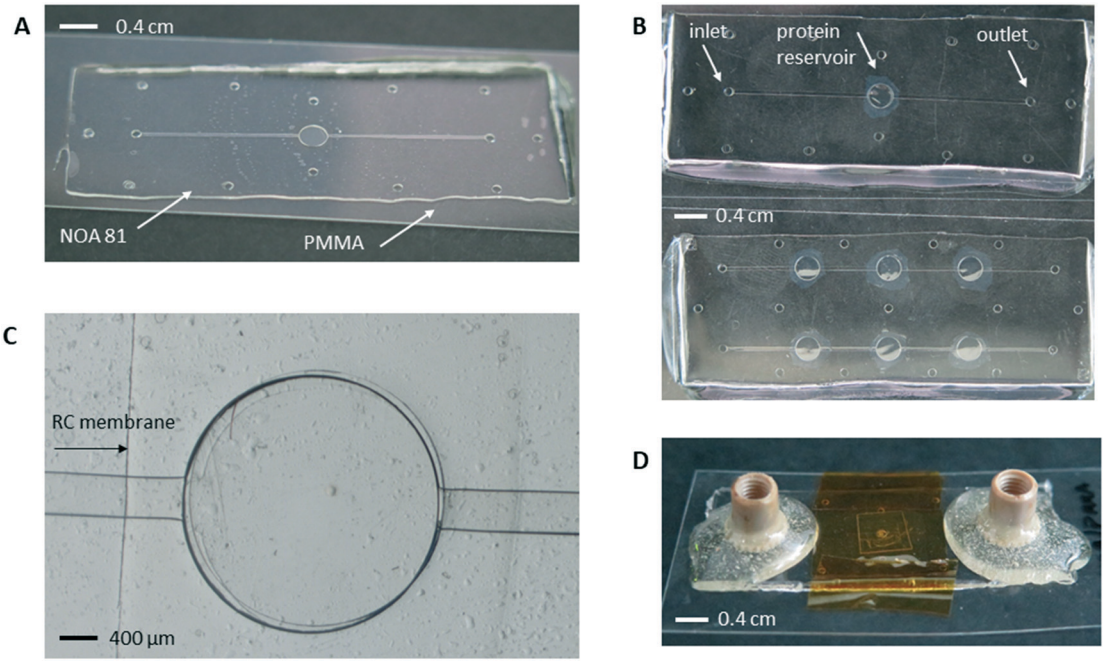

Fig. 2 NOA 81 microfluidic chips embedding an RC dialysis membrane for the on-chip crystallization of proteins and *in situ* X-ray measurements. (A) NOA 81 microchip on a 175 μm thick PMMA substrate. Volume of protein reservoir: 0.7 μL. (B) Top view of the chip illustrated in (A) where the inlet/outlet for the fluidic connectors and the protein reservoir are shown (top). A microchip containing 6 protein reservoirs (0.7 μL each) for investigating phase diagrams *via* composition and temperature control (bottom). (C) Top view of the protein reservoir through an optical microscope. The RC dialysis membrane incorporated into the microchip can be distinguished. (D) Picture of a microchip ready-to-use for the on-chip crystallization of proteins. The protein sample is encapsulated in the central reservoir by a piece of PMMA and Kapton tape. Peek Nanoport connectors are bonded on the inlet and outlet of the device with fast epoxy glue.

solution of constant concentration is deposited in all six reservoirs at the same time. The crystallization solution introduced in one of the linear channels has an initial concentration C_1 and the solution introduced in the other channel has an initial concentration C_2. The temperature of the reservoirs can be controlled by Peltier modules in pairs by supporting the chip on three different copper plates (T_1, T_2, and T_3), as described in more details in the section for the development of the temperature control prototype (see the ESI†). In this case, six different crystallization conditions can be monitored simultaneously on one single microchip and by varying the temperature or the concentration of the crystallization solutions, more crystallization conditions can be investigated on the same device with the less possible consumption of protein sample. We study extremely slow processes that can last up to 50 days as shown in Fig. 5. Under such conditions, and because the osmotic pressure difference across the membrane is very small (dilute protein solutions), there is no significant solvent trans-membrane flux, and solute diffusion homogenizes the concentration of the crystallizing agents (salts/PEGs in our case) in the protein reservoirs connected in series.

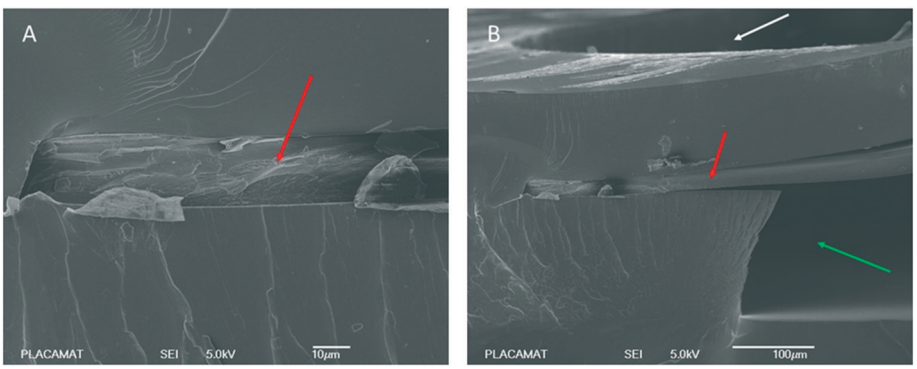

Fig. 3 SEM images obtained from a profile cross section of the chip. (A) The dialysis membrane integrated into the NOA resin and (B) a view highlighting the protein reservoir (white arrow) and the microfluidic channel (green arrow). The red arrows in both cases indicate the RC dialysis membrane.

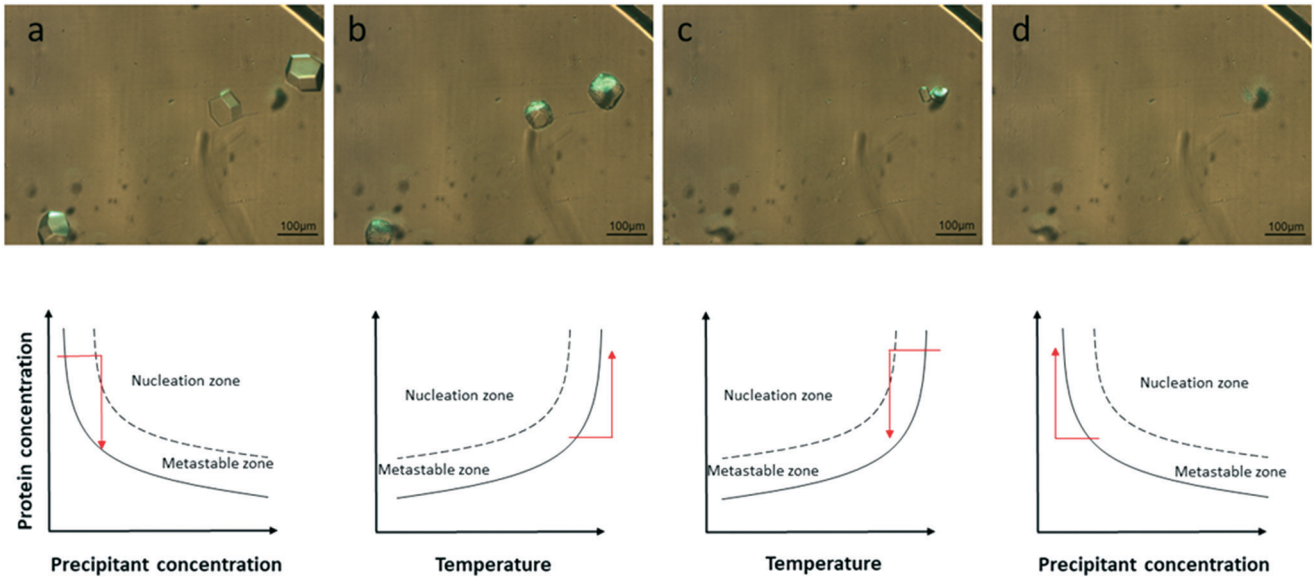

Fig. 4 Crystallization and dissolution experiment performed on-chip *via* the micro-dialysis method using ~30 mg mL^{-1} lysozyme. a) Nucleation and growth at 293 K, NaCl 0.75 M. b) Dissolution at 300 K, NaCl 0.75 M. c) Fast nucleation at 293 K, NaCl 0.75 M. d) Dissolution at 293 K, NaCl 0 M. The top figures show crystals of lysozyme grown inside the protein reservoir of the microfluidic chip for conditions a–d. The bottom figures are a schematic view of the respective phase diagrams as a function of the precipitant concentration (a and d) when the temperature is constant or as a function of temperature (b and c) when the precipitant concentration is constant. The red arrows illustrate the kinetic trajectory for the dialysis crystallization experiments.

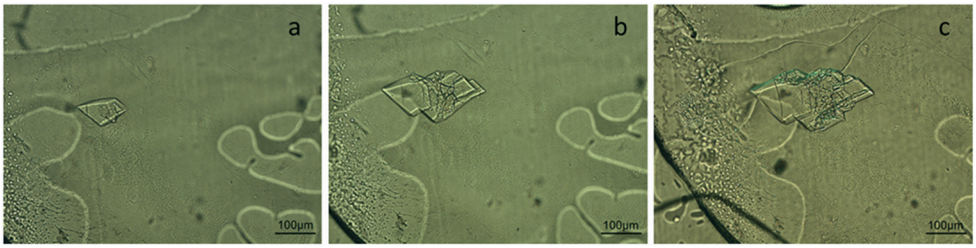

Fig. 5 Crystals of IspE (~10 mg mL^{-1}) grown on-chip *via* the micro-dialysis method after a) 6 days, b) 19 days and c) 50 days from the onset of the experiment. Crystallization conditions: 8% w/v PEG 8000, 5 mM $MgCl_2$, 5 mM ATP, 0.1 M sodium citrate pH 6 and T = 293 K.

As described so far, the reservoir dedicated to be used for the deposition of the protein sample remains open to the atmosphere. We used the following method to encapsulate the protein sample within the dialysis reservoir. Once the droplet of protein solution is deposited inside the reservoir right upon the dialysis membrane, silicone grease is placed around the protein reservoir and a small piece of PMMA is gently placed on the top. The contact between the NOA sticker and the PMMA piece is a solid/solid interface and the presence of the silicon grease between them doesn't ensure any kind of bonding or irreversible sealing. The only way to produce irreversible sealing would be to expose again the NOA resin to UV radiation while being in contact with the PMMA piece. However, this is not feasible considering that the NOA was completely polymerized after the second exposure during the fabrication of the microchips. In order to circumvent this limitation and to ensure a good sealing of the protein reservoir, a piece of Kapton tape is set above the PMMA layer in order to improve air tight closure of the reservoir, as shown in Fig. 2D. The Kapton tape is not in contact with the protein reservoir directly but with the PMMA piece that is first set above the reservoir. The PMMA piece ensures that no contamination of the protein sample can occur and the Kapton tape will not fold or collapse into the reservoir. Another way to encapsulate the protein sample and seal the reservoir would be to directly set the Kapton tape right above the protein reservoir. However, this way of sealing would bring the sticky part of the Kapton tape in direct contact with the reservoir and would possibly have a negative influence on the crystallization process. The assembly also ensures the absence of leakages from the reservoir and the materials are bio compatible and show good transparency to X-rays for *in situ* measurements. The PMMA piece used for the encapsulation of the protein sample is the same as the sheet used as a substrate for the NOA stickers with a thickness of 175 μm. Moreover, the permeability of PMMA to gas is very low. PMMA has been characterized as impermeable to air.[36] Peek NanoPort connectors were bonded on the inlet and outlet of the

microfluidic channel using fast epoxy glue (Fig. 2D). Tubes plugged on these connectors were used to connect the microchip with the pressure driven system for fluid handling and mixing.

Once the protein is encapsulated within the dialysis reservoir, the filling of the chips is carried out by pushing the crystallization solutions into the microfluidic chip using the MFCS-EZ pressure system (Fluigent). The inlet pressure value varies depending on the solution used. Thus, for a solution with a viscosity close to that of water, the injection/inlet pressure varies between 20 and 60 mbar depending on the desired flow rate and between 50 and 150 mbar for more viscous solutions such as PEG (PEG 8000) at concentrations above 15% w/v. The solute diffusion across the membrane is imposed by a difference in concentration of the crystallizing agents (salt/PEG) between the two compartments of the microchip that are separated by the dialysis membrane. In our device, crystallization of the proteins occurs under static conditions regarding the protein solution and not under flowing conditions.[40] This is a major asset as crystallizing the protein solutions under flowing conditions can be challenging and can affect the quality of the growing crystals.[42,43] However, the crystallization solution can flow continuously within the microfluidic channel of our device, offering the possibility to exchange dynamically crystallization conditions while using the same protein sample, thus reducing also the consumption of the valuable protein sample.

The chips can be reused several times depending on the kind of crystallization solution used during the experiments. The Kapton tape and the PMMA piece can be easily removed from the protein reservoir. In the case of low viscosity solutions (salts), the chips can be reused several times if the dialysis membrane or the bonding of NOA on PMMA is not damaged. In the case of viscous solutions (PEG), it is better not to re-use the chip, unless the PEG solution can be removed from the channels using a water flow. Visual inspection of the dialysis membrane under a microscope after each experiment is the most direct way to observe any changes or damage to the membrane. Another way to observe changes in the membrane is by using water flow. If the membrane is damaged, the solution leaks through the protein reservoir and there is no effluent in the outlet point of the microchip. This way is more efficient to indirectly inspect the dialysis membrane because leakages occur every time, even when the membrane is not completely damaged. Both ways of inspecting the membrane are non-invasive and they don't alter the surface or the functionality of the membrane. The average lifetime of a microchip after its fabrication has been empirically estimated to be 6 months. After this time period, the chips become more fragile, especially regarding the NOA–PMMA adhesion.

SEM characterization of the microchips

Scanning electron microscopy (SEM) has been performed using a tabletop SEM microscope (TM3030, Hitachi). The SEM photographs (Fig. 3) zoom in the area where the RC dialysis membrane is embedded into the layer of the NOA resin. In Fig. 3A, a profile cross section of the microchip shows exactly the integration of the RC membrane into the layer of NOA. No traces of liquid NOA is observed to be absorbed on the membrane and this can be seen clearly in Fig. 3B. Fig. 3B is a SEM image taken after cutting the microchip near the central protein reservoir where the RC membrane is located. Specifically, in Fig. 3B we can observe a cross section of the area (after cutting the chip) where the dialysis membrane is indicated with a red arrow, the protein reservoir with a white arrow and the microfluidic channel with a green arrow. As may be seen, the membrane is not chemically bonded to the resin. Despite this fact, no leakages were observed across the membrane and between the dialysis reservoir and the fluidic channel, for our operating pressure range (20–60 mbar for aqueous solutions or 50–150 mbar for more viscous solutions) during the crystallization experiments.

Crystallization experiments

Chicken egg-white lysozyme was purchased from Sigma Aldrich as a lyophilized powder, dissolved in distilled water and filtered to obtain a solution with a final concentration of $\sim$30 mg mL^{-1}. Insulin from porcine pancreas was also purchased from Sigma Aldrich as a lyophilized powder, dissolved in 0.5 M hydrochloric acid at pH 3 and filtered to obtain a solution with a final concentration of $\sim$2.5 mg mL^{-1}. IspE, a kinase from *Agrobacterium tumefaciens*, was used with a final concentration of $\sim$10 mg mL^{-1} (F. Borel *et al.*[48]). All protein solutions were filtered through 0.22 μm Millipore filters prior to their use. The membranes integrated into the chip were the standard regenerated cellulose (RC) membranes Spectra/Por® (Spectrum Labs). The crystallization mixtures were all centrifuged and filtered to remove all solid particles (precipitate, dust or nuclei of crystals) prior to their use. Table 1 summarizes the experimental conditions (protein concentration, initial concentration of the crystallization solution, MWCO of the membrane, and temperature) for the on-chip crystallization of lysozyme, IspE and insulin through the dialysis method.

Results and discussion

Crystallization experiments

The crystallization tests were carried out using three different proteins. These proteins have various molecular weights and diverse conditions to crystallize which enables the investigation of the versatility of the microfluidic chip. For example, we tested the resistance of the microchip against the different chemicals used during the crystallization experiments like sodium chloride (NaCl), sodium acetate (CH_3COONa), sodium citrate ($Na_3C_6H_5O_7$), polyethylene glycol (PEG) of molecular weight from 1 to 8 kDa, acetone (C_3H_6O) and hydrochloric acid (HCl) or additives like magnesium

Table 1 Experimental conditions for the on-chip crystallization of 3 soluble proteins *via* the dialysis method. Less than 1 μL of protein was placed in the protein reservoir of the microfluidic chip for each crystallization experiment

Protein	Protein concentration (mg mL^{-1})	Initial concentration of reservoir solution	Membrane MWCO (kDa)	Temperature (K)
Lysozyme	~30	0.75–0.85 M NaCl 100 mM CH_3COONa pH 4	6–8	293–300
IspE	~10	18% (w/v) PEG 8000 5 mM $MgCl_2$ 5 mM ATP 100 mM $Na_3C_6H_5O_7$ pH 6	12–14	293
Insulin	~2.5	1 mM HCl 5 mM $ZnCl_2$ 50 mM $Na_3C_6H_5O_7$ pH 6 10% (v/v) C_3H_6O	3.5	293

chloride ($MgCl_2$), zinc chloride ($ZnCl_2$) or adenosine triphosphate (ATP).

Chicken egg-white lysozyme

In this section, we describe the crystallization of lysozyme on the microchips in order to demonstrate the control over the crystallization process and verify the reversibility of the dialysis method by modifying the temperature or the concentration of the precipitant solution. The experimental conditions are summarized in Table 1. Temperature and concentration gradients were used to nucleate, grow and dissolve the crystals. Fig. 4 (top) shows the nucleation and growth of lysozyme crystals (a), the dissolution of the crystals using temperature (b), their re-nucleation (c) and finally their re-dissolution using concentration as a variable (d). The respective phase diagrams showing the kinetic pathway for each case are illustrated in Fig. 4 (bottom). The red arrows show the kinetic trajectory of the dialysis method for crystallization. During the onset of the experiment, the temperature was set at 293 K. Nucleation occurred and lysozyme crystals grew within the protein reservoir, as shown in Fig. 4a. Then, the temperature was increased gradually up to 300 K, while the concentration of the crystallization solution remained constant, in order to dissolve the crystals (Fig. 4b top). This step is consistent with the fact that lysozyme has a direct solubility, *i.e.* the solubility increases with temperature rise. After total dissolution of the crystals, the temperature was then rapidly decreased to the initial temperature value (293 K) and new, smaller crystals nucleated and subsequently grew (Fig. 4c). This second nucleation event appeared faster than the first one (Fig. 4a), as the protein reservoir was already at equilibrium with respect to the precipitant concentration. The last step of the experiment (Fig. 4d) was to exchange the crystallization solution circulating within the microfluidic channels with buffer solution (without salt), in order to dissolve the newly formed crystals. The second dissolution occurred due to the concentration gradient between the protein reservoir and the buffer solution, while the temperature remained constant at 293 K. The first dissolution event achieved through temperature control was completed within 15 min and the second one, achieved through control over the precipitant concentration, was completed after 60 min. This observation is not peculiar, since equilibrium concentration needs to be reached inside the protein reservoir before dissolution occurs.

In Fig. 4a tetragonal lysozyme crystals can be seen. Crystals with the same morphology were also observed by Hansen *et al.*[22] who used free interface diffusion (FID) in a microfluidic device. This crystallization method promoted the formation of large single lysozyme crystals. However, in the rest of the photos in Fig. 4 this typical morphology is changing since the lysozyme crystals undergo temperature- or concentration-based variations. Variations in the morphology of lysozyme crystals were also reported by Talreja *et al.*[17] who developed an evaporation-based crystallization platform. In this device crystallization occurs through evaporation: protein and precipitant solutions are mixed in a droplet which gradually gets concentrated through evaporation of the solvent.

IspE from *Agrobacterium tumefaciens*

A crystallization experiment of IspE from *Agrobacterium tumefaciens* was conducted to demonstrate the compatibility of the microfluidic chips for experiments with long duration. The experimental conditions are summarized in Table 1. Fig. 5 shows the nucleation and growth of IspE crystals at different time intervals from the onset of the experiment. Specifically, IspE crystals are shown after 6 days from the beginning of the experiment (Fig. 5a), after 19 days (Fig. 5b) and after 50 days (Fig. 5c). The MWCO of the dialysis membrane used for this experiment was sufficient to allow the diffusion of PEG through the membrane and protein retention. During this experiment, the crystallization solution flows continuously within the microfluidic channel with a pressure of approximately 90 mbar. In order to ensure continuous flow within the microfluidic channel, the external reservoir containing the crystallization solution was refilled when it was necessary.

For experiments with long duration, dynamically monitoring the on-chip protein crystallization *via* the dialysis method would provide further information on the kinetics of the process and we are currently working towards this direction. For the experiments conducted in the present work, only photos of the crystallization process in specific time

intervals were taken with the aid of a digital camera connected to a microscope.

IspE and insulin for serial X-ray data collection

The dialysis method allows the growth of numerous, isomorphous micro crystals required to perform serial X-ray diffraction experiments. A large number of micro crystals of IspE (Fig. 6a) and insulin (Fig. 6b) were grown. The conditions of the experiments are given in Table 1. In the microdialysis experiment in the case of IspE, the crystallization solution circulated in the microfluidic channel (Table 1) was balanced against the solution of the mixture of the protein (~10 mg mL^{-1} in 50 mM Hepes pH 7, 3 mM DTT, 0.1 M NaCl, 1 mM $MgCl_2$) with ATP (5 mM) in $Na_3C_6H_5O_7$ buffer pH 6, housed in the dialysis reservoir of the microchip. The main difference between the crystallization experiments illustrated in Fig. 5 and 6a is the final supersaturation obtained in the dialysis chamber (*i.e.* the concentration of PEG 8000). Therefore, compared to Fig. 5, which shows the low symmetry monoclinic IspE crystal in the presence of 8% PEG 8000, at 18% PEG 8000 (Fig. 6a), the number of these crystals is much larger while their size is much smaller.

For the crystallization of IspE, ATP is one of the molecules comprising the solution of the protein reservoir. Due to its molecular weight, ATP can diffuse across the dialysis membrane, thus lowering the ATP concentration in the protein reservoir and modifying crystallization conditions. Therefore, it is mandatory that ATP is also present in the composition of the crystallizing agent and has to be used as a co-factor in the crystallization process. In this case, it is better to inject the crystallizing agent sequentially instead of preserving continuous flow within the channel of the microfluidic chip. For the experiments carried out with insulin, the chosen crystallization conditions contained up to 10% v/v acetone. These conditions were first tested to grow insulin crystals by the vapor diffusion method (hanging drop). Insulin crystals were grown under the same conditions within the chip, despite the use of highly volatile acetone in the synthesis of the crystallization solution. Acetone proved to be compatible with the materials of the microfluidic device and the RC dialysis membrane. In Fig. 6b, rhombohedral insulin crystals were grown at 293 K *via* dialysis. There are many examples in the literature where insulin crystals are grown in various crystallization experiments and using various techniques. For example, Kwon and Kim[45] grew insulin crystals using the seeding method, and Parambil *et al.*[46] used flow in capillarities to enhance the nucleation of insulin crystals, while Borgstahl *et al.*[47] grew large well-ordered insulin crystals in microgravity. However, the morphology of the crystals also depends on the crystallization method. Dialysis offers a different kinetic pathway compared to other crystallization methods.

Material characterization for *in situ* X-ray diffraction

When microfluidic devices are used for on-chip *in situ* X-ray diffraction experiments, the contribution of the interactions between the materials composing the chip and the X-rays must be considered. The diffraction signal from the crystals is added to the signal known as background noise. Background noise is generated by the diffusion of X-rays through the materials used to manufacture the chip and any other materials that interfere between the chip and the detector, as for example the air. This signal-to-noise ratio between the diffraction signal coming from the crystals and the background noise generated by attenuation or scattering of X-rays through matter should be maintained as high as possible during data collection. Thus, it is crucial to characterize the materials used for fabricating the microfluidic devices in order to minimize phenomena that degrade the signal-to-noise ratio of the diffracted crystals.[14] The materials of such a device should generate a minimum background signal, while being biocompatible and compatible with mechanical constraints imposed by the application.

Diffraction data of lysozyme, IspE and insulin crystals grown on-chip with the microdialysis method were collected at the BM30A-FIP beamline at the European Synchrotron Radiation Facility (ESRF) using an X-ray wavelength of 0.98 Å. The beamline is equipped with an ADSC Quantum 315r detector with a matrix of 3 × 3 CCD for an active surface of 315

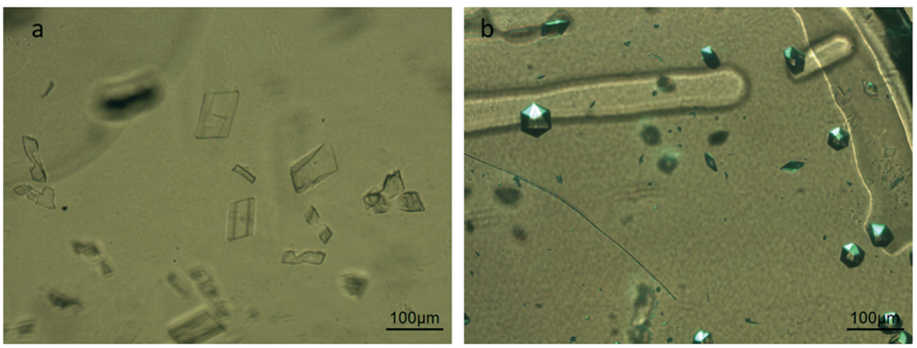

Fig. 6 Multiple isomorphous single a) IspE and b) insulin crystals grown on-chip *via* the micro-dialysis method, used for collecting *in situ* X-ray diffraction data. Crystallization conditions: for IspE 18% w/v PEG 8000, 5 mM $MgCl_2$, 5 mM ATP, and 0.1 M $Na_3C_6H_5O_7$ pH 6 and for insulin: 1 mM HCl, 5 mM $ZnCl_2$, 50 mM $Na_3C_6H_5O_7$ pH 6 and 10% v/v acetone. Crystals of both proteins were grown at 293 K.

× 315 mm and resolution of 9.4 mega pixels. The microchips were mounted in front of the X-ray beam using the robotic arm G-Rob and a sample support that we designed for these experiments (Fig. ESI 4†).

Before the data collection of protein crystals, the microchips were characterized in the same facility. The microchips were placed on the support, mounted on the beamline and exposed to the same wavelength (0.98 Å). In order to perform on-chip X-ray diffraction experiments, it is essential to select appropriate materials for the microchips.[14] Thus, prior to data collection from protein crystals, the scattering background of the microfluidic chip that we developed was compared to the background noise generated by two conventional plates for crystallization screening and *in situ* X-ray diffraction, Greiner CrystalQuickX and Crystal Cube by Cube Biotech. The part of the microfluidic device that is exposed to the X-ray beam is only the protein reservoir composed of the Kapton tape (~20 μm thickness), the PMMA piece below the Kapton tape and the PMMA substrate of the microchip (350 μm thickness both) and the RC dialysis membrane (~40 μm thickness). The distance between the chip/commercial plate and the detector was 200 mm. Fig. 7a illustrates the intensity *versus* resolution graphs for the microchip and the two commercial plates. The intensity corresponds to the value recorded by the detector for each device, after subtracting the measurement done without any sample (chip or plate) in front of the beam, *i.e.* subtracting the measurement for the atmosphere surrounding the materials, which in this case is helium. It is obvious that our device generates less background noise compared to the other two crystallization plates, as indicated by the broad peak in Fig. 7a. Reducing the thickness of the device is crucial for *in situ* data collection.[3,14] Low thickness translates to less matter interference in the path of the X-ray beam. The protein reservoir of the microfluidic chip that we designed has a total thickness of ~410 μm which is affected by the interaction with X-rays because the layer of NOA is out of the X-ray beam path, while the respective thickness for the CrystalQuickX plate is ~700 μm. However, a very low thickness can lead to excessive evaporation and issues associated with the rigidity of the microchip itself.[8] Our microchip proposes a fair compromise between the rigidity of the device and the reduction of background noise for data collection.

Apart from the thickness of the microfluidic assembly, the scattering signal of each material composing the device was also measured. Using low density materials to fabricate the chip is as important as reducing the thickness, because high molecular weight materials add up matter across the way of the X-ray beam resulting in increased background noise. The materials investigated were the Kapton tape, the RC dialysis membrane and the PMMA sheet. Each material was exposed for 20 s to the X-rays (wavelength 0.98 Å) and each measurement was followed by an exposure of 20 s to the surrounding environment. For example, the exposure of the PMMA sheet was followed by an exposure to an empty space, where no material apart from air interfered between the beam and the detector, and so on. However, instead of air we used helium flux, as it is lighter than air and contributes less to scattering effects. The amplitude of X-ray scattering increases with the atomic number of each element. The distance between the sample and the detector was 200 mm. Scattering images were viewed using Adxv and radial intensity plots were designed using ROOT. In Fig. 7b, the intensity of background scattering of various materials is plotted against resolution (Å). For PMMA, a wide peak is present between 4 and 8 Å and then the intensity decreases. The broad peak corresponds to the diffusion of X-rays in the material. In the case of Kapton tape, the peak is even more diffuse. On the other hand, even if the contribution of the RC dialysis membrane to the total background noise is very small, a peak can be observed between 4 and 5 Å. The noise generated from the microchip is maximum (peak) at low resolution (6–7 Å), which is less critical for processing the data at higher resolution. Moreover, the background noise obtained from the microchip is still 15

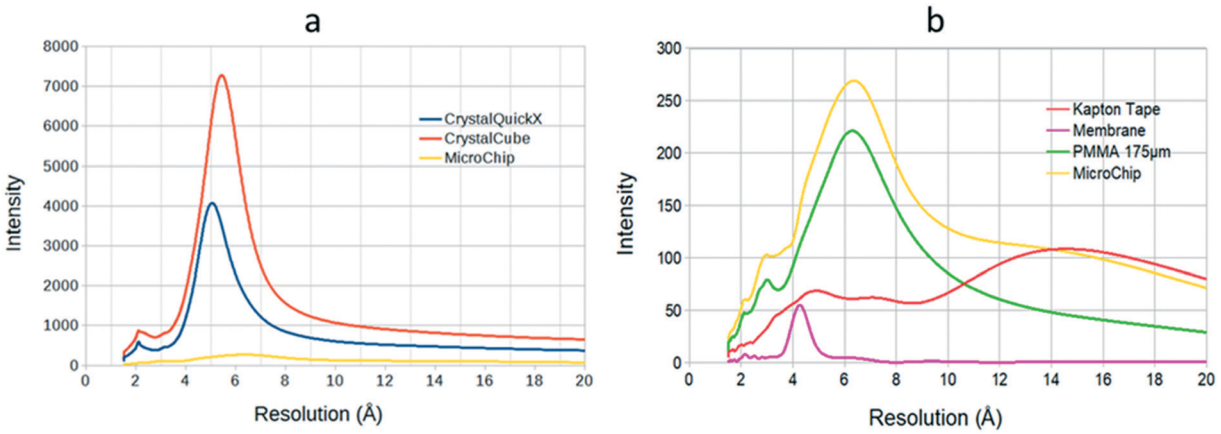

Fig. 7 a) Background scattering intensity as a function of resolution (Å) for the microfluidic chip developed in the present work and conventional crystallization plates (CrystalQuickX and CrystalCube). b) Background scattering intensity as a function of resolution (Å) from the materials composing the microfluidic assembly (2 × 175 μm thick PMMA sheet, ~20 μm thick Kapton tape and ~40 μm thick RC dialysis membrane).

to 27 times lower than the background noise of commercial crystallization plates (Fig. 7a). The intensity in all the curves corresponds to the value recorded by the detector for each material, after subtracting the measurement done without any sample in a helium atmosphere. Helium flux can also be used while collecting diffraction data from protein crystals. This way, the surrounding environment during X-ray diffraction measurements and the one during the experiments conducted for the characterization of the chip's materials are the same and can be used as reference and be subtracted from each measurement.

In situ X-ray diffraction measurements from protein crystals

In situ X-ray diffraction data from lysozyme, IspE and insulin crystals grown on-chip were collected at the BM30A-FIP beamline (ESRF). The wavelength of the X-ray beam was 0.98 Å and the exposure times and the oscillation angles used for all the crystals were comparable. The data collection was carried out at room temperature. The microchips containing the protein crystals were mounted on the beamline using the 3D printed support described in Fig. ESI 4.† Reflections were processed, indexed and integrated using XDS.[37] Molecular replacement and refinement were performed using the CCP4 suite.[38]

Diffraction data sets were collected from single crystals grown within the protein reservoir of the chip and data were eventually merged. Statistics for different crystals of lysozyme, IspE and insulin, as well as merged data, are shown in Table 2. The composition of the crystallization solutions is given in Table 1. However, for the *in situ* X-ray diffraction experiments, lysozyme crystals were grown in 0.85 M NaCl (2nd column, Table 2) or 0.75 M NaCl (3rd column, Table 2) and IspE was crystallized in 20% w/v PEG 8000 (4th and 5th column, Table 2). The mosaicity of the crystals grown on-chip and analyzed *in situ* by X-ray diffraction at room temperature is significantly lower compared to the respective value obtained from crystals of the same protein crystallized using another experimental set up and analyzed by X-rays at cryogenic temperature.[9] Specifically, for lysozyme crystals grown on-chip in a crystallization solution with 0.75 M NaCl, the measured mosaicity at room temperature was 0.07° (Table 2). On the other hand, the observed mosaicity at cryogenic temperature of lysozyme crystals grown with the conventional vapor diffusion (hanging drop) method under the same crystallization conditions was much higher, 0.328°, and the respective value for crystals grown with the previously described dialysis method was 0.128°.[9] It is noteworthy that the compared values of the mosaicity were obtained *via* XDS statistics, on the same ESRF beamline, with the beam of photons of equivalent intensity and on crystals comparable in size. Therefore, such an observation can be attributed to the slowly varying conditions required for early crystal nucleation and relatively undisturbed lattice formation of crystals that we are able to achieve in the chip as well as the further absence of handling the crystals. This observation is in agreement with similar results reported elsewhere.[13] In addition, recently it has been demonstrated that specific and global radiation damage are much less decoupled at room temperature than they are at cryogenic temperatures.[39] These observations illustrate the interest in reviving the practice of collecting X-ray diffraction data of biological macromolecules at room temperature at synchrotron sources.

In the case of lysozyme (Table 2), complete data sets have been obtained from single crystals. Indeed, due to the high symmetry of lysozyme crystals, there was no need to use X-ray serial crystallography in order to collect data sets from various crystals and then merge these data. Despite the fact that the data collection was carried out at room temperature, no damage of the crystals was observed. In contrast, IspE symmetry and accessible angle amplitude did not allow the collection of a complete data set from one crystal. The statistics for a merged data set obtained combining the data sets from six isomorphous IspE crystals randomly oriented with various crystals qualities are shown in Table 2 (5th column). In the case of insulin, the partial data sets of six

Table 2 Crystallographic statistics obtained *via* XDS from lysozyme, IspE and insulin crystals grown within the microfluidic chip. The 5th and 7th column correspond to data collected from six isomorphous crystals of IspE and insulin, respectively, and merged to a complete data set. Values in parentheses correspond to the highest resolution shell

Protein	Lysozyme (1 crystal)	Lysozyme (1 crystal)	IspE (1 crystal)	IspE (6 crystals)	Insulin (1 crystal)	Insulin (6 crystals)
Resolution (Å)	50–1.60 (1.70–1.60)	50–1.45 (1.54–1.45)	50–2.15 (2.28–2.15)	50–2.30 (2.40–2.30)	50–2.00 (2.12–2.00)	40–2.10 (2.20–2.10)
Mosaicity (°)	0.06	0.07	0.11		0.18	
Space group	$P4_32_12$	$P4_32_12$	$C2$	$C2$	$R3$	$R3$
Unit cell parameters	79.23, 79.23, 37.90 90, 90, 90	79.27, 79.27, 37.94 90, 90, 90	72.48, 82.91, 51.01 90, 109.08, 90	72.73, 82.92, 51.17 90, 109.20, 90	82.58, 82.58, 34.11 90, 90, 120	82.58, 82.58, 34.12 90, 90, 120
Total reflections (observed)	50 351	65 652	19 362	91 062	7353	34 986
Unique reflections (observed)	14 911	12 725	9716	22 461	4194	9612
Redundancy	3.38 (3.13)	5.16 (3.83)	1.99 (1.91)	4.05 (2.88)	1.75 (1.66)	3.64 (2.77)
Completeness (%)	90.5 (93.4)	57.8 (63.0)	62.1 (64.8)	89.5 (74.0)	71.5 (74.7)	94.9 (91.1)
I/σ	13.1 (2.9)	15.3 (2.3)	8.0 (2.0)	5.8 (1.9)	6.8 (2.0)	7.0 (2.7)

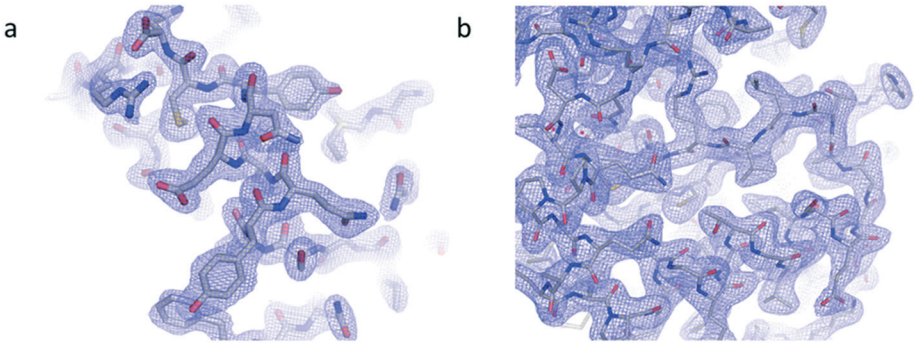

Fig. 8 Electron density maps derived from crystallographic data collected from multiple crystals of a) insulin and b) IspE. The maps at 2.1 Å and 2.3 Å resolution, respectively, are contoured at 1σ.

isomorphous crystals were merged in order to provide a complete data set (Table 2, 7th column). However, insulin crystals were much smaller than IspE crystals (<50 μm). Despite the presence of microcrystals, it was feasible to collect data *in situ* using the microfluidic device that we developed.

Electron density maps

Electron density maps from insulin and IspE (Fig. 8 a and b) have been obtained at 2.1 Å and 2.3 Å resolution, respectively. Structure refinement worked correctly as indicated by *R*-work factors of 0.15 and 0.16 and *R*-free factors of 0.20 and 0.21, respectively for insulin and IspE. The derived electron density maps, generated from the merging of various data sets obtained through *in situ* X-ray diffraction for both proteins, illustrate the quality of detailed structural information that can be achieved. In addition, our diffraction analyses demonstrate the compatibility of our microfluidic chips with serial X-ray crystallography.

Conclusions

A microfluidic chip has been developed for on-chip protein crystallization using the micro-dialysis method. The device was designed in order to integrate commercially available RC dialysis membranes within the chip in a reproducible way for on-chip protein crystallization. The MWCO range of the RC membranes can vary from 3.5 to 14 kDa depending on the protein sample and the crystallization conditions. The flexibility of choosing the MWCO of the membrane, the rapid prototyping of the microfluidic chips and the relatively low cost of the materials enable the fabrication of numerous chips. The protocol presented in this work can be upgraded in order to fabricate microchips with different types and MWCOs of the embedded membranes.

Once protein crystals were grown on-chip, *in situ* X-ray diffraction data were collected for all three proteins investigated in this work. Complete data sets were collected at room temperature from single crystals of lysozyme, whereas diffraction data from six isomorphous microcrystals of IspE and insulin were merged to yield complete data sets, demonstrating the compatibility of our microfluidic device with serial X-ray crystallography experiments. *In situ* data collection was rendered feasible due to the relatively high X-ray transparency of the materials chosen to produce the microchips and the low background noise of the microfluidic assembly. Indeed, diffraction data were collected from the materials composing the microfluidic chip in order to evaluate the background noise generated by the scattering and attenuation of X-rays. The low level of background scattering of the microchip, especially at high resolution values required for structure determination in protein crystallography, is evidence that high quality diffraction data can be collected. Moreover, this chip allows the *in situ* collection of X-ray diffraction data at room temperature, avoiding problems encountered with conventional cryoprotectants. The automation level of the whole process is enhanced by the use of a 3D printed support, adapted to mount up to 3 chips simultaneously in front of the beam at automated *in situ* X-ray diffraction beamlines. Therefore, there is no need to harvest crystals from the crystallization setup and transfer them to the beam, steps that can add up stress to the fragile protein crystals. We have developed a microfluidic chip that includes all the stages in the crystallization pipeline, from crystal growth using micro-dialysis to *in situ* data collection and does not require any handling of the protein crystals prior the X-ray diffraction experiment. In addition to using relatively inexpensive materials for fabrication, the chips can be reused several times as long as they are sufficiently washed, they don't show any mechanical damage and the dialysis membrane is not detached from the NOA sticker.

Our microchips can be used also for screening and optimizing crystallization conditions for mapping temperature–precipitant concentration phase diagrams. A large number of isomorphous crystals suitable for serial X-ray crystallography can be grown on-chip through reversible control over the concentration and temperature conditions, using a low volume (0.2–0.7 μL) of the protein sample. The combination of precise and dynamic chemical composition control, a prototype for temperature control, real time observation and *in situ* X-ray diffraction studies is promising for new, challenging areas of investigation such as the crystallization of membrane proteins. We expect that this inexpensive device would

contribute significantly to the field of structural biology through serial X-ray crystallography studies at synchrotron and XFEL sources.

Conflicts of interest

There are no conflicts to declare.

Acknowledgements

MBS thanks the CEA's International Doctoral Research Program (Irtelis) for the PhD Fellowship to NJ, and SJ acknowledges the Horizon 2020 Research and Innovation Program of the European Union under grant no. 722687 for the fellowship MARIE SKŁODOWSKA – CURIE. MBS acknowledges the support of the MI/CNRS under the contract Instrumentation at the limits 2014–2015. The authors extend their special thanks to Dr Jean-Luc Ferrer (Synchrotron Group, IBS, Grenoble), who took active interest in taking forward the protein crystallization problem for protein crystallography. JBS acknowledges CNRS and Solvay for funding. MBS, NJ and SJ thank LIPhy for the clean room to perform microfabrication. IBS acknowledges integration into the Interdisciplinary Research Institute of Grenoble (IRIG, CEA).

References

1 J. M. Martin-Garcia, C. E. Conrad, J. Coe, S. Roy-Chowdhury and P. Fromme, *Arch. Biochem. Biophys.*, 2016, **602**, 32–47.
2 R. L. Owen, D. Axford, D. A. Sherrell, A. Kuo, O. P. Ernst, E. C. Schulz, R. J. Dwayne Miller and H. M. Mueller-Werkmeister, *Acta Crystallogr., Sect. D: Struct. Biol.*, 2017, **73**, 373–378.
3 Y. Gicquel, R. Schubert, S. Kapis, G. Bourenkov, T. Schneider, M. Perbandt, C. Betzel, H. N. Chapman and M. Heymann, *J. Visualized Exp.*, 2018, **134**, e57133.
4 H. N. Chapman, *et al.*, *Nature*, 2011, **470**, 73–78.
5 S. Sui and S. L. Perry, *Struct. Dyn.*, 2017, **4**, 032202.
6 S. Guha, S. L. Perry, A. S. Pawate and P. J. A. Kenis, *Sens. Actuators, B*, 2012, **174**, 1–9.
7 V. Miralles, A. Huerre, F. Malloggi and M.-C. Jullien, *Diagnostics*, 2013, **3**, 33–67.
8 S. Sui, Y. Wang, K. W. Kolewe, V. Srajer, R. Henning, J. D. Schiffman, C. Dimitrakopoulos and S. L. Perry, *Lab Chip*, 2016, **16**, 3082–3096.
9 N. Junius, E. Oksanen, M. Terrien, C. Berzin, J.-L. Ferrer and M. Budayova-Spano, *J. Appl. Crystallogr.*, 2016, **49**, 806–813.
10 Š. Selimović, F. Gobeaux and S. Fraden, *Lab Chip*, 2010, **10**, 1696–1699.
11 P. Laval, C. Giroux, J. Leng and J.-B. Salmon, *J. Cryst. Growth*, 2008, **310**, 3121–3124.
12 J. Leng and J.-B. Salmon, *Lab Chip*, 2009, **9**, 24–34.
13 S. L. Perry, S. Guha, A. S. Pawate, A. Bhaskarla, V. Agarwal, S. K. Nair and P. J. A. Kenis, *Lab Chip*, 2013, **13**, 3183–3187.
14 K. Dhouib, *et al.*, *Lab Chip*, 2009, **9**, 1412–1421.
15 C. L. Hansen, E. Skordalakes, J. M. Berger and S. R. Quake, *Proc. Natl. Acad. Sci. U. S. A.*, 2002, **99**, 16531–16536.
16 B. Zheng, L. S. Roach and R. F. Ismagilov, *J. Am. Chem. Soc.*, 2003, **125**, 11170–11171.
17 S. Talreja, D. Y. Kim, A. Y. Mirarefi, C. F. Zukoski and P. J. A. Kenis, *J. Appl. Crystallogr.*, 2005, **38**, 988–995.
18 L. Li, D. Mustafi, Q. Fu, V. Tereshko, D. L. Chen, J. D. Tice and R. F. Ismagilov, *Proc. Natl. Acad. Sci. U. S. A.*, 2006, **103**, 19243–19248.
19 W. Du, L. Li, K. P. Nichols and R. F. Ismagilov, *Lab Chip*, 2009, **9**, 2286–2292.
20 C. Sauter, K. Dhouib and B. Lorber, *Cryst. Growth Des.*, 2007, **7**, 2247–2250.
21 B. Zheng, J. D. Tice, L. S. Roach and R. F. Ismagilov, *Angew. Chem., Int. Ed.*, 2004, **43**, 2508–2511.
22 C. L. Hansen, S. Classen, J. M. Berger and S. R. Quake, *J. Am. Chem. Soc.*, 2006, **128**, 3142–3143.
23 G. Kisselman, W. Qiu, V. Romanov, C. M. Thompson, R. Lam, K. P. Battaile, E. F. Pai and N. Y. Chirgadze, *Acta Crystallogr., Sect. D: Biol. Crystallogr.*, 2011, **67**, 533–539.
24 J. M. Schieferstein, A. A. Pawate, M. J. Varel, S. Guha, I. Astrauskaite, R. B. Gennis and P. J. A. Kenis, *Lab Chip*, 2018, **18**, 944–954.
25 M. Heymann, A. Opthalage, J. L. Wierman, S. Akella, D. M. E. Szebenyi, S. M. Gruner and S. Fraden, *IUCrJ*, 2014, **1**, 349–360.
26 M. Budayova-Spano, FR10/57354, UJF, 2010, (extension: EP117730945, US13821053, JP2013528746).
27 M. Spano, J.-B. Salmon and N. Junius, FR3044685A1, UJF, 2015.
28 J. Shim, G. Cristobal, D. R. Link, T. Thorsen and S. Fraden, *Cryst. Growth Des.*, 2007, **7**, 2192–2194.
29 J. de Jong, R. G. H. Lammertink and M. Wessling, *Lab Chip*, 2006, **6**, 1125–1139.
30 M. Kornreich, M. Heymann, S. Fraden and R. Beck, *Lab Chip*, 2014, **14**, 3700–3704.
31 L. Li and R. F. Ismagilov, *Annu. Rev. Biophys.*, 2010, **39**, 139–158.
32 Y. Li, J. Xuan, R. Hu, P. Zhang, X. Lou and Y. Yang, *Talanta*, 2019, **204**, 569–575.
33 B. G. Abdallah, S. Roy-Chowdhury, R. Fromme, P. Fromme and A. Ros, *Cryst. Growth Des.*, 2016, **16**, 2074–2082.
34 D. Bartolo, G. Degré, P. Nghe and V. Studer, *Lab Chip*, 2008, **8**, 274–279.
35 M. Morel, J.-C. Galas, M. Dahan and V. Studer, *Lab Chip*, 2012, **12**, 1340–1346.
36 H. Y. Tan, W. K. Loke and N.-T. Nguyen, *Sens. Actuators, B*, 2010, **151**, 133–139.
37 W. Kabsch, *Acta Crystallogr., Sect. D: Biol. Crystallogr.*, 2010, **66**, 125–132.
38 M. D. Winn, *et al.*, *Acta Crystallogr., Sect. D: Biol. Crystallogr.*, 2011, **67**, 235–242.
39 G. Gotthard, S. Aumonier, D. De Sanctis, G. Leonard, D. von Stetten and A. Royant, *IUCrJ*, 2019, **6**, 665–680.
40 M. Skou, S. Skou, T. G. Jensen, B. Vestergaard and R. E. Gillilan, *J. Appl. Crystallogr.*, 2014, **47**, 1355–1366.
41 M. I. Vaquez, P. Galan, J. Casado, M. J. Ariza and J. Benavente, *Appl. Surf. Sci.*, 2004, **238**, 415–422.

42 P. G. Vekilov and F. Rosenberger, *J. Cryst. Growth*, 1998, **186**, 251–261.
43 A. Kadowaki, I. Yoshizaki, L. Rong, H. Komatsu, O. Odawara and S. Yoda, *J. Synchrotron Radiat.*, 2004, **11**, 38–40.
44 A. A. S. Bhagat, P. Jothimuthu and I. Papautsky, *Lab Chip*, 2007, **7**, 1192–1197.
45 J.-H. Kwon and C.-W. Kim, *J. Cryst. Growth*, 2004, **263**, 536–543.
46 J. V. Parambil, M. Schaepertoens, D. R. Williams and J. Y. Y. Heng, *Cryst. Growth Des.*, 2011, **11**, 4353–4359.
47 G. E. O. Borgstahl, A. Vahedi-Faridi, J. Lovelace, H. D. Bellamy and E. H. Snell, *Acta Crystallogr., Sect. D: Biol. Crystallogr.*, 2001, **57**, 1204–1207.
48 F. Borel, S. Richard, F. Pojer, L. Jacquamet, T. Baiga, J. A. Ramsey, A. Iannello, M. Bowman, J. P. Noel and J.-L. Ferrer, unpublished data.

